TECHNOLOGY FOR THE ADVANCEMENT OF DIE CASTING TOOLING

by

Corey Vian

A Dissertation

Submitted to the Faculty of Purdue University

In Partial Fulfillment of the Requirements for the degree of

Doctor of Philosophy

Purdue Polytechnic Institute

West Lafayette, Indiana

August 2021

THE PURDUE UNIVERSITY GRADUATE SCHOOL

STATEMENT OF COMMITTEE APPROVAL

Dr. Xiaoming Wang, Chair

Department of Engineering Technology

Dr. Milan Rakita

Department of Engineering Technology

Dr. Haiyan Zhang

Department of Engineering Technology

Dr. Solomon Berman

President & CEO, IBC Materials and IBC Coatings

Approved by:

Dr. Kathryne Newton

This work is dedicated to my father Ronald, mother Tina, wife Wei, son Leonardo, and sister Megan. Thank you for your loving support and patience.

ACKNOWLEDGMENTS

Thank you to Xiaoming Wang, Qingyou Han, Milan Rakita, Haiyan Zhang, and Solomon Berman for guidance in my studies.

Thank you to Jeff Foster for your CAD modeling support.

Thank you to Corbin Kuntz in support for manufacturing hot chamber tooling components.

Thank you to Neil Hurlock, Rick Webb, Mike Cole, and Brian Hanthorn for your help in performing dunk testing and friction factor testing.

Thank you to Aaron Reiff, Scott Becom, Keith Hughes, and Kent Mosher for your support and guidance in the metallurgical laboratory.

Thank you to Gregg Whealy and the team at Delaware Dynamics, and Solomon Berman and the team at IBC Coatings, for helping with dunk specimen manufacturing.

TABLE OF CONTENTS

LIST OF TABLES

LIST OF FIGURES

ABSTRACT

High pressure die casting is an industrial metal casting process used to manufacture goods for use in many aspects of society. Within this manufacturing process, the tooling is subjected to chemical attack from molten aluminum while also being responsible for heat removal during solidification. The purpose of this study is to develop and test materials that allow the tools to better withstand the chemical attack, and to develop design rules to guide the use of additive manufacturing for improving the heat exchange function of by way of conformal cooling.

Within the material studies, a gooseneck with a niobium lining was developed to allow the successful implementation of hot chamber aluminum die casting. In addition, a manufacturing plan is described that will allow the niobium gooseneck design to be easily sourced by die casting companies. The material studies also included dunk testing of several coatings, including a plasma assisted chemical vapor deposition silicon doped diamond like carbon (PACVD Si-DLC). The Si-DLC coating performed the best in the dunk testing as compared to bare and nitrocarburized tool steel, and a number of other coating architectures.

Within the study of additively manufactured conformal cooling design, a finite difference model is developed that allows a simulated experiment that produced a number of useful equations that guide the design of die casting tooling. During the development of the models, it was discovered that little is known regarding the friction factors of additively manufactured steel pipes, so a factorial experiment was employed top empirically determine said friction factors. Charts allowing design engineers to quickly determine pressure drops and heat transfer coefficients of conformal cooling designs was produced as well.

CHAPTER 1. INTRODUCTION

High pressure die casting is a metal casting process used with aluminum, magnesium, and zinc. In this process, a hydraulic cylinder opens and closes a die, while another hydraulic cylinder, with the aid of specially designed pump components, injects metal into the die while it is closed. Together, the metal injection pump components and die are commonly referred to as die casting tooling (North American Die Casting Association, 2007; Andersen, 2004; Doehler, 1952; Harvill & Jordan, 1945).

Within high pressure die casting there are two methods for injection of the molten material into the mold, the cold chamber method, and the hot chamber method. Although there are economic and metallurgical benefits to using the hot chamber method, the manufacture of aluminum die castings has been limited to the cold chamber process due to the chemical affinity of the molten aluminum to the steels used to build the hot chamber metal injection pump. This hot chamber pump, commonly referred to as a gooseneck, is partially submerged in the molten aluminum holding furnace, which leads to the dissolution of the pump. Although the cold chamber metal pump components are not subjected to continuous submersion in molten aluminum, they still experience extreme service conditions, with wear from repeated exposure to molten aluminum and friction (North American Die Casting Association, 2007; Andersen, 2004; Doehler, 1952; Harvill & Jordan, 1945).

The dies also experience extreme service conditions while serving the important functions of forming the casting to near net shape as the molten metal fills the die cavity and exchanging heat to facilitate and control the solidification of the casting. During the filling of the die cavity,

molten metal can move at velocities over 1000 inches per second, while at the end of filling pressures within the molten metal, and hence on the die cavity, can exceed 15,000 pounds per square inch. Throughout the casting cycle, the temperature of the die rapidly increases during the filling with molten aluminum, and rapidly cools from both internal cooling lines and externally applied water and die release agents. These temperature fluctuations cause thermo-mechanical loads which lead to thermal shock and thermal fatigue, with a large portion of the surface stress caused by external cooling (North American Die Casting Association, 2007; Andersen, 2004; Doehler, 1952; Harvill & Jordan, 1945).

The goal of this research is to help improve the aluminum die casting process by developing technologies within the design of die casting tooling to enable hot chamber aluminum die casting and the reduction, or possible elimination, of the need for external die cooling.

1.1 Scope

The scope of the research included the design and manufacture of multi-material goosenecks, the testing of surface coatings in molten aluminum, and the simulation and design of additively manufactured die cooling lines.

1.2 Significance

The die casting process is currently used to produce a large quantity of the aluminum castings used today, and though the hot chamber process would be preferred due to its faster cycle and improved part quality, only the cold chamber process can be applied due to the short service of the steel gooseneck when trying to apply the hot chamber process. By developing a gooseneck that allows the hot chamber process to be used with aluminum alloys, one gives the ability to

produce high volume aluminum castings at a significant technical advantage to those made with the cold chamber process. The die casting process is also hindered by the need to use externally applied die cooling and release agents. The application of these cooling and release agents causes a reduction in manufacturing throughput by increasing the cycle time and reducing the part quality. It is envisioned that the results of this research allow the aluminum die casting industry to attempt to utilize the hot chamber process with aluminum alloys, and eliminate, or greatly reduce, the need for die release agents.

1.3 Research Questions

The hot chamber process offers technical advantages over the cold chamber process; however, the steel pumping mechanism currently employed cannot withstand submersion in molten aluminum for any extended length of time. When submerged, the aluminum chemically attacks the steel, quickly dissolving the pump housing, which in turn leads to catastrophic failure of the liquid metal pump. By developing a hot chamber injection tooling system capable of prolonged submersion in molten aluminum, the hot chamber process will be able to be applied with aluminum alloys.

Research Question #1:

- What materials and processes can be used in the design and manufacture of goosenecks for use with aluminum hot chamber die casting?

Die casting dies are currently subjected to large temperature cyclic temperature variations caused by inadequate internal cooling, and the subsequent use of external cooling to meet the required cycle times. The use of external cooling can be greatly reduced, or possibly eliminated, by

designing a die in such a fashion as to remove all required heat internally. Eliminating the external cooling is expected to greatly reduce the cycle time of the process and reduce thermal stress on the tooling.

Research Question #2:

- How can die cooling lines be designed and manufactured to provide optimized internal cooling?

1.4 Assumptions

The assumptions of this study were:

- The physical constants selected for the cooling line design simulation were proper for the case of aluminum die casting.

1.5 Limitations

The limitations of this study were:

- The aluminum dunk experiment was limited to the use of Aluminum Association E380 aluminum alloy.
- The gooseneck design was limited to the build requirements of the available die casting machine.
- The maximum available water supply pressure for friction factor testing was 50 psi.

1.6 Delimitations

The delimitations of this study were:

- This study included only one possible method for manufacturing multi-material tooling.

- Only one possibly acceptable refractory metal was used in the production of the multi-material goosenecks.
- The cooling line simulations were limited in the levels and ranges of the various design inputs.
- The coatings selected for study were down selected from commercially available coatings based on previous research and theory of untested coatings. Not all available coatings could be tested.
- Only straight tubes were tested in the friction factor experiment.

1.7 Summary

This chapter served to introduce and detail the aluminum die casting research proposed. It included sections on the scope, significance, research question, assumptions, limitations, delimitations, and definitions.

CHAPTER 2. LITERATURE REVIEW

2.1 Direct Research in Hot Chamber Aluminum Die Casting

The quest for hot chamber aluminum die casting has, to this point, not yielded any commercially acceptable methods of gooseneck production, as evident by the fact that no companies perform hot chamber aluminum die casting. However, with the fact that hot chamber die casting can achieve production rates up to twice that of the cold chamber process (Anderson, 2004) and create products with superior quality (Okayasu, Yoshifuji, Mizuno, Hitomi, & Yamazaki, 2009), there is still a strong need for the ability to be discovered. This review of the current literature on the subject will focus on the limited attempts made, as well as on studies of candidate materials, including coatings, that could be used to construct an accepted gooseneck.

At this point, there have been few attempts at producing aluminum die castings with the hot chamber process. An early attempt was made by Van Wagner with the invention of a plunger-less, direct pneumatic injection gooseneck in 1907. However, the dissolution of the iron gooseneck by molten aluminum still led to issues of gooseneck failure and alloy composition change (Andersen, 2004).

Modern attempts at inventing a gooseneck for aluminum hot chamber die casting have focused on the use of ceramic silicides and borides starting with the patenting of the concept by Hinterman and Hertz in 1985 (United States Patent 4,556,098, 1985) and enhancements of the ceramic gooseneck design by Miki in 1999 (United States Patent 5,983,979). Silicon nitride (Si3N4) ceramic material was used for the construction of the gooseneck for the most recent hot chamber aluminum research found. The research conducted by Okayasu, Hitomi, and Yamazaki

(2008), showed the feasibility of producing a gooseneck of silicon nitride. However, the silicon nitride was soon infiltrated by aluminum when placed into service, which ultimately led to catastrophic failure due to embrittlement. Although their research did not lead to a suitable gooseneck for hot chamber aluminum, it did prove that aluminum die castings made with the hot chamber process show better quality than those made with the cold chamber process (Okayasu et al., 2009). Based on the analysis of the failure mechanisms in the initial research, Okayasu proposed modifications to the ceramic gooseneck system to help alleviate the failures and make it easier for failed components to be replaced (Okayasu, Hitomi, & Yamazaki, 2010). No results were found in the literature to indicate that Okayasu's ideas for improvements to the ceramic gooseneck system were tested.

2.2 Failure of Materials in Molten Aluminum

The situation of a tool in molten can be fundamentally described as a physical chemistry problem regarding a solid-liquid interface. At the interface, multiple possibilities exist including chemical reaction at the solid tool – liquid aluminum alloy interface, dissolution of the solid tool into the liquid aluminum alloy, diffusion of the liquid aluminum alloy into the solid tool, some combination of the previously mentioned, or no interaction. The following describes physical chemistry theories regarding these possibilities at the solid tool – liquid aluminum interface.

2.2.1 Dissolution of the Solid Tool into Liquid Aluminum

In the situation of the solid tool dissolving into the liquid aluminum, the aluminum can be thought of as a solvent and the tool a solute. Noyes & Whitney (1897) created an empirical model describing the effect of the concentration of the solute in the solution on the rate of dissolution. The Noyes-Whitney model is defined:

$$\frac{dx}{dt} = C(S - x)$$

Where x is the concentration of the solute in the solution, t is time, C is a constant, and S is the concentration of the solute at which the solution is saturated.

2.2.2 Diffusion of Liquid Aluminum into the Solid Tool

In 1855 Adolf Fick proposed two laws on diffusion. The first, that diffusion occurs in the direction of high concentration to low concentration at a rate that is proportional to the gradient of the concentration. The second, that as the diffusion process progresses the gradient of the concentration decreases (Fick, 1855). Fick's first law is now commonly mathematically defined as:

$$J = -D\nabla\varphi$$

Where J is the diffusion flux with units of distance squared per time, D is the diffusivity with units of distance squared per time, and φ is the concentration with units of the amount per volume (Mehrer, 2007).

Work by Arrhenius in the rate of chemical reactions (Arrhenius, 1889) led to the formulation of an empirical equation describing reaction rates. The Arrhenius equation for the rate of reactions is defined as:

$$k = Ae^{\frac{-E_a}{RT}}$$

Where k is the reaction constant, A is a factor dependent on conditions, E_a is the activation energy, R is the universal gas constant, and T is the absolute temperature. For many solids in many situations, the diffusivity term found in Frick's first law can be accurately described using the Arrhenius equation in the form of:

$$D = D_0 e^{\frac{-E_a}{RT}}$$

Where D_0 is the diffusivity at infinite temperature or some other initialization temperature. However, it should be noted, that there are known examples of this relation not holding with diffusion in solids. When the relation holds, a plot of ln(D) versus 1/T, commonly referred to as an Arrhenius plot, allows for the calculation of D_0 and E_a (Mehrer, 2007).

Another theory of note for the situation of diffusion in solids is that of diffusion through vacancy defects. Frenkel (1926) was the first to propose the theory of defects in crystal lattices. Soon after theories and experimental evidence emerged that explained how vacancies in the lattice allow for the movement of solute atoms into and through the solvent lattice (Mehrer, 2007). Interestingly, the exponential nature of diffusion rate with temperature may be caused by the compounding factors of an increase in vacancies in solids as temperature increases, an increase in lattice parameters of the solid as temperature increases, and the increase in available energy for activation of jumps of the solute atoms as the temperature increases.

2.3 Research in Tooling Materials and Coatings

With the limited amount of published research into investigations of producing hot chamber goosenecks for aluminum casting, other areas of focused research must be explored for related information. Although the cold chamber die casting process allows for extended life of steel shot tooling when casting aluminum (Kaye & Street, 1982), there has been extensive research in extending the life of cold chamber tooling which could offer insight into possible materials that could be used to construct a hot chamber gooseneck.

2.3.1 Refractory Metals

Molybdenum and tungsten alloys are detailed as possibly improved tooling materials by Kaye and Street (1982) and are also suggested as tooling materials for the thixomolding of ferrous alloys by Hirt and Kopp (2009). One group of high-temperature materials to be avoided for prolonged submersion in molten aluminum is nickel alloys. Dybkov (1993) found the solubility of nickel to be four times higher than that of iron in molten aluminum at 700°C. Nickel alloys were also tested by Zhu, Schwam, Wallace, and Birceanu (2004) with die casting alloys and their results showed nickel alloys to have poorer resistance to dissolution in the molten aluminum than H13 tool steel.

The results of Y. Zhu et al. (2004) merit further discussion. Their tests consisted of using H13 tool steel, nickel (Ni-718), molybdenum (Mo-785), titanium (Ti-6Al-4V), and tungsten (Anviloy 1150) core pins impinged by the gate flow in a squeeze casting machine and determining the volume loss of core pins after cleaning with sodium hydroxide (NaOH). The aluminum used was A356 and the holding furnace temperature was 730°C. They estimated the impingement velocity of aluminum on the core pins to be 6000mm/sec (236in/sec). The test showed that Ni-718 performed slightly worse than H13, while Mo-785, Ti-6Al-4V, and Anviloy 1150 all performed far better. The results are summarized in Table 1.

Table 1. Results from Y. Zhu et al. (2004) as visually estimated from a line graph in the original text.

Casting Cycles	Volume loss of core pins, mm^3				
	H13	Ni-718	Mo-785	Ti-6Al-4V	Anviloy 1150
25	8	10	0.4	0.2	0.0
50	16.4	N/A	0.6	0.4	0.1
100	N/A	N/A	1	0.6	0.2

Recent work by Zhu (2014), showed that niobium, molybdenum, tungsten, and titanium alloys all performed better than H13 tool stool in dissolution testing in molten aluminum, with niobium being the best material tested. In this test, small pucks of material were spun in a small holding furnace and mass loss measured after cleaning the specimen in sodium hydroxide. A set of specimens were also spin reacted and the reaction products evaluated with scanning electron microscopy.

Table 2. Mass loss found during spin testing by Zhu (2014).

Nb	0.17%
Mo	0.20%
W	0.65%
Ti	2.13%
H13	19.05%

Xiao, Chen, & Liu (2012) tested a tungsten alloy (91.3W-6.0Ni-2.7Fe), a titanium aluminum alloy (66.7Ti-33.3Al), QT700 (64.3Fe-3.5C-2.2Si), and H13 (91.7Fe-5.1Cr-1.1Mo-0.9V-0.9Si-0.3C) by static immersion in two kilograms of 750° aluminum (no composition of the aluminum used was given by the authors). Their results of surface thickness loss are summarized in Table 3. It shows that the tungsten alloy exhibits less than half the loss of H13, while the titanium-aluminum alloy exhibits a greater loss than H13. It is possible that the high level of aluminum (33.3 weight percent) in the titanium alloy caused the extreme loss rate, as Ti-6Al-4V has been reported to be an order of magnitude better than tool steels by Mihelich and Decker (WO 97/45218, 1996) and Zhu (2014).

Table 3. Thickness loss per dunk time as summarized from Xiao et al. (2012). Thicknesses reported in this table were converted from a graph in the source.

Material	The thickness of lost material (um) at dunk time				
	1h	2h	4h	6h	8h
H13	30	220	440	720	800
QT700	40	140	280	420	720
91W	20	100	200	330	360
TiAl	100	360	520	750	880

An extensive amount of information on the reactions of refractory metals with molten aluminum was found in Dybkov's work (2013). The work compiles both theories and empirical data on the solubility limits, dissolution rate constants, and diffusion coefficients for many transition metals, including all the refractory metals, submerged in molten aluminum under various conditions. The data presented shows niobium to have the lowest solubility limit in molten aluminum with a value of 0.0197% at 700°C and only rising to 0.101% at 850°C, while vanadium shows the lowest dissolution rate constant. All the refractory metals are reported to have lower solubility limits than iron. Table 4 and Table 5 show solubility and Arrhenius type dissolution rate equation parameters presented by Dybkov (2013).

Table 4. Solubility limits of various metals in molten aluminum at various temperatures reproduced from Dybkov (2013). Solubility units are weight percent and temperature units are degrees Celsius.

	700	750	800	850	900
Titanium	0.214	0.33	0.51	0.73	1.06
Vanadium	0.28	0.46	0.73	0.96	1.4
Chromium	0.72	1.29	2.5	4.1	6.7
Iron	2.5	3.4	5.3	7.9	9.9
Cobalt	1.6	2.4	4.2	6.9	11.3
Nickel	10.0	13.5	19.5	27.0	31.0
Zirconium	0.156	0.276	0.46	0.66	1.11
Niobium	0.0197	0.0337	0.057	0.101	No data
Molybdenum	0.215	0.44	0.71	1.14	No data
Tantalum	0.105	0.17	0.25	0.37	No data
Tungsten	0.23	0.40	0.84	1.16	No data
Rhenium	0.24	0.61	1.21	1.8	2.8

Table 5. Arrhenius type equation parameters for dissolution of various metals in aluminum over a temperature range of 973 to 1173K from Dybkov (2013).

	D_0 (10^{-7} m^2/s)	E (kJ/mol)
Titanium	4.5±0.7	42.8±1.5
Vanadium	2.8±0.3	47.4±0.8
Chromium	2.6±1.3	39.1±3.8
Cobalt	0.43±0.13	22.8±2.4
Nickel	6.2±3.5	43.5±5.8
Zirconium	0.80±0.22	29.5±2.1
Niobium	1.50±0.89	36.9±4.0
Molybdenum	2.82±0.90	40.2±2.7
Tantalum	2.62±0.55	41.2±1.7
Tungsten	3.54±1.80	41.9±5.0
Rhenium	2.1±0.6	37.8±2.3

Tang et al. (2012) studied pure cobalt and pure iron (99.9 weight percent) held in pure aluminum (99.99 weight percent) at temperatures from 680 to 770°C. They found thickness loss of the samples to be less for cobalt than iron, with the results summarized in Table 6. They also found the thickness of the intermetallic layer in the cobalt sample to be approximately one third the thickness than that of the iron sample.

Table 6. Thickness loss per dunk time from Tang et al. (2012). The thicknesses are calculated from regression equations provided in the source.

Material	The thickness of lost material (um) at dunk time			
	10 sec	600sec	1800sec	3600sec
Iron	31	253	439	622
Cobalt	8	47	126	244

2.3.2 Coatings on Steel

The literature detailed in the previous sections is focused on the idea that other materials could be substituted for steel in the manufacture of a gooseneck. However, it may also be possible to enhance a steel component with surface coating technology to make it acceptable for the task of hot chamber aluminum die casting. The use of coatings to enhance steel has been studied extensively in attempts to increase the life of steel tooling used in die casting and other manufacturing processes.

2.3.2.1 Physical Vapor Deposition (PVD) Coatings

Research by Wang (1997) tested titanium nitride (TiN), titanium aluminum nitride (TiAlN), and chromium nitride (CrN) physical vapor deposition coatings with and against base materials of H10, H13, H19, and two different maraging steels in aluminum dip testing. The base material compositions are shown in Table 7 and the results of the tests are shown in Table 8. All coatings tested improved the corrosion resistance of the base steel. The ability to distinguish differences in the coating materials was attributed to the testing times used. Wang suggests that differences might be able to be seen if the dunk times were extended.

Table 7. Base steel compositions tested by (Y. Wang, 1997).

		Material				
		H10	H13	H19	Maraging (Marlok)	Maraging (HWM)
Nominal Alloy Composition, percent weight	Cr	3.25	5.25	4.25	<0.01	5.00
	Si	1.00	1.00	0.30	-	-
	C	0.40	0.40	0.40	-	0.02
	Mo	2.50	1.50	0.40	5.00	7.50
	Mn	-	0.35	0.30	-	-
	Co	-	-	4.25	11.00	11.00
	Ni	-	-	-	18.00	2.00
	V	0.40	1.00	2.00	-	-
	Ti	-	-	-	0.30	-
	W	-	-	4.25	-	-
	P	-	<0.025	-	<0.003	-
	S	-	<0.005	-	<0.003	-

Table 8. Normalized ranking of corrosion resistance by Wang (1997). A larger number is better resistance.

Surface Treatment	Base Steel				
	H10	H13	H19	Marlok	HWM
Bare	3	5	4	4	6
TiN	9.5	9.5	9.5	9.5	9.5
TiAlN	9.5	9.5	9.5	9.5	9.5
CrN	9.5	9.5	9.5	9.5	9.5

Gulizia, Jahedi, and Doyle (2001) tested TiN, CrN, and TiCN PVD coated H13 core pins against bare H13 using a specially designed die ran in a 250 ton die casting machine. The die was designed to create conditions that are harsher than normal die casting practices with a gate velocity of 50m/s (1970in/s). The aluminum alloy used was ADC-12 and the holding furnace was set at 680°C. The results showed that all three coatings greatly reduced die soldering, with the TiN and CrN performing better than the TiCN.

Schwam, Wallace, Zhu, Courtright, and Adkins (2005) tested commercially available chromium carbide (CrC), chromium nitride (CrN), chromium nitride with tungsten (CrN+W), and titanium

aluminum nitride (TiAlN) physical vapor deposition coatings on various tool substrates. The testing was conducted in a squeeze casting tool with aggressive casting gate conditions and A356 aluminum. The results were that the coatings slowed the soldering of aluminum to the specimen and increased the washout resistance. The CrC coating performed the best in the test with less than 0.005 grams of dissolution after 240 cycles, while the bare substrate showed 0.124 grams of dissolution after only 45 cycles.

Tentardini et al. (2008) took an interesting approach to the study of PVD coatings for use with molten aluminum. In their work, they used differential scanning calorimetry (DSC) to measure the temperature at which reaction of the coatings began with pure aluminum. They determined the reaction between H13 and aluminum to begin at approximately 770K, the reaction between TiN and aluminum to begin at approximately 875K, and the reaction of CrN with aluminum to start at approximately 1080K.

2.3.2.2 Plasma Assisted/Enhanced Chemical Vapor Deposition (PACVD) Coatings

2.3.2.2.1 Zirconium Borides and Carbides

Rie, Pfohl, Lee, and Kang (1997) produced zirconium boride and carbide coatings on 1.1181 and 1.2344 tool steels by plasma assisted chemical vapor deposition (PACVD). The coatings were produced with various processing parameters that allowed the nitrogen and carbon contents in the coatings to vary. The process temperatures varied from 200 to 430°C and $CpZr(BH_4)_3$ was the metal donor. The coatings were then tested in molten aluminum spin and thermal shock tests. For the aluminum spin tests, the samples were rotated at 800 revolutions per minute for 20 minutes in aluminum at 700°C. For the thermal fatigue tests, specimens were heated to 680°C for 400 seconds in air and then cooled with compressed air for 200 seconds. The thermal fatigue test

was stopped at the start of visible cracking. Unfortunately, the experiment did not include testing of bare substrates for direct comparison, however, the results show that increasing the nitrogen content of the coating to 45 atomic percent increased the corrosion resistance to molten aluminum and increased the thermal fatigue life of the coatings. They also found the coatings to be quite smooth with R_a values from 0.02 to 0.05 micrometers.

2.3.2.2.2 Titanium Nitride, Titanium Carbide, and Titanium Boron Nitride

Pfohl, Gebauer-Teichmann, and Rie (1999) were able to produce titanium nitride (TiN), titanium carbide (TiC), and titanium boron nitride (TiBN) coatings on X40CrMoV5 hot work tool steel with a plasma assisted chemical vapor deposition (PACVD) process. The PACVD process used titanium chloride (TiCl4) as the donor material and were optimized within a substrate temperature of 500°C, pressure ranges of 80 to 250 megapascals, voltage ranges of 400 to 700 volts, pulses of 200 to 600 microseconds, and pauses of 100 to 600 microseconds. Although the paper talks of XRD, SEM, and EDS work to select the optimized coating parameters, there is no optimized settings or micrographs of coatings given. Coatings were then applied to tooling used in an actual die casting production process. The lifetime of the cores was measured by looking for tearing of the casting surface with the results shown in Table 9. All the coatings exhibited better performance than the uncoated steel, however, the titanium boron nitride coating was determined to be the best performer. It should be noted that the table contains the same coating in multiple columns. This is because the tests included varying the nitrogen and carbon content with the coatings. It was found that higher carbon and nitrogen contents helped to improve service life.

Table 9. Results of coating trials in actual die casting process by (Pfohl et al., 1999).

Coating	None	TiN Ti(C,N) TiN	TiN	TiC TiN	TiBN
Cycles to failure	1,000	7,000	14,000	16,000	>30,000

2.3.2.2.3 Aluminum Oxide

The production of PACVD aluminum oxide coatings on X38CrMoV5 steel molds for the thixomolding of steel has been studied by Jiang, Münstermann, Günther, and Schneider (2010). The steel was first nitrided with N_2-H_2-Ar gas and then the coating was produced with an $AlCl_3$-O_2-H_2-Ar atmosphere. The aluminum donor was produced in situ by passing HCl gas over 99.9% pure aluminum chips at 450 to 500°C. The coating compositions could be made amorphous, gamma, alpha, or combinations of, by adjusting the negative pulse length and cathode voltage. Coatings of 3 to 5 micrometers in thickness were grown with 8 hours at a temperature of 590°C.

2.3.2.2.4 Diamond Like Carbon (DLC)

Baba, Hatada, Flege, and Ensinger (2014) were able to coat the internal surface of steel tubes with relatively uniform 4 to 5 micrometer coating using plasma source ion implantation and deposition with a -5 kilovolt pulse voltage, 1 kilohertz pulse frequency, 10 microsecond pulse length, and acetylene (C_2H_2) gas at 25 megapascals. The substrates were SUS304 steel tubes with lengths of 100 and 200mm and inner diameter of 20mm. The time required to produce the coatings was between 0.43 and 0.5 hours. The coatings were found to be slightly thicker at the middle of the tube than the ends of the tube. No substrate temperatures were provided in the previously described research, however, Owens, Brühl, Simison, Forsich, and Heim (2015) compared soft and hard DLC coatings produced with a PACVD process with substrate temperatures ranging from 400 to 550°C.

2.3.2.2.5 Vanadium Carbide

Deutschmann, Messelhäuser, Suhr, Herrmann, and Härter (1994) were able to produce vanadium carbide, vanadium oxide, and vanadium carbo-oxide coatings using a PACVD process. The process used vanadocene Cp_2V, with Cp being $C_5H_5^{\theta}$, and deposition temperatures ranging from 50 to 450°C. Near oxygen-free coatings were produced.

2.3.2.3 Thermo-Reactive Diffusion (TRD) Coatings

2.3.2.3.1 Vanadium Carbide

Yu, Chu, and Shivpuri (1993) tested the reactivity of various coatings with molten aluminum, including a TRD vanadium carbide coating, against H13 tool steel in an immersion test. Reactivity was characterized by measuring the diameter change of specimen after being held in 390.2 aluminum alloy at a temperature of 680°C for various times and then cleaned by submersion in sodium hydroxide (NaOH), with a ph level of 12, for 24 hours. The test showed the TRD vanadium carbide to perform the best, with no measurable change in pin diameter after 5 hours of immersion. However, evidence of aluminum infiltration through the coating was observed in the micrographs, visible as iron aluminide beneath the coating surface. Although their tests are significant in identifying TRD vanadium carbide as a good candidate coating, it should be noted that their use of NaOH cleaning ruined the opportunity to study dissolution and diffusion as separate phenomena, meaning other coatings may still be acceptable if they had low dissolution and simply allowed diffusion.

2.3.2.3.2 Niobium Carbide

Yan et al. (2014) studied the growth of niobium carbide coatings on AISI 52100 by TRD at various temperatures and times. The bath used consisted of 77.5wt% $Na_2B_4O_7$, 10wt% Nb_2O_5,

2.5%wt% B_4C, and 10wt% NaF. They were successful in producing coatings on the steel, and the thickness results are shown in Table 10.

Table 10. Niobium carbide coating thicknesses from the tests of Yan et al. (2014). Visually estimated from a scatter plot given in the original text.

Temperature, K	Coating thickness at processing time, micrometers			
	1 hour	2 hours	4 hours	6 hours
1123	1.5	2	4	6
1173	2.5	5.5	7	10
1223	5.5	8	10	13.5

OrjuelaG., Rincón, and Olaya (2014) produced a niobium carbide coating on AISI 1045 steel by a thermo-reactive diffusion deposition process. The process was performed at 1020°C for four hours with salt compositions of 4% aluminum, 88 to 76% borax, and 8 to 20% ferroniobium. It was found that increasing the ferroniobium content from 8 to 20% caused the niobium content in the coating to increase from 72 to 80%. The critical load in scratch testing was statistically unchanged with changing ferroniobium content. No tests of niobium carbide TRD coatings in molten aluminum were found during the literature review.

2.3.2.3.3 Niobium Boride

Sen, Pazarlıoglu, and Sen (2008) were able to produce niobium boride coatings on AISI M2 steel through a multistep process. Boronizing was done in a bath of borax, boric acid, and ferro-silicon at 1000°C for two hours. The boronized steel was then niobized by packing in a powder mixture of ferro-niobium, ammonium chloride, and alumina at 900°C for 1 to 4 hours. The coatings consisted of an iron boride diffusion layer approximately 30 micrometers thick and a niobium boride layer that varied from 1 to 3 micrometers thick depending on treatment time. EDS of the

niobium boride layer showed evidence of residual iron in the coating. No tests of niobium boride TRD coatings in molten aluminum were found during the literature review.

2.3.2.3.4 Molybdenum Disulfide

Akbarzadeh, Zandrahimi, and Moradpour (2017) detail the production of molybdenum disulfide coatings on AISI 316 steel by a multistage TRD process. The process consists of a molybdizing stage and a sulfurizing stage. The molybdizing phase was completed by immersing the steel in molybdenum oxide (MoO_3) powder at temperatures between 650 to 750°C and times of 2 to 8 hours. The sulfurizing phase was completed in a stainless steel chamber at 650, 700, and 750°C for 4 hours. Both phases utilized an argon blanket to avoid unwanted oxygen and nitrogen pick up. The amount of molybdenum sulfide in the coating, as compared to molybdenum and molybdenum oxide, increased with increasing sulfurizing temperature. Coatings between 20 and 50 micrometers thick were produced. No tests of molybdenum disulfide TRD coatings in molten aluminum were found during the literature review.

2.3.2.4 Diamond Like Carbon (DLC)

Diamond like carbon (DLC) coatings are of interest since their pure carbon composition might offer corrosion protection for steels in molten aluminum. However, the only previous attempt at using DLC coatings with molten aluminum (Hairy & Richard, 1997) did not fare well, as the coatings eroded. Although this result might discourage the use of DLC coatings in die casting, little is understood about the nature of the coating used and the failure modes. Advancements in DLC coating technology that have occurred since 1997 could merit revisiting their possible use.

2.3.2.5 Aluminum Oxide by Aluminizing then Oxidation

Aluminum oxide coatings on steel can be produced through a multi-step method of aluminizing the steel and then oxidizing the aluminized surface. Deqing, Ziyuan, & Longjiang (2003) describe this method and found it to be extremely effective in protecting the sample from molten aluminum, reporting little to no surface modification after submersion times of 240 hours, with the same immersion test completely dissolving the bare steel specimen in 10 hours. The passivation effects of an aluminum oxide layer are also confirmed by the work of Mohsenifar, Aboutalebi, and Seyedein (2014).

2.3.2.6 Laser Clad Coatings

2.3.2.6.1 Vanadium Carbide (VC)

A study of the production of laser clad VC coatings on steel and their molten aluminum corrosion resistance was made by Shah and Dahotre (2002). In their work, a slurry of 99.9% pure VC powder with a mean particle size of 10 micrometers and water-based organic liquid was sprayed on acetone cleaned H13 plates and then dried for 1 hour at a temperature of 70°C. After drying the thickness of the slurry coating was between 75 and 105 micrometers. The surface was then subjected to a laser melting process. The laser process parameters used are shown in Table 11. VC and iron were present in the coating. The coating was shown to slow the onset and rate of reaction with molten A356 aluminum. The iron remaining in the coating likely reduced the corrosion resistance. An opportunity exists to improve the laser cladding of vanadium carbide coatings for use with molten aluminum.

Table 11. Laser process setup used by Shah and Dahotre (2002).

Type	Power	Beam Shape	Scan speed
Continuous wave Nd:YAG	2 watts	3.5 mm line	17 mm/s

2.3.2.7 Electrodeposited Zirconium Diboride

Q. Wang, Wang, Liu, and Zeng (2017) produced 25 micrometer zirconium diboride coatings on 201 stainless steel substrates using an electrodeposition process with a salt of NaCl-KCl-K_2ZrF_6-KBF_4 and tested the coatings against bare substrates in an aluminum dip test. The dip test used 6061 aluminum at 800°C and varied in dip times from two to four hours for the bare steel samples and four to 120 hours for the coated samples. The bare steel showed gross attack by the aluminum melt at two hours while coated samples were able to withstand 72 hours without noticeable corrosion. The coatings began to show corrosion at localized areas at 96 hours, however, much of the coating remained unattacked at 120 hours. The source contains several micrographs detailing the coatings and the dip tests.

2.3.2.8 Thermal Spray Coatings

2.3.2.8.1 Tungsten Carbide Cobalt Coatings

Lopez and Rams (2015) show that steel is effectively protected by a thermal spray tungsten carbide cobalt (WC-Co) cladding when submerged for lengthy periods in molten aluminum. After 24 hours of submersion in a casting aluminum alloy (8.74Si-2.8Cu-0.98Zn-0.75Fe-0.28Mg-0.14Mn) at 700°C, the uncoated steel (0.4% carbon) was dissolved by 280um while the WC-Co coating showed no dissolved thickness. There was a small (approximately 3um) reaction zone on the coating.

2.3.2.8.2 Titanium Aluminum Oxide Coatings

Salman, Gabbitas, Cao, and Zhang (2011) studied composite thermal sprayed coatings consisting of a metallic binder of titanium and titanium-aluminum with ceramic aluminum oxide (Al_2O_3). The tests consisted of submersing samples in an aluminum alloy (7% silicon and 0.34% magnesium) at 700°C. Their results showed that a coating produced using a three to four ratio of titanium oxide to aluminum powder reduced the weight loss seen in the tests by a factor of ten at five hours of submersion.

2.3.3 High Carbon Ferrous Alloys

In the review of literature of material tests in molten aluminum, research was found that characterized the effects of a ferrous alloy's carbon content on the reaction with molten aluminum. Hwang, Song, & Kim (2005) tested steels with carbon contents ranging from 0.2% to 1.1% and observed an indirect linear relationship between carbon content and both dissolved mass and intermetallic layer thickness. Their results show a reduction of approximately 50% for dissolved mass and reaction layer when increasing the carbon content from 0.2% to 1.1%.

Balloy, Tissier, Giorgi, & Briant (2010) tested ferrous alloys with carbon contents of 0.37%, 3.50%, and 3.71%. The results confirm that increasing carbon content greatly reduces the thickness of the intermetallic diffusion zone. Table 12 summarizes the diffusion zone thickness measurements shown as EDS scans in the literature. It should be noted that the ferrous samples were held in molten aluminum with 4% iron. This would greatly reduce, or possibly eliminate, the dissolution of iron into the melt, ensuring that the intermetallic diffusion zone thickness would be an accurate measurement of the total activity between the melt and the ferrous samples.

Table 12. Summary of diffusion couple results from Balloy et al. (2010). Intermetallic diffusion zone thickness is visually estimated from EDS line scans shown in the paper.

Carbon content of ferrous alloy, Percent weight	Intermetallic diffusion zone thickness, um	Time held in 690° C molten aluminum, hours
0.37	230	2
3.50	55	2
3.71	100	8

Carrera et al. (2017) also carried out studies on various ferrous alloys, including a grey iron. Their tests included spinning samples in a low iron aluminum alloy (less than 0.2 weight percent iron) at 710°C. The surface speed of the sample in the melt was 1.2m/s (approximately 47in/s). The ferrous materials used, and results of the spin tests, are shown in Table 13 and Table 14. The results show that a grey iron alloy of 3.17% carbon, 2.65% silicon, and 0.57 manganese exhibited no weight loss in the tests, while a common 5% chromium tool steel exhibited an 18% weight loss in the most aggressive test.

Table 13. Composition of ferrous alloys used by Carrera et al. (2017). Units are weight percent. Iron is the balance.

Material	C	Cr	Mo	Si	Mn	Other
A	<0.008	<0.30	4.5	<0.1	<0.1	14 Ni, 10.5 Co, 0.2 Ti, 0.6 V
B	0.35	5.0	2.3	0.2	0.5	0.6 V
C	0.31	0.08	3.1	0.17	0.16	1.85 W, 0.1 Cu
D	0.40	5.25	1.35	1.0	0.4	1.0 V
E	3.17	-	-	2.65	0.57	-
F	1.7	18	1.0	0.8	0.3	3.0 V

Table 14. Percent weight loss of specimen from spin tests performed by Carrera et al. (2017).

Material	10 cycles of 120 sec	30 cycles of 90 sec	30 cycles of 130 sec
A	25.75	53.89	61.88
B	0.14	0.40	1.59
C	0.05	0.17	0.56
D	0.29	4.43	18.14
E	0	0	0
F	2.55	9.82	8.15

2.4 Die Cooling Line Design and Manufacture

No single authority on the design of die casting die cooling lines was found in the literature, although many make at least some mention of the importance of die temperatures or give a high-level understanding of the basic heat transfer elements (Andersen, 2004; Doehler, 1952; Harvill & Jordan, 1945). One disappointment of note came from Herman and Kirkman (n.d.). This publication from the North American Die Casting Association greatly simplifies the discussion on cooling line heat transfer and makes erroneous steady-state assumptions as to the cooling line surface temperatures in order to avoid determining the heat transfer coefficient at the water line surface.

Studies were found for some of the traditional designs used in die casting. Hu et al. (2004), studied how flow rate impacted the cooling rates for a traditional tube in tube design which is commonly used. They found the tube in tube design to have a varying heat transfer coefficient due to differences in the flow regimes that occur throughout this type of heat exchanger. Kind (2011) studied the effects on cooling line diameter given a constant flow rate and found that increasing the diameter of line reduced its ability to pull heat from the die, due to the reduction of the Reynolds number, and subsequent reduction of the heat transfer coefficient.

2.4.1 Conformal Cooling in Dies

Studies were also found on a concept known as conformal cooling. The concept of creating non-traditional, free form water lines have been studied for some time at this point. The earliest found study (Lin, 2003) did not refer to the cooling line design as “conformal” but it details water lines that follow the free form surface of a die, which is essentially the definition of a conformal cooling line. This study focused on how to automate the CAD for creating water lines that match the surface geometry but did not consider the actual heat transfer performance of the lines.

Several studies were found pertaining to the use of conformal cooling for the plastic injection molding process, which shares similarities to die casting. Dimla et al. (2005) studied the use of conformal cooling for improving the operations of a plastic injection molding process. The study was specific to a single part geometry and only characterized a single possible conformal cooling design against the traditional die. They found the conformal cooling led to a reduction in cycle time. Shayful et al. (2013) also studied the use of conformal cooling in injection molding, however their method of producing the conformal cooled inserts was unique in that they used two traditional manufactured die components assembled to sandwich a cooling line at the seam line. They then simulated this design concept and found operational benefits to the conformal cooling design. Marques et al. (2015) used an Autodesk simulation software to test various conformal cooling line design concepts on the production performance of a simple part geometry. Their results were qualitative in nature and suggests that a series flow configuration is preferred to a parallel flow configuration, however they identify that the pressure drop in series configurations could be a concern. Wang et al. (2015) detail an algorithm that could be used to auto generate conformal cooling lines. Like Lin (2013), the study is purely geometric matching to the tool surface and does consider the heat transfer performance of the lines. Jahan (2016)

studied the effect of various conformal cooling channel designs for use with plastic injection molding using a simplified geometry simulated in ANSYS. The results attempt to give design guidance, but the guidance is constrained to specific simple part geometries and are not able to be generalized.

Studies on using conformal cooling in die casting were found to begin more modern literature as compared to injection molding. Armillota et al. (2014) detail a study of using conformal cooling tools, made by a hybrid process in which the laser powder bed additive process is used to print on top of a forged billet base, to improve a zinc die casting process. The test showed a decrease in cycle time, improved part quality, and reduction in die lubricant usage. Schwam (2015 and 2016) studied a conformally cooled die insert for use with aluminum die casting and found the surface temperature was reduced by more than 200°F. The work also details the use of a directed energy deposition process to create a copper tool clad with tool steel to create a high thermal conductivity material based conformal cooling strategy. Sames et al. (2016) detail a simulated study performed with Abaqus in which conformally cooled cold chamber die casting shot tooling, including a shot block and shot tip, is compared to traditional designs. The results are reduction of solidification time by 33%. The study assumed the same heat transfer coefficient (3000 W/m^2K) for the traditional and conformally cooled lines. The conformal cooling lines studied were of a milled square groove variety. Huang (2017) studied thermal stress in various cooling line configurations using a steady state analysis and found conformal cooling to be able to create configurations that reduce the thermal stress as compared to traditional cooling line designs. The study is flawed in its use of a steady state heat transfer assumption and constant heat transfer coefficient for all cooling line geometries (7000 W/m^2K).

2.4.2 Thermodynamics, Heat Transfer, and Fluid Mechanics Pertaining to Die Casting Dies

2.4.2.1 Energy Balance in the Die Casting Cycle

The die casting process can be analyzed as a thermodynamic cycle to determine all heat flows into and out of a control volume that consists of the die casting tooling. Doing this leads to several useful equations.

The net energy into the die casting tooling can be positive, negative, or zero at different times of operation. When starting up the process, heat is absorbed by the tool causing it to rise in temperature. During continued operation, the tooling reaches cyclic equilibrium with no net energy change. When the process is stopped or interrupted, the tool will continue to lose heat to the surroundings and cool down.

For a warm-up cycle: $Q_{In} > Q_{Out}$

For a cycle in equilibrium: $Q_{In} = Q_{Out}$

For a cool-down cycle: $Q_{In} < Q_{Out}$

The heat inputs into the tooling are few, consisting of the heat carried into the tooling with the molten metal, and from heat applied by any die heating technologies.

Heat In: $Q_{In} = Q_M + Q_{DH}$

Heat carried into the tooling by the molten metal and can be calculated with the metal's mass and enthalpy at time of injection.

Heat Injected with Molten Metal: $Q_m = mH_{alloy}$

Heat can be added to the tooling through die heating technologies. The heat carried into the system by hot oil can be calculated with the total mass that flows through the entrance and the enthalpy of the oil. An electric resistance cartridge heater inputs heat at a rate equal to its efficiency multiple by its electrical energy consumption.

Heat Input by Die Heating: $Q_{DH} = mH_{oil} + eE$

The sources of heat removal from the tooling throughout the cycle include the tooling's internal cooling system, external cooling, radiant heat transfer to the surroundings, and the heat carried away with extraction of the casting from the tool.

Heat Out: $Q_{Out} = Q_{IC} + Q_{EC} + Q_R + Q_C$

The tool's internal cooling can be calculated using the heat transfer fluids mass, specific heat, and change in temperature. This assumes no phase change occurs or else a latent heat term would need to be included. In practice there are many cooling lines, so the total heat removed is the summation of each individual line's heat removal.

Tooling Internal Cooling: $Q_{IC} = mC\Delta T = \sum_{l=1}^{n} m_l\, C_l \Delta T_l$

The external cooling from die spray is a two-phase problem, with the spray first sensibly heating to the boiling point, and then latent heating while boiling. This requires accounting for both sensible and latent heat terms.

External Cooling from Die Spray: $$Q_{EC} = m\Delta H_{vap} + mC\Delta T$$

Heat is also lost to the surroundings through radiation and is dependent on the emissivity and area of the tool, and the difference between the tool's temperature raised to the fourth power and the surrounding's temperature raised to the fourth power.

Heat Radiated by Tooling: $$Q_{Rad} = \varepsilon\sigma A(T_2^4 - T_1^4)$$

When the casting is extracted from the die casting tooling, it is still at a temperature well above ambient. As such, an amount of heat equal to the mass of the casting and the enthalpy of the metal at the extraction temperature is removed from the tool along with the casting.

Heat extracted with casting: $$Q_C = mH_{alloy}$$

2.4.3 Heat Transfer in Die Casting Tooling

Heat transfer in die casting tooling is governed by three primary phenomena, the interfacial heat transfers between the cast metal and the tools, conduction through the tools, and the interfacial heat transfer in the tool cooling lines.

2.4.3.1 Interfacial Heat Transfer Between the Cast Metal and Tooling

Poirier and Poirier (1994) detail various modes of heat transfer in metal casting processes and have created analytical models for the interface of a casting with its mold. The interfacial heat transfer between cast metal and the tooling is a complicated situation. During the filling of the casting, molten metal contacts the surface and quickly cools forming a dense skin of solidified metal. As molten metal makes better contact with the die surface than solidified metal, the heat transfer coefficient at the interface is not constant throughout the cycle.

Interfacial Heat Transfer: $$\dot{Q} = h_{ict} A \Delta T$$

When using this equation, one must handle the changing interfacial heat transfer coefficient between the casting and tooling, h_{ict}. The literature gives estimates for the coefficient before and after an air gap forms, however there is no guidance in determining when exactly the change occurs during the solidification process.

2.4.3.2 Conduction through the Tooling

The movement of heat through the tooling materials is governed by transient conduction. Using conservation of energy, the one-dimensional energy equation for conduction in a material with uniform thermal conductivity can be derived, which is convenient for use in determining temperature variations in the tooling with respect to time.

1-D Energy Equation for Conduction: $$\frac{\partial T}{\partial t} = \left(\frac{k}{\rho C_p}\right)\frac{\partial^2 T}{\partial x^2} = \alpha \frac{\partial^2 T}{\partial x^2}$$

When the tooling can be considered as semi-infinite, the error function can be employed to determine instantaneous heat conduction.

Transient Conduction of Heat: $\dot{Q} = q_t A = \frac{kA(T_0 - T_t)}{\sqrt{\pi \alpha t}}$

2.4.3.3 Interfacial Heat Transfer in Cooling Lines

This type of heat exchanger is governed by the convective heat transfer at the interface of the pipe wall and flowing fluid. The following is summarized and derived from Cengel (2007).

Convective heat transfer in pipe: $\dot{Q}_{Convective} = hA(T_2 - T_1)$

To use the convective heat transfer equation, a heat transfer coefficient, h, is required. This is derived using the Nusselt number.

$$Nu = \frac{hD}{k}$$

$$h = Nu\frac{k}{D}$$

From empirical studies the following equation has been developed when laminar flow is present.

HTC for laminar flow: $h = \left[\frac{k}{D}\right][3.66 + \left[\frac{0.065RePr\frac{D}{L}}{1+0.04\left(RePr\frac{D}{L}\right)^{\frac{2}{3}}}\right]]$

When the flow is turbulent, the following relationship has been developed.

HTC for turbulent flow: $$h = \frac{\frac{k}{D}\left(\frac{f}{8}\right)(Re-1000)Pr}{1+12.7\left(\frac{f}{8}\right)^{0.5}(Pr^{\frac{2}{3}}-1)}$$

Both equations require the Reynolds number, Re, and Prandlt number, Pr. The Reynolds number for flow in a circular tube is shown here.

$$Re = \frac{\dot{V}D}{Av}$$

$$\mathrm{Pr} = \frac{v}{\alpha}$$

The use of this HTC for turbulent flow equation requires the Darcy friction factor, f. For rough surfaces, f can be estimated with the Haaland equation.

$$f = -1.8\log[\frac{6.9}{Re} + \left(\frac{\frac{\epsilon}{D}}{3.7}\right)^{1.11}]$$

However, in the use of this equation, the friction factor should be restricted to a maximum of four times the friction factor of a smooth pipe, as the HTC will not continue to increase beyond that point. Also, the Prandlt number, Pr, should be between 0.5 and 2000, and Reynold's number, Re, should be between 3000 and 5000000. A downfall of this approach is that the absolute roughness must be known.

The friction factor can also be determined empirically using the following equation, where d is a characteristic dimension for the flow, which is equal to the internal diameter for round tubes.

$$f = \frac{2d}{\rho V^2 l}\Delta P$$

The heat flux at an interface can also be calculated from empirical data and the use of an energy balance equation. By measuring the change in temperature and total mass of flow of the liquid moving through the cooling line the total heat removed can be calculated. Then, using the area of the interface and the time of the test, the time average interfacial heat flux is resolved.

Heat flux using energy balance: $$\dot{Q}_{Convective} = \frac{mC(T_{out} - T_{in})}{At}$$

2.5 Summary

The literature presented in this section detailed the need for research in hot chamber aluminum die casting by showing the limited work in the area and the benefits that are possible through hot chamber as compared to cold chamber casting. Previous studies focused on ceramic goosenecks and the microstructural benefits of the process. The results with ceramic goosenecks were not promising, with failure of the ceramic gooseneck at low cycle counts. However, the aluminum microstructures possible with the hot chamber process are of better quality than those made with the cold chamber method. Other research of interest showed that the use of refractory metals and coating methods might prove to be the answer to creating a gooseneck that can withstand the demanding environment of hot chamber aluminum die casting.

CHAPTER 3. PROCEDURES AND DATA COLLECTION

The research performed consisted of a systems analysis of die casting tooling, and subsequent work in two foci: tooling material systems and tooling cooling line design. The following sections detail the research approaches used.

3.1 Research Approach for Question #1

The literature review was used to down select candidate material systems for testing. These material systems were then tested to characterize and compare the reaction rates in conditions like those experienced by a gooseneck in hot chamber die casting. Then, the best performing material systems were tested on both a small, laboratory hot chamber machine and in an industrial die casting facility.

3.1.1 Hot Chamber Tooling Designs with Refractory Metals and Coatings

To test the viability of refractory metals for hot chamber tooling, a system engineering approach was used to design and manufacture components to be ran on a 17-ton hot chamber machine located within a Purdue University laboratory. To begin, the cast iron tooling of the hot chamber machine was reverse engineered through laser scanning, manual measurement, and CAD modelling due the fact that prints and/or models were not available. The tooling components identified that needed material solutions to allow for use with aluminum consisted of the gooseneck, nozzle, plunger, and plunger rings.

Figure 1. 17-ton hot chamber die casting machine used in the study.

3.1.2 Dunk Testing of Coatings in Molten Aluminum

A factorial experimental design was used to collect measurements of the reaction of selected materials held in molten E380 aluminum at various times and is shown in Table 15. The design of the sample used is shown in Figure 2. The steel pins were machined from a standard grade H13 tool steel.

Table 15. Factorial design for reaction dunk testing in molten aluminum.

	1150°F			1250°F		
	30 minutes	120 minutes	1440 minutes	30 minutes	120 minutes	1440 minutes
H13 Tool Steel						
H13 NC						
H13 PACVD SI-DLC						
H13 TRD VC						
H13 PVD VCN						
H13 PVD Al_2O_3						
H13 PVD AlCrN						

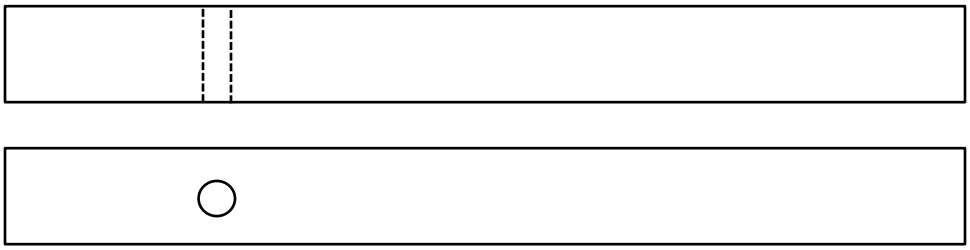

Figure 2. Specimen design. Length of 6” and diameter of 0.75”. Through hole of 0.25”, centered 1.5” from end.

Dunking was performed at Fiat Chrysler Automobiles’ Kokomo Casting Plant, in an industrial holding furnace filled with 6600 pounds of an E380 aluminum alloy. The specimens were mounted to an industrial ladling machine with the aid of a custom mounting plate, which allowed for the simultaneous dunking of up to eight specimens at a time. The mounting configuration is shown in Figure 3. For this study, only seven spaces were used due to the experimental design, and the positions of each specimen within a testing subgroup were randomized using a number generator. The ladling machine was equipped with a metal level indicator that allowed repeatable positioning during the dunking process. Figure 4 shows the position of the specimens during the dunking. The temperature of the furnace stayed at the experimental set points with a maximum

deviation of ±5°F and was verified with a digital readout on the furnace controller, which received a signal from a thermocouple in the dip well of the furnace. The furnace temperature controller readout is shown in Figure 5. After dunking, the specimens were air-cooled and then protected with bubble wrap during transport to the materials laboratory.

Figure 3. Subgroup of specimens mounted for dunking.

Figure 4. Subgroup of specimens being dunked.

Figure 5. Furnace controller readout.

The dunked specimens were sectioned at one inch from the dunked end, perpendicular to their length, to measure the critical aspects of the reactions, including the change in diameter of the pin and the thickness of the reaction layer. The coating surfaces of non-dunked specimens were also analyzed with scanning electron microscopy.

3.1.3 Scanning Electron Microscopy of Dunk Specimens

To analyze the performance of the coatings in the dunk test, images were acquired with a Tescan Mira3 SEM, which was also equipped with an Oxford EDS. Specimens were sectioned with a carbide wet saw one inch from the dunked end, and the cross sections mounted. The mounted specimens were then polished with a process that ended with a one-micron poly diamond suspension. After polishing, the specimens were etched by rubbing the surface with a cotton tipped applicator saturated with a 3% nital solution.

3.2 Research Approach for Question #2

A finite difference model is employed to perform a simulated experiment that allows the development of empirical models using die cooling line design elements, casting design elements, and process control variables as inputs. The models developed will be designed to predict the die surface temperature before closing, the time required to solidify the casting, the total cycle time, and the heat collected by the water line.

During construction of the model, it was realized that not enough was known of laser powder bed manufactured cooling lines to be able to reasonably estimate the friction factor using the Haaland equation. Therefore, an experiment was designed and conducted to empirically determine the friction factors in laser powder bed cooling line.

3.2.1 Mathematical models of the physical system

A finite-difference model was designed to allow manipulation of the primary cooling line design factors affecting die casting cycle time and die temperatures. This allowed changing the casting thickness, water line diameter, water line distance to die surface, distance between water lines, water line flow rate, and die thickness. The physical concept for the model is shown in.

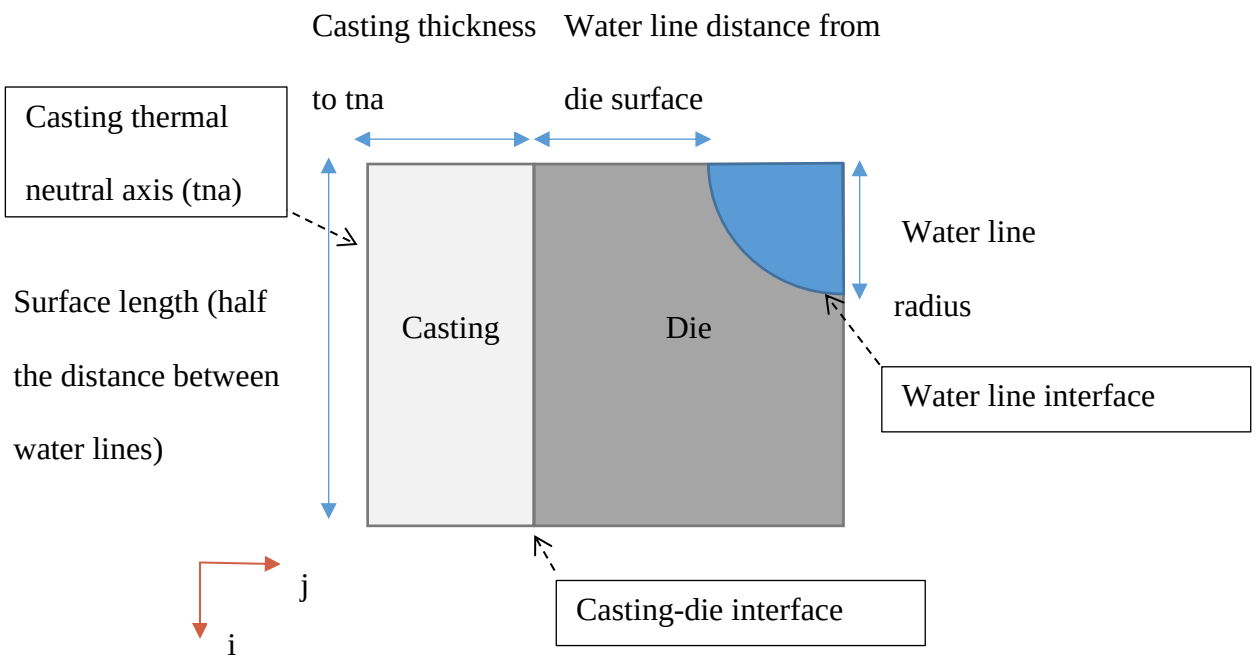

Figure 6. Physical concept for finite difference model.

3.2.1.1 The casting

The casting was modeled as a 2d (i,j) array of control volumes, with all boundary volumes modelled with half node size. Two different physical models were employed to handle the conduction through casting nodes, and the interfacial heat transfer with the die. For volumes not on the die interface, the 2D heat equation was used with symmetry applied on the boundaries. For the interface nodes, an energy balance was applied, and the heat through each node face

accounted. A phase change also needed to be accounted for, with the apparent specific heat method implemented.

3.2.1.2 The casting-die interface

For the interface between the casting and the die, the convection equation was employed. The solid phase state of the casting's interface nodes was monitored, and the interfacial heat transfer coefficient selected based on whether the interface was liquid-solid or solid-solid. The heat transfer coefficient was set to 3000 W/(m^2K) for a liquid-solid interface, and 1000 W/(m^2K) for a solid-solid interface, based on recommendations from Poirier and Poirier (1994).

3.2.1.3 The die

The die was modeled as a 2d (i,j) array of control volumes, with all boundary volumes modelled with half node size, except for the boundaries with the water line which are discussed below.

3.2.1.4 The water line – die interface

The interface between the water line and the die was modeled using the convection heat transfer equation. The heat transfer coefficient was calculated using the empirically determined friction factors and equations discussed in section 2.5.2.3. For die nodes touching the interface, the energy flow through each node face was accounted for, with conduction for the faces touching other die nodes, and convection for the faces touching the water line nodes.

3.2.1.5 The water line

The water line was modeled as an approximated semi-circle with the radius as a model parameter. Nodes whose center point was inside the calculated water line boundary were set to a

constant water temperature of 30 Kelvin. The constant temperature assumption was determined to be allowable due to the size of the spatial resolution selected.

3.2.1.6 Heat absorbed by the water line

The calculated heat convected from die node faces touching the water line nodes was summed throughout the simulation.

3.2.1.7 The cycle

The cycle consisted of two distinct periods, the first with the casting material in contact with the die and the second after the casting has been ejected. For this study, the length of the first period was determined by the solidification time of the casting, which was monitored by observing the temperature array of the casting at each time step. Once all the casting nodes reached the solidus temperature, the simulation moved to the period of the cycle where the casting is ejected. A model input called cooling time was used to set the amount of time for this period. During this cooling time, the heat input at the surface of the die was set to zero, with convection to the atmosphere ignored, while the water line continued to remove heat through its interface with the die.

To improve the accuracy of the predictions from the simulation, the warmup period for the die was considered with the casting cycle was repeated five times, using the die temperature results at the end of the previous cycle as the starting values for the next. For the first cycle, the initial die temperature was set at 423 Kelvin (150°C). This allowed for faster stabilization of the cyclic temperature profile.

3.2.1.8 Python coding of mathematical models

The Python programming language was employed for the finite-difference modeling and was executed using Jupyter Notebooks.

3.2.2 Friction factor experiment

To determine the friction factors in laser powder bed conformal cooling lines a factorial experiment was conducted in which the pressure drop across printed specimen with different internal flow diameters was measured at various flow rates. The specimen design is detailed in Figure 7, and the specimens were produced in M300 maraging steel on a Concept Laser M2 laser powder bed machine. The printed specimens are shown in Figure 8. A meter flow control scheme was employed, with a manual ball valve used as a throttle to achieve various flow rates while taking flow rate and pressure measurements. The flow rate was measure with an IFM magnetic inductive flow meter, and pressure measure taken with IFM pressure sensors. All sensors included a manual readout which allowed the measurements to read directly from the sensors.

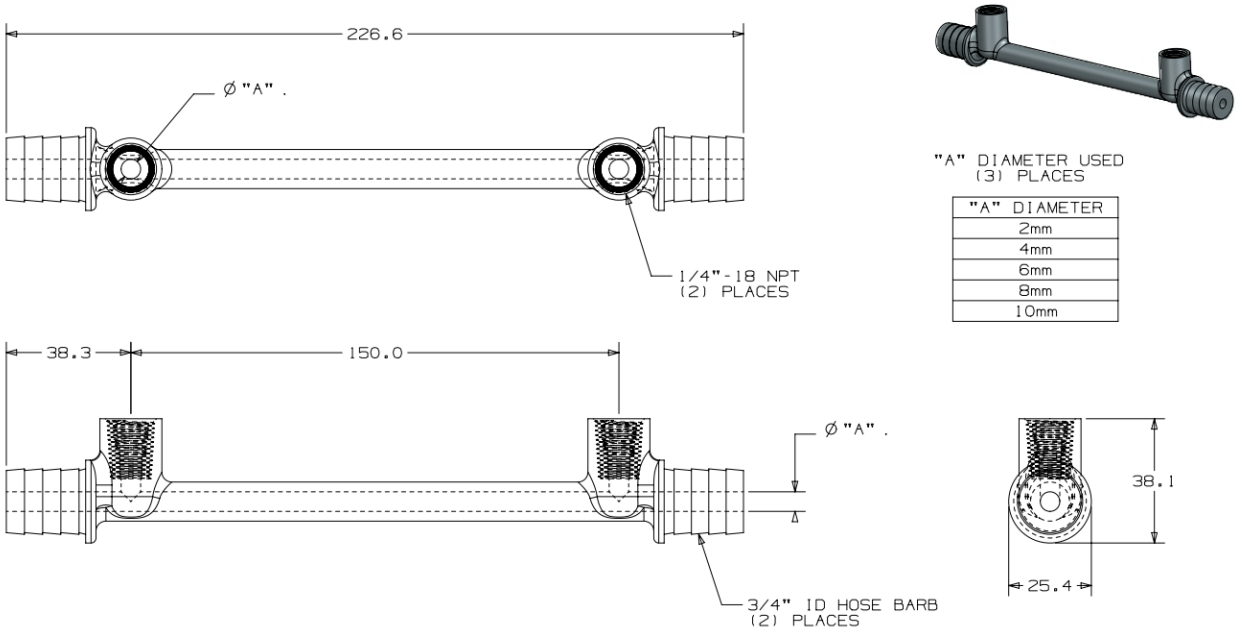

Figure 7. Friction factor specimen design. Units are in millimeters except where noted.

Figure 8. Printed friction factor specimens.

3.2.3 Factorial experiment with mathematical model

A 3^6 full factorial experiment was ran using the finite-difference model, with three levels for each input of casting thickness, surface length, the distance of water line to die surface, water line diameter, water line flow rate, and cooling period. Outputs from the model were the time for all nodes of the casting material to solidify, the average die surface temperature at the end of the cycle, the maximum die surface temperature at the end of the cycle, and the amount of heat absorbed by the water line.

3.2.4 Data analysis of mathematical model experiment

Ordinary least squares regression was performed using the data collected from the factorial simulation experiment to attempt to create models that could predict the die max and average temperatures, the solidification time, and the heat input to the water line from the input design features. The regressions were completed using the Statsmodels package implemented with Python. For each dependent variable, a model with no interactions, a model with all interactions, a backward selected model to a p-value limit, and a backward selected model to an adjusted R-square target was produced. In anticipation of complex physical relationships, all input terms were included with their squares and square roots.

3.3 Summary

The previous section documented the research methodology including the methods for data collection and analysis.

CHAPTER 4. RESULTS AND ANALYSIS

4.1 Design and Manufacture of Hot Chamber Tooling with Refractory Metals and Coatings

4.1.1 Multi-material Gooseneck with Niobium Lining

A multi-material gooseneck was designed and produced using a niobium alloy (Nb1Zr) weldment, integrally cast within gray iron. An industrial grade additive manufacturing process was employed to create the sand mold used in the casting process. The niobium liner weldment was packed with mold sand to ensure the channels would not fill with gray iron, and then placed into the printed sand mold as a core. The mold was assembled, and the gooseneck casting poured. The gooseneck was then machined to finish dimensions before installation in the die casting machine.

Figure 9. Production of a bimetallic gooseneck of gray iron and niobium alloy.

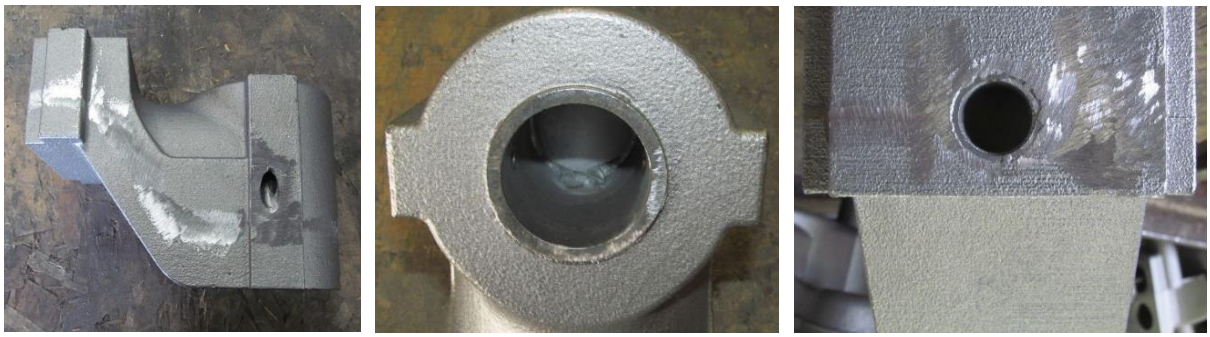

Figure 10. Multi-material gooseneck casting of gray iron with niobium alloy liner, ready for finish machining.

4.1.2 Solid Refractory Metal Nozzle

The nozzle was designed and produced of an industrial tungsten alloy with trade name Anviloy 1150, which contained 90% tungsten. The Anviloy material was not the most ideal for aluminum reactivity, due to the use of nickel in the alloy. However, Anviloy 1150 products are readily obtainable on the market, and the nozzle is not continuously subjected to molten aluminum. The component was shaped using a powder metallurgy process and finished machined to final dimensions.

4.1.3 Coated Hot Work Steel Plunger and Plunger Rings

The plunger was designed of a material system consisting of H26 tool steel which was coated for protection against molten aluminum. The plunger rings were made of an H21 steel and then coated with vanadium carbide for protection. The plunger and plunger rings are relatively small and replaceable, so the coated steel design helps to reduce cost in the tooling system. These components also do not have internal channels, which make them good candidates for line-of-sight coating processes, such as PVD or thermal spray.

4.2 Coating Dunk Test

The following is a summary of the qualitative and quantitative observations of the dunk testing specimens. The supporting SEM images and EDS maps are shown in subsequent sections.

For the bare H13 specimens dunked at 1150°F, shown in Figure 11 through Figure 15, after 30 minutes of dunking there is evident intermetallic reaction material on the surface of the specimen, with a reaction front is of irregular shape. The irregular shape indicates a reaction that begins at preferential sites along the surface of the specimen, and then grows both horizontally and laterally as the reaction feeds on the solid H13. After 120 minutes of dunking, the interface of the intermetallic region with the H13 is of a uniform shape, and this uniform reaction geometry is maintained in the 1440-minute test. It is believed that as the reaction progresses from preferential sites, these sites grow into each other and reorganize into the uniform shape due to a minimization of energy. EDS indicates that the intermetallic material that formed includes aluminum, iron, manganese, chromium, copper, and magnesium in solution, while the vanadium present in the H13 in the form of vanadium carbides remains stable. These chemically stable vanadium carbides are physically moved through the intermetallic region and eject into the melt along the rear interface. Also noted, is the formation of large intermetallic phases in the melt region of the attached material. These particles are likely a mix of solidification products that formed during the cooling of the liquid, or possibly semi-solid, aluminum melt which was enriched with iron, manganese, and chromium, and intermetallic particles that are being ejected from the melt interface of the intermetallic reaction zone. The intermetallic zone also shows two distinct regions. The first region is aluminum, iron, and silicon rich, and manganese and chromium depleted, and located at the interface with the H13 steel. The second region contains

aluminum, silicon, iron, chromium, and manganese. The second region also has an appearance that would indicate a porous intermetallic structure, with the pores filled by aluminum melt.

For the bare H13 specimens dunked at 1250°F, shown in Figure 16 through Figure 20, after 30 minutes of dunking, a uniform intermetallic reaction zone has formed, containing the characteristic two zone intermetallic. Relatively large intermetallic particles are seen to be ejecting from the interface with the melt. This intermetallic zone is maintained in thickness at approximately 75 microns through the 120 and 1440 minute tests. This is in comparison to the 1150°F test, in which the intermetallic zone grows to a thickness of approximately 400 microns. This shows a greatly increased dissolution rate at the higher temperature. Vanadium carbides in the H13 are found to be stable in this test, like the test at 1150°F.

For the nitrocarburized H13 specimens dunked at 1150°F, shown in Figure 24 though Figure 33, after 30 minutes of dunking low-level magnification does not reveal evident reaction, however the beginning stages of reactions are seen at high magnification. These beginning stages of reaction include areas along the interface where iron has been pulled from the H13 matrix, but the aluminum melt has not begun to infiltrate said matrix. Intermetallic particles on the order of a few microns in cross sectional size is seen at the interface of the aluminum melt and H13. It is possible that these particles are the beginnings of reaction, but it is also possible that these particles solidified from the melt due to the freezing that occurred in the time period of the melt and H13 specimen coming to thermal equilibrium. At high magnification, it is also evident that an oxide layer is present on the surface of the H13 specimen, which may have been produced during the nitrocarburization process, or formed in open air before the dunk testing occurred.

This oxide layer helps to reduce the reactivity of the melt at the interface. The nitrocarburized layer has a relatively deep nitride, on the order of 100 microns thick, with a relatively thin carbide/oxide layer, on the order of a few microns thick. After 120 minutes, still no stable intermetallic layer has formed on the surface of the pin. However, there are many intermetallic particles found at the interface, indicating the progression of the small, local reactions seen in the 30-minute test. After 1440 minutes, there is an approximately 600 micron thick intermetallic reaction layer, which exhibits the multiphase phase structure. The nitrocarburized surface layer is still evident in the 1440-minute specimen, with a remaining thickness of approximately 100 microns, indicating that the pin has only dissolved a few microns at this time.

For the nitrocarburized H13 specimens dunked at 1250°F, shown in Figure 30 though Figure 42, after 30 minutes of dunking no clear evidence of intermetallic reactions was found, however relatively large silicon particles were found at the interface. It is possible that the silicon is working to strip the protective nitro-carbo-oxide surface layers, or it is possible that these particles solidified as primary silicon on the surface of the pin due to the pin acting as a heat sink. After 120 minutes, intermetallic reactions have formed at various sites, which must have had conditions that favored the reactions, or possibly, these were the sites of early silicon attack. Evidence of the iron depletion phenomena is found at many sites along the reaction interface, with EDS indicating the intermetallic reaction is feeding on iron and manganese from the H13 specimen. After 1440 minutes, the intermetallic reactions have merged to form a single reaction front encompassing the entire interface. The intermetallic reaction zone exhibits the multiple phase structure, and is approximately 400 microns in total thickness, which indicates the

dissolution of the intermetallic into the melt is reduced in the NC specimen, as compared to the bare H13 specimen dunked in the same conditions.

For the silicon doped DLC coated specimens dunked at 1150°F, shown in Figure 48 though Figure 52, after 30 minutes no evidence of reaction is found. In addition, the thin aluminum foil on the specimen flaked off during sample preparation. After 120 minutes, no clear evidence of reaction was found, however relatively large silicon and iron/manganese/aluminum particles are seen at the interface. The coating was broken during the sample preparation procedure. After 1440 minutes, the specimen shows no infiltration of the coating through to the H13, however there are reaction materials evident with high magnification EDS. Magnesium from the melt has accumulated at the interface and has possibly infiltrated the first few microns of the coating. In addition, there seems to be carbon leaving the surface of the coating and reacting with the aluminum melt.

For the silicon doped DLC coated specimens dunked at 1250°F, shown in Figure 53 though Figure 61, after 30 and 120 minutes there is no evidence of infiltration of the melt through the coating to the H13 substrate. After 1440 minutes, there is evidence of the melt passing through small wormholes in the coating. The reaction of magnesium from the melt with the surface of the coating is evident, and in addition chromium is also seen to be forming a reaction product at the surface as well. EDS indicates that the chromium is transported from the H13 through the wormhole towards the melt, while aluminum, magnesium, and silicon from the melt is transported through the wormhole into the solid H13 substrate. The chromium reaction product at the coating interface appears to be an aluminum-chromium-carbide.

For the TRD vanadium carbonitride coated specimens dunked at 1150°F, shown in Figure 66 though Figure 73, after 30 minutes the coating is mostly intact and unreacted, however small areas of the iron depletion phenomena were found. After 120 minutes, the number of areas showing iron depletion has greatly increased, and large intermetallic particles are found in the adhered melt at the surface of the coating. After 1440 minutes, several of the iron depleted areas have progressed into sites of intermetallic reaction where the intermetallic reaction front is progressing into the H13 substrate.

For the TRD vanadium carbonitride coated specimens dunked at 1250°F, shown in Figure 74 though Figure 80, after 30 minutes there are many sites showing the iron depletion phenomena. After 120, these many of these sites have progressed to sites of intermetallic reaction, where the H13 substrate is being dissolved as the intermetallic front advances. After 1440 minutes, the coating has been completely compromised, and is seen floating in the melt. The reactions sites have merged into a single uniform reaction zone, which exhibits the multiple phase intermetallic structure.

For the PVD vanadium carbonitride coated specimens dunked at 1150°F, shown in Figure 84 though Figure 90, after 30 minutes of dunking, a site of iron depletion was found, along with what appears to be a pinhole defect. Intermetallic material is found on the surface coating directly opposite the area of iron depletion. After 120 minutes, a site is seen that shows evidence of the coating being attacked by a relatively large silicon particle, and sites are seen with iron depletion. Surprisingly, the specimen dunked for 1440 showed only small sites of iron depletion. It is possible that additional cross sections could have found evidence of advanced reactions.

For the PVD vanadium carbonitride coated specimens dunked at 1250°F, shown in Figure 91 though Figure 93, after 30 minutes there are several small sites showing the iron depletion phenomenon. After 120 minutes, relatively large sites of iron depletion are seen. After 1440 minutes, some sites have progressed into areas of intermetallic reaction zones, with the H13 solid being dissolved as the intermetallic front progresses into the specimen. However, much of the coating is still intact after the 1440-minute dunk.

For the aluminum oxide coated specimens dunked at 1150°F, shown in Figure 97 though Figure 100, after 30 minutes some small sites showing iron depletion phenomenon are evident, with several intermetallic particles along the melt-coating interface. After 120 minutes, there are relatively large sites of iron depletion. After 1440 minutes, the reaction has progressed to areas of intermetallic formation, with the H13 pin being dissolved as the intermetallic progresses into the specimen.

For the aluminum oxide coated specimens dunked at 1250°F, shown in Figure 101 though Figure 105, after 30 minutes there are small sites of iron depletion. After 120 minutes, approximately half of the interface has progressed to coalesced intermetallic front, while the other half still contains individual sites that are growing but are yet to coalesce. After 1440 minutes, the intermetallic reactions have merged into a single reaction zone progressing into the specimen with the multiple phase intermetallic structure.

For the aluminum chromium nitride coated specimens dunked at 1150°F, shown in Figure 110 though Figure 122, after 30 minutes there are sites of the iron depletion phenomenon, and there

was a site found where the coating had delaminated, with aluminum melt sandwiched between the coating and the H13 substrate. Intermetallic particles are found along the melt-coating interface. After 120 minutes, there are sites of iron depletion, and evidence of some sites beginning to progress to melt infiltration and intermetallic formation within the substrate. Intermetallic particles are found along the melt-coating interface. After 1440 minutes, sites have progressed to zones of intermetallic reactions with the intermetallic fronts moving into the H13 substrate.

For the aluminum chromium nitride coated specimens dunked at 1250°F, shown in Figure 123 though Figure 129, after 30 minutes there are sites of the iron depletion phenomenon. After 120 minutes, a large portion of the interface has progressed to intermetallic reaction zones with the intermetallic fronts moving into the H13 substrate. After 1440 minutes, the entire interface has progressed to being a single intermetallic reaction front, with the dual phase structure.

4.2.1 H13 Bare (H13)

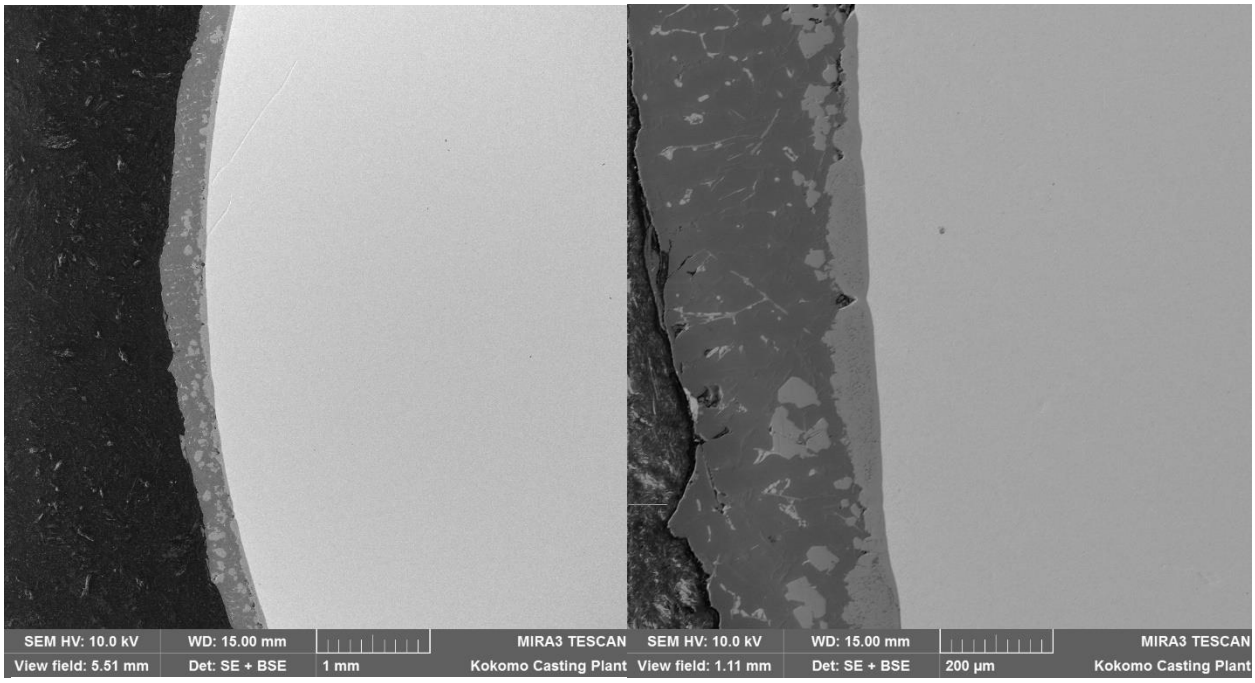

Figure 11. 50x and 250x SEM images of the bare H13 specimen dunked for 30 minutes at 1150°F.

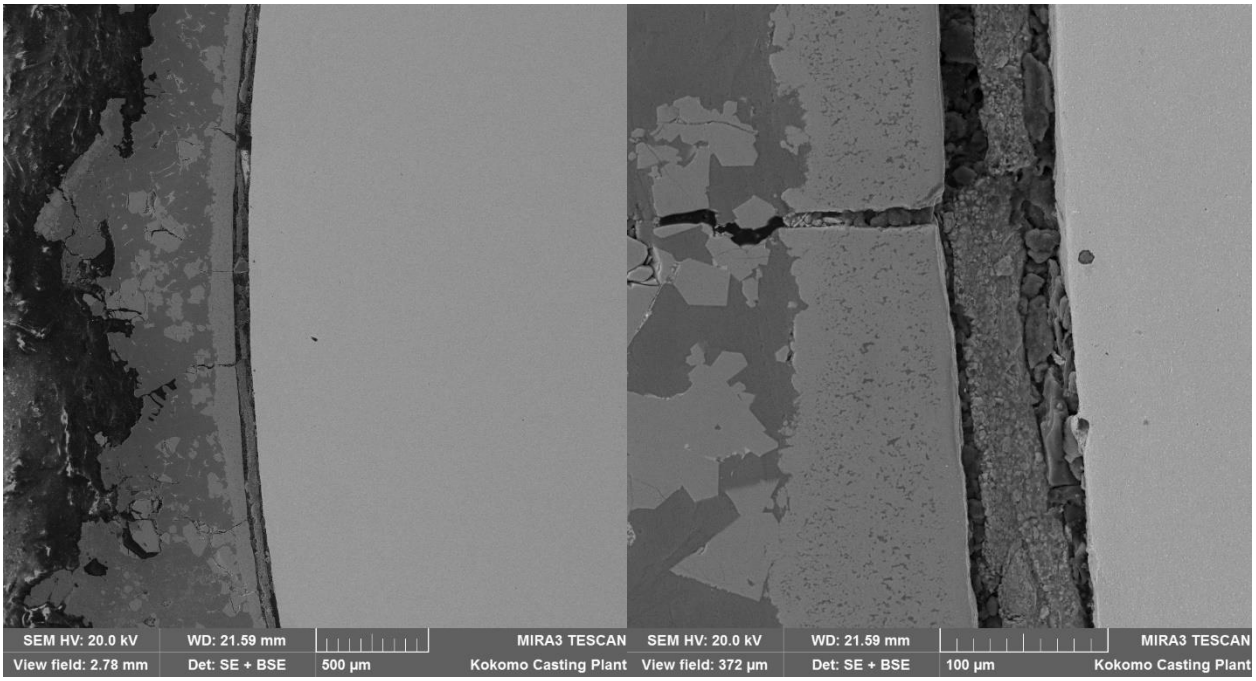

Figure 12. 100x and 750x SEM images of the bare H13 specimen dunked for 120 minutes at 1150°F.

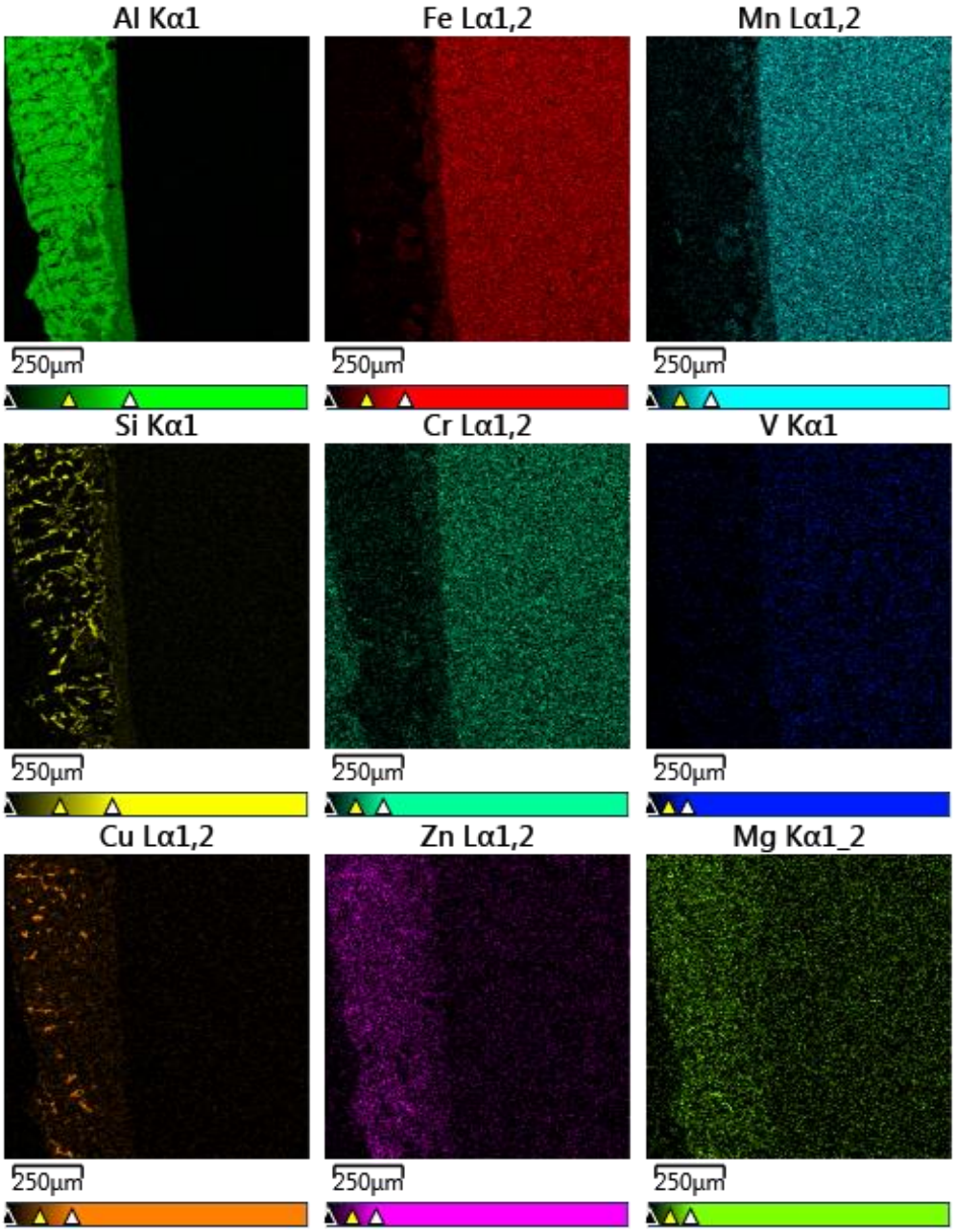

Figure 13. EDS maps corresponding to the 250x image in Figure 11.

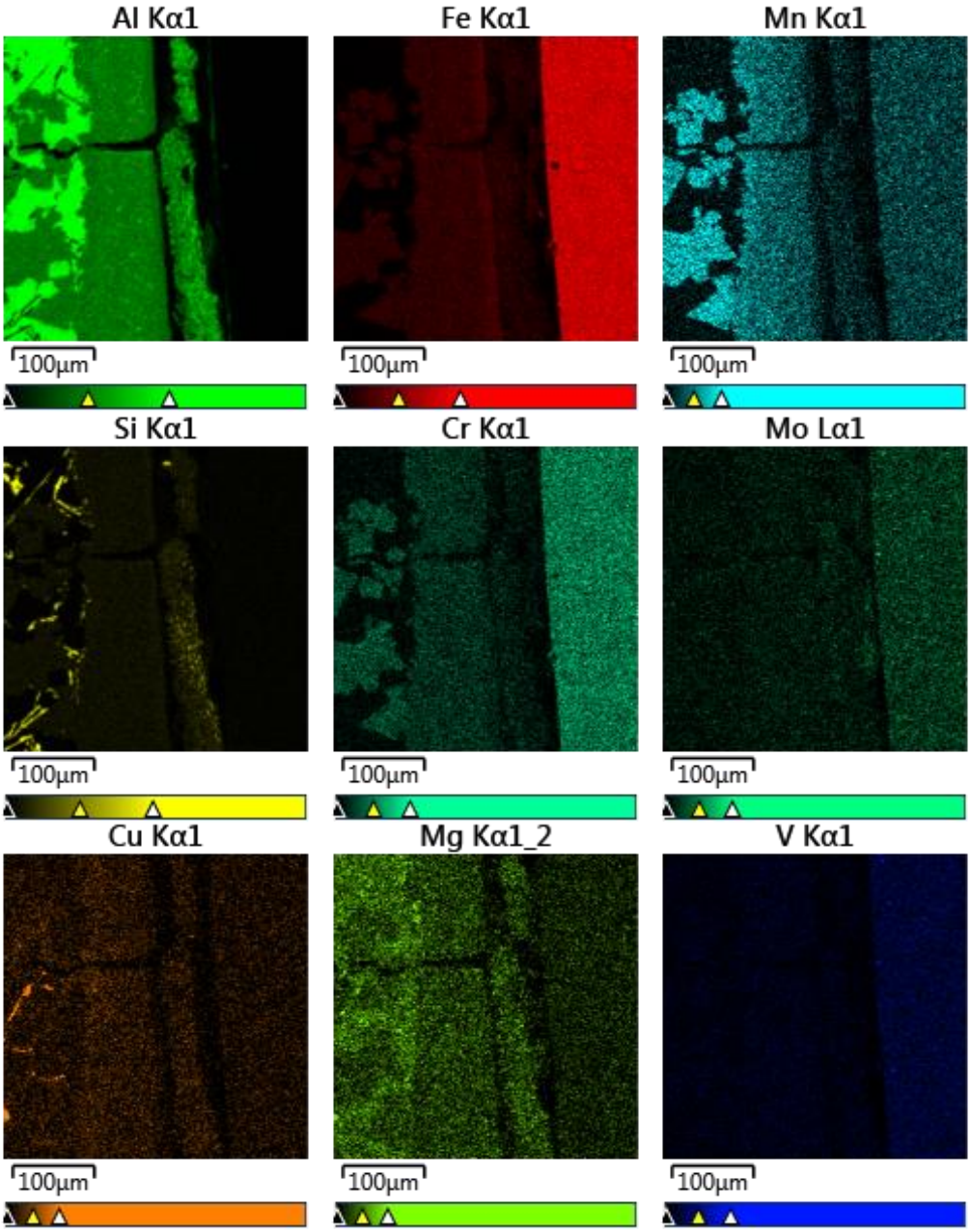

Figure 14. EDS maps corresponding to the 750x image in Figure 12.

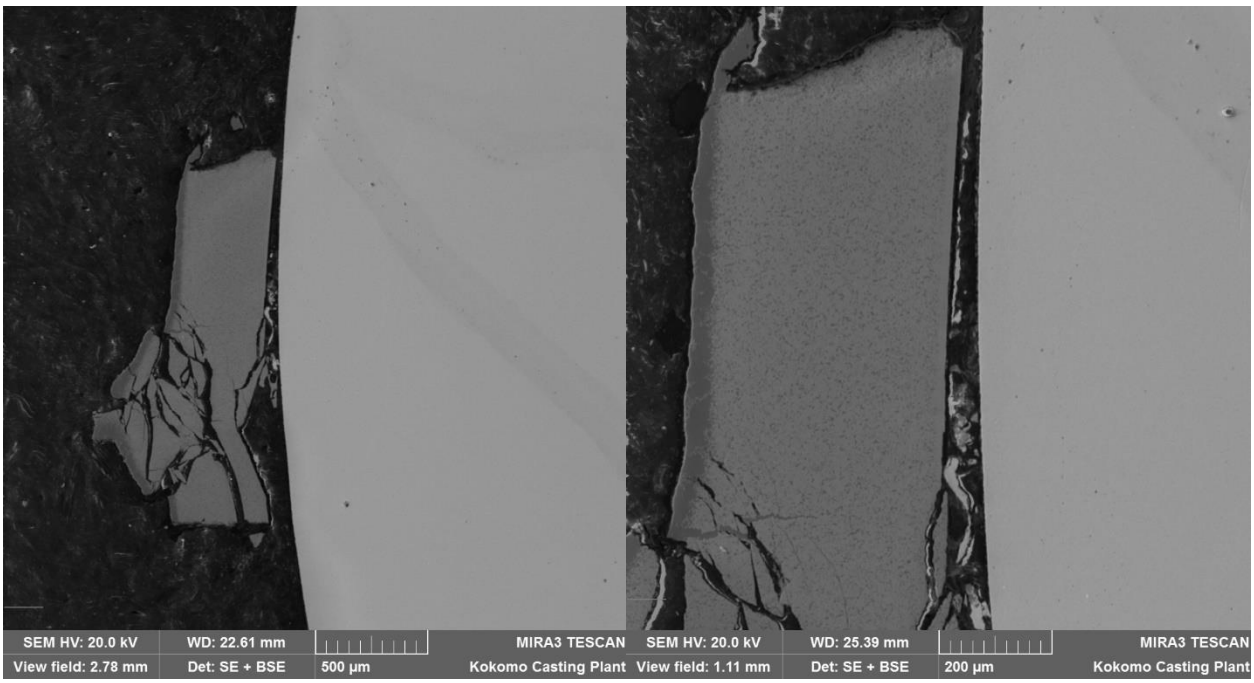

Figure 15. 100x and 250x SEM images of the bare H13 specimen dunked for 1440 minutes at 1150°F.

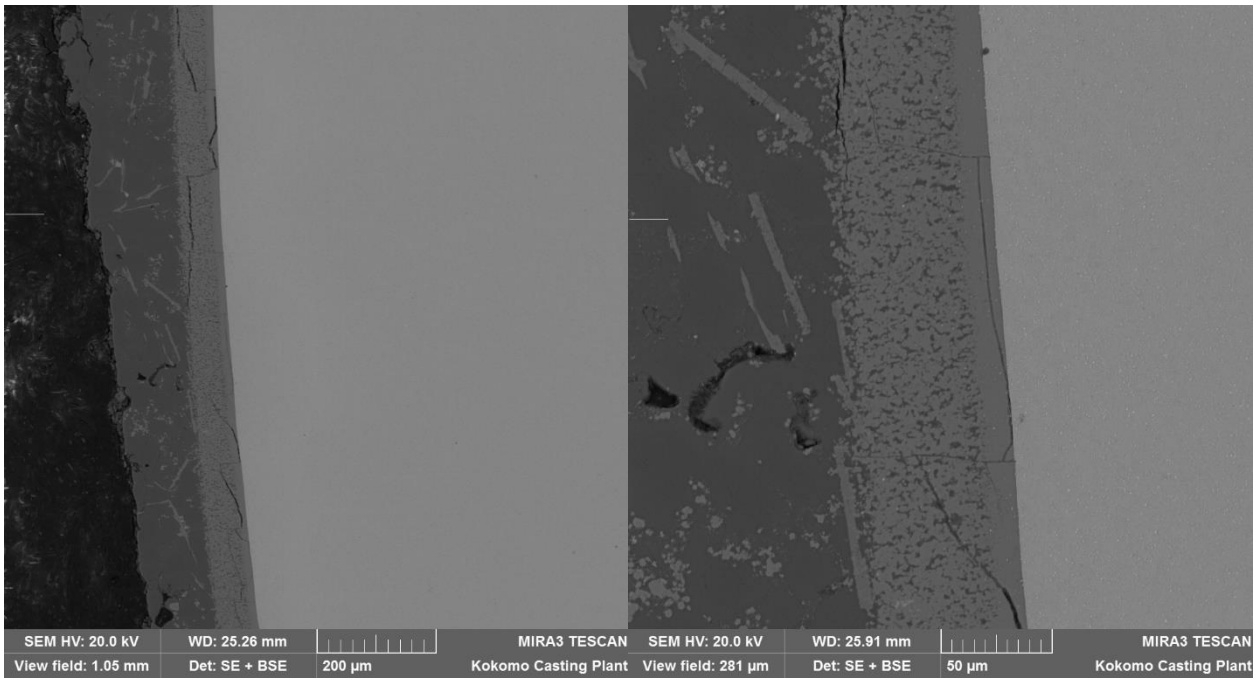

Figure 16. 250x and 1000x SEM images of the bare H13 specimen dunked for 30 minutes at 1250°F.

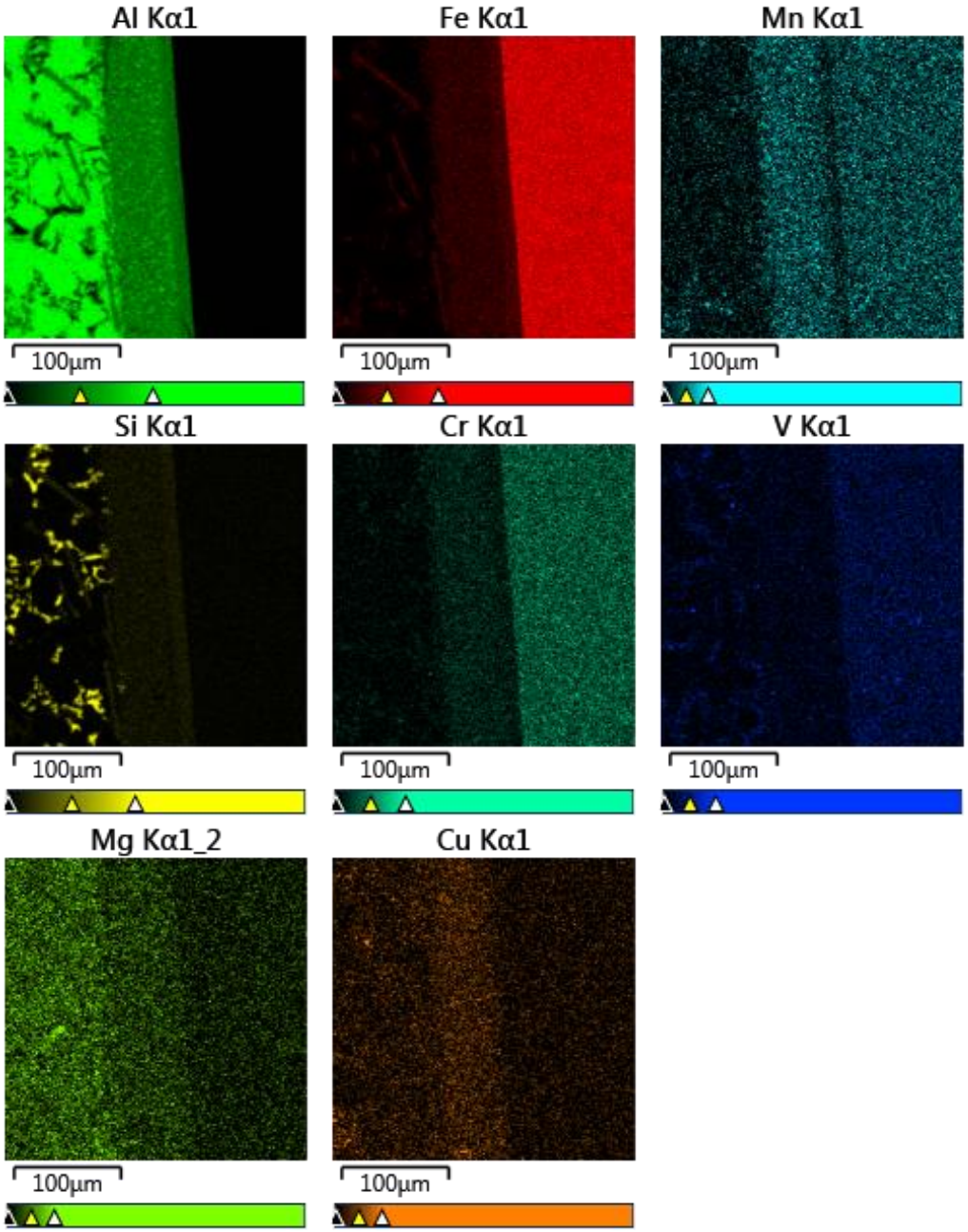

Figure 17. EDS maps corresponding to the 1000x image in Figure 16.

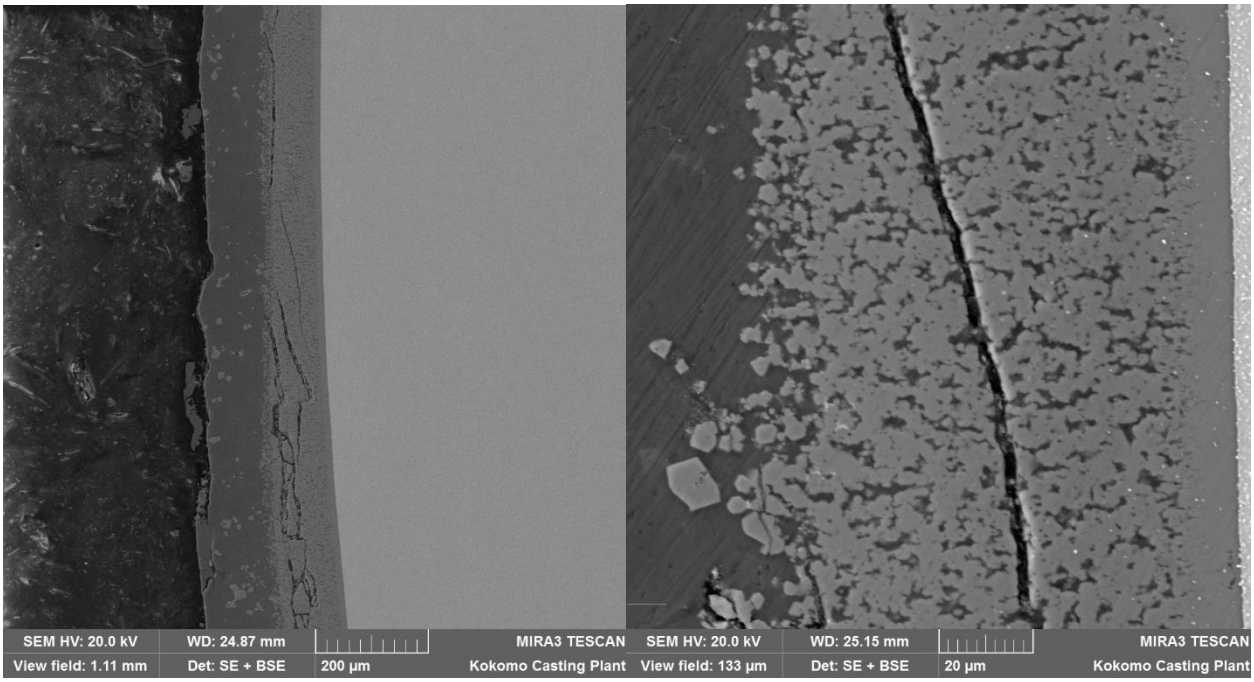

Figure 18. 250x and 2000x SEM images of the bare H13 specimen dunked for 120 minutes at 1250°F.

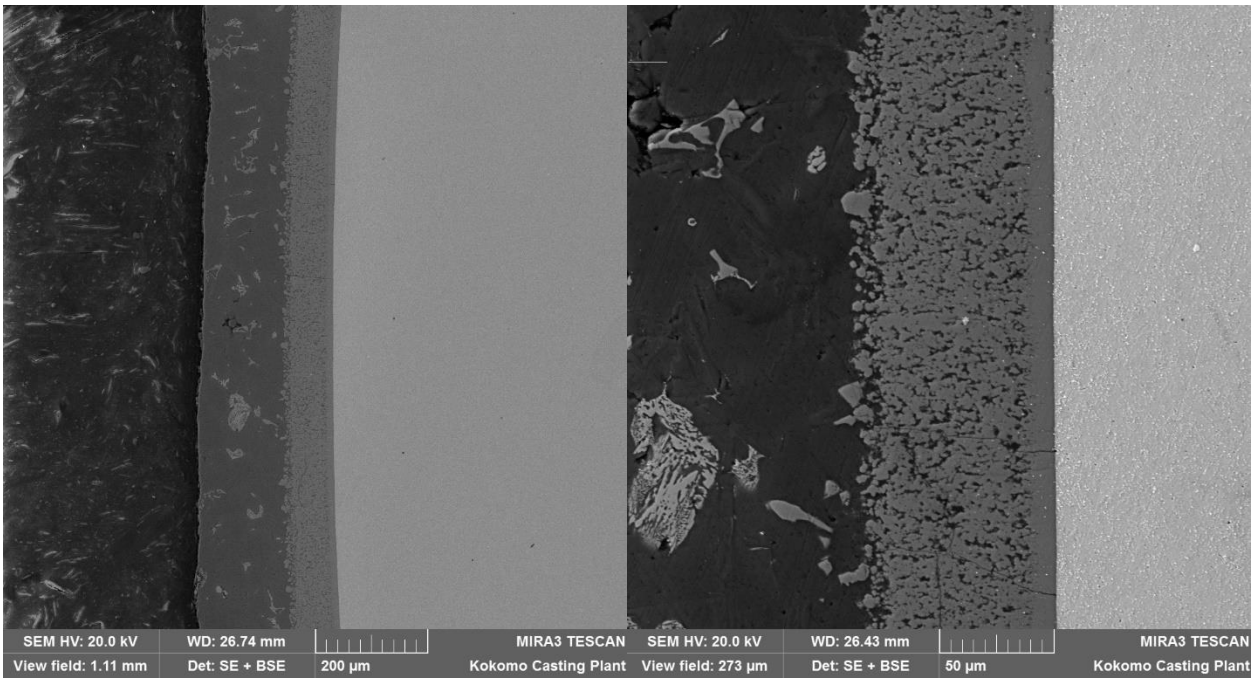

Figure 19. 250x and 1000x SEM images of the bare H13 specimen dunked for 1440 minutes at 1250°F.

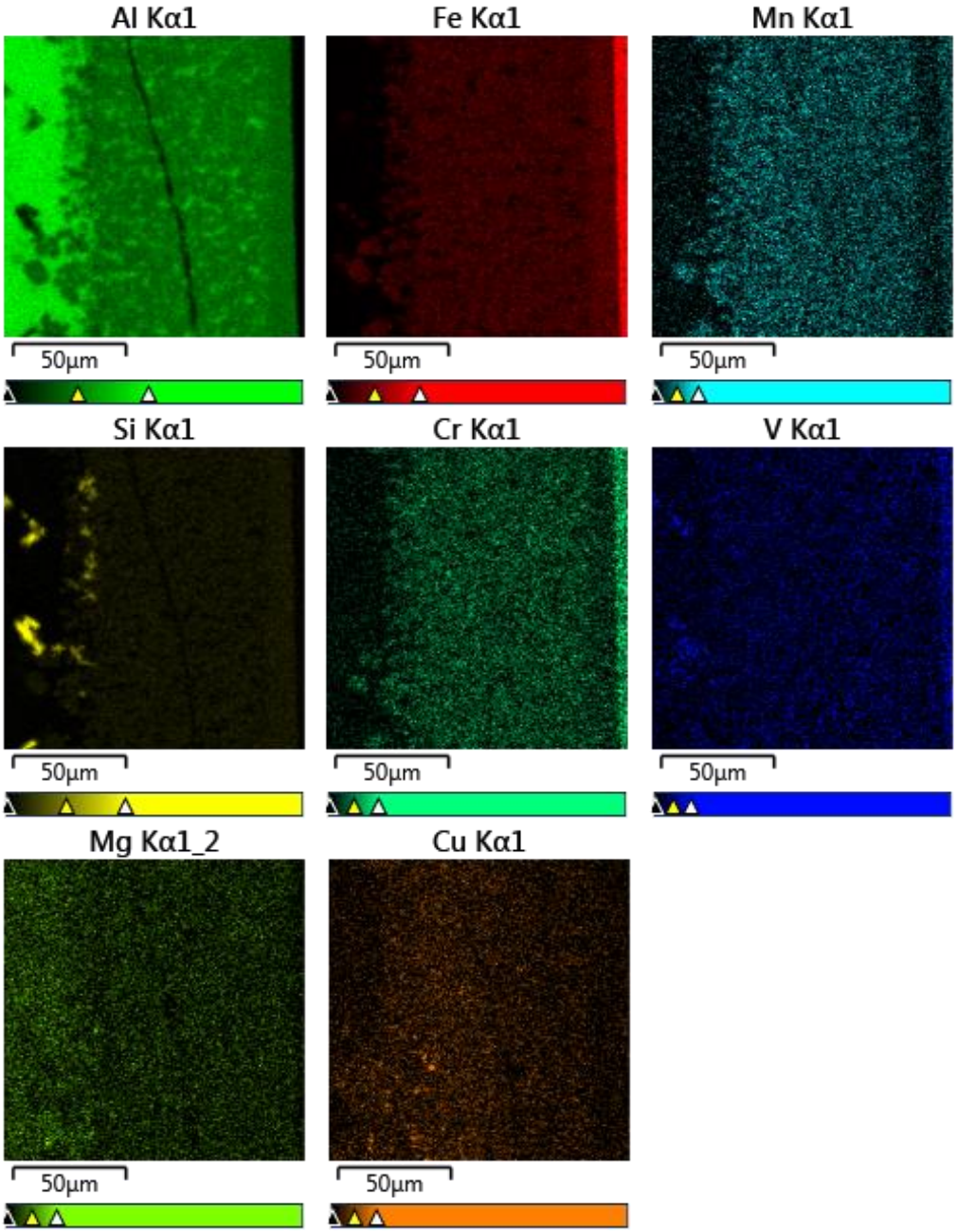

Figure 20. EDS maps corresponding to the 2000x image in Figure 18.

4.2.2 H13 Nitrocarburized (H13 NC)

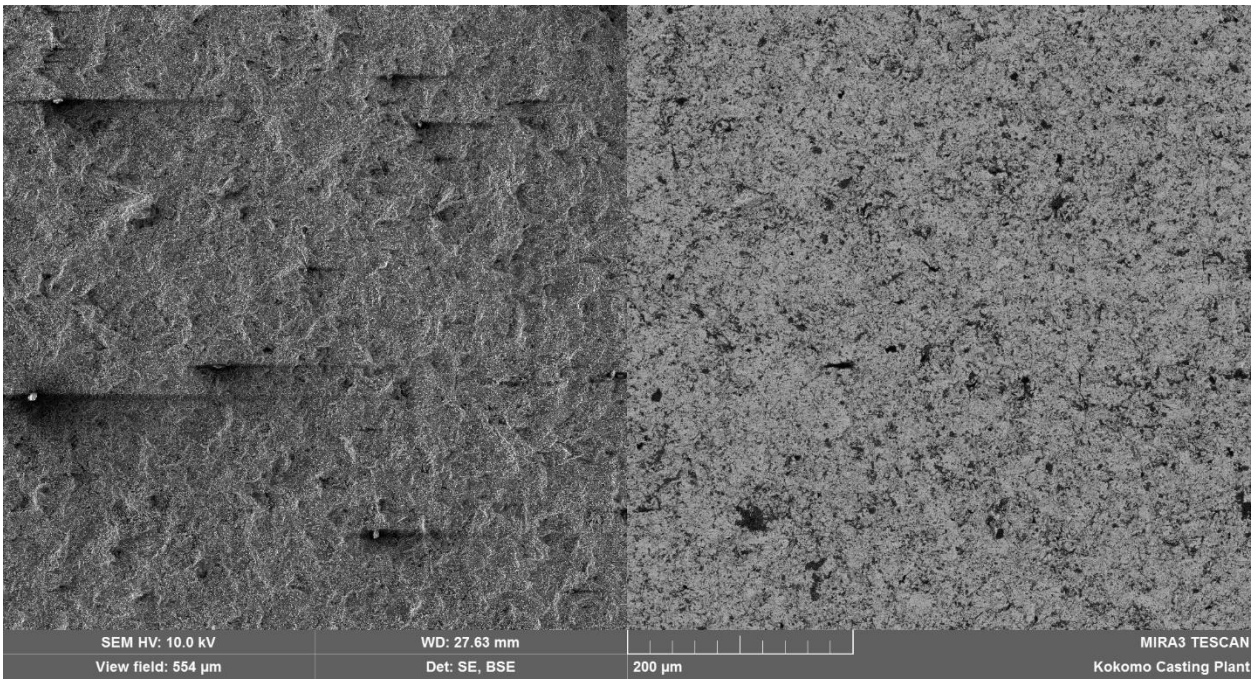

Figure 21. 500x SEM image of the NC coating.

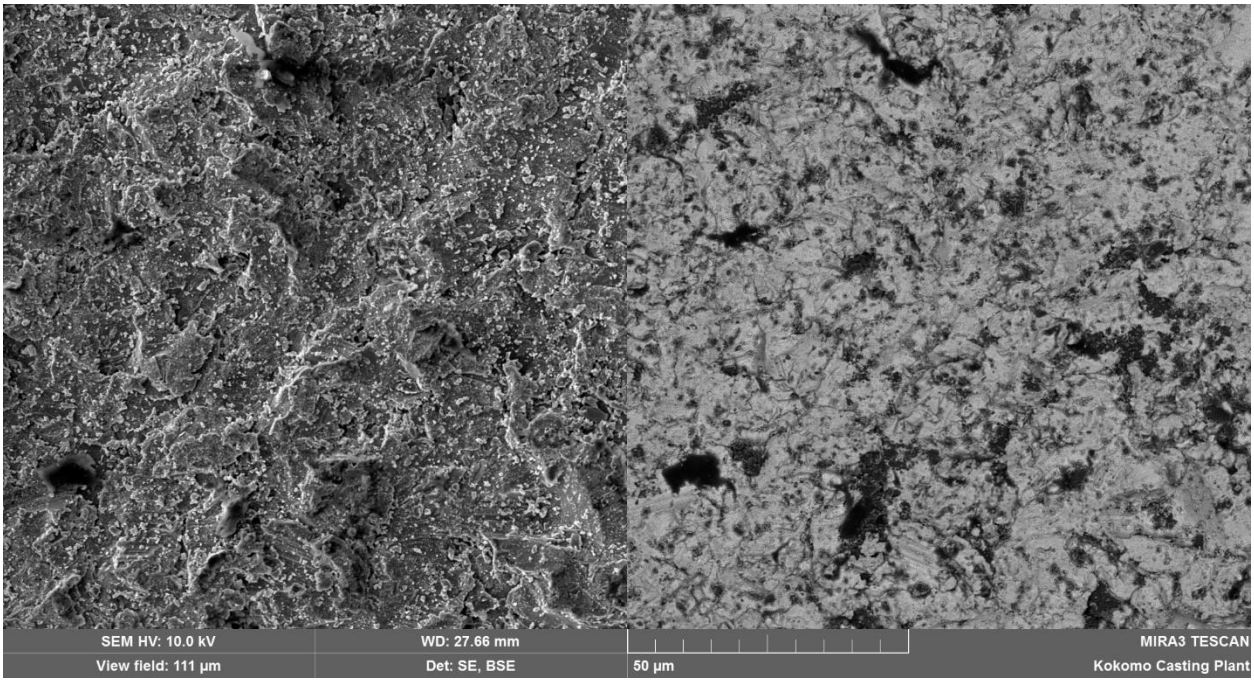

Figure 22. 2500x SEM images of the NC coating.

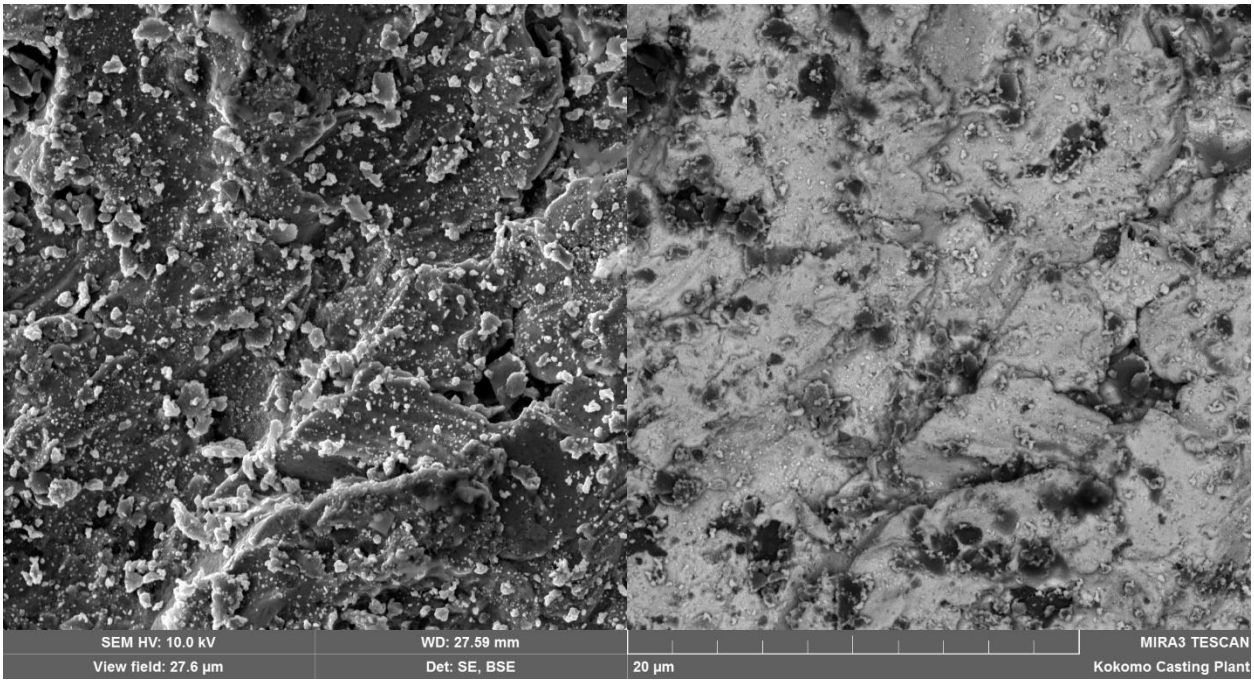

Figure 23. 10000x SEM images of the NC coating.

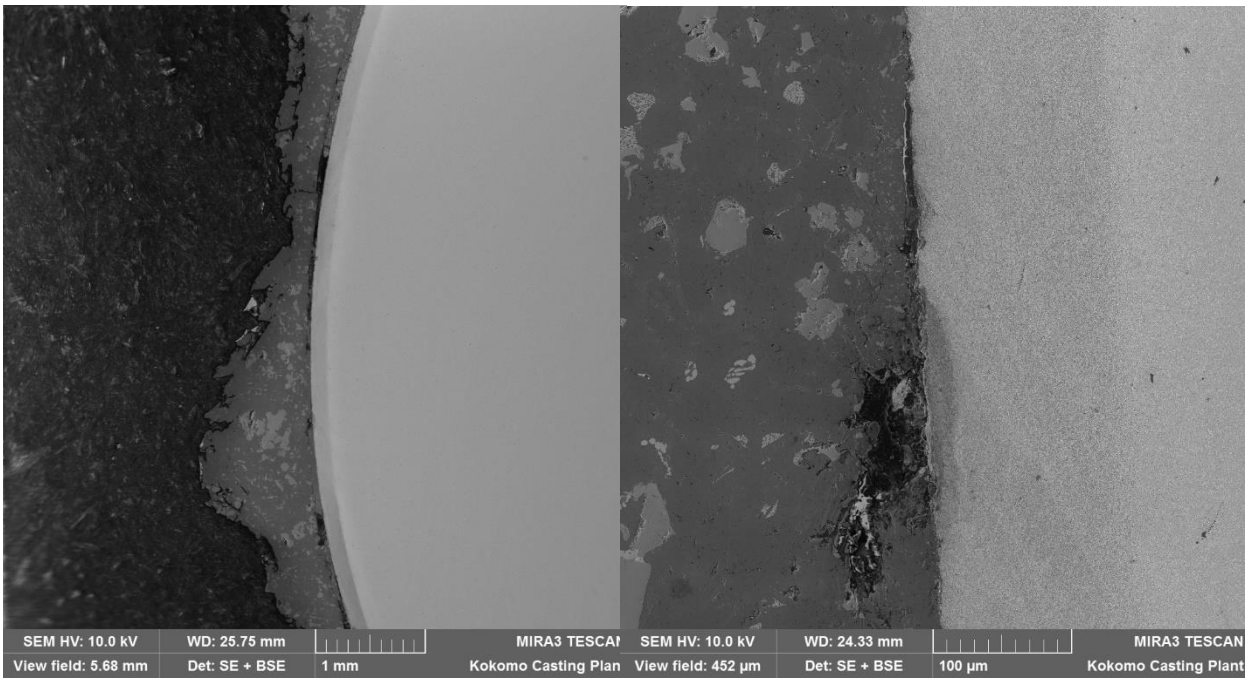

Figure 24. 50x and 600x SEM images of the H13 NC specimen dunked for 30 minutes at 1150°F.

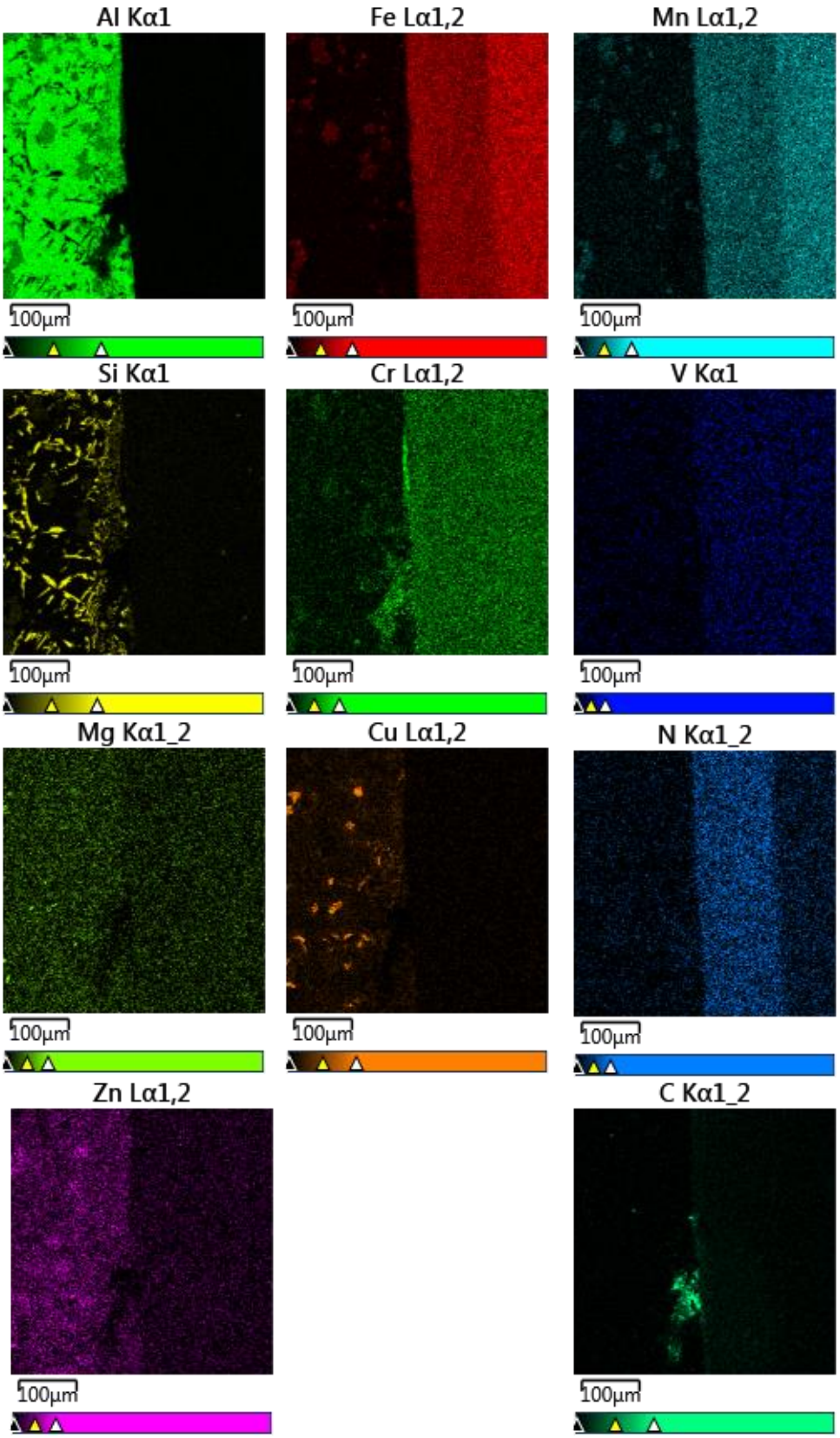

Figure 25. EDS maps corresponding to the 600x image in Figure 24.

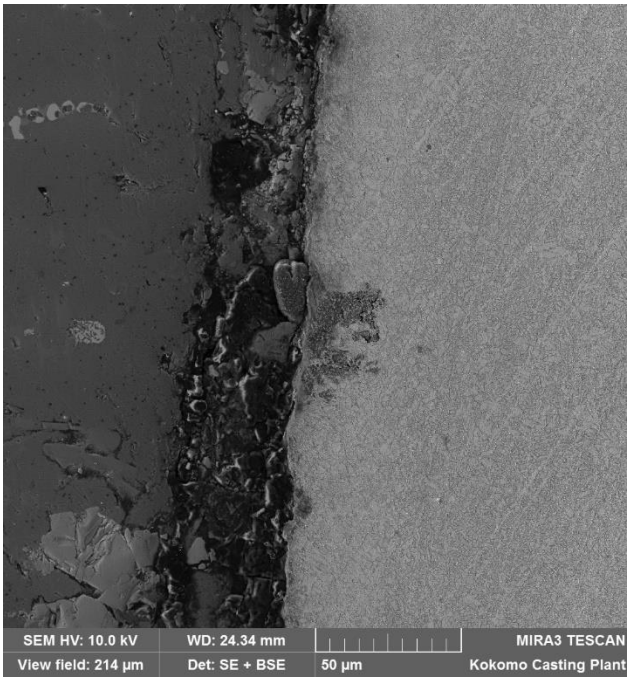

Figure 26. 1300x SEM image of the H13 NC specimen dunked for 30 minutes at 1150°F.

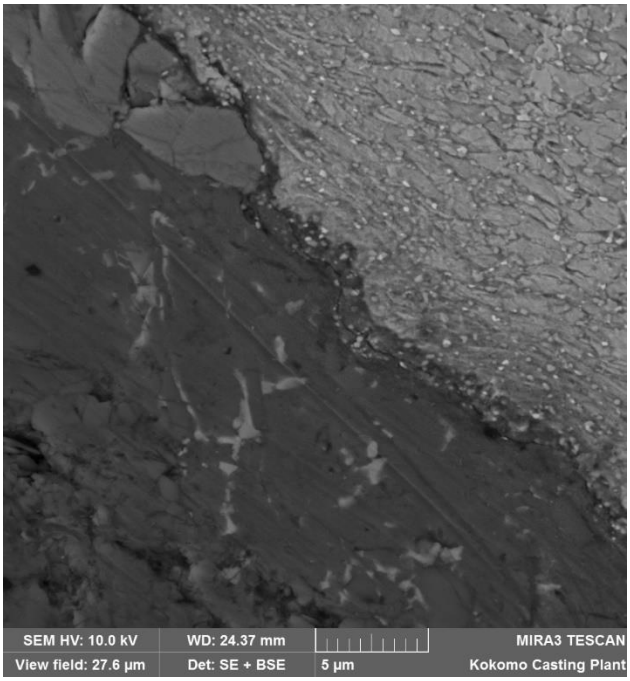

Figure 27. 10000x SEM image of the H13 NC specimen dunked for 30 minutes at 1150°F.

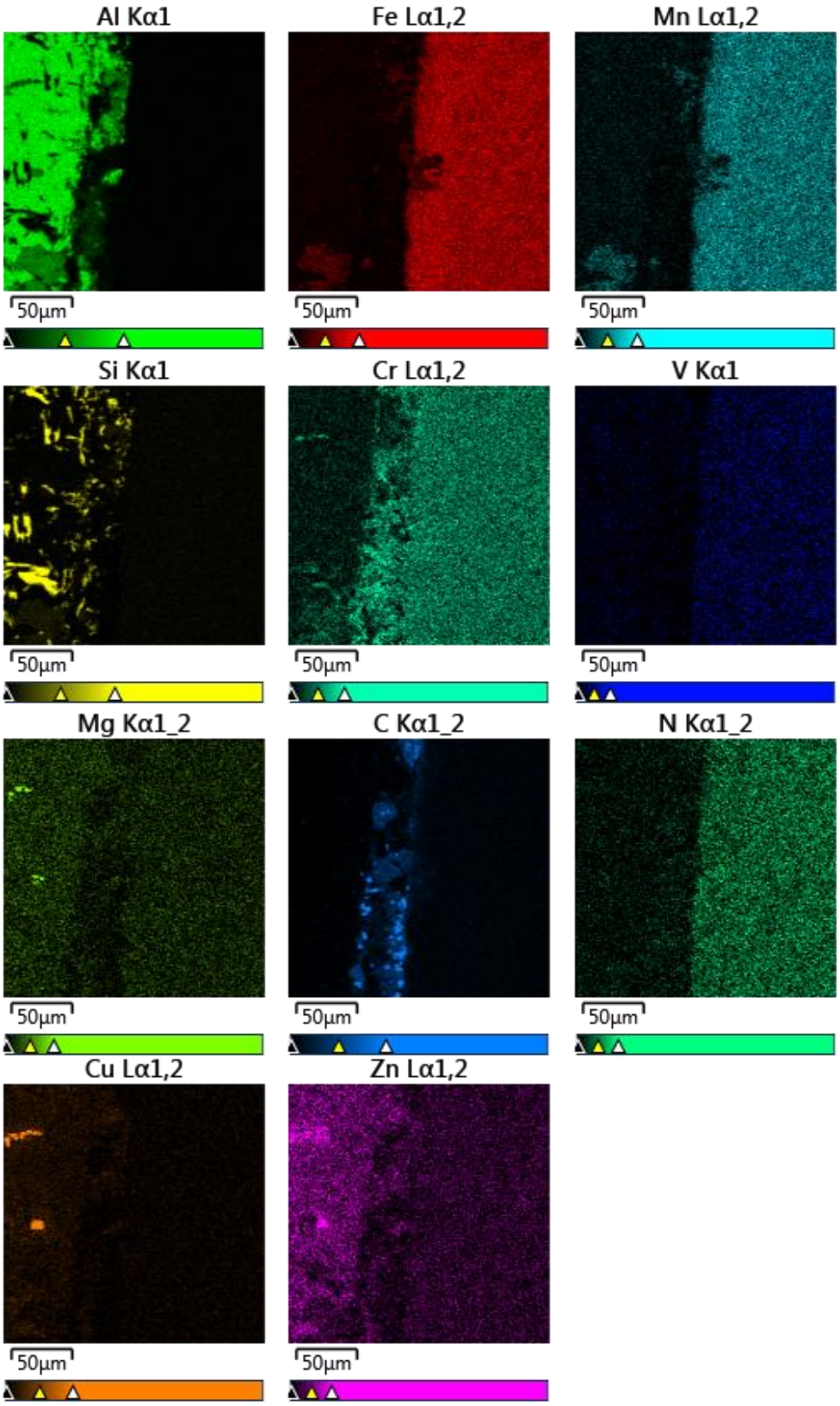

Figure 28. EDS maps corresponding to Figure 26.

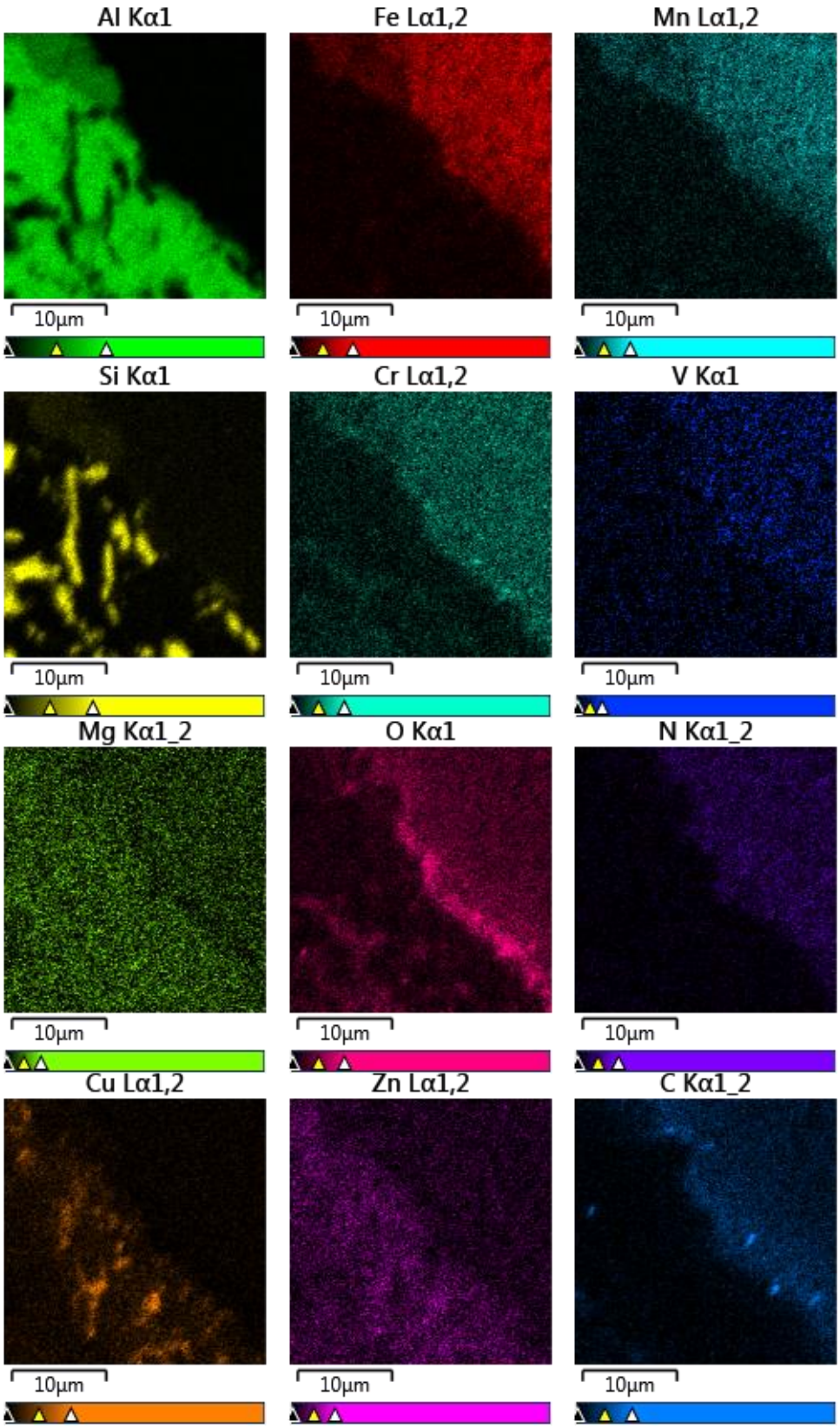

Figure 29. EDS maps corresponding to Figure 27.

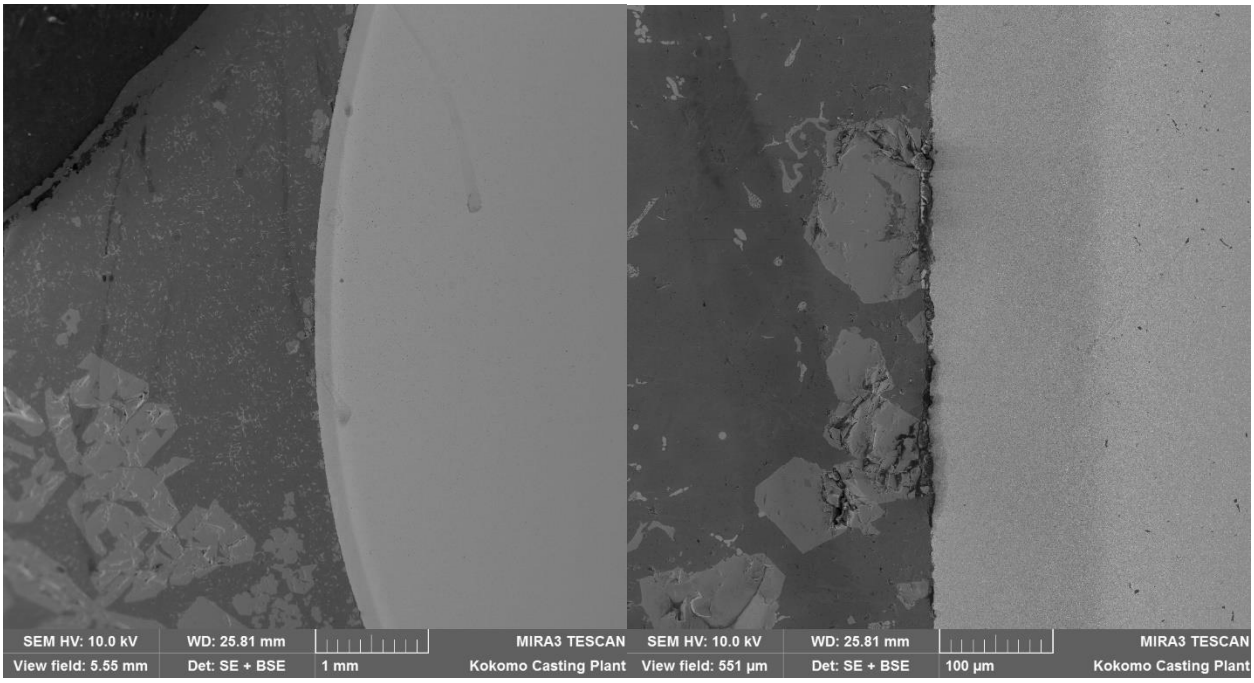

Figure 30. 50x and 500x SEM images of the H13 NC specimen dunked for 120 minutes at 1150°F.

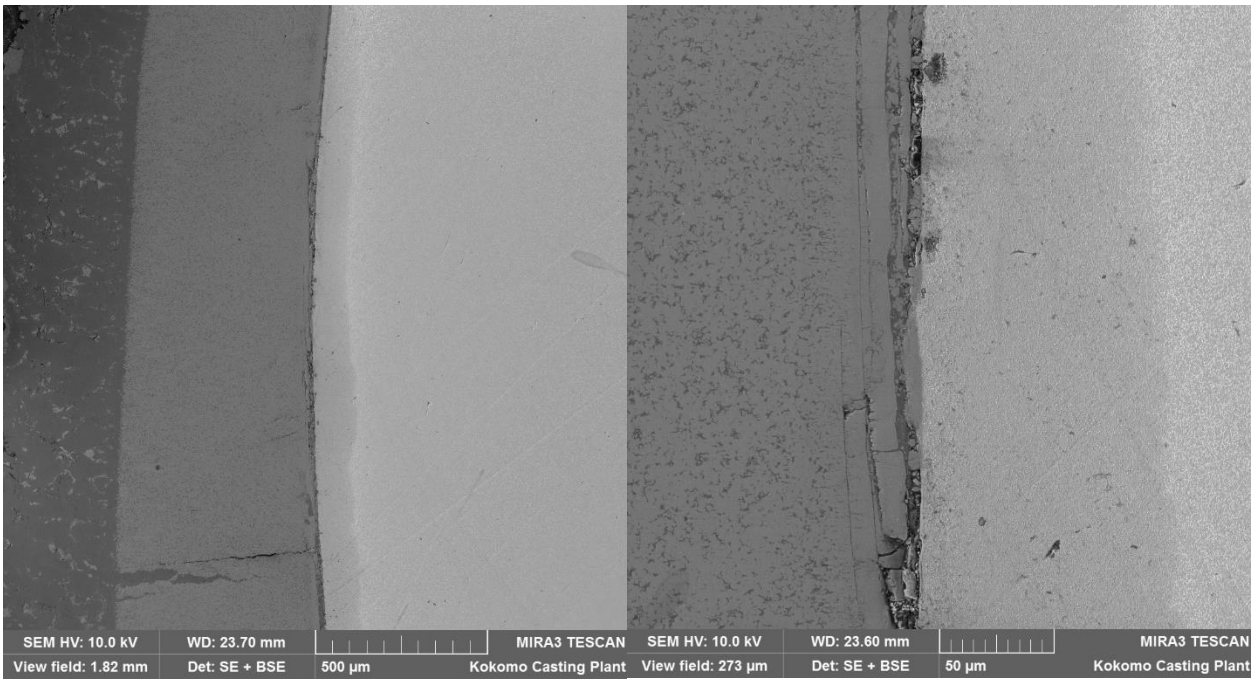

Figure 31. 150x and 1000x SEM images of the H13 NC specimen dunked for 1440 minutes at 1150°F.

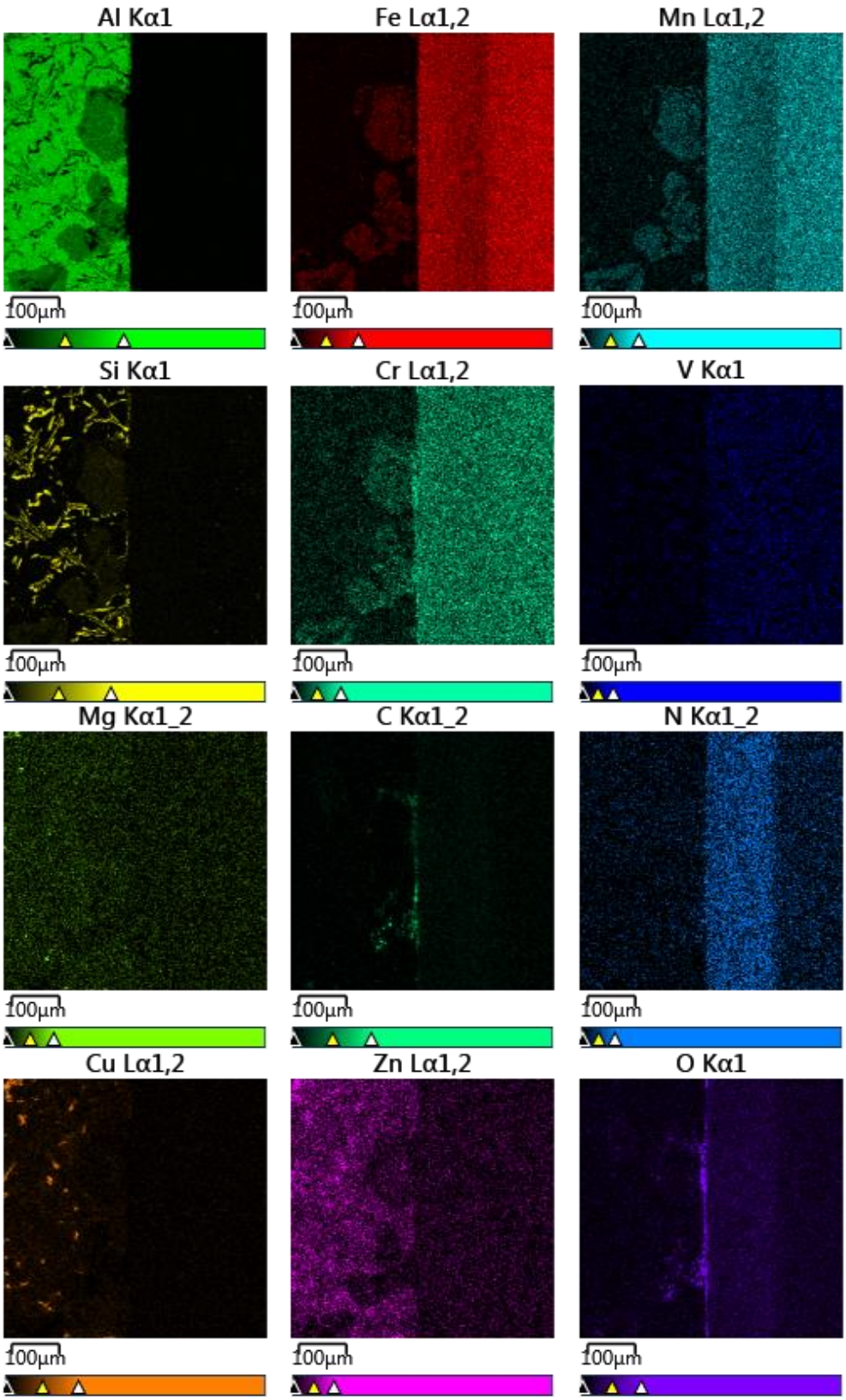

Figure 32. EDS maps corresponding to the 500x image in Figure 30.

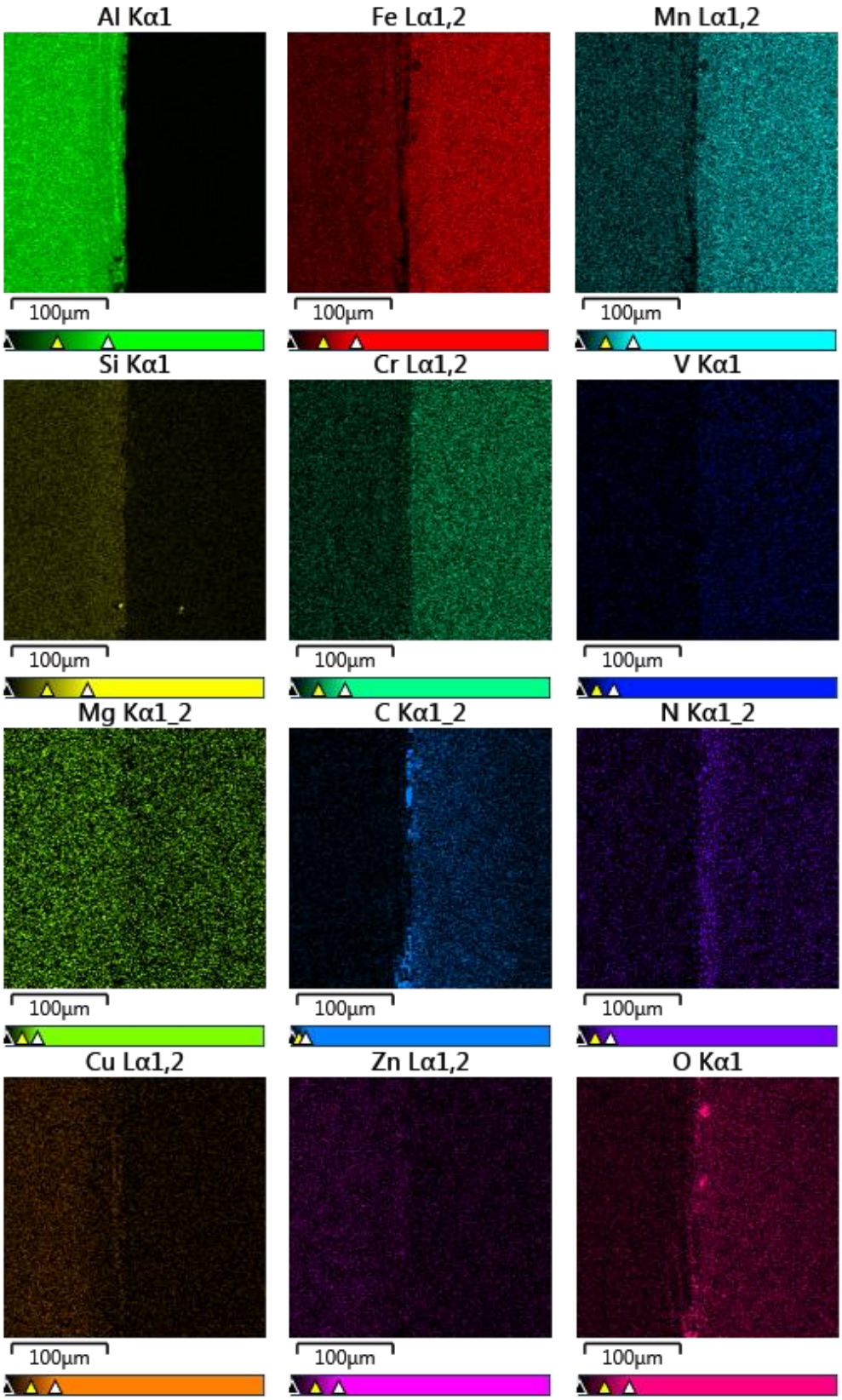

Figure 33. EDS maps corresponding to the 1000x image in Figure 31.

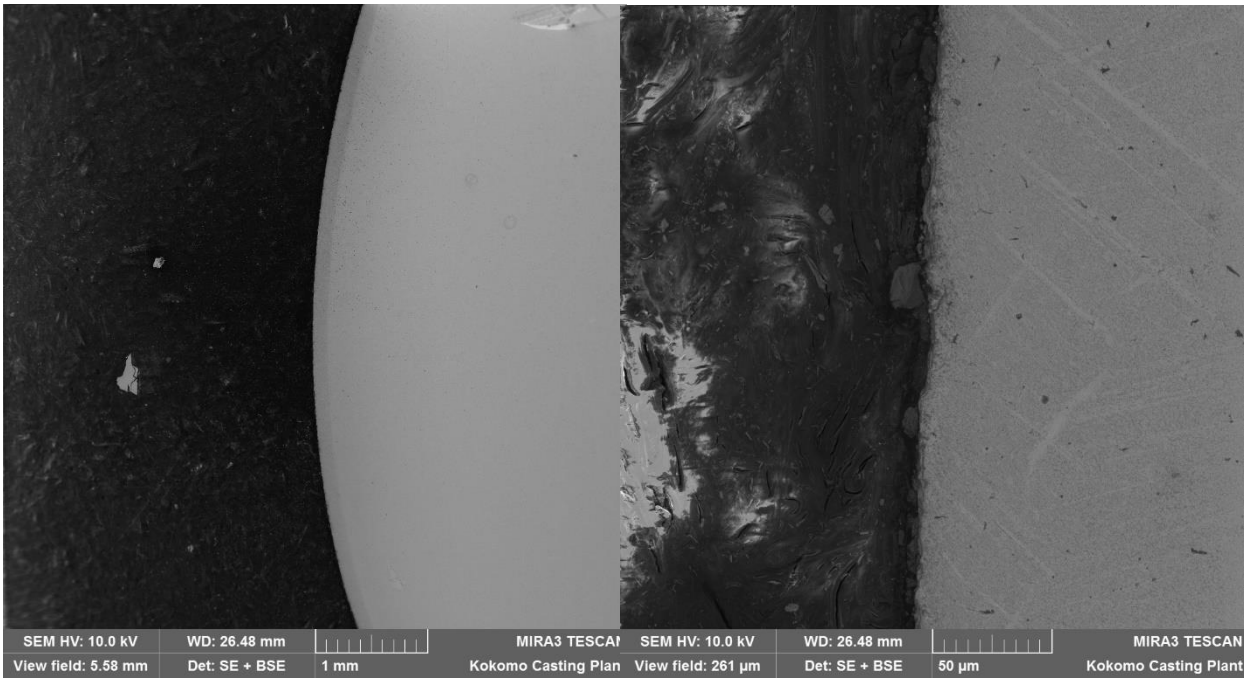

Figure 34. 50x and 1000x SEM images of H13 NC specimen dunked for 30 minutes at 1250°F.

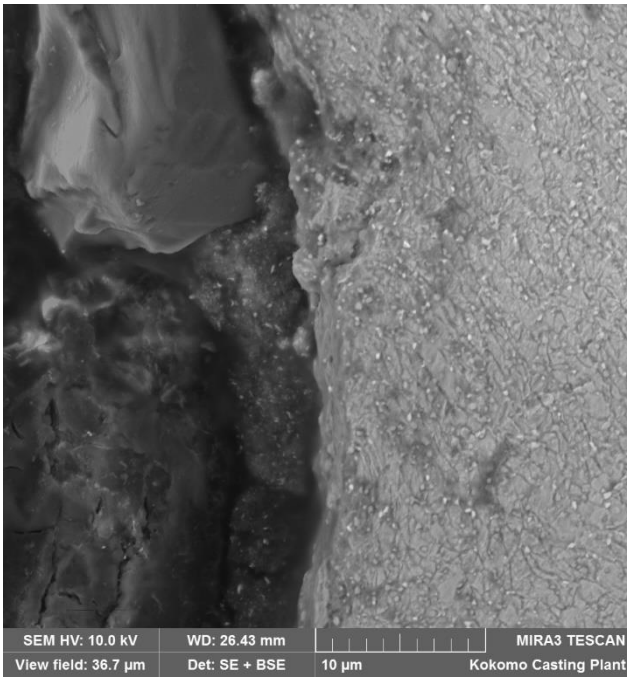

Figure 35. 7500x SEM image of the H13 NC specimen dunked for 30 minutes at 1250°F

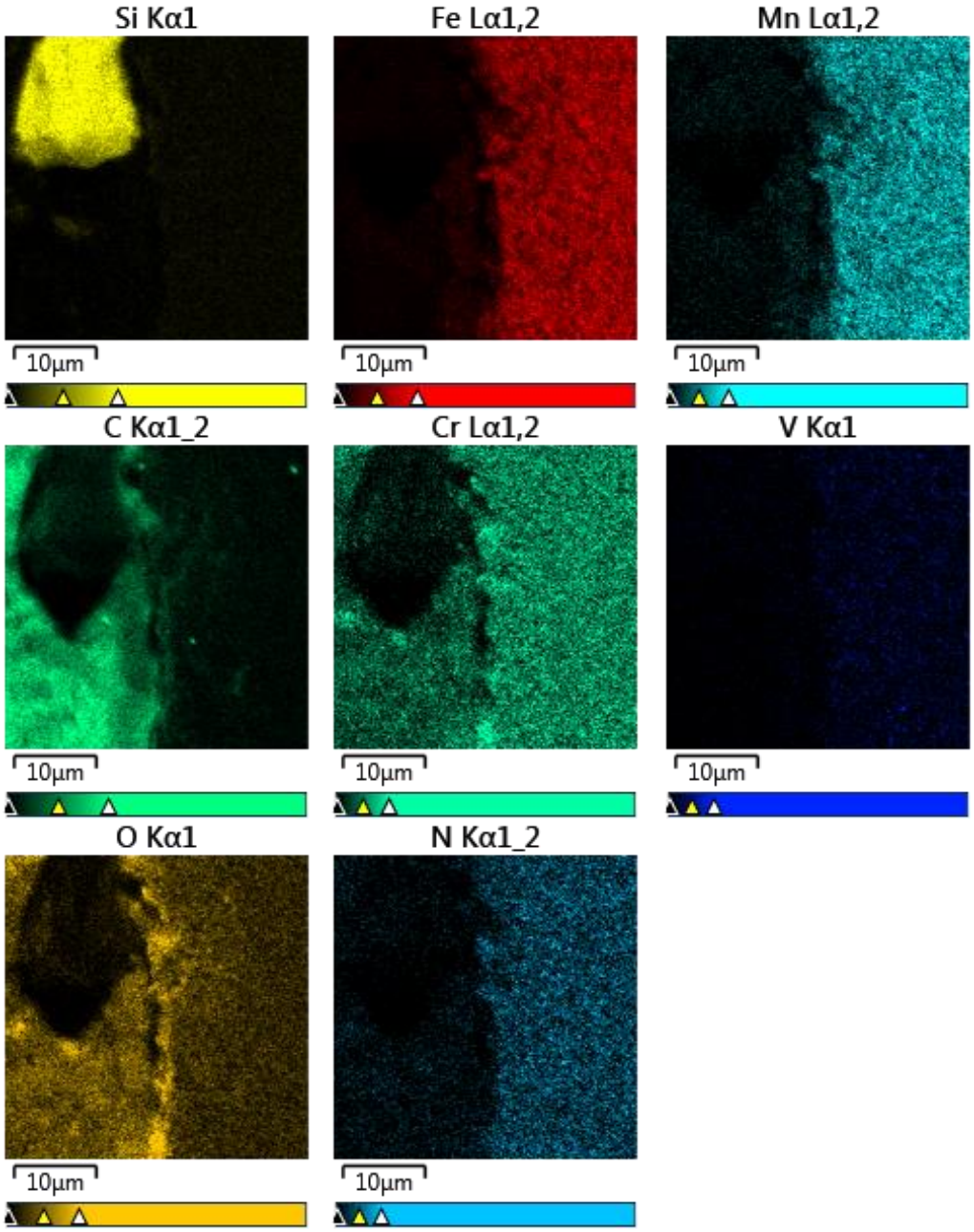

Figure 36. EDS maps corresponding to Figure 35.

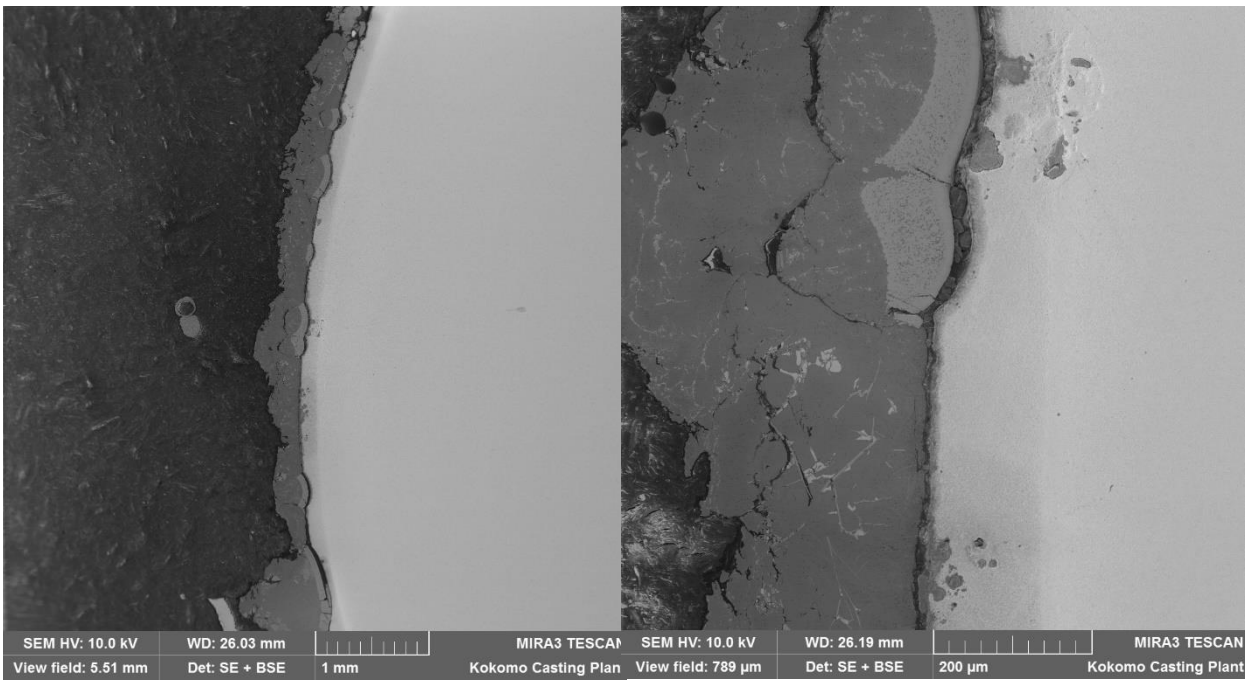

Figure 37. 50x and 350x SEM images of the H13 NC specimen dunked for 120 minutes at 1250°F.

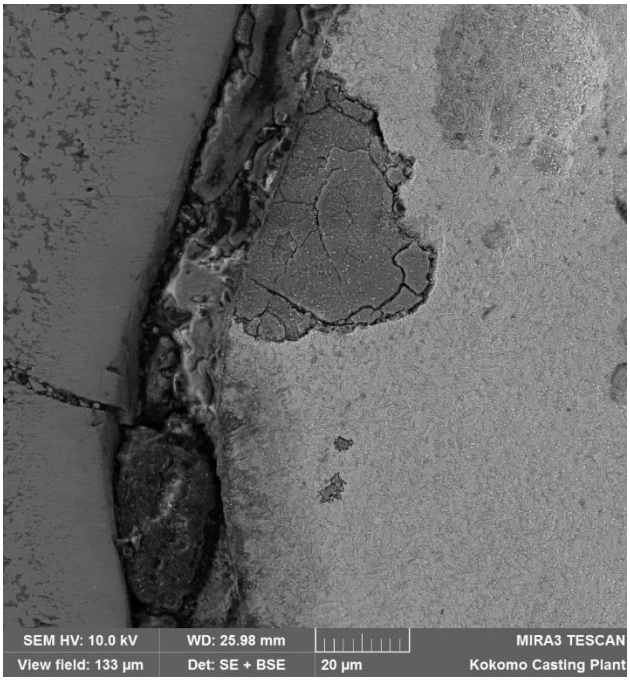

Figure 38. 2000x SEM image of the H13 NC specimen dunked for 120 minutes at 1250°F.

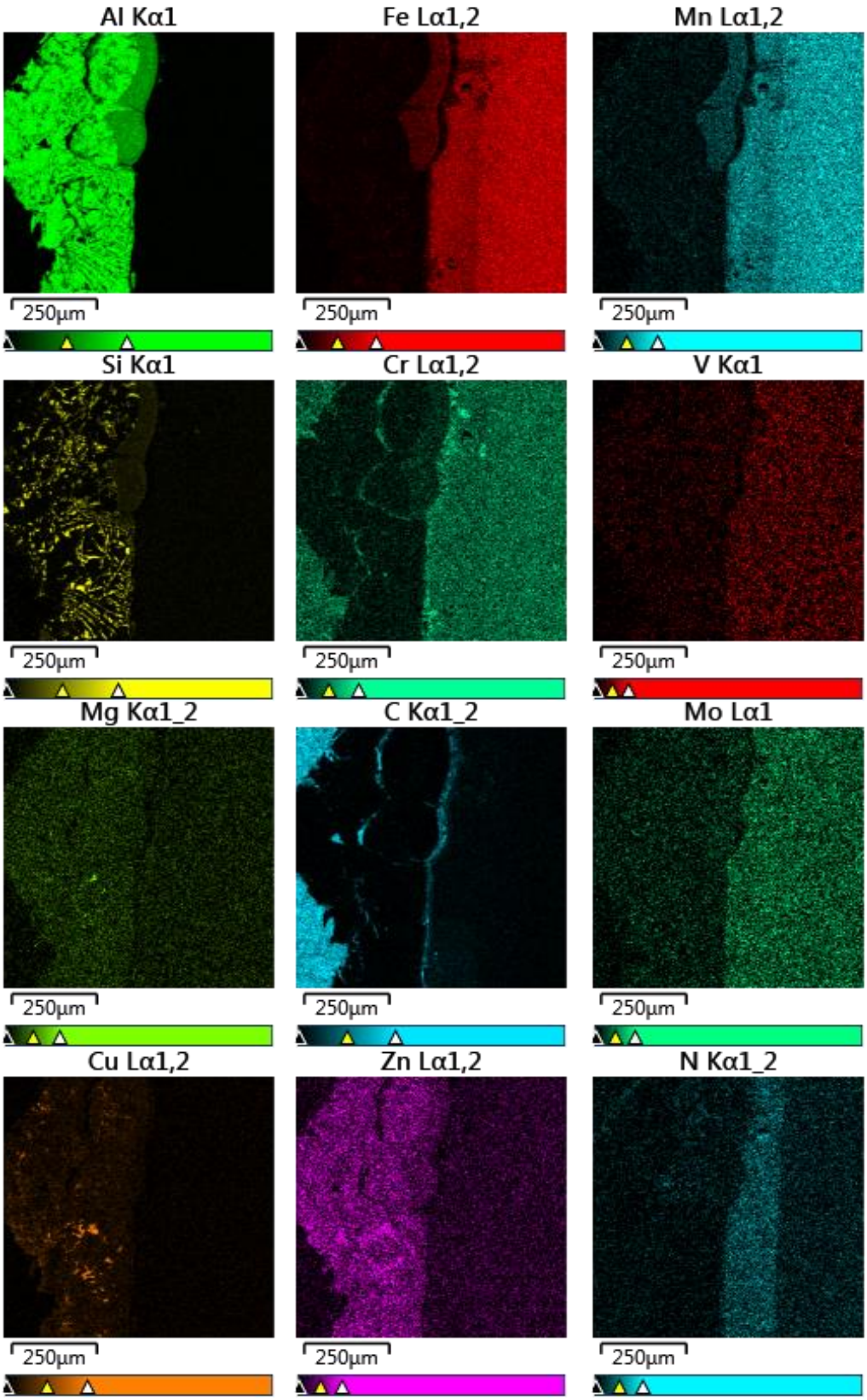

Figure 39. EDS maps corresponding to the 350x image in Figure 37.

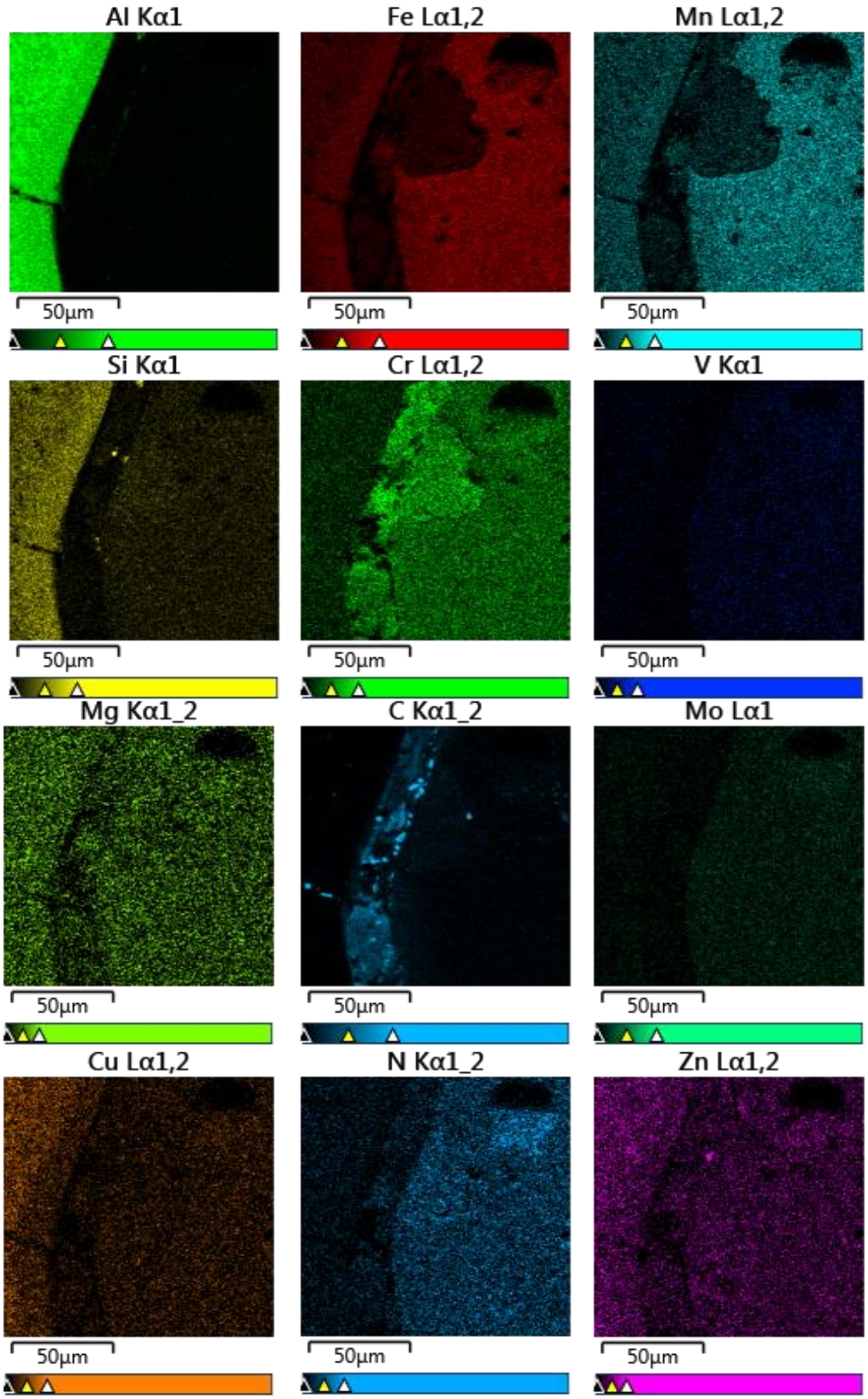

Figure 40. EDS maps corresponding to Figure 38.

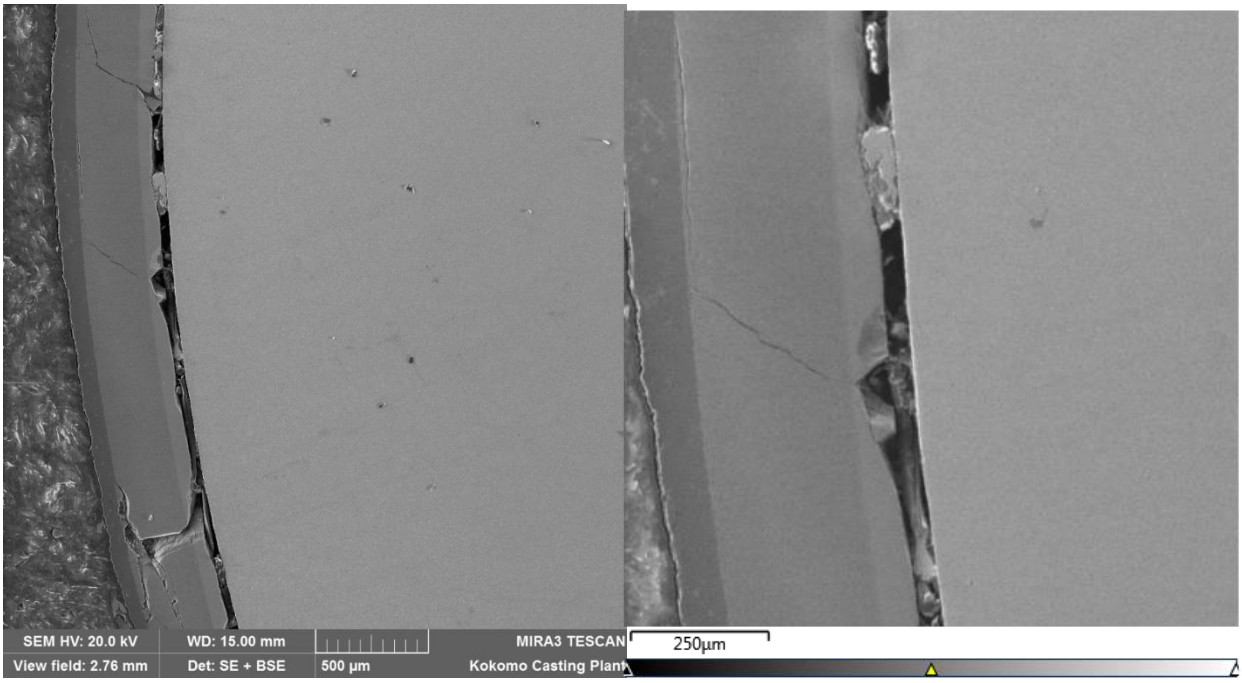

Figure 41. 100x and 250x SEM images of the H13 NC specimen dunked for 1440 minutes at 1250°F.

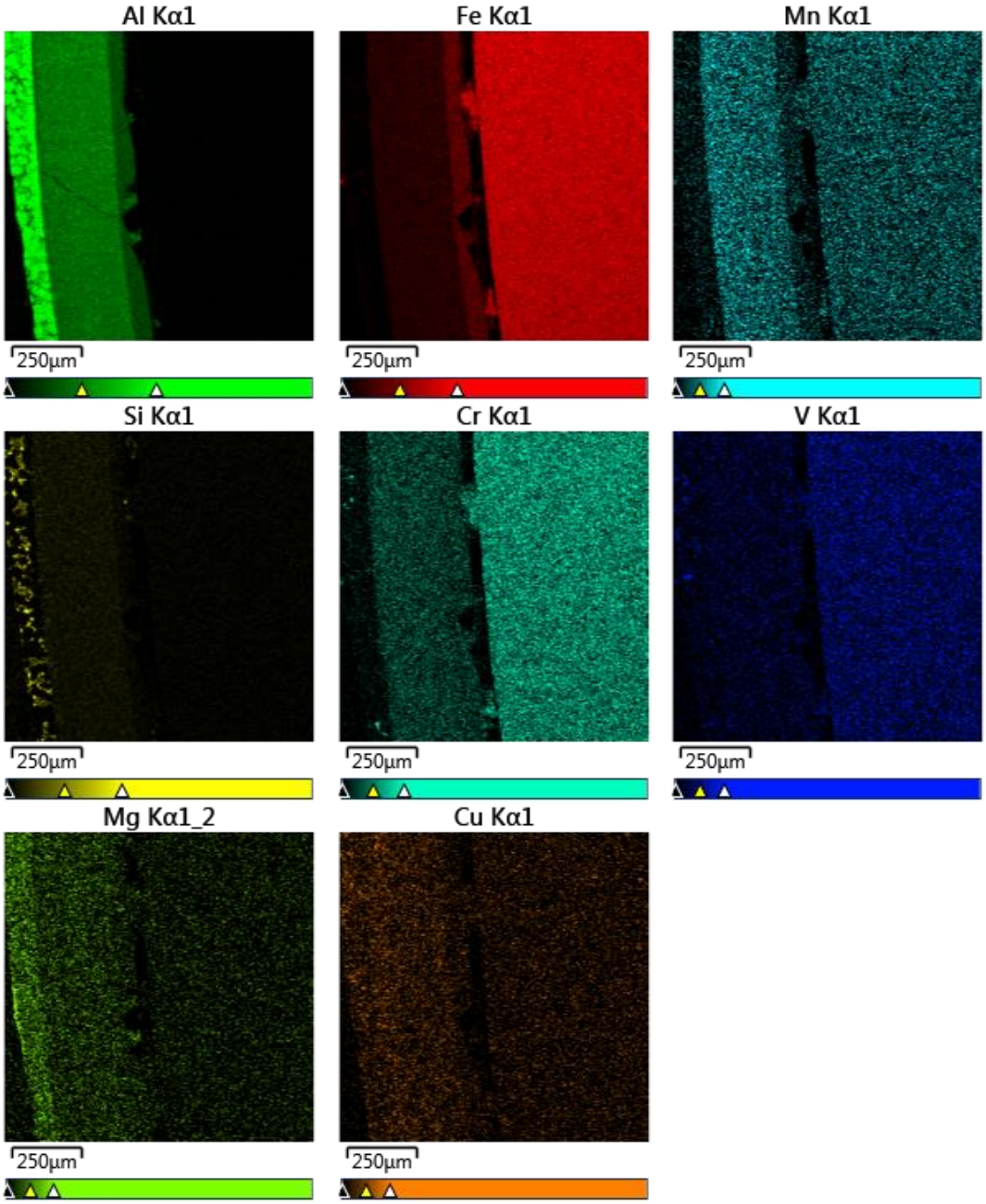

Figure 42. EDS maps corresponding to the 250x image in Figure 41.

4.2.3 H13 with Silicon Doped Diamond Like Carbon (H13 Si-DLC)

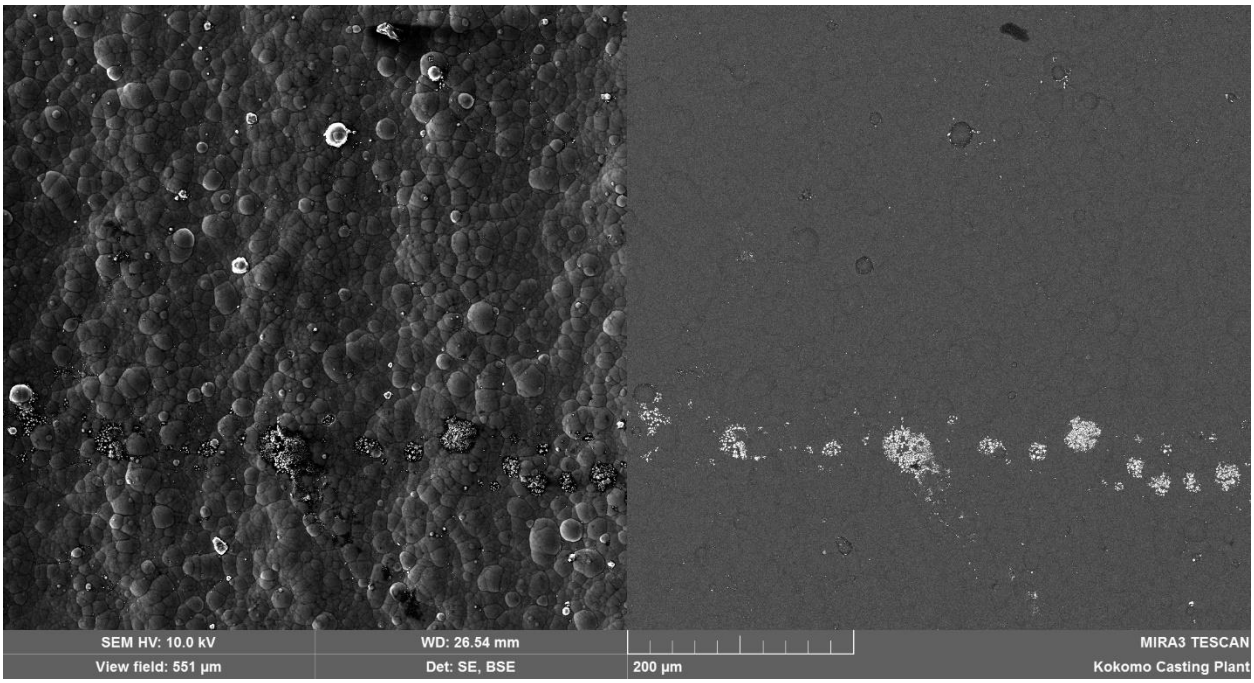

Figure 43. 500x SEM images of the Si-DLC coating.

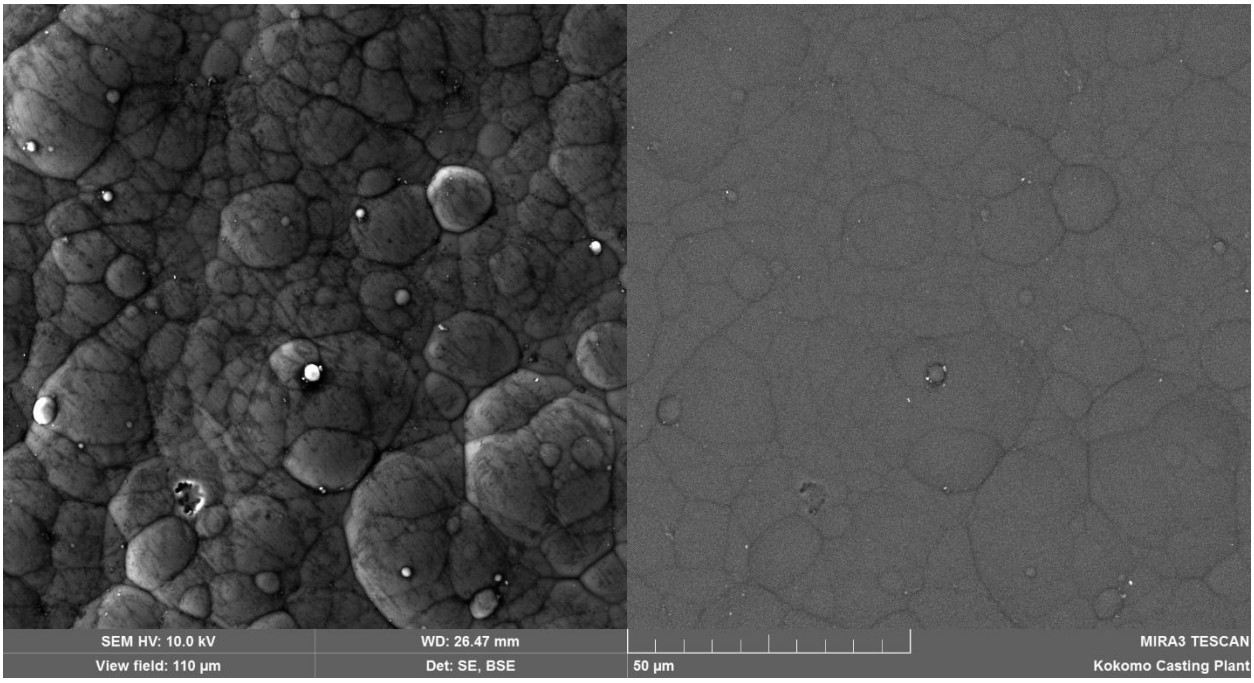

Figure 44. 2500x SEM images of the Si-DLC coating.

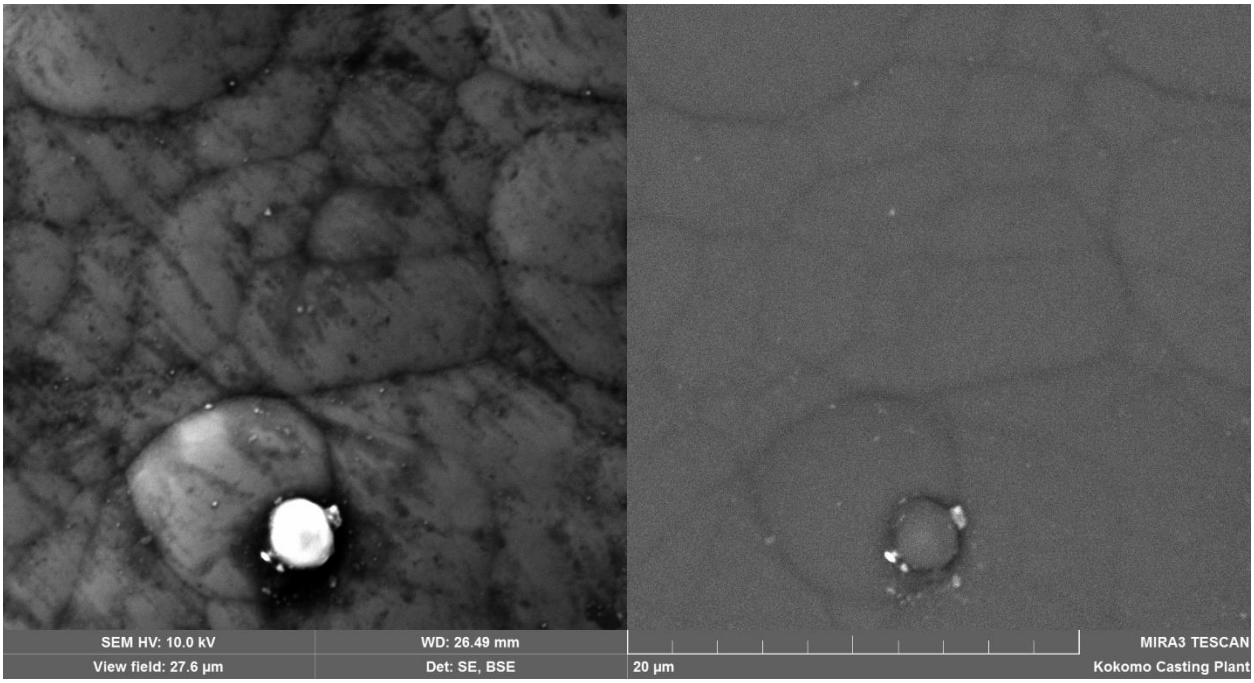

Figure 45. 10000x SEM images of the Si-DLC coating.

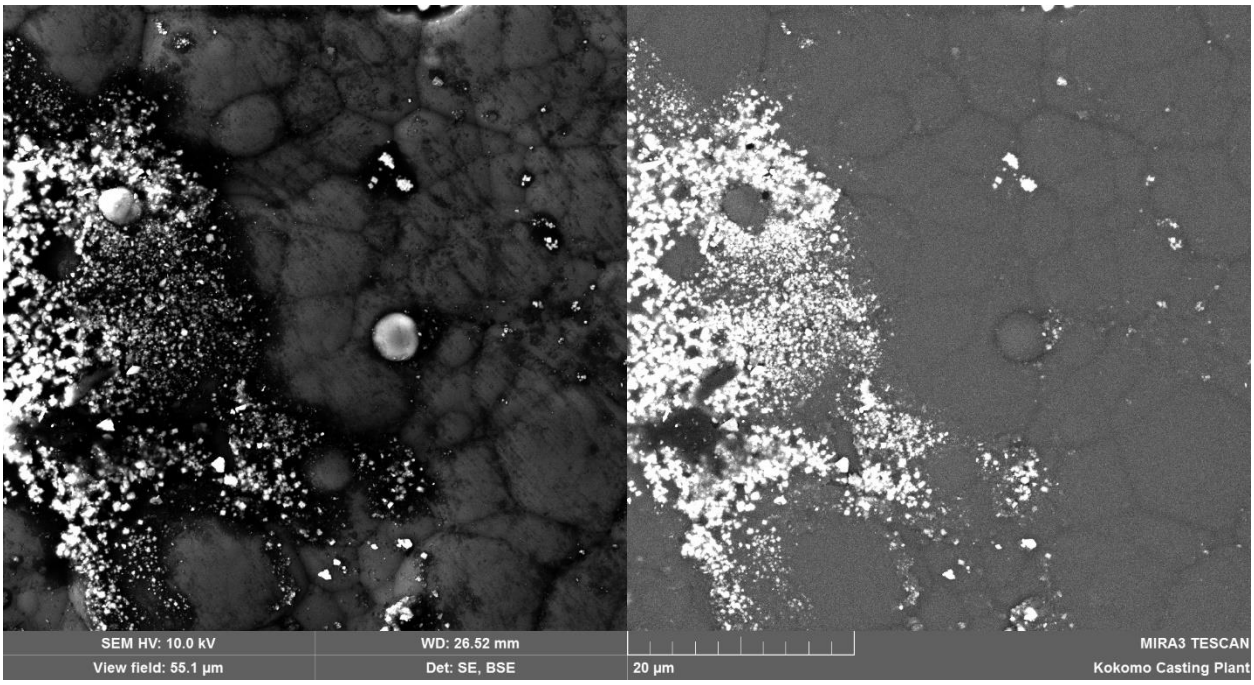

Figure 46. 5000x SEM images of the Si-DLC coating.

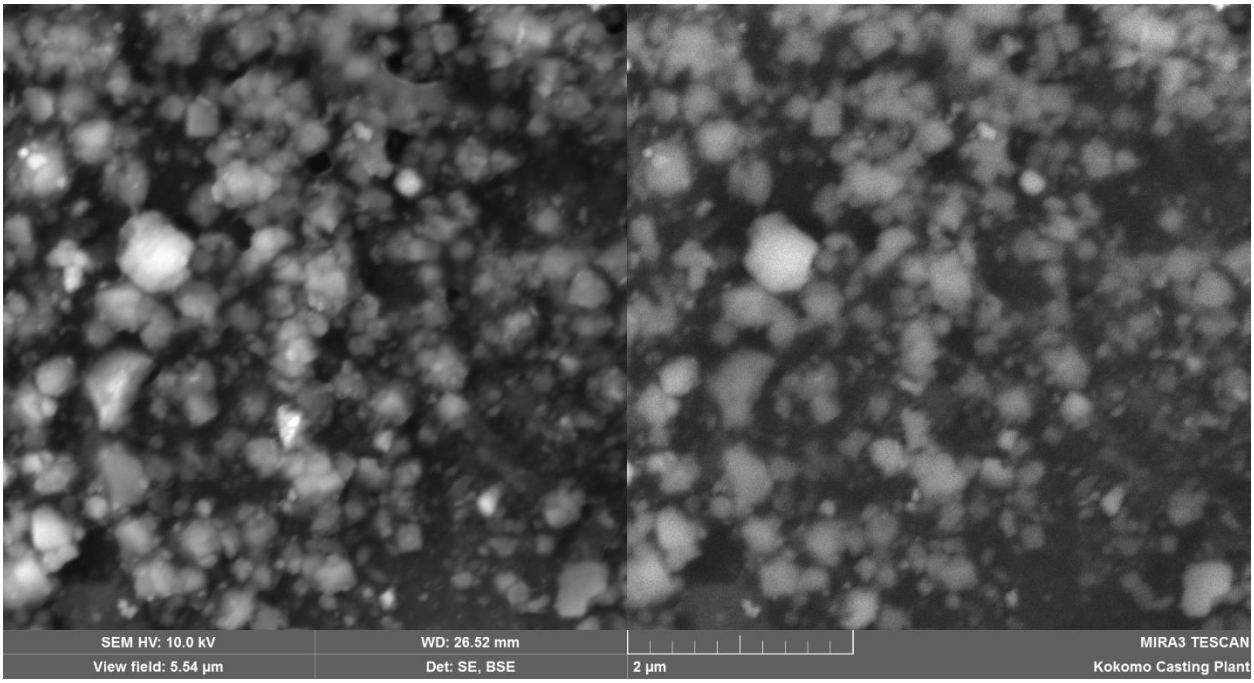

Figure 47. 50000x SEM images of the Si-DLC coating.

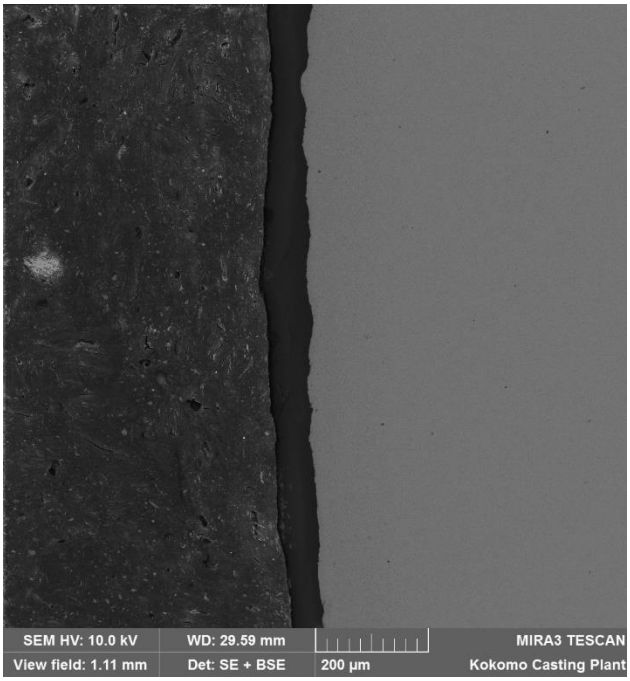

Figure 48. 250x SEM image of the H13 Si-DLC specimen dunked for 30 minutes at 1150°F.

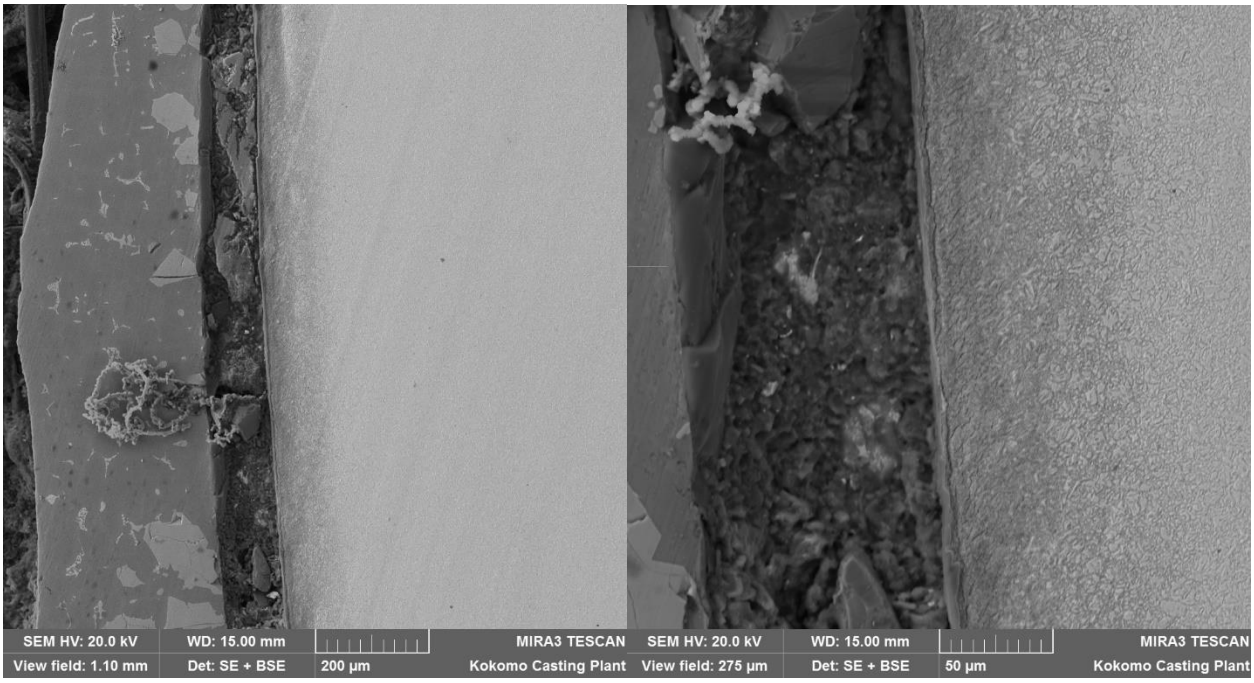

Figure 49. 250x and 1000x SEM images of the H13 Si-DLC specimen dunked for 120 minutes at 1150°F.

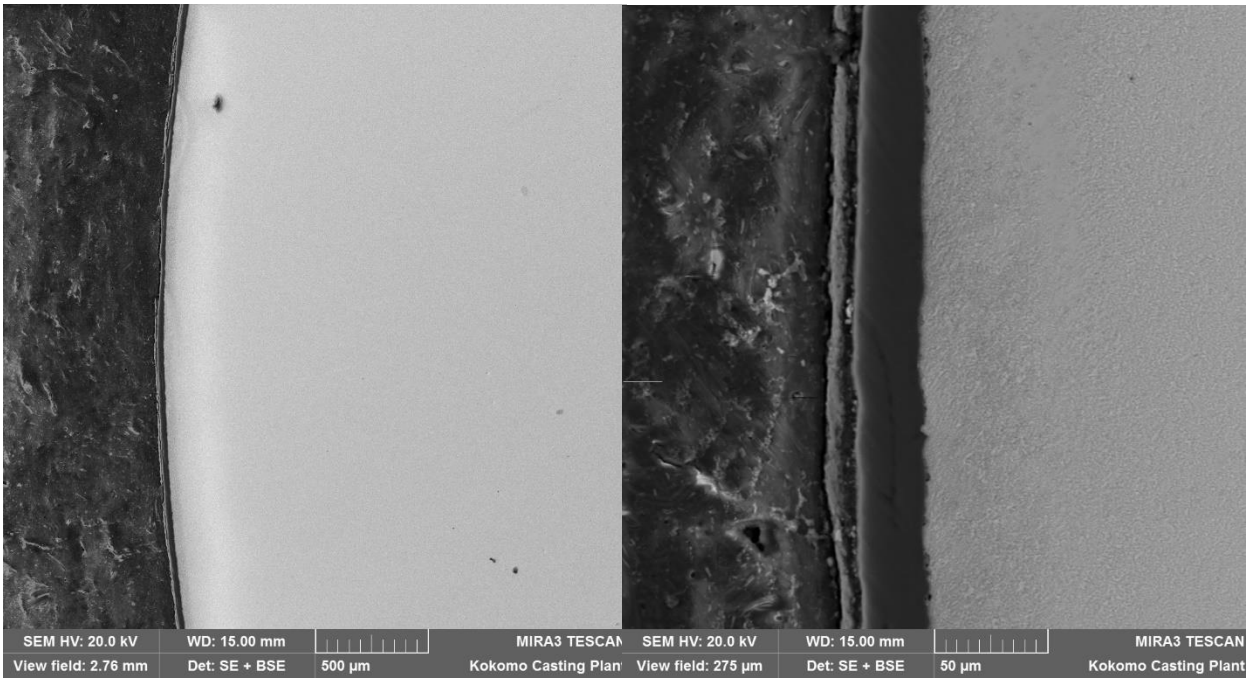

Figure 50. 100x and 1000x SEM images of the H13 Si-DLC specimen dunked for 1440 minutes at 1150°F.

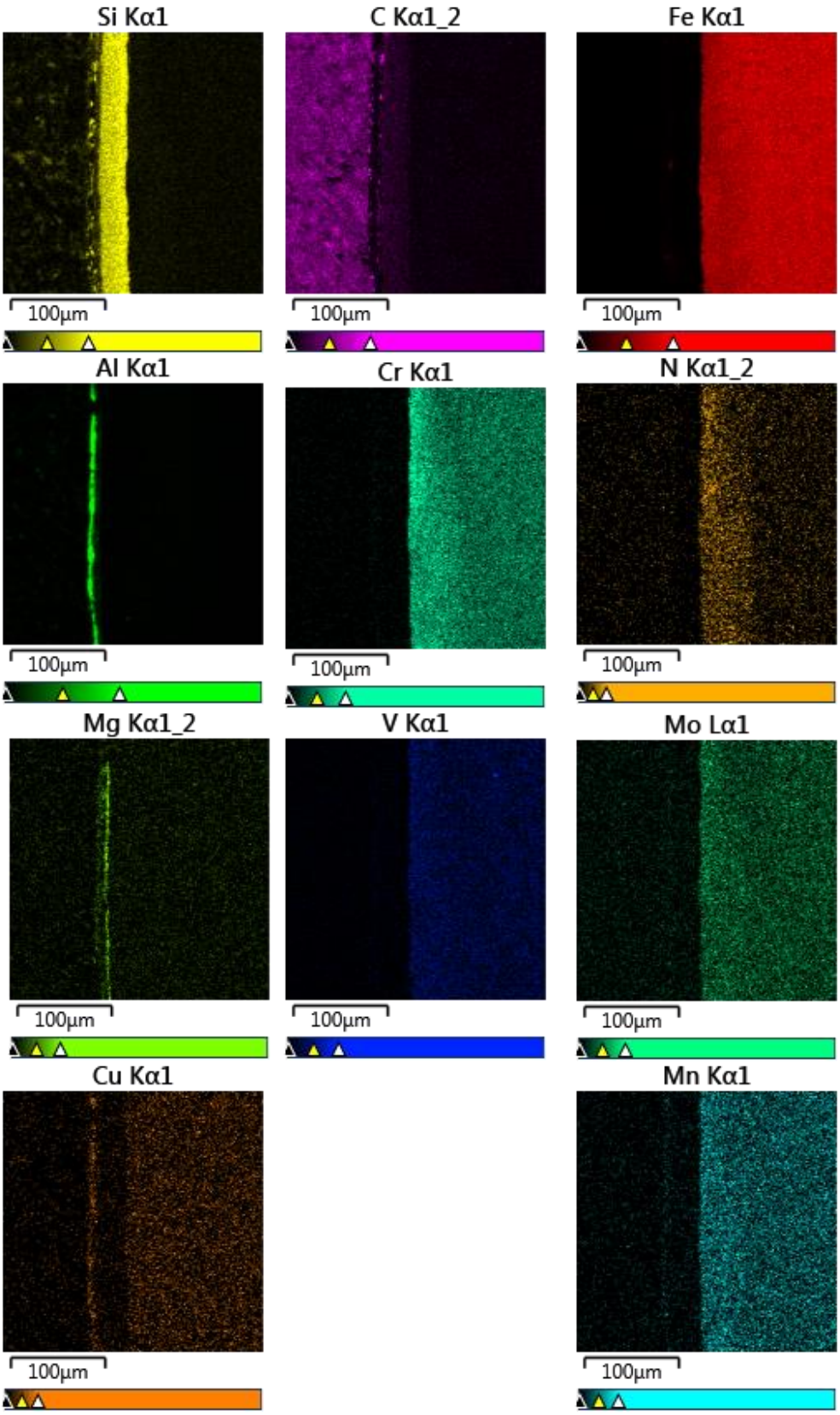

Figure 51. EDS maps corresponding to the 1000x image of Figure 50.

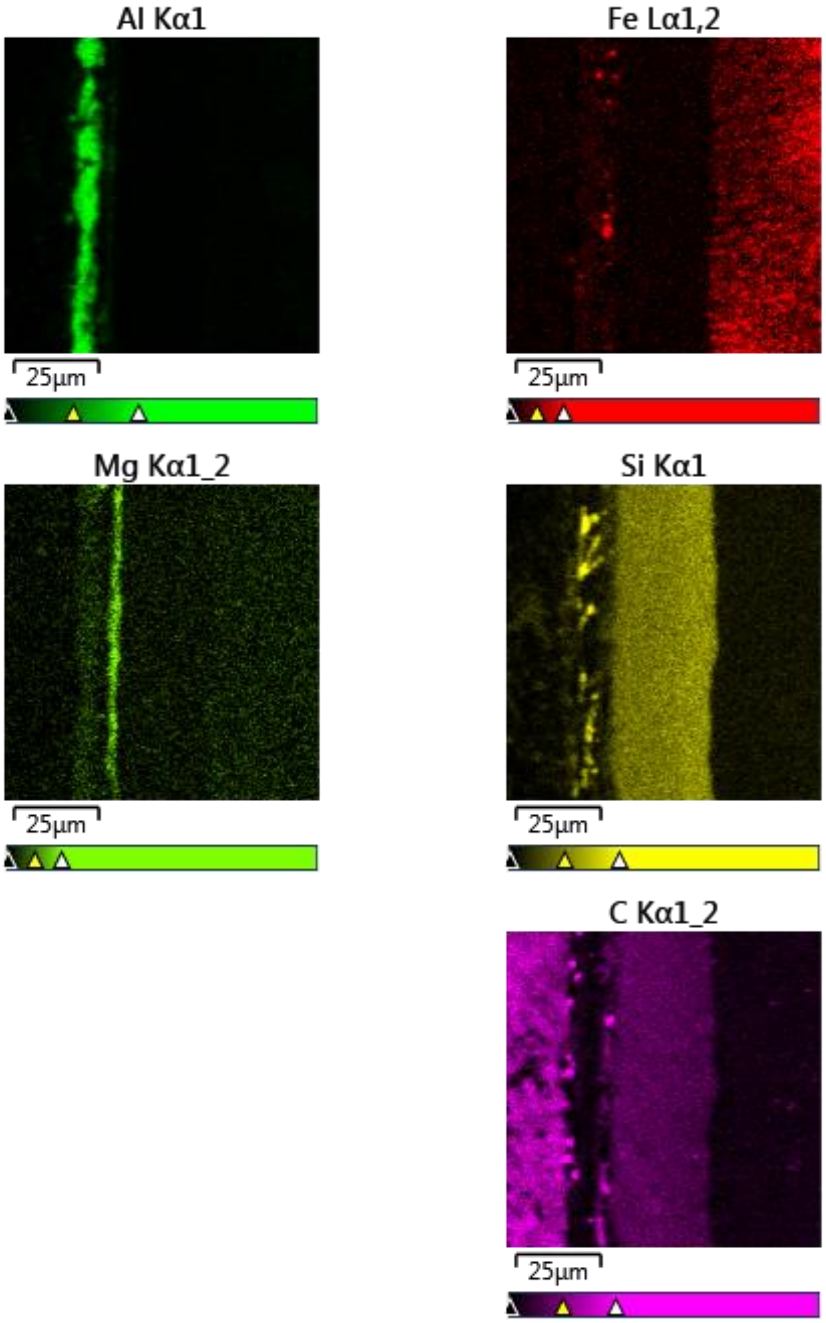

Figure 52. EDS maps at 3000x detailing the accumulation of magnesium at the surface of the silicon doped Si-DLC specimen dunked for 1440 minutes at 1150°F.

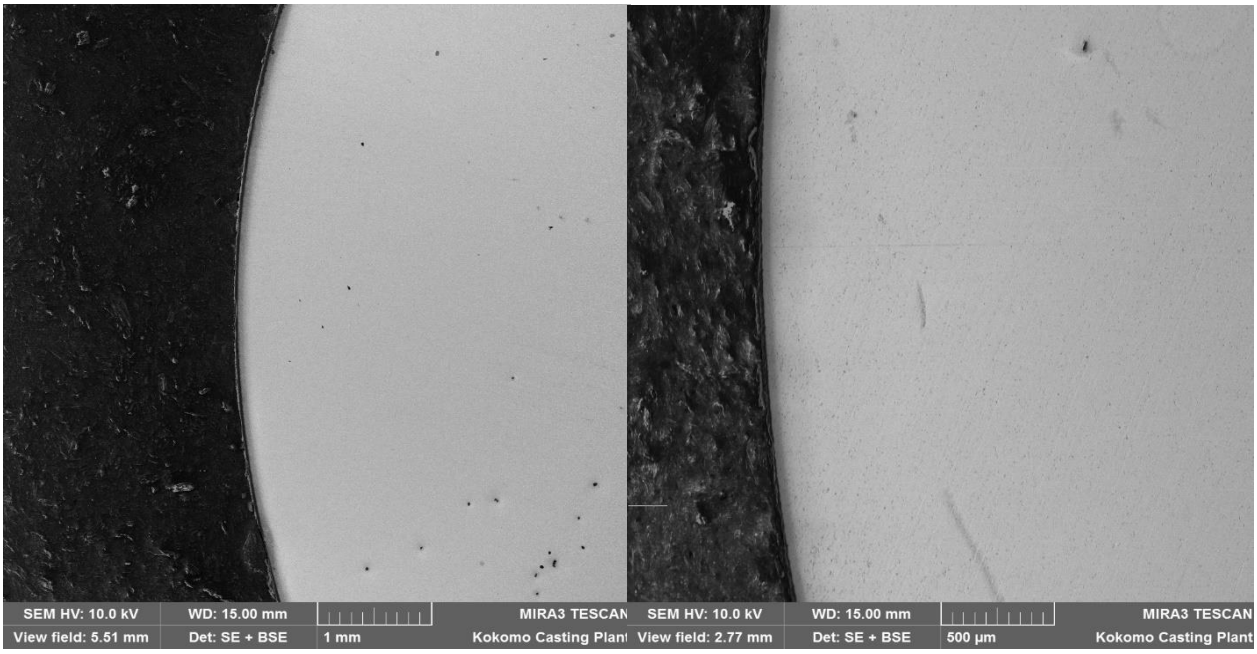

Figure 53. 50x SEM image of the H13 DLC specimen dunked for 30 minutes at 1250°F and 100x SEM image of the H13 DLC specimen dunked for 120 minutes at 1250°F.

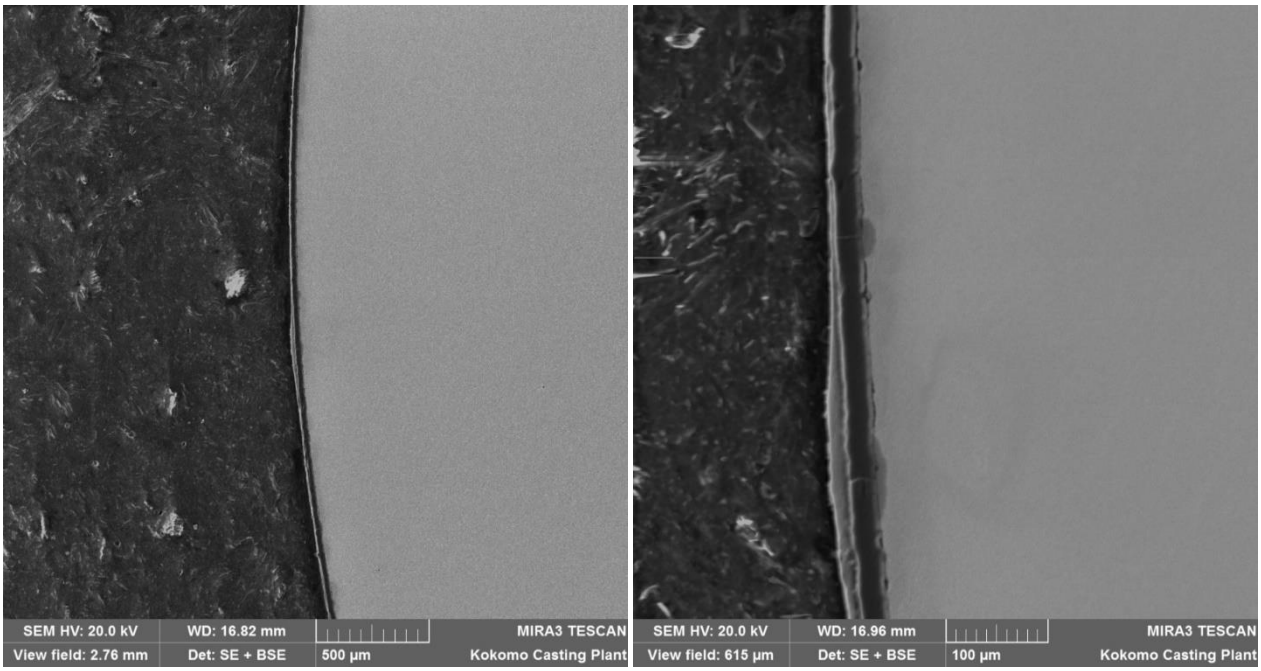

Figure 54. 100x and 450x SEM images of the H13 Si-DLC specimen dunked for 1440 minutes at 1250°F.

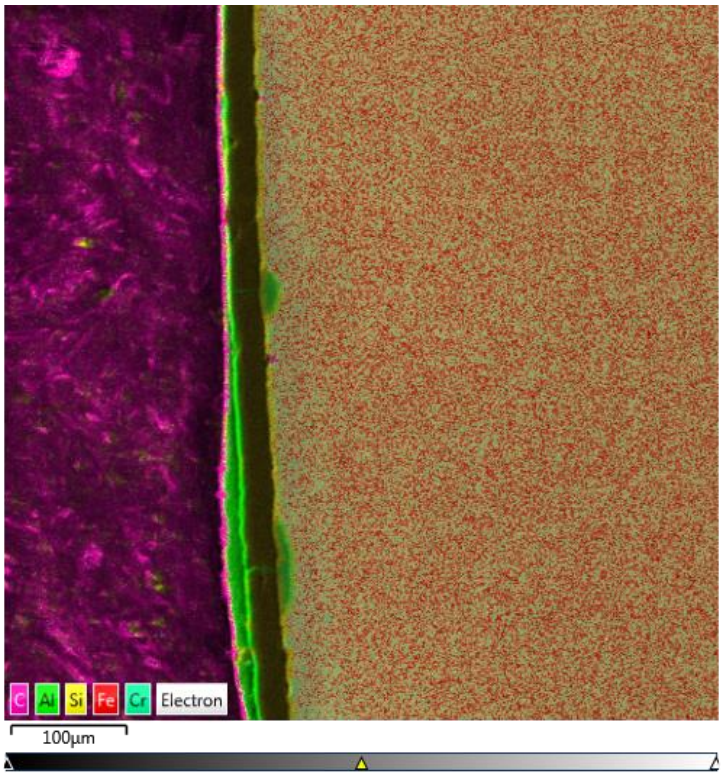

Figure 55. EDS maps corresponding to the 450x image in Figure 54.

Figure 55 continued.

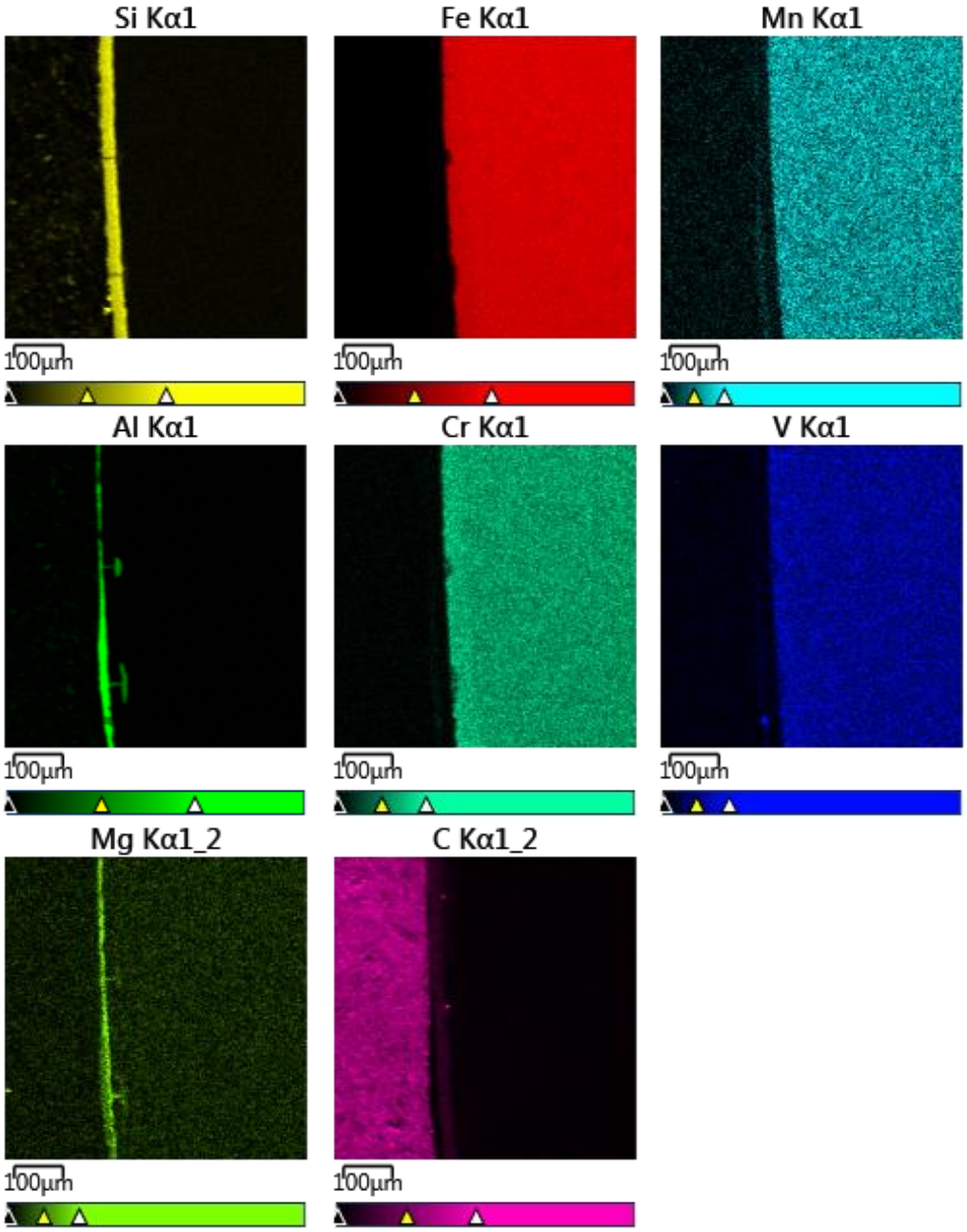

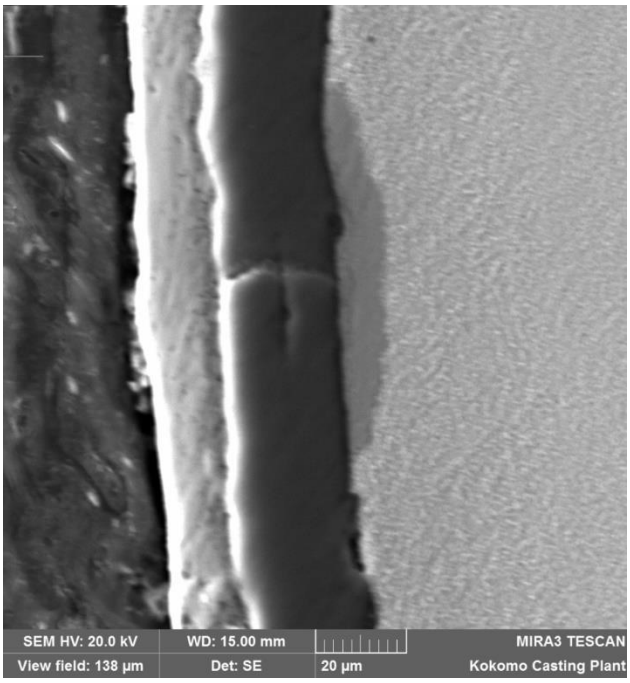

Figure 56. 2000x SEM image of the H13 Si-DLC specimen dunked for 1440 minutes at 1250°F.

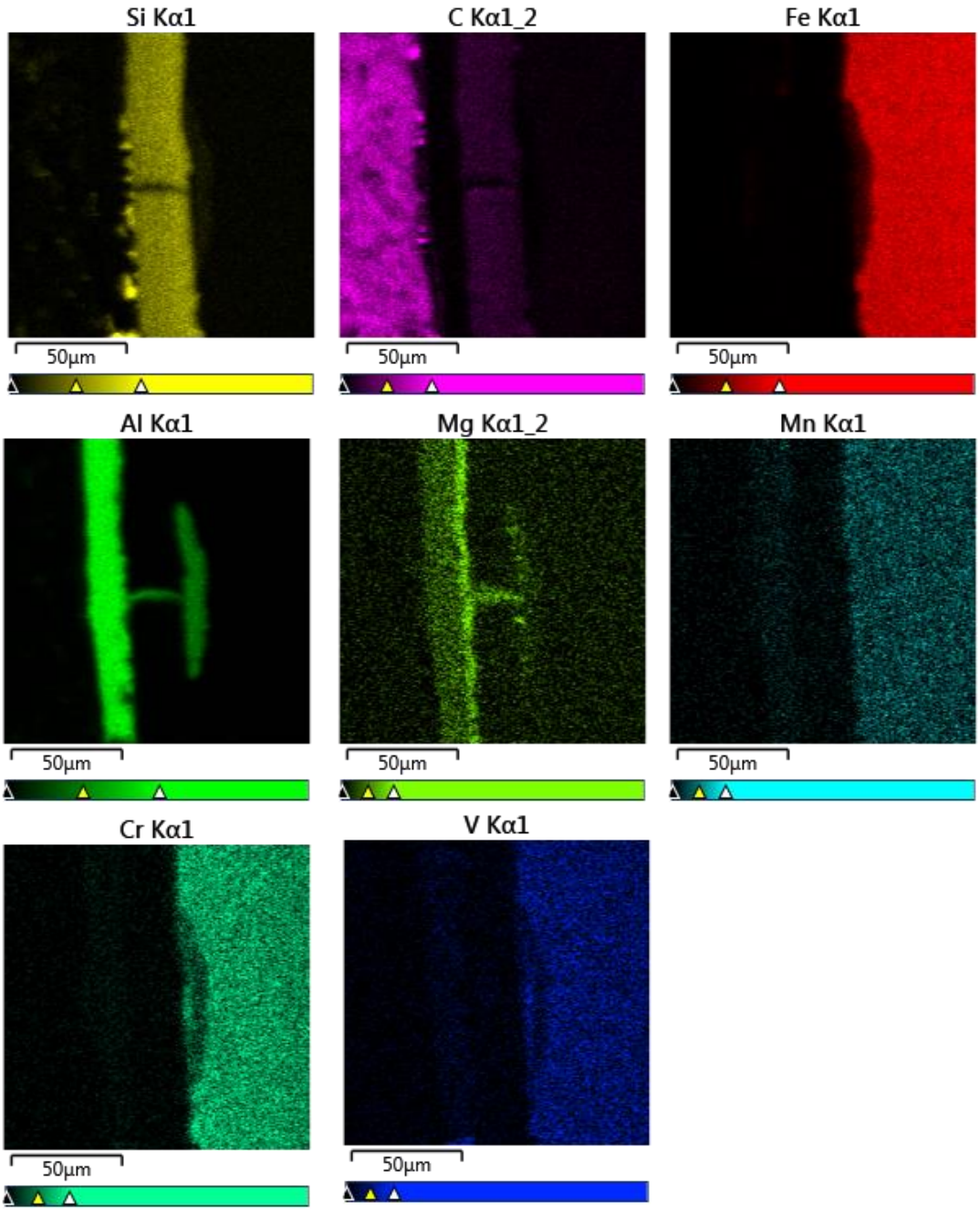

Figure 57. EDS maps corresponding to Figure 56.

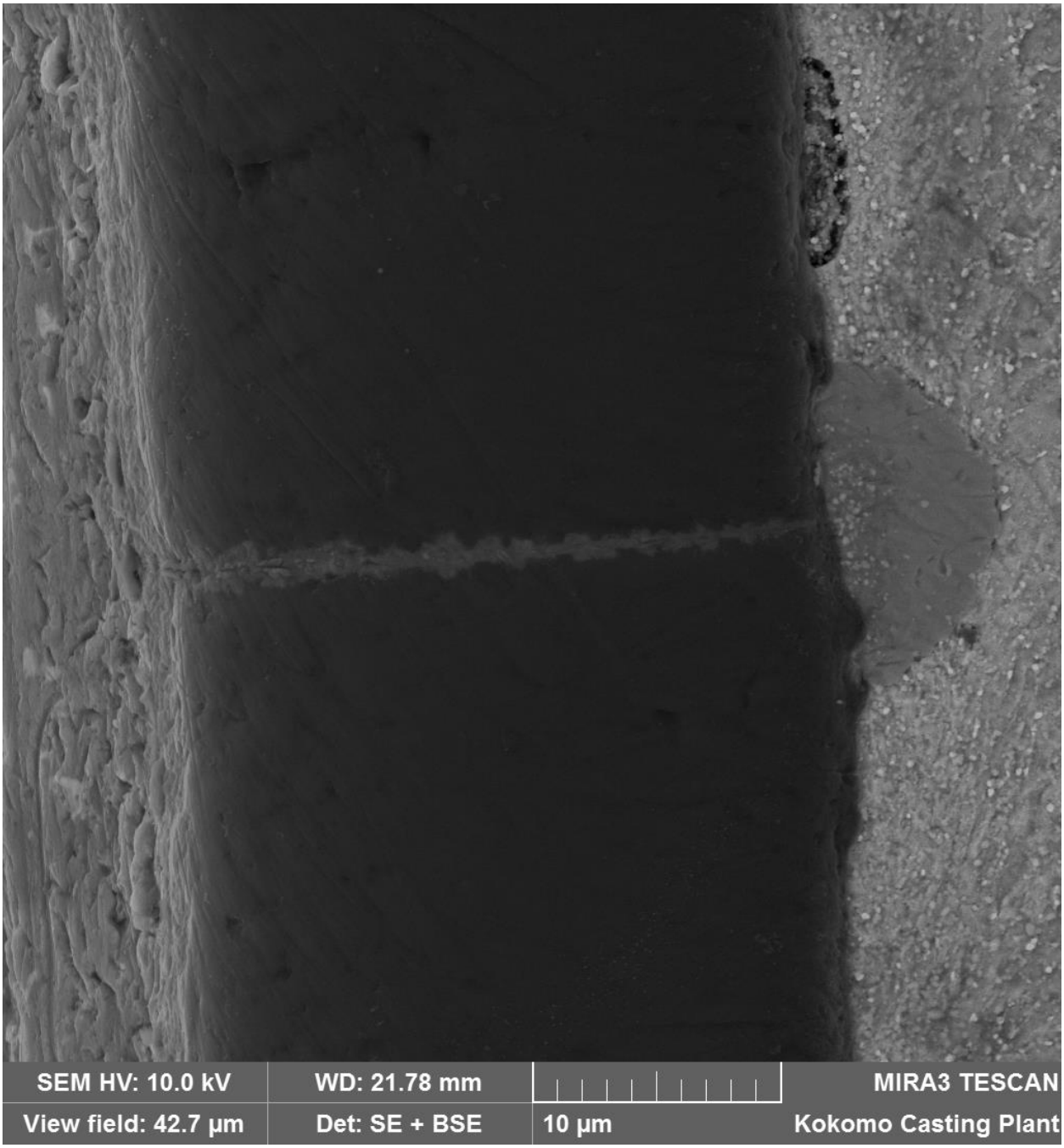

Figure 58. 6480x SEM image of the H13 Si-DLC specimen dunked for 1440 minutes at 1250°F.

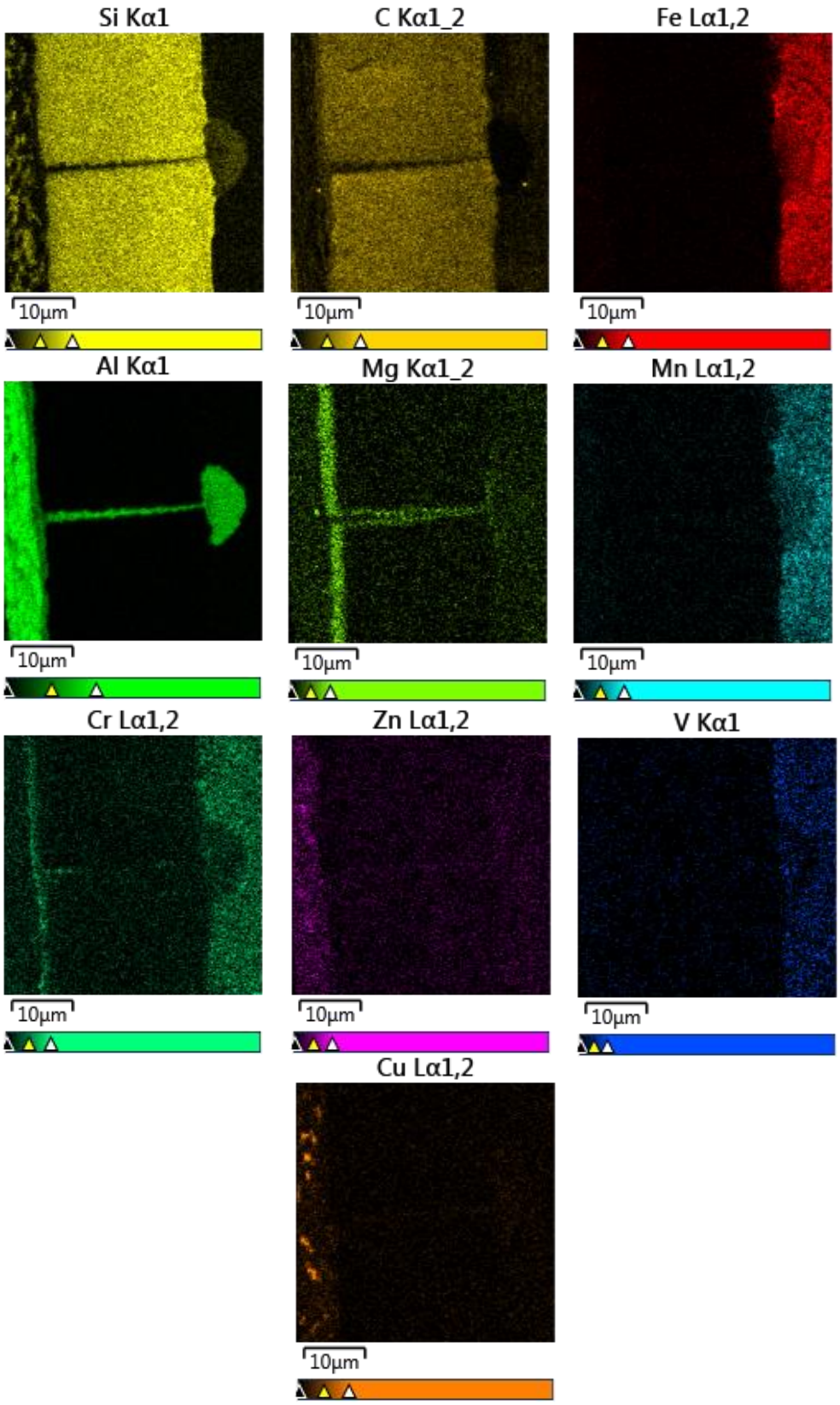

Figure 59. EDS maps corresponding to Figure 58.

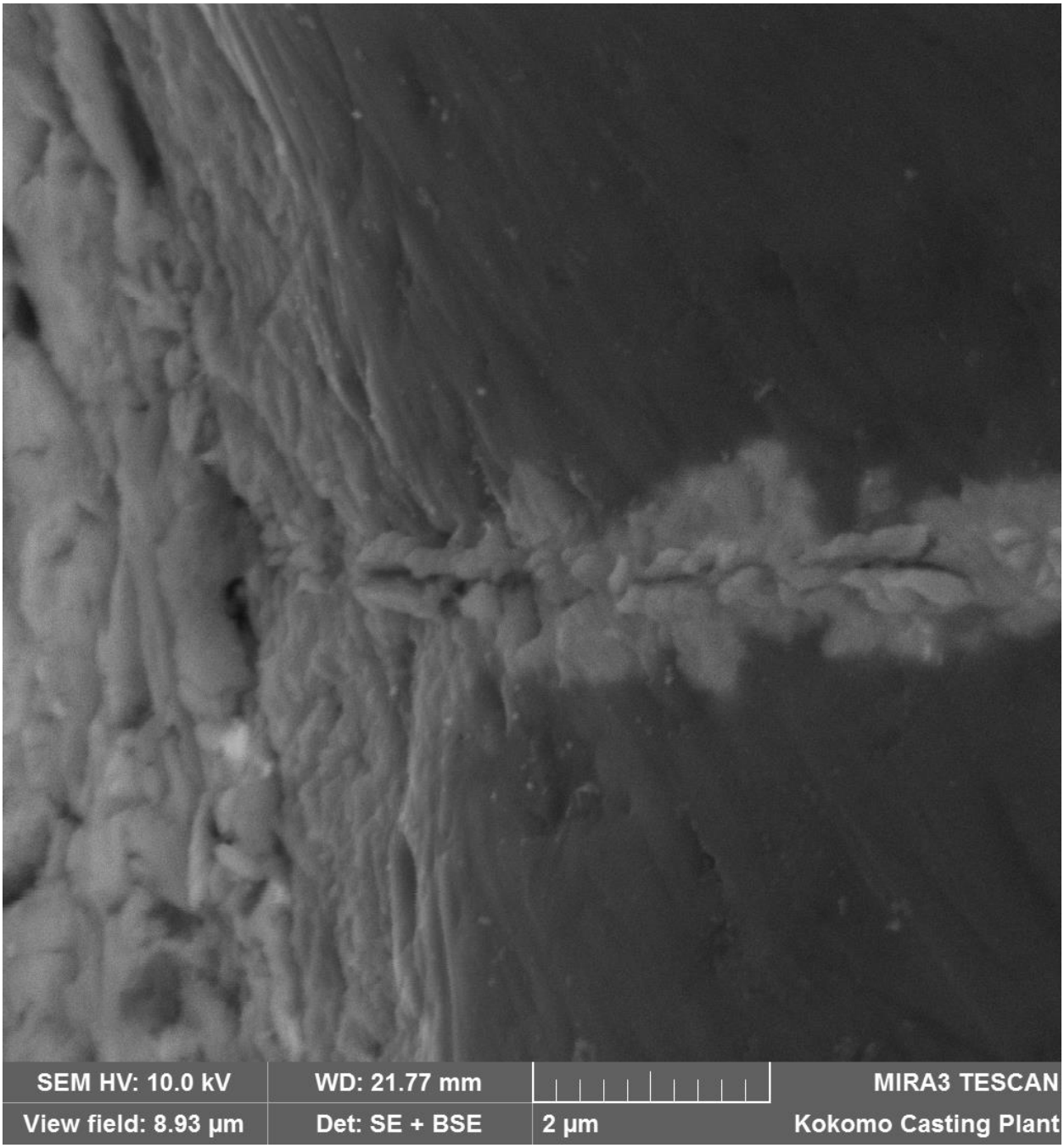

Figure 60. 31000x SEM image of the H13 Si-DLC specimen dunked for 1440 minutes at 1250°F.

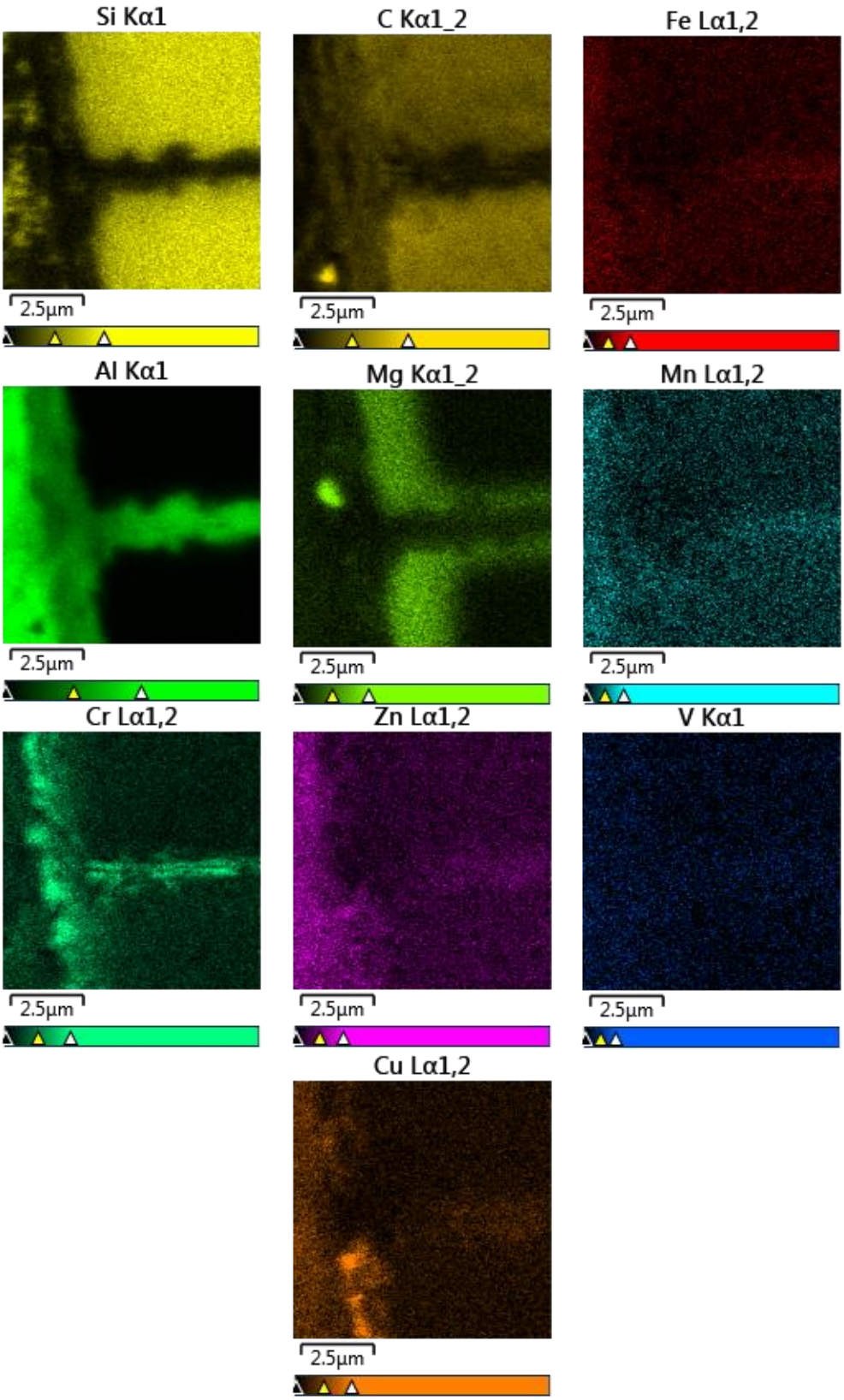

Figure 61. EDS maps corresponding to Figure 60.

4.2.4 H13 with TRD Vanadium Carbide (H13 VC)

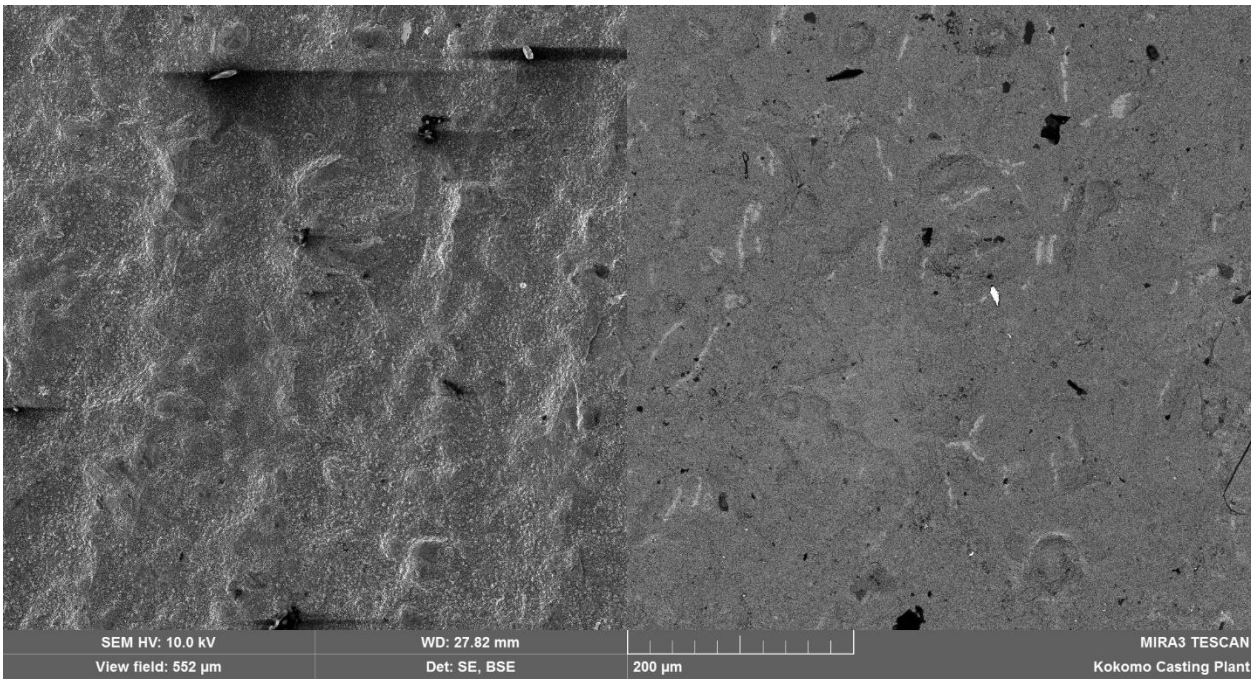

Figure 62. 500x SEM images of the VC coating.

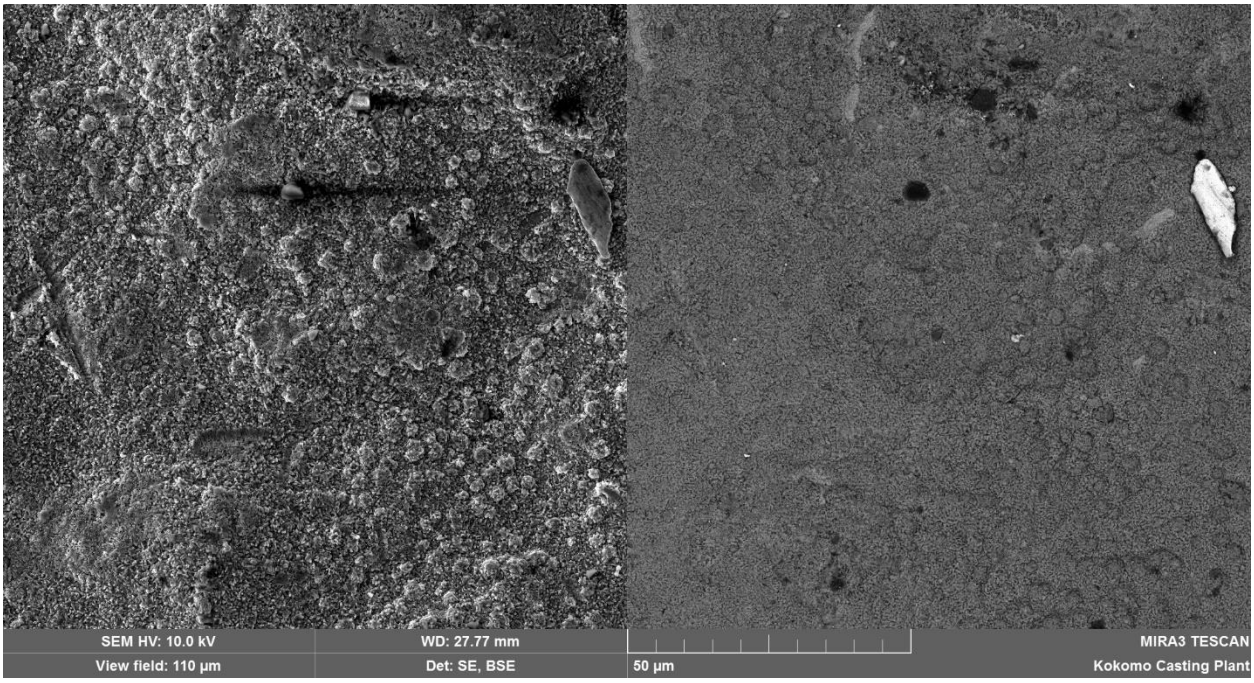

Figure 63. 2500x SEM images of the VC coating.

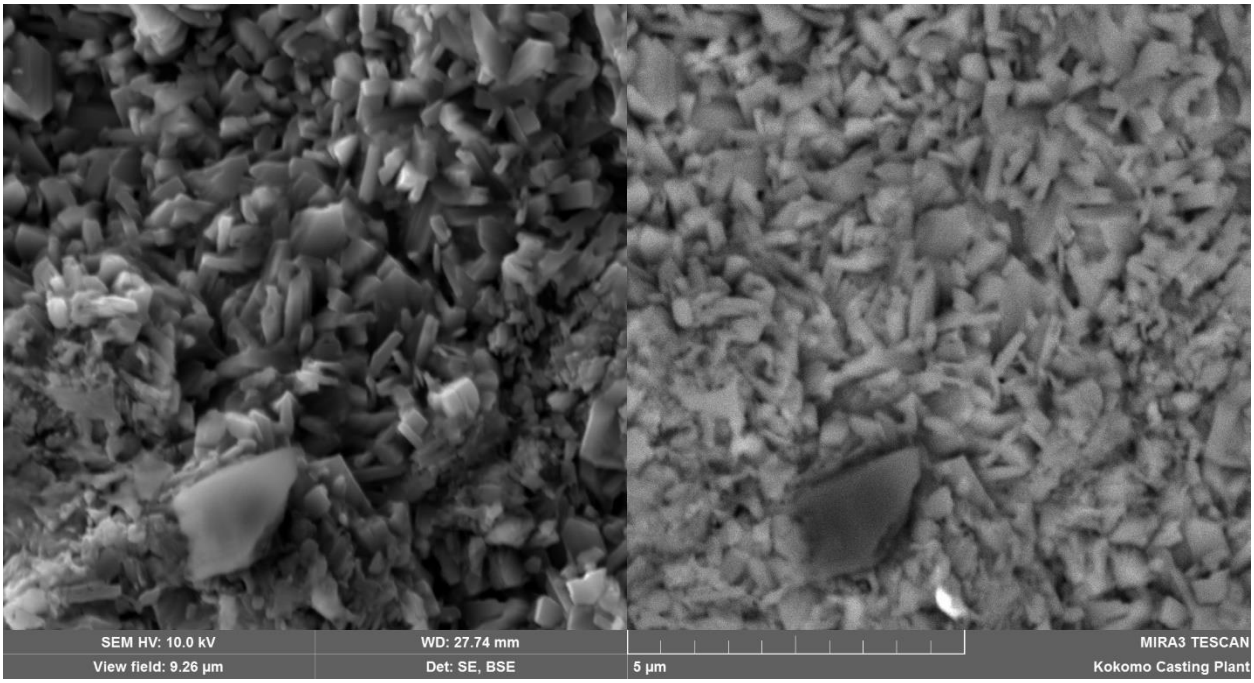

Figure 64. 30000x SEM images of the VC coating.

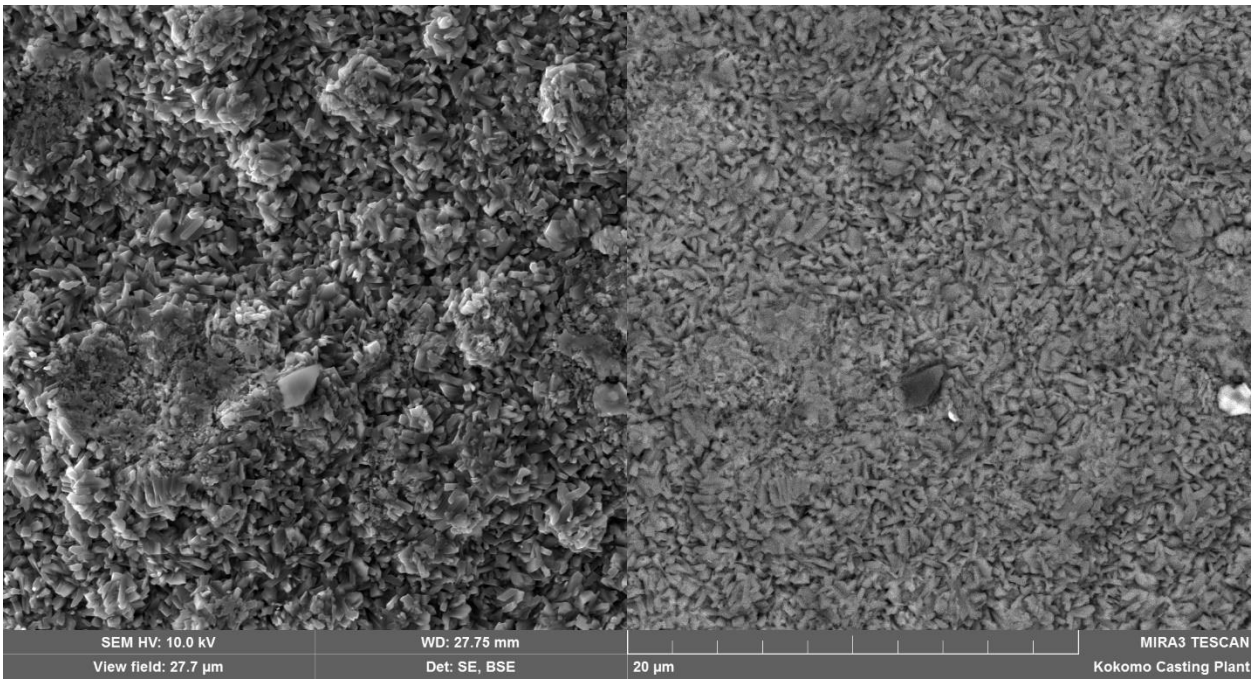

Figure 65. 10000x SEM images of the VC coating.

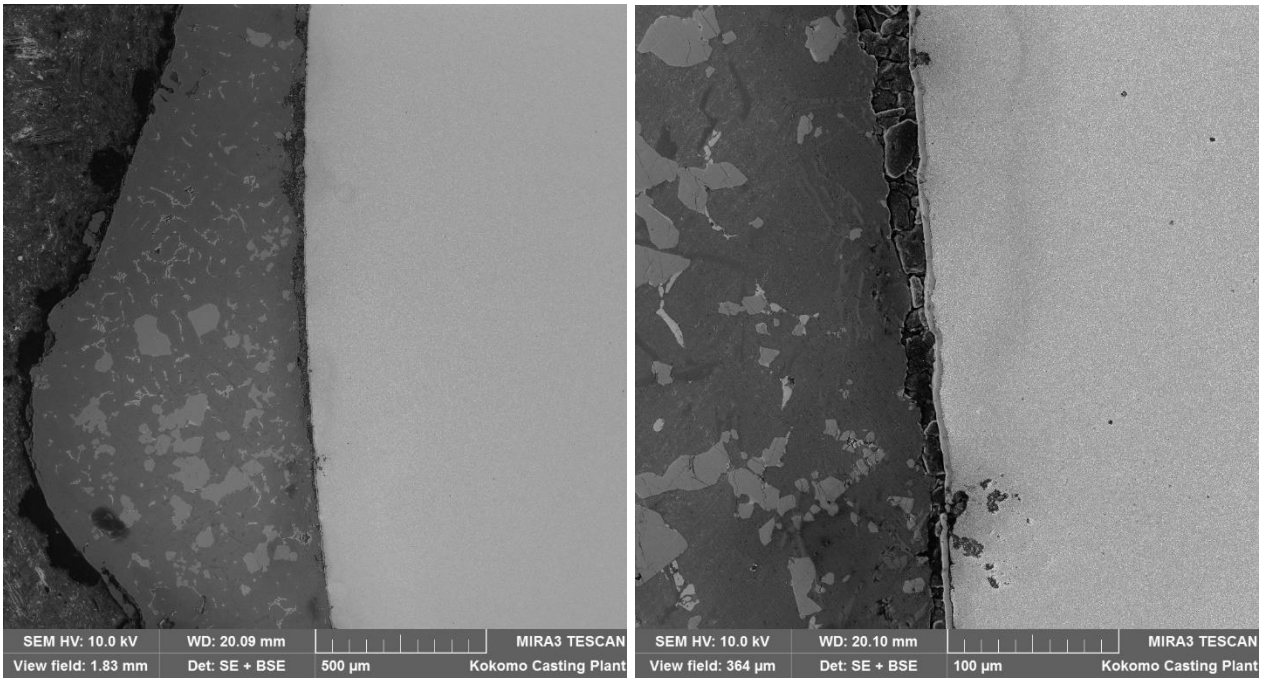

Figure 66. 150x and 7505x SEM images of the H13 VC specimen dunked for 30 minutes at 1150°F.

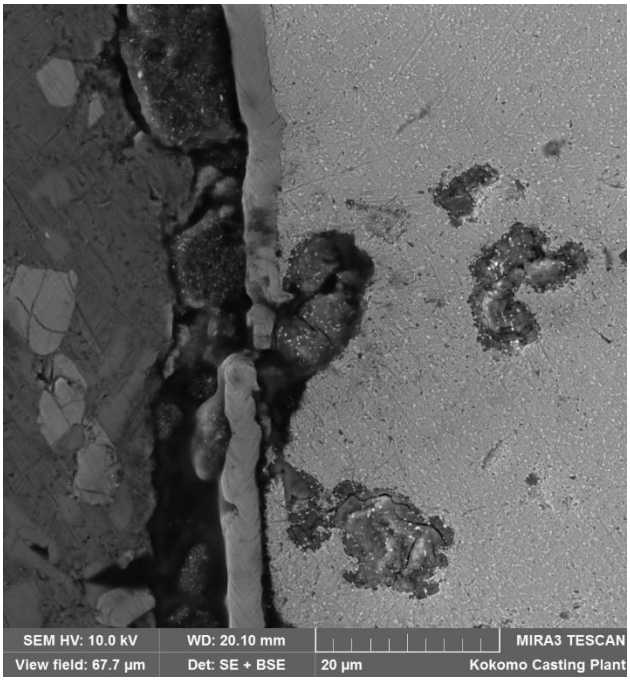

Figure 67. 4000x SEM image of the H13 VC specimen dunked for 30 minutes at 1150°F.

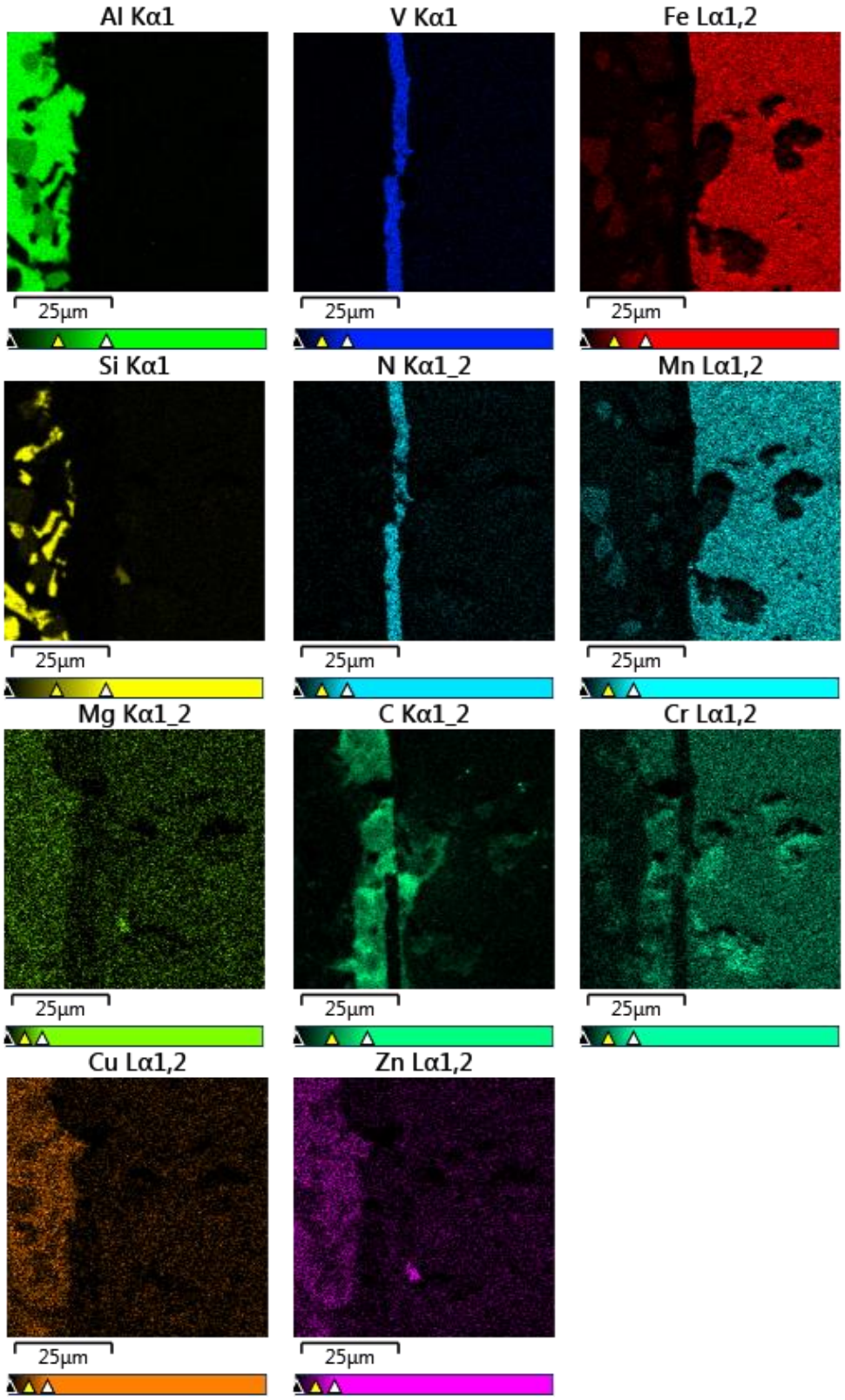

Figure 68. EDS maps corresponding to Figure 67.

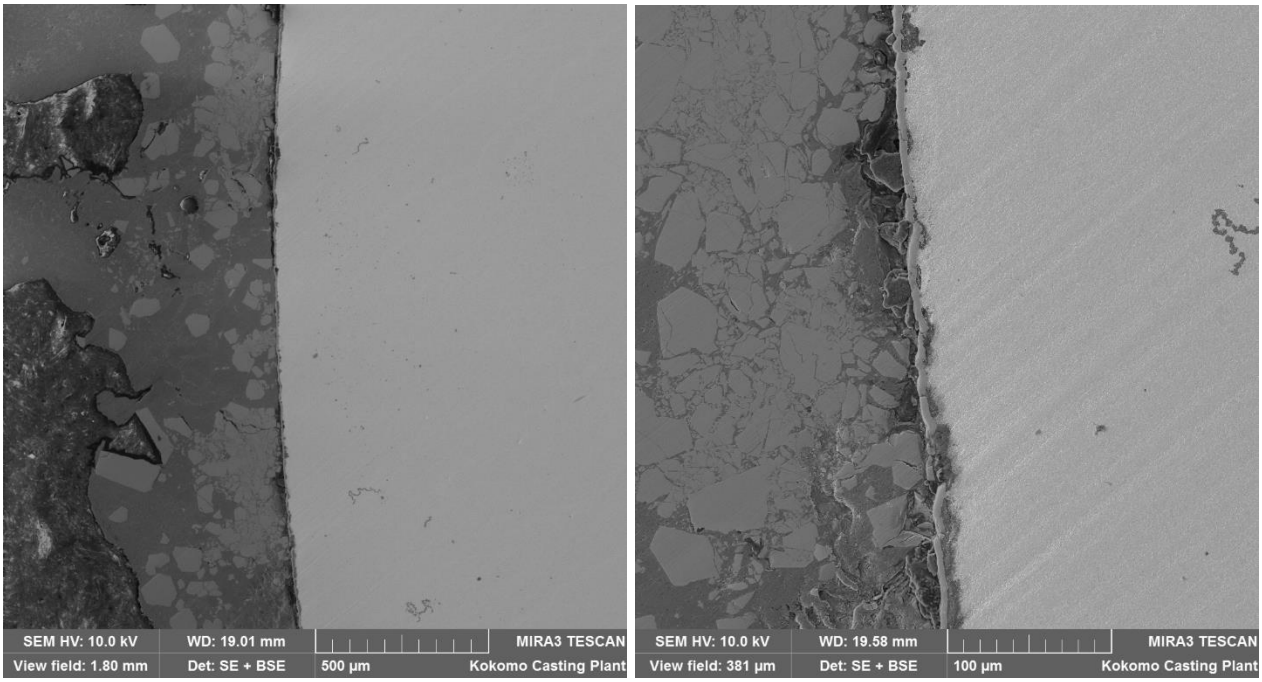

Figure 69. 150x and 725x SEM images of the H13 VC specimen dunked for 120 minutes at 1150°F.

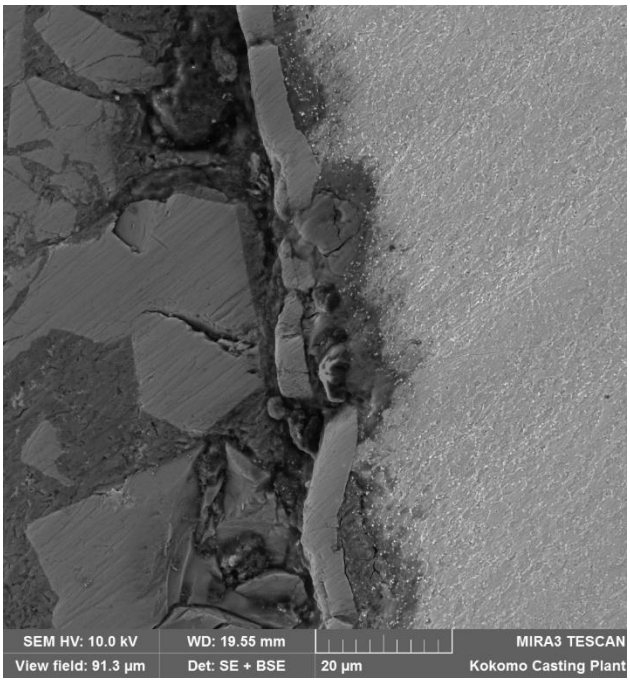

Figure 70. 3000x SEM image of the H13 VC specimen dunked for 120 minutes at 1150°F.

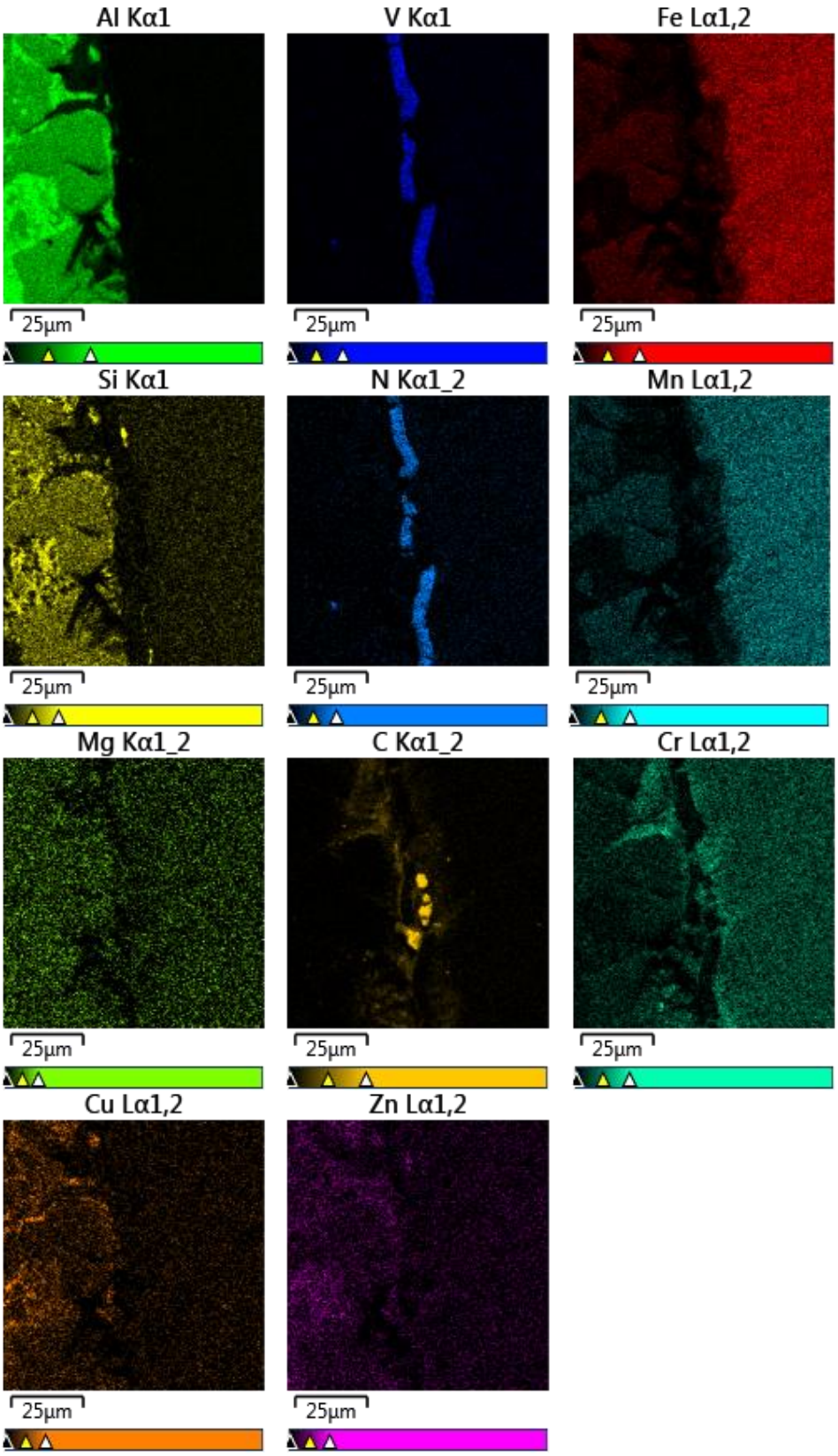

Figure 71. EDS maps corresponding to Figure 70.

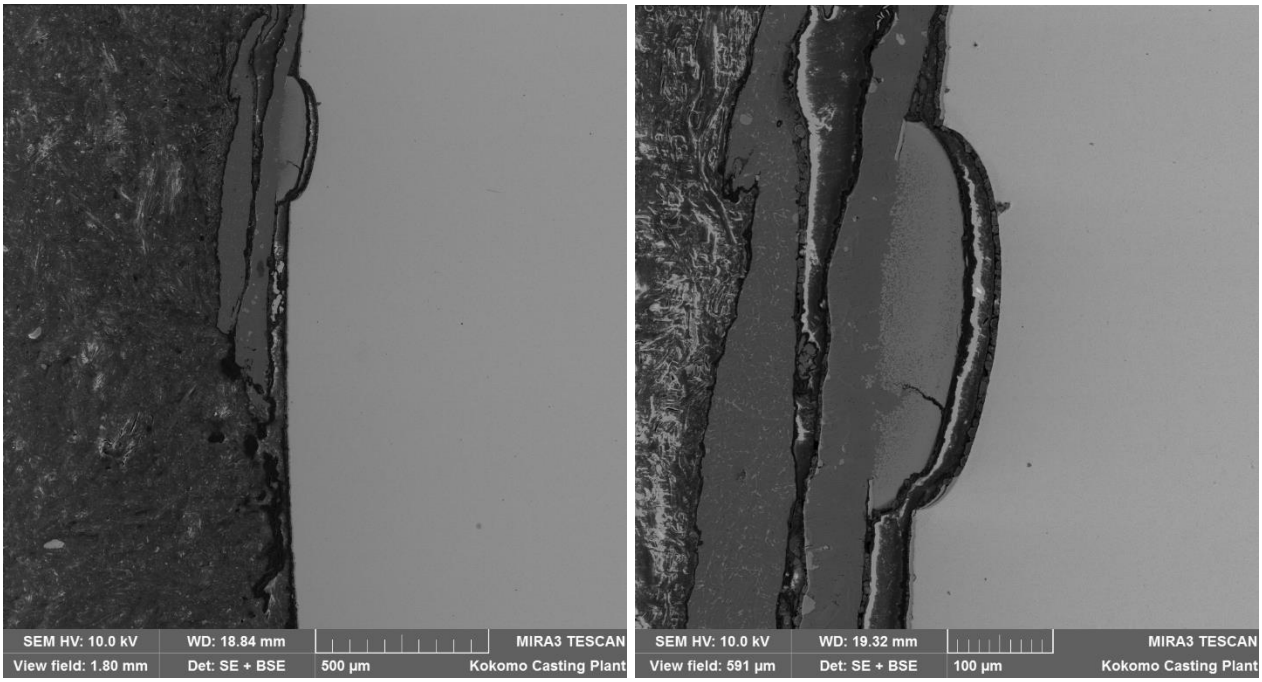

Figure 72. 150x and 470x SEM images of the H13 VC specimen dunked for 1440 minutes at 1150°F.

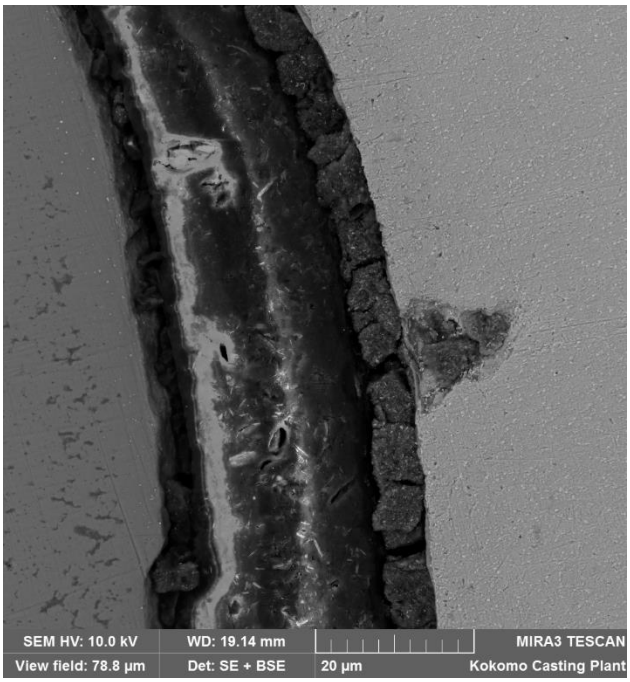

Figure 73. 3500x SEM image of the H13 VC specimen dunked for 1440 minutes at 1150°F.

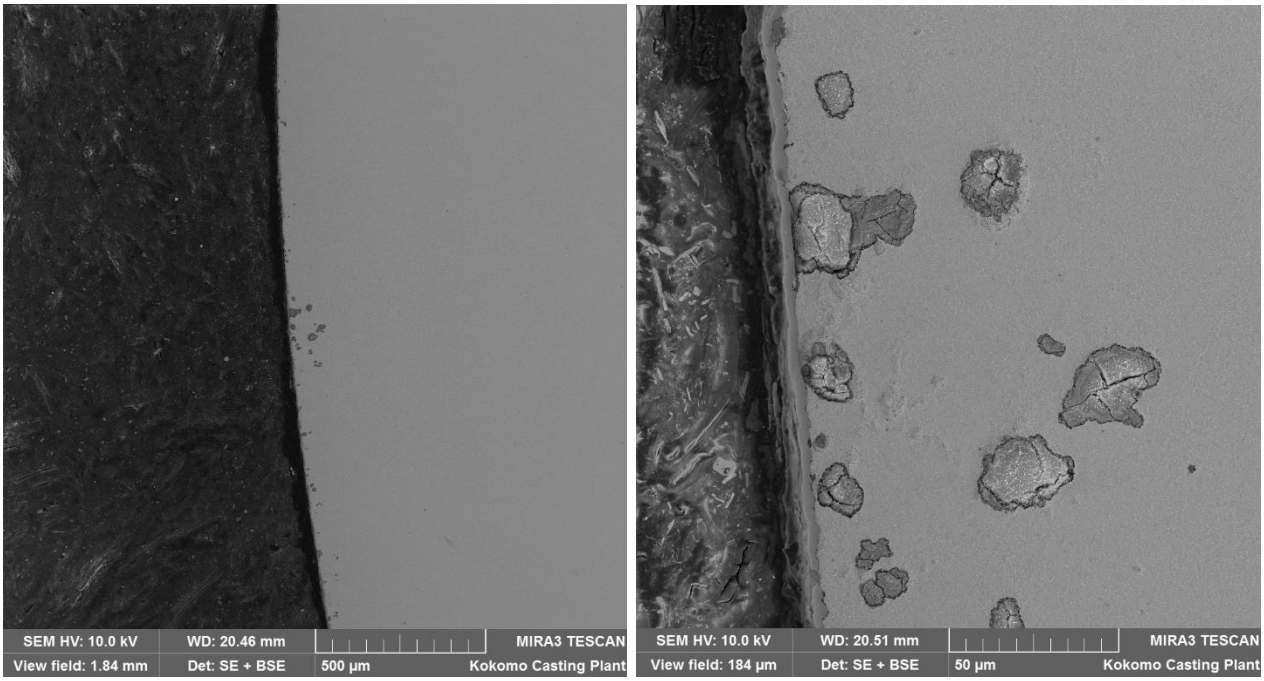

Figure 74. 150x and 1500x SEM images of the H13 VC specimen dunked for 30 minutes at 1250°F.

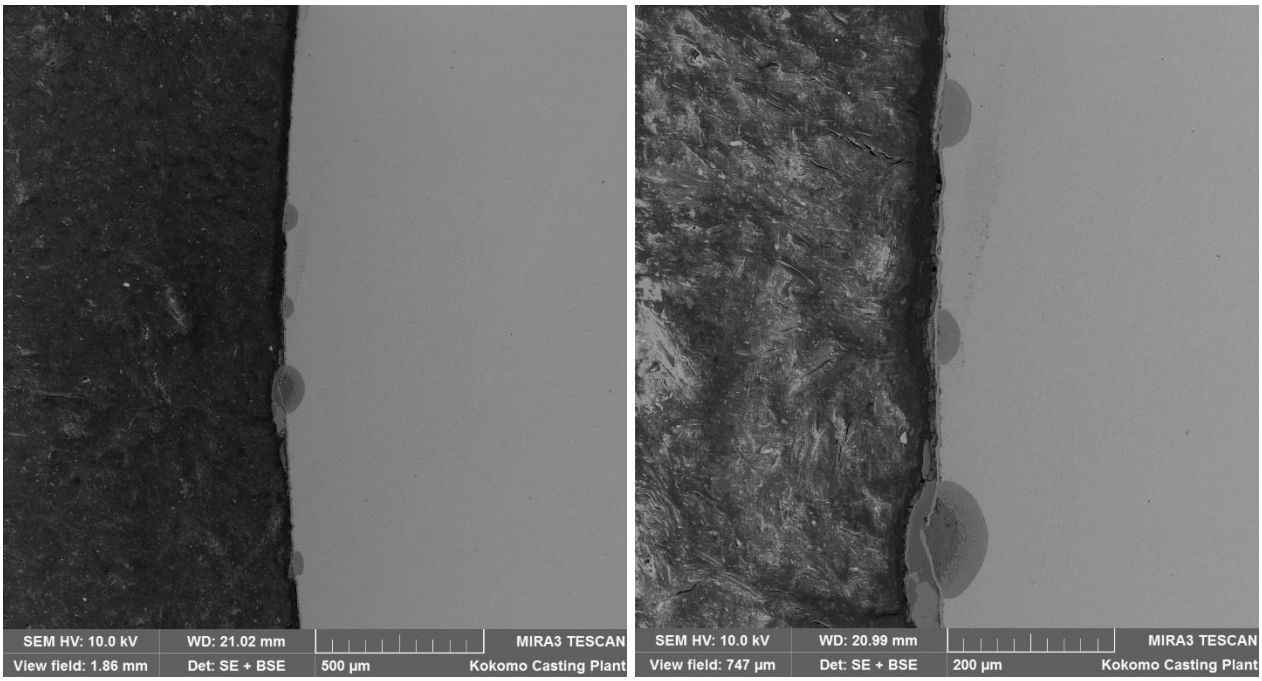

Figure 75. 150x and 370x SEM images of the H13 VC specimen dunked for 120 minutes at 1250°F.

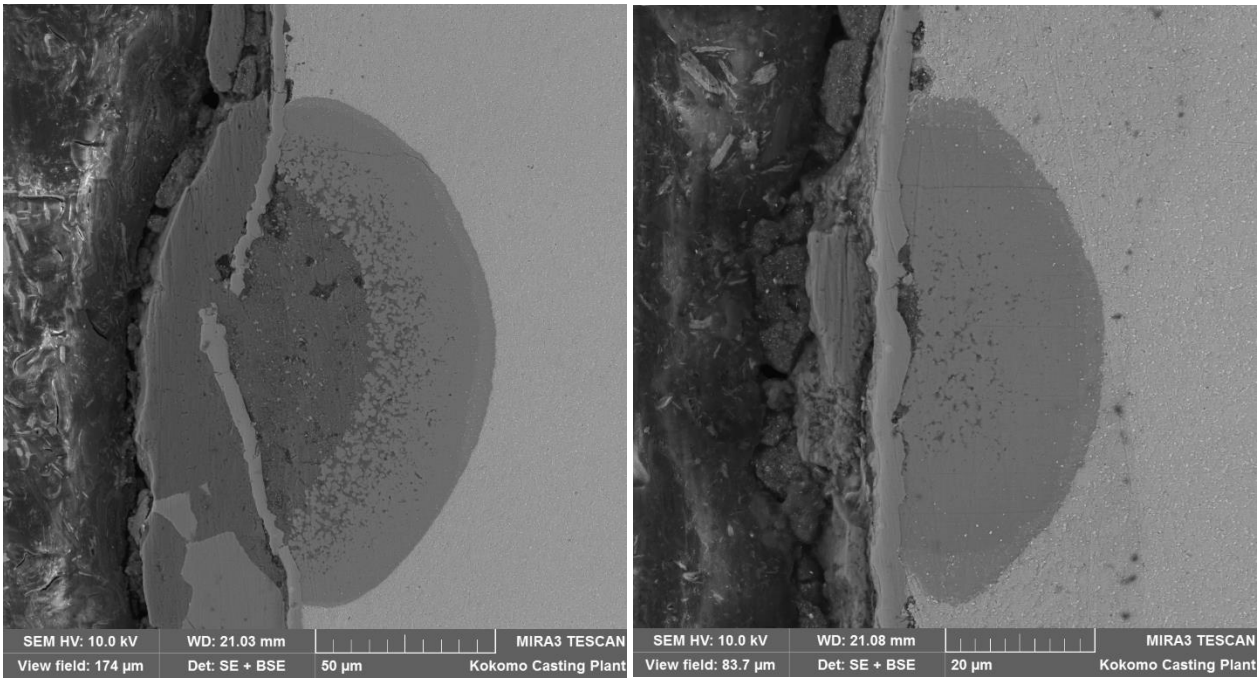

Figure 76. 1600x and 3300x SEM images of the H13 VC specimen dunked for 120 minutes at 1250°F.

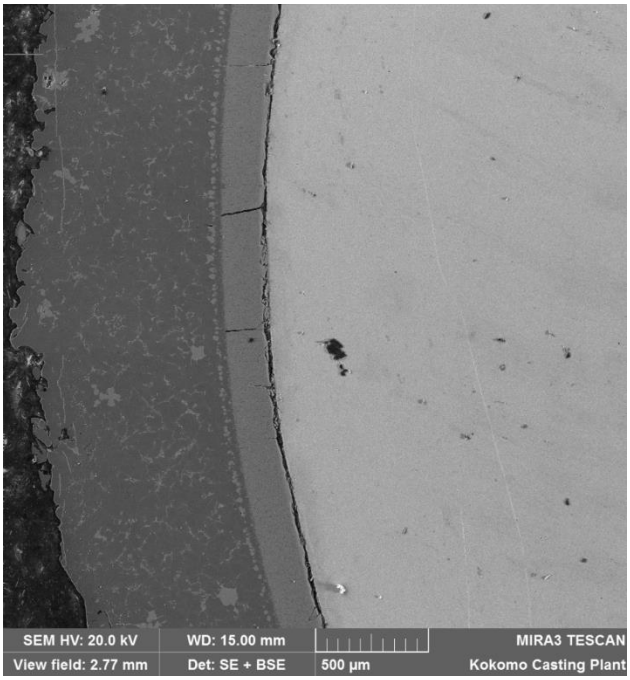

Figure 77. 100x SEM image of the H13 VC specimen dunked for 1440 minutes at 1250°F.

Figure 78. EDS maps corresponding to Figure 77.

Figure 78 continued.

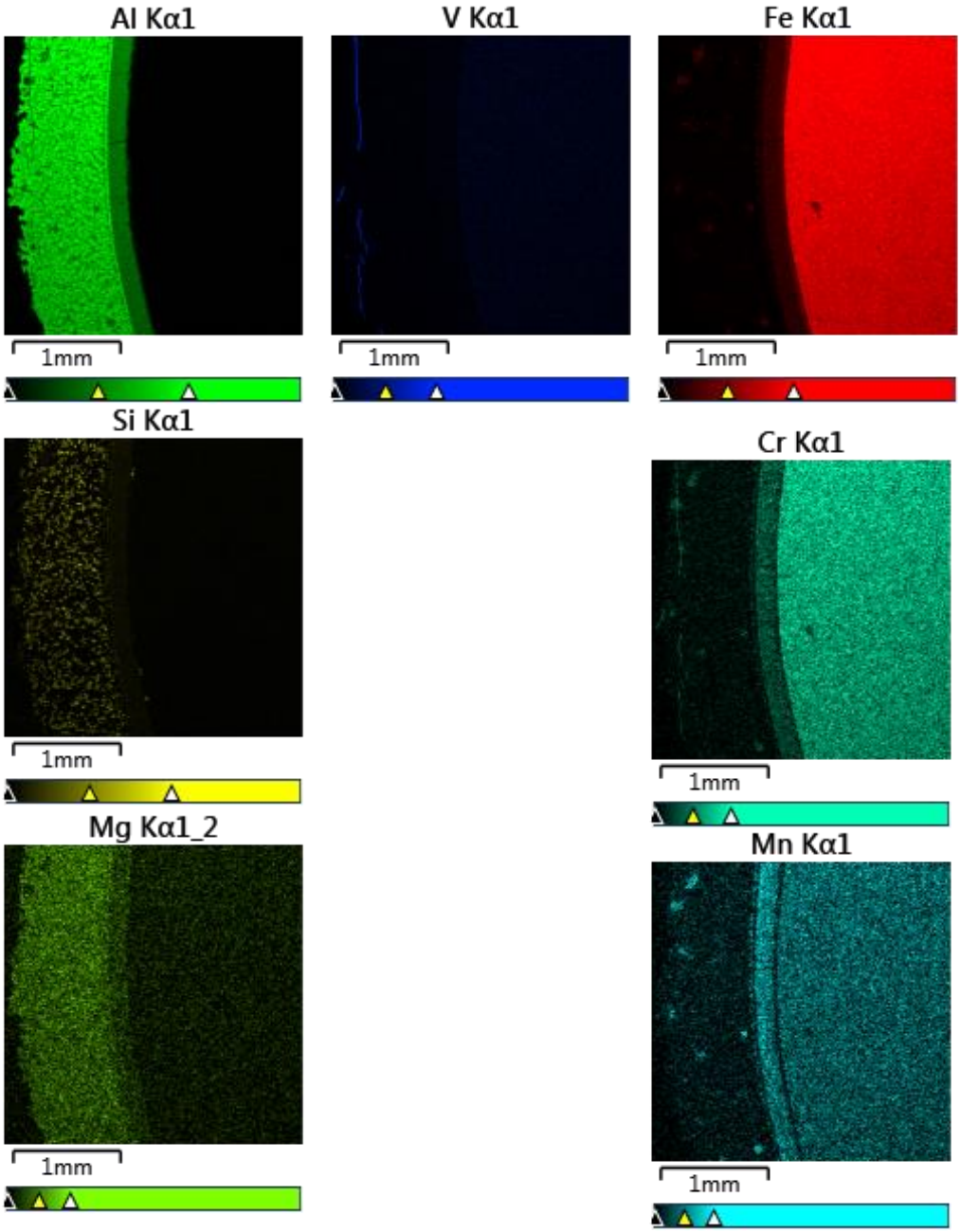

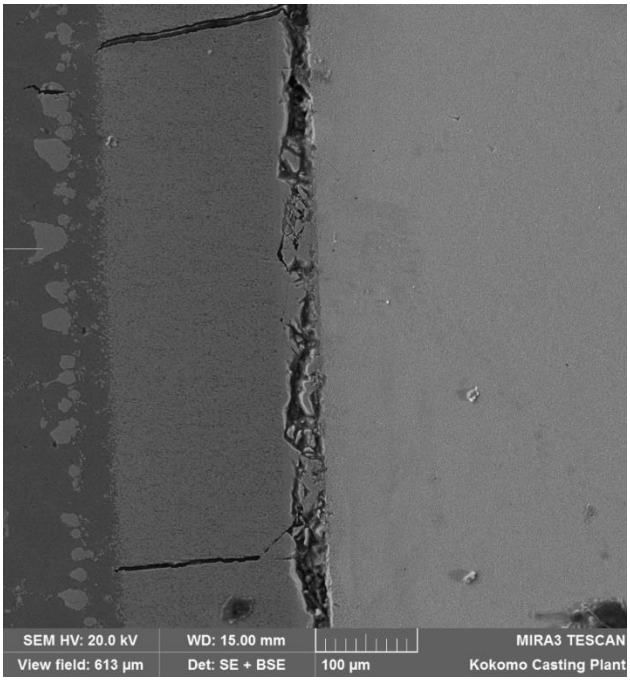

Figure 79. 450x SEM image of the H13 VC specimen dunked for 1440 minutes at 1250°F.

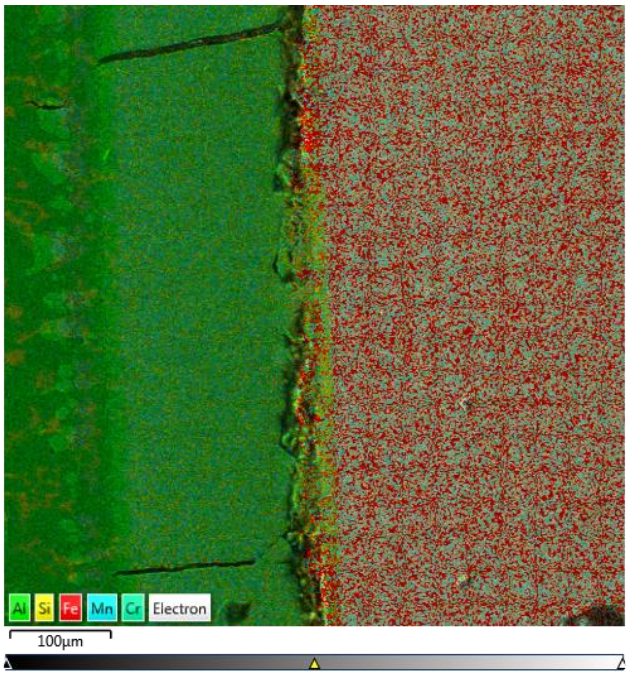

Figure 80. EDS maps corresponding to Figure 79.

Figure 80 continued.

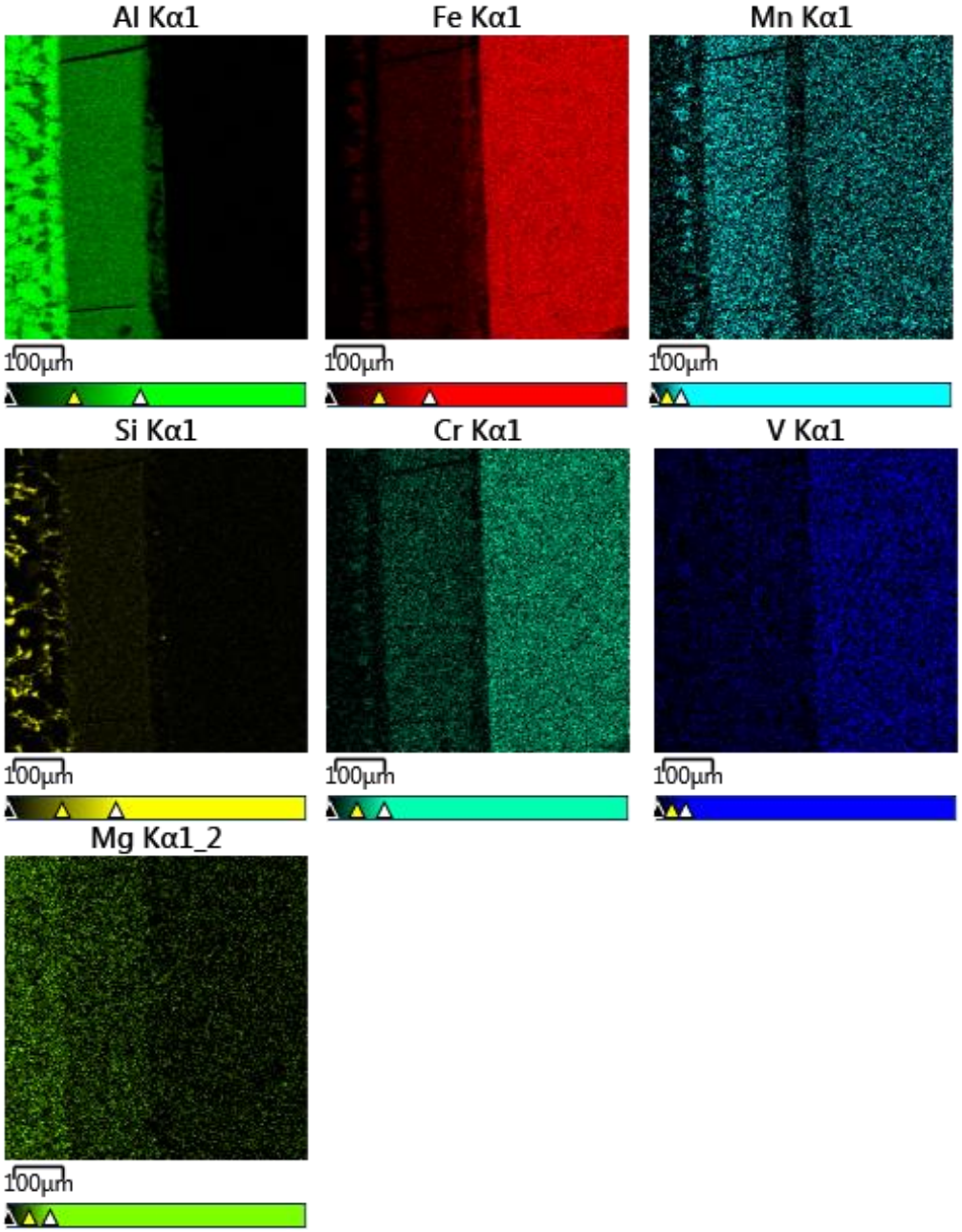

4.2.5 H13 with PVD Vanadium Carbonitride (H13 VCN)

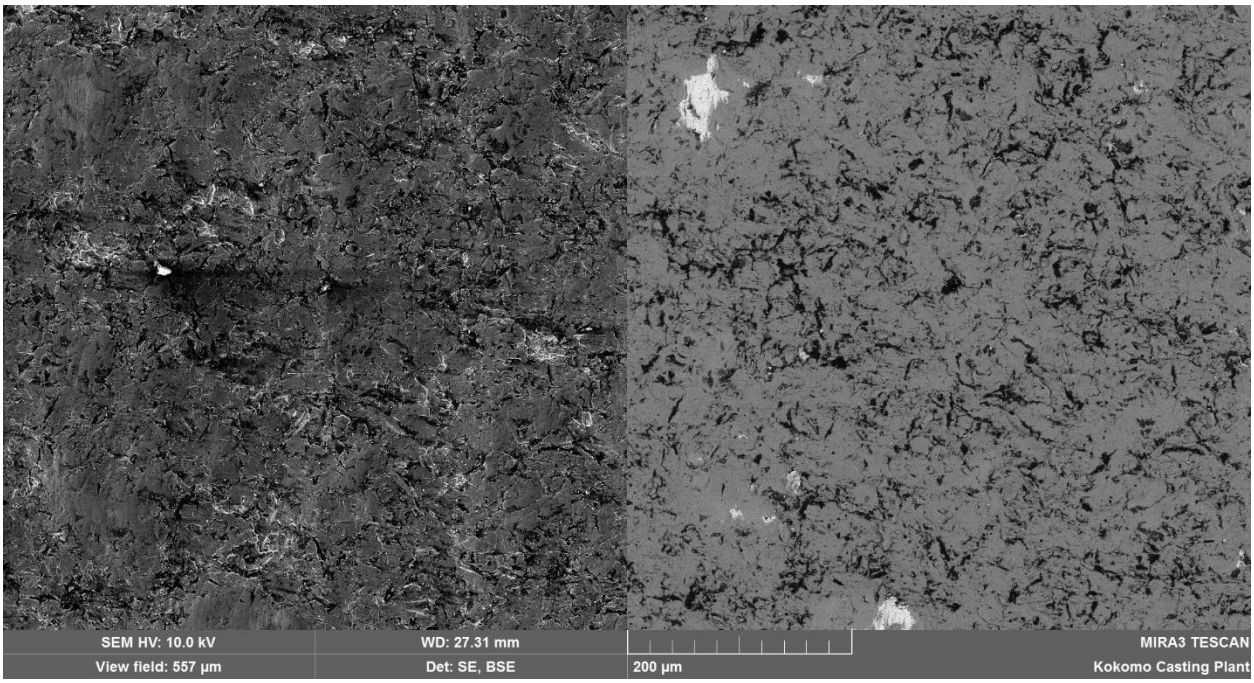

Figure 81. 500x SEM images of the VCN coating.

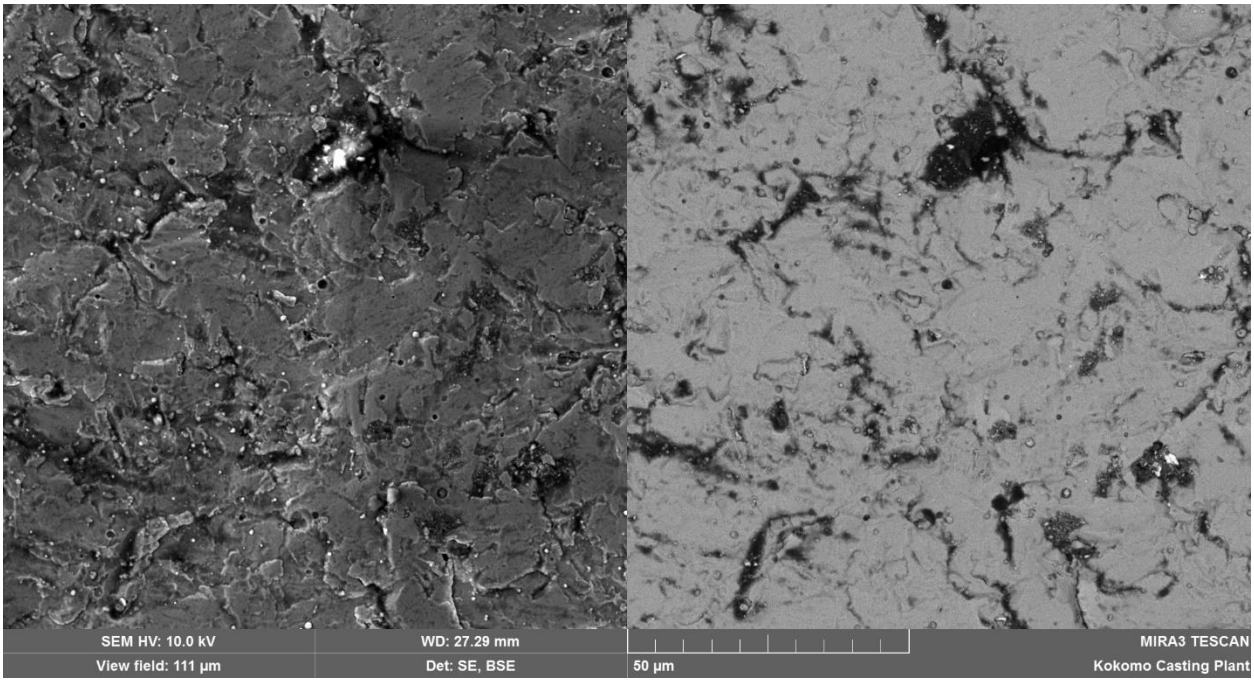

Figure 82. 2500x SEM images of the VCN coating.

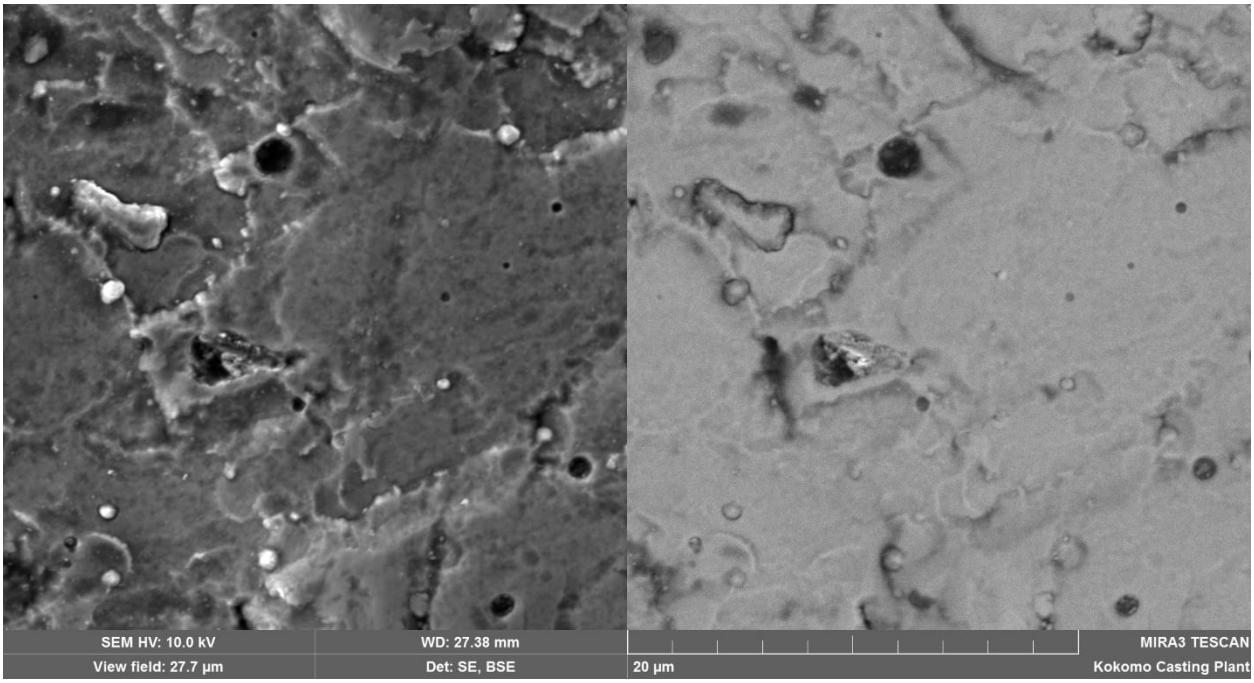

Figure 83. 10000x SEM images of the VCN coating.

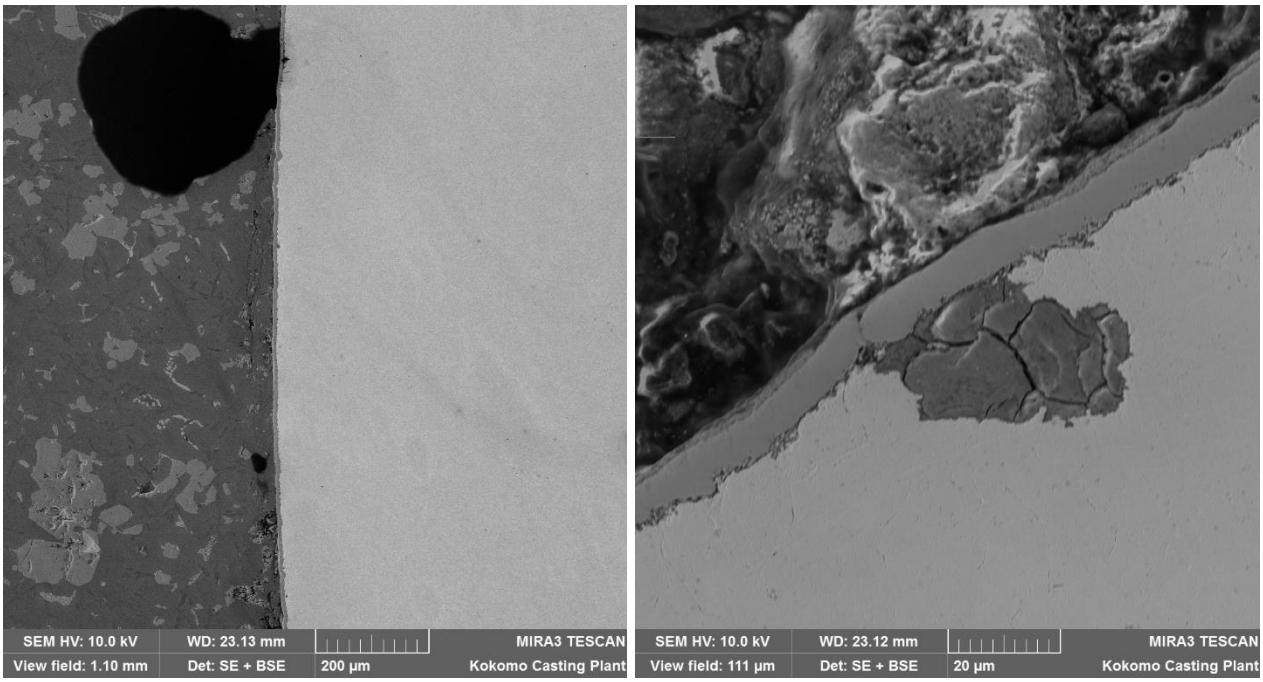

Figure 84. 250x and 2500x SEM images of the H13 VCN specimen dunked for 30 minutes at 1150°F.

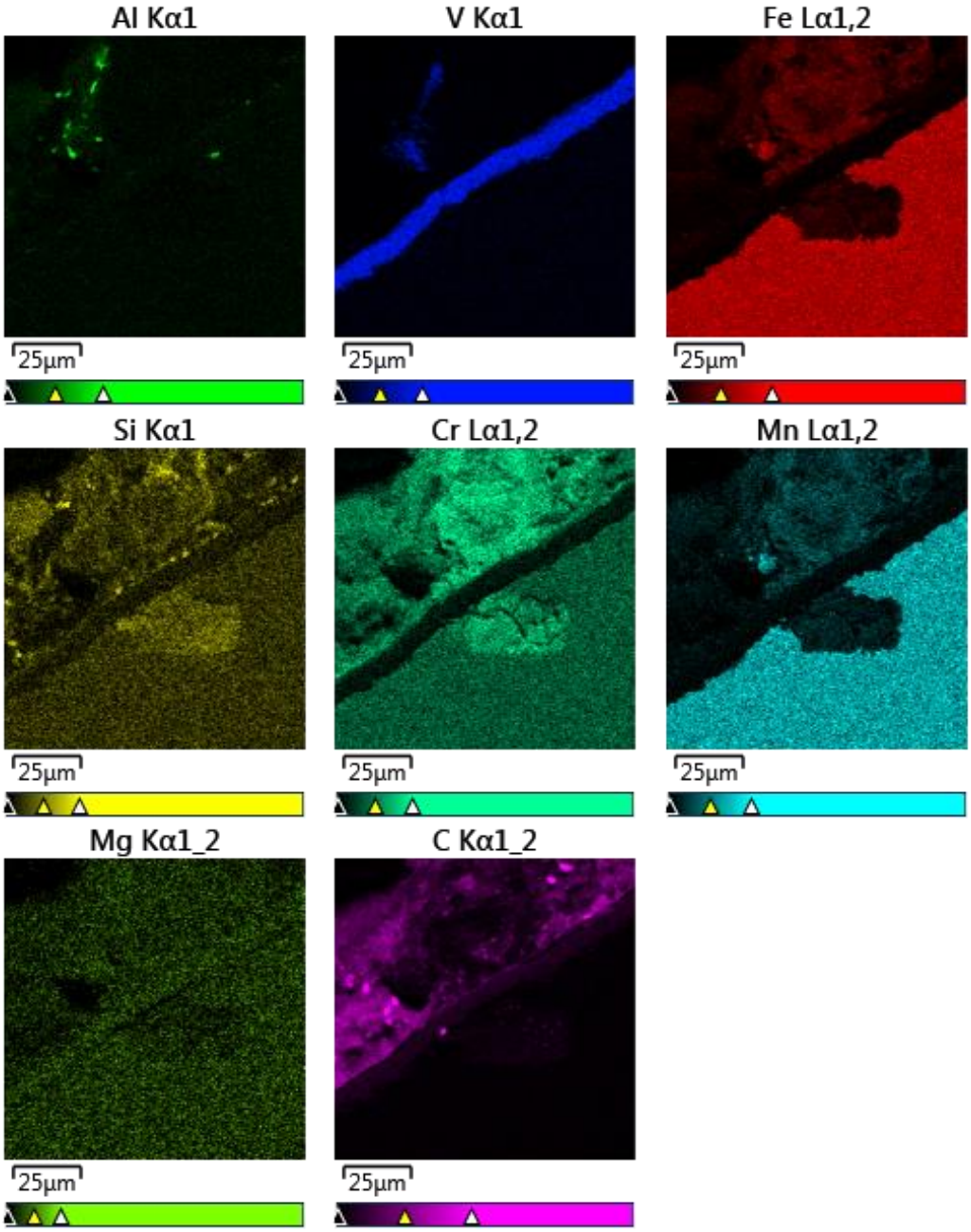

Figure 85. EDS maps corresponding to the 2500x image in Figure 84.

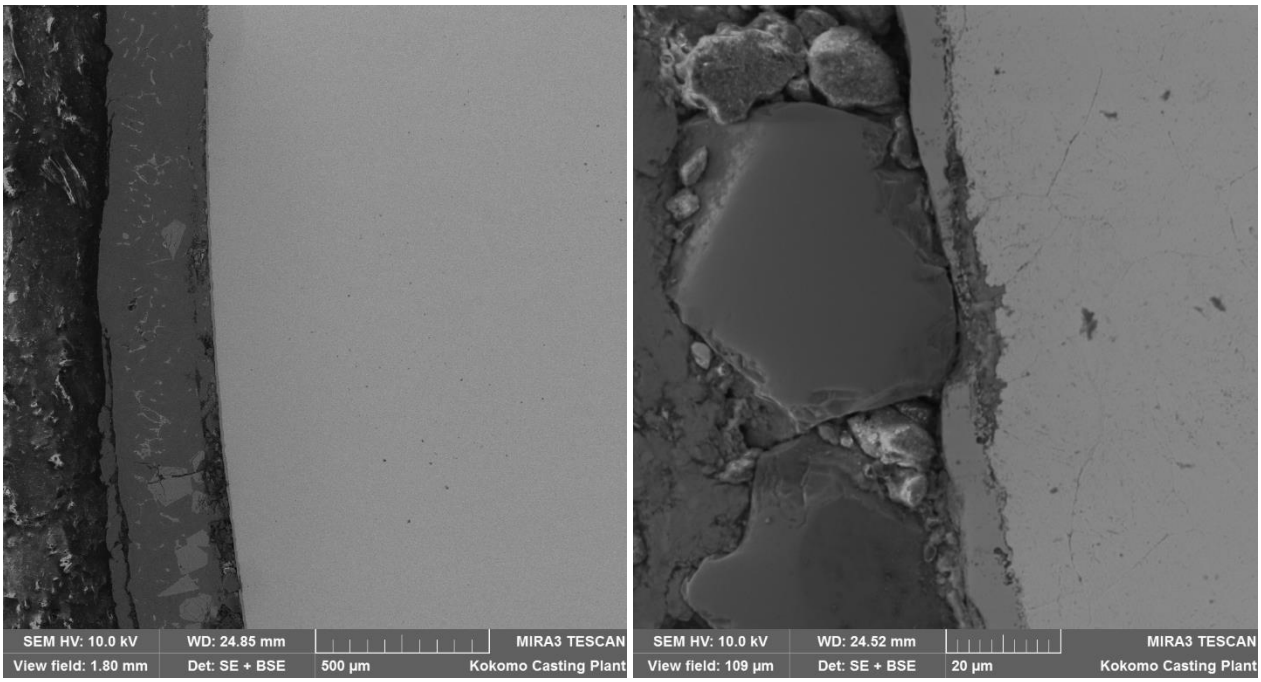

Figure 86. 150x and 2500x SEM image of the H13 VCN specimen dunked for 120 minutes at 1150°F.

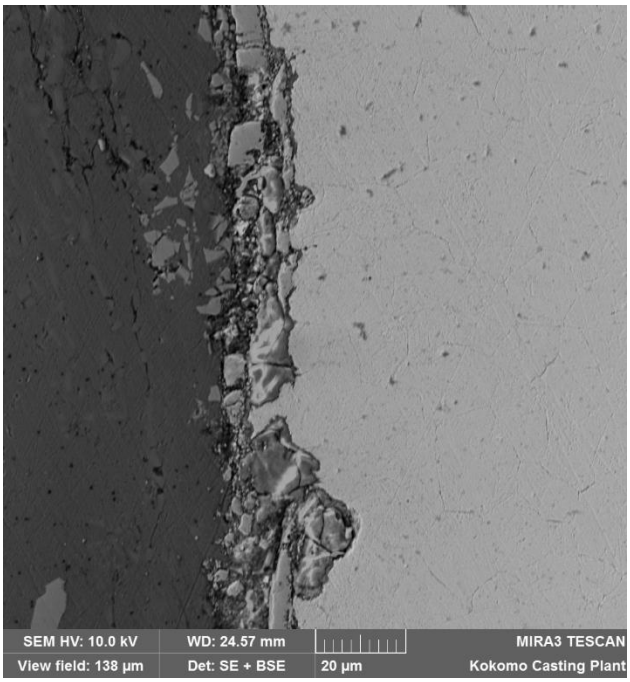

Figure 87. 2000x SEM image of the H13 VCN specimen dunked for 120 minutes at 1150°F.

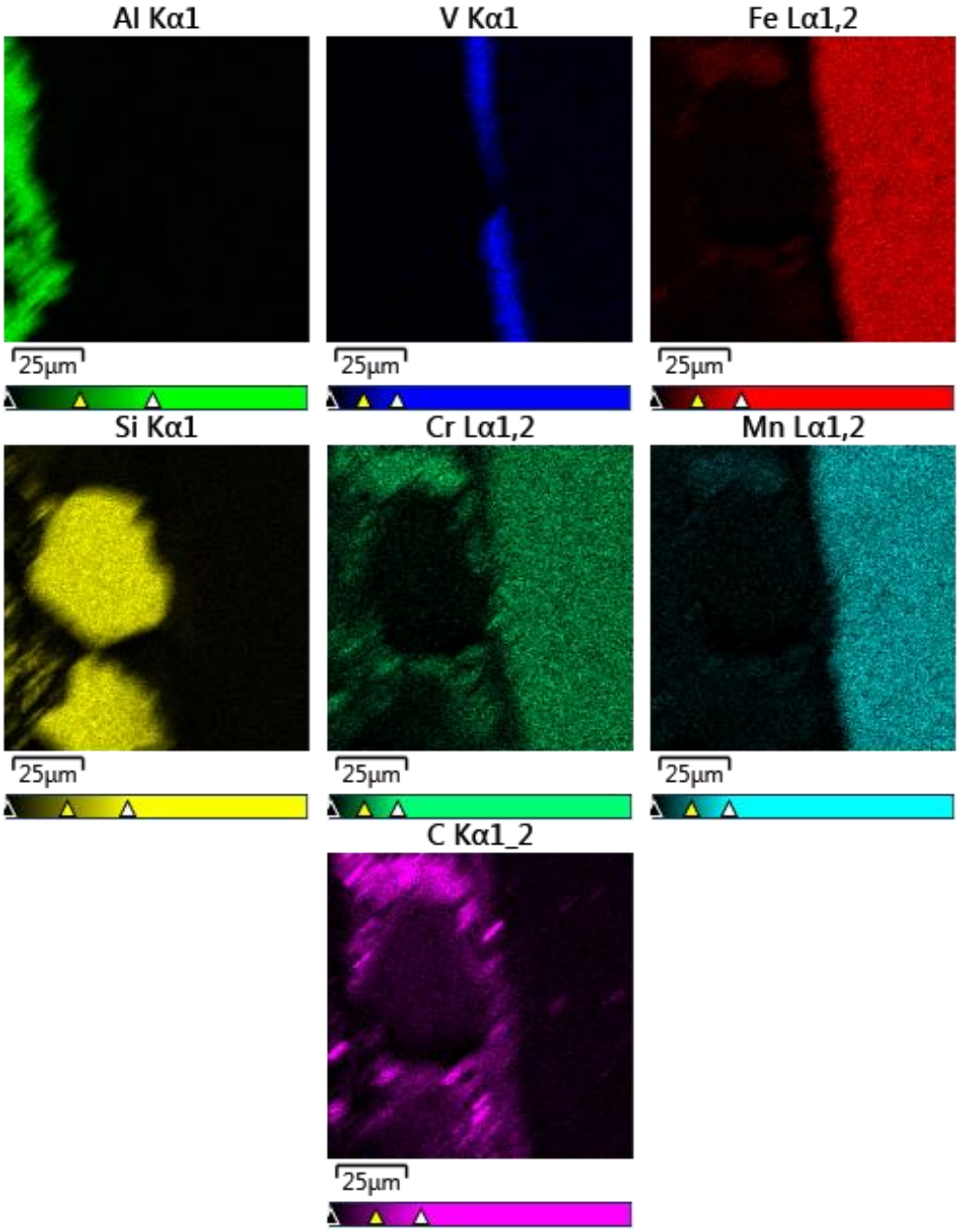

Figure 88. EDS maps corresponding to the 2500x image in Figure 86.

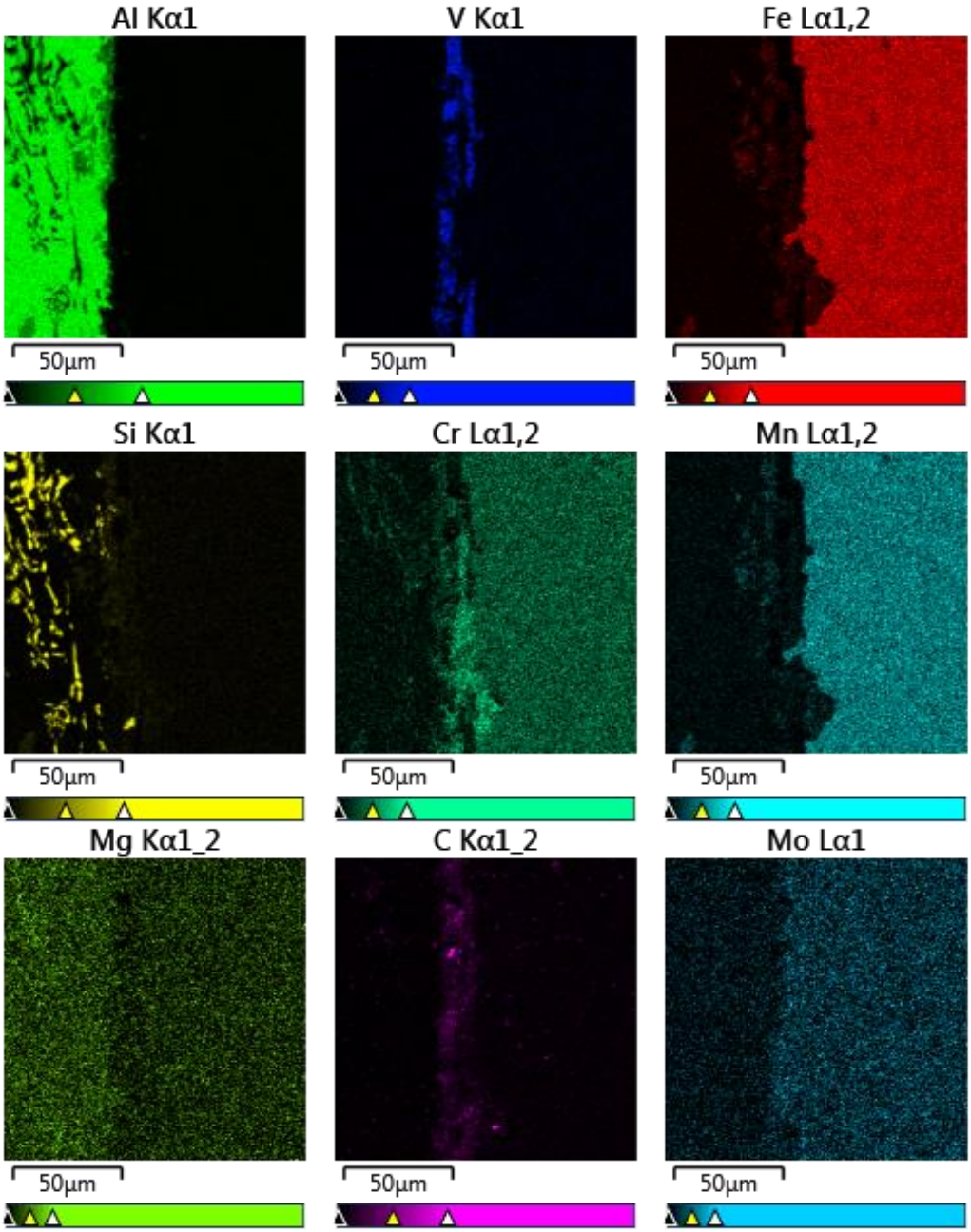

Figure 89. EDS maps corresponding to Figure 87.

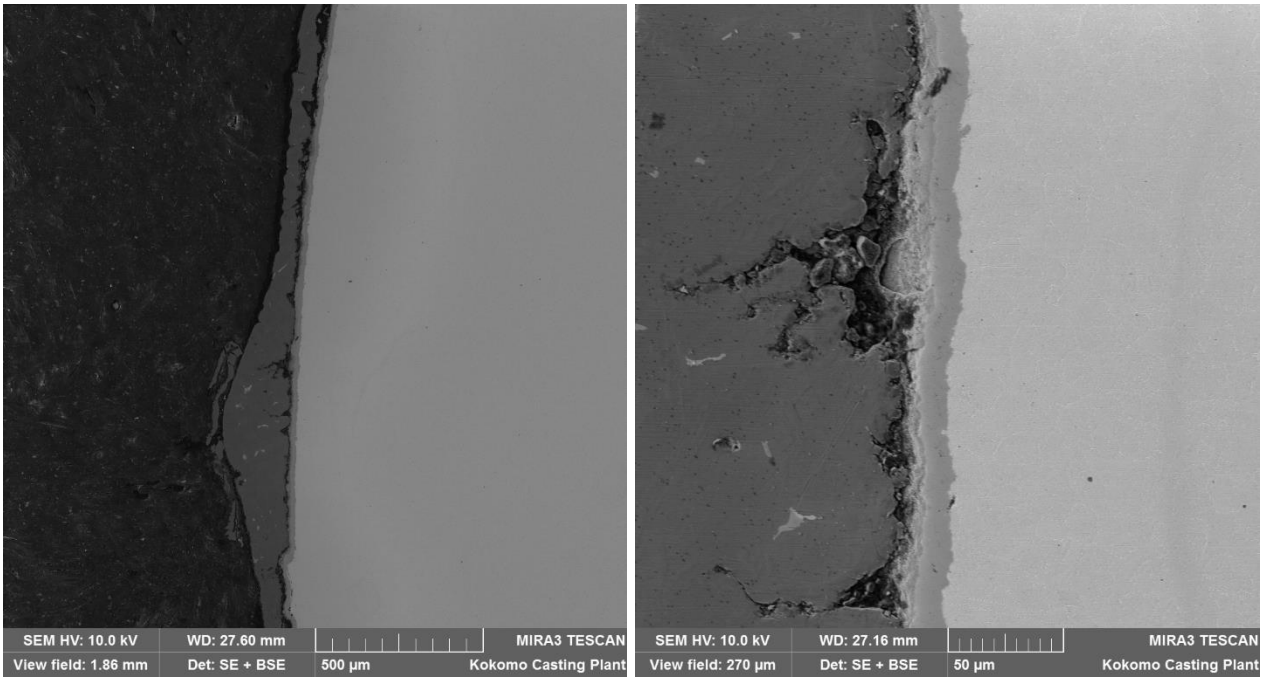

Figure 90. 150x and 1000x SEM images of the H13 VCN specimen dunked for 1440 minutes at 1150°F.

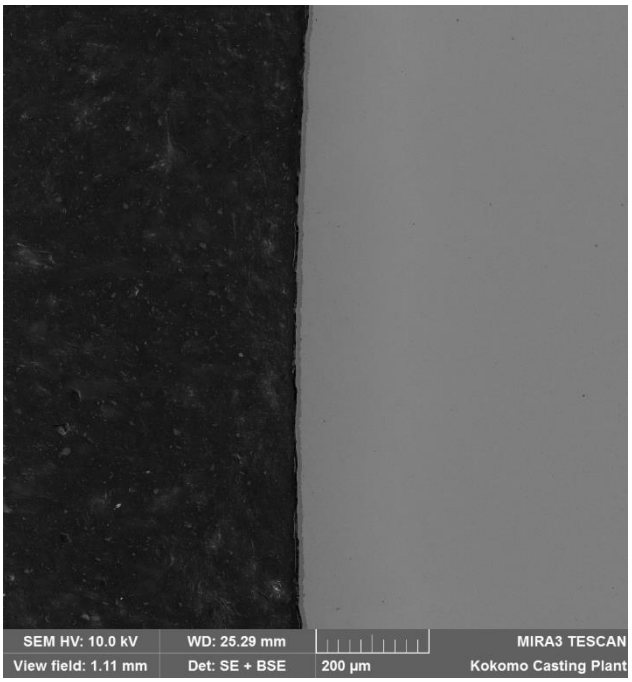

Figure 91. 250x SEM image of the H13 VCN specimen dunked for 30 minutes at 1250°F.

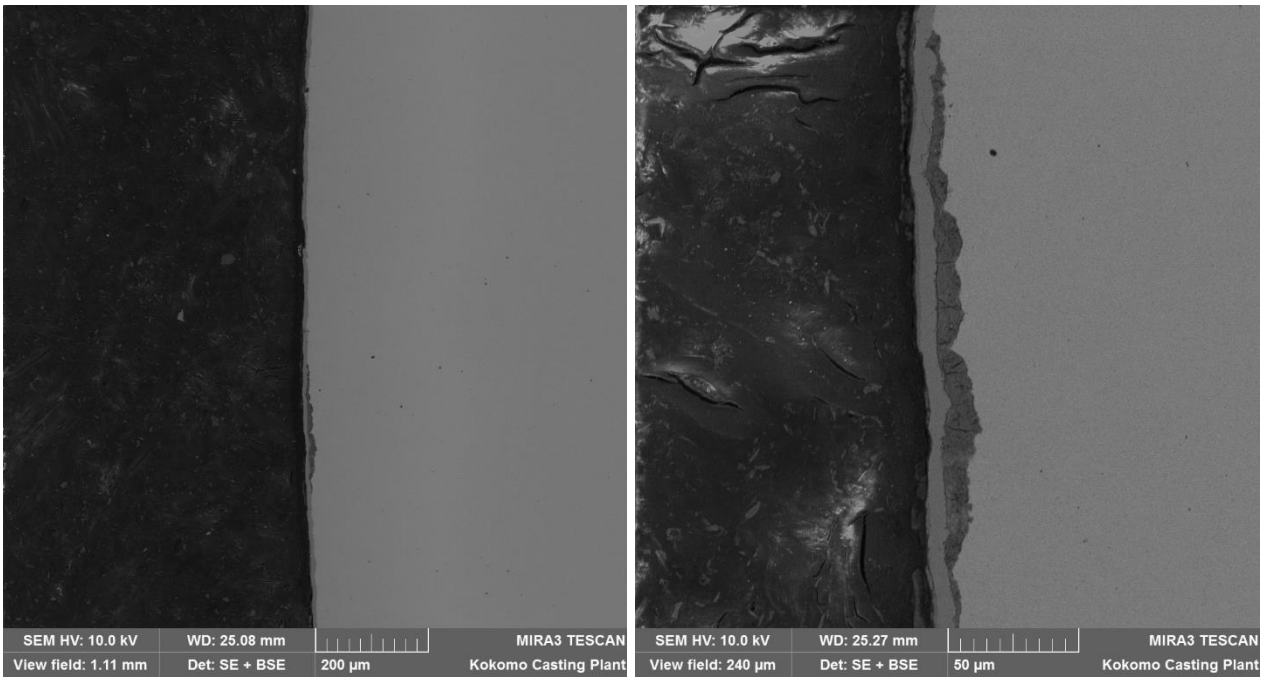

Figure 92. 250x and 1150x SEM images of the H13 VCN specimen dunked for 120 minutes at 1250°F.

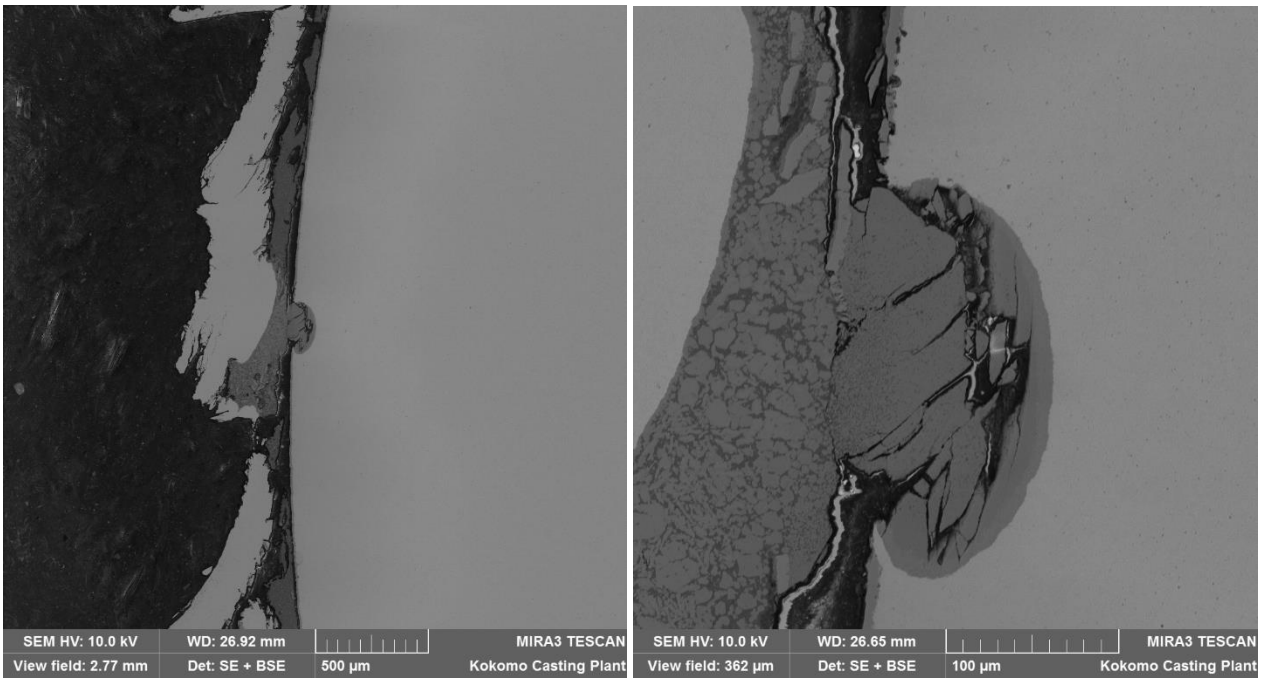

Figure 93. 100x and 750x SEM images of the H13 VCN specimen dunked for 1440 minutes at 1250°F.

4.2.6 H13 with PVD Aluminum Oxide (H13 Al2O3)

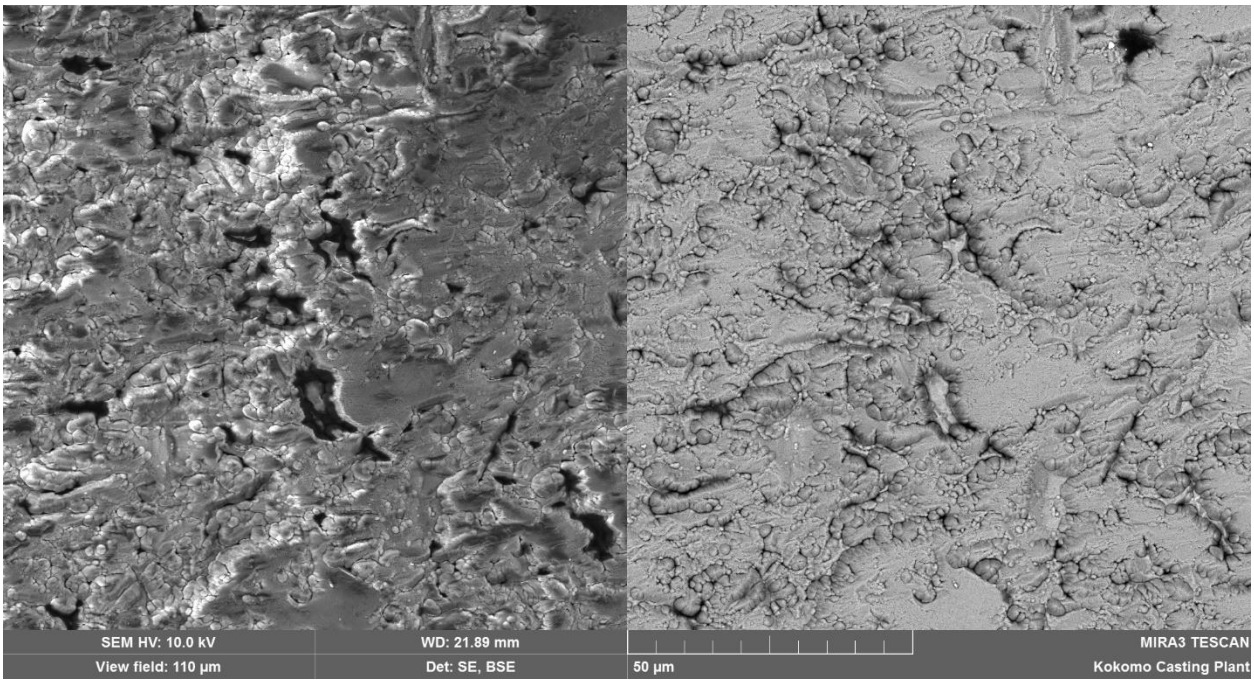

Figure 94. 2500x SEM images of the Al2O3 coating.

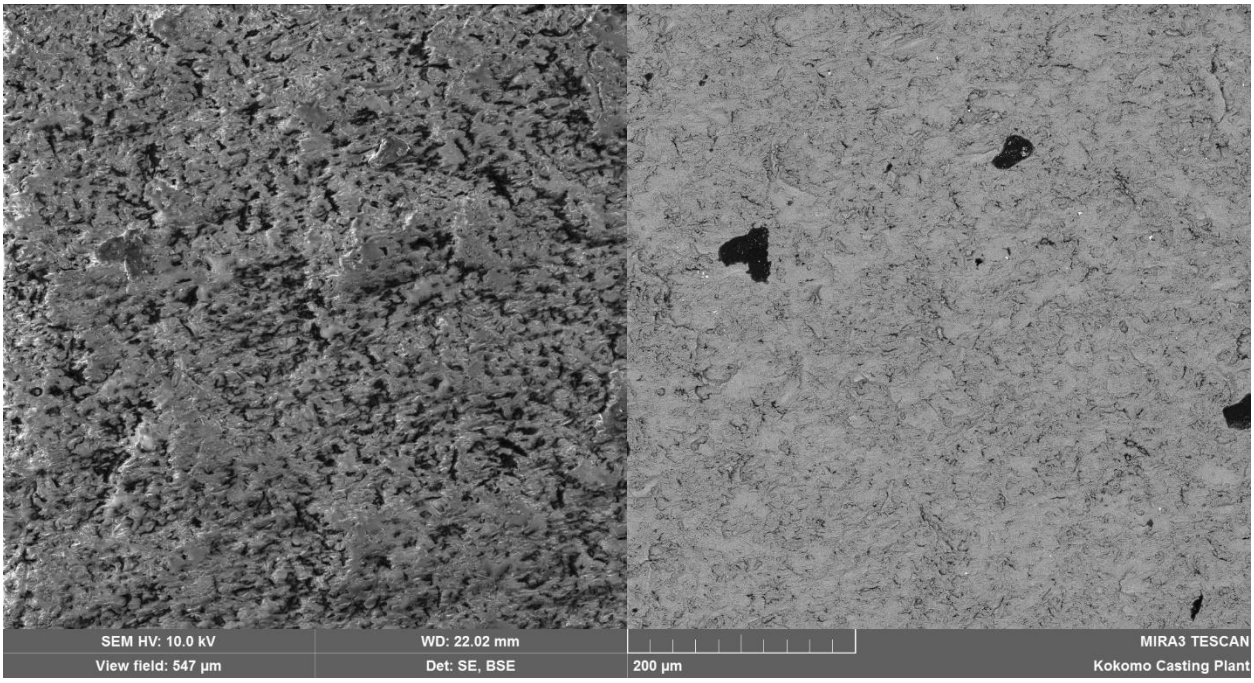

Figure 95. 500x SEM images of the Al2O3 coating.

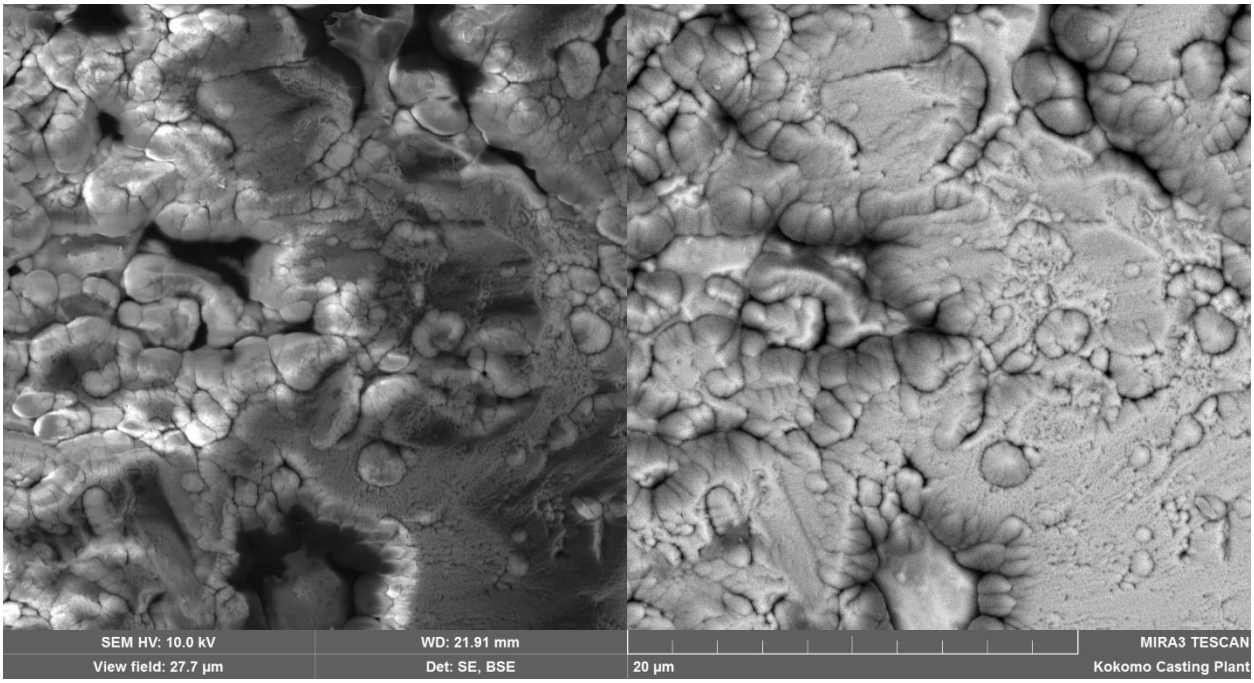

Figure 96. 10000x SEM images of the Al2O3 coating.

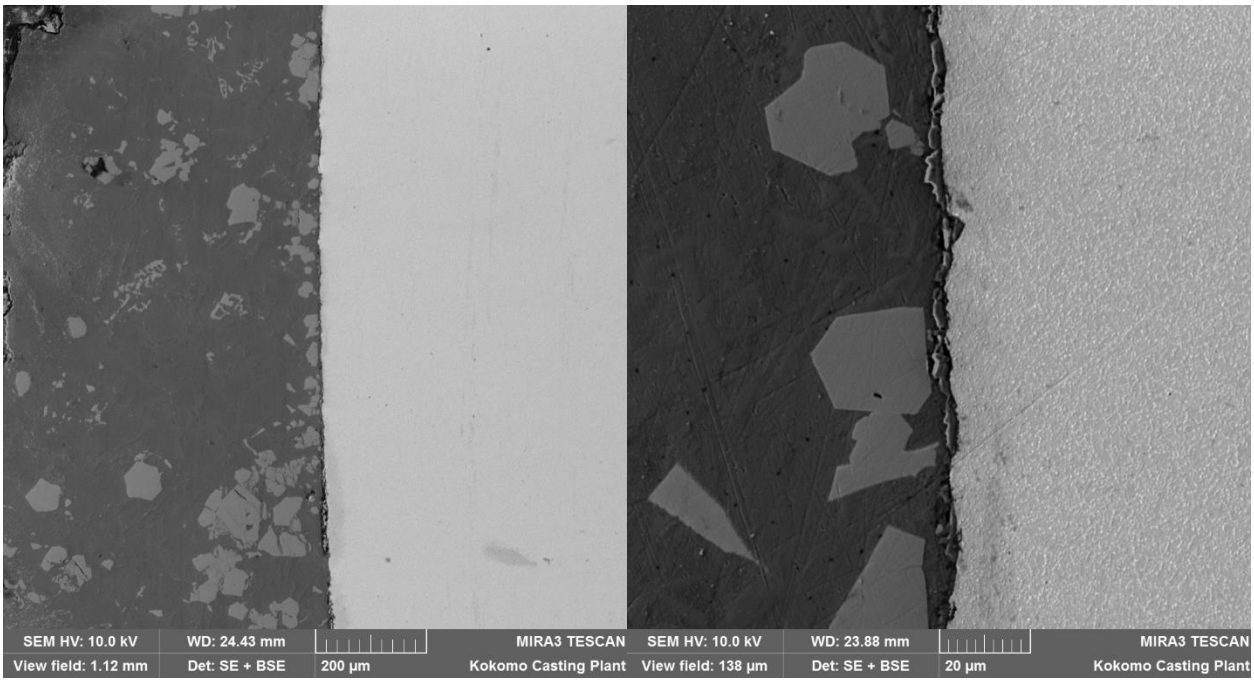

Figure 97. 250x and 2000x SEM images of the H13 Al2O3 specimen dunked for 30 minutes at 1150°F.

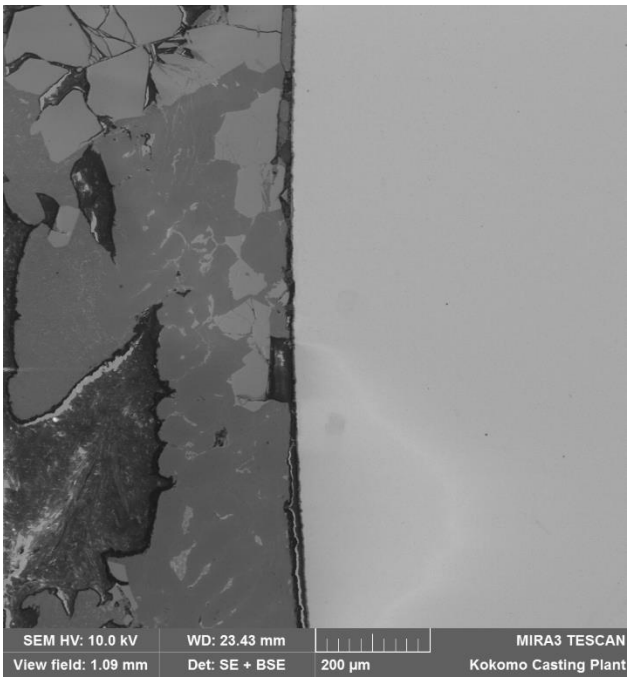

Figure 98. 250x SEM image of the H13 Al2O3 specimen dunked for 120 minutes at 1150°F.

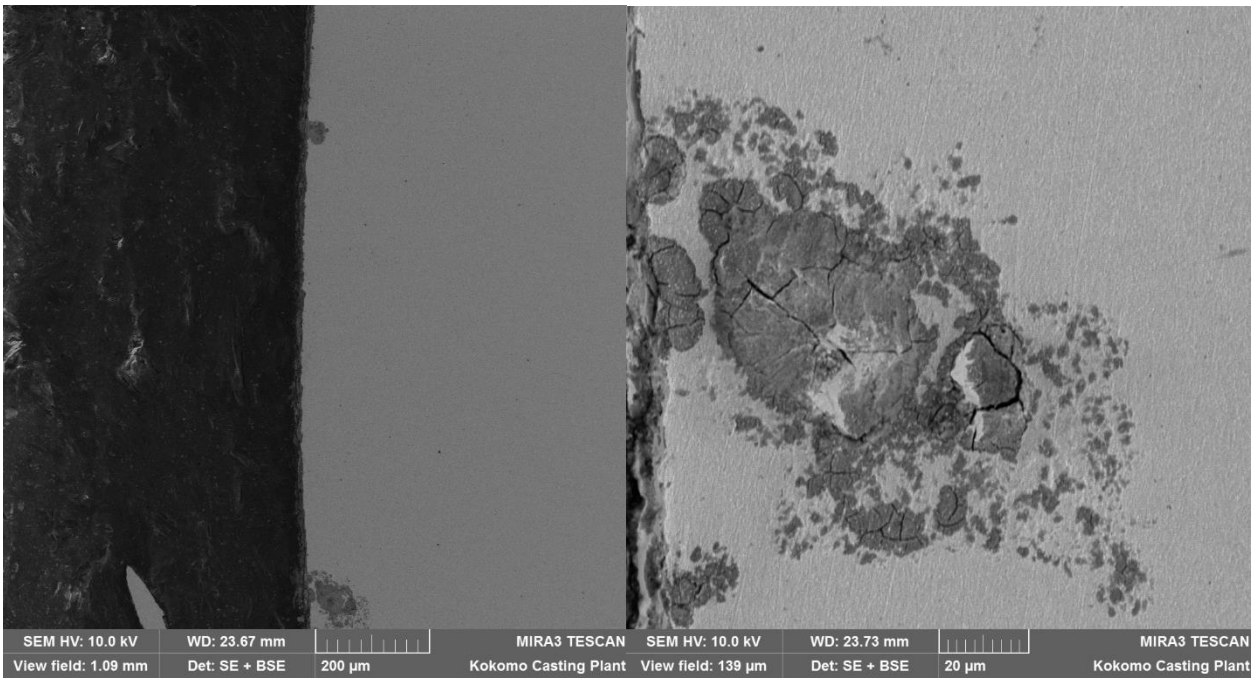

Figure 99. 250x and 2000x SEM images of the H13 Al2O3 specimen dunked for 120 minutes at 1150°F.

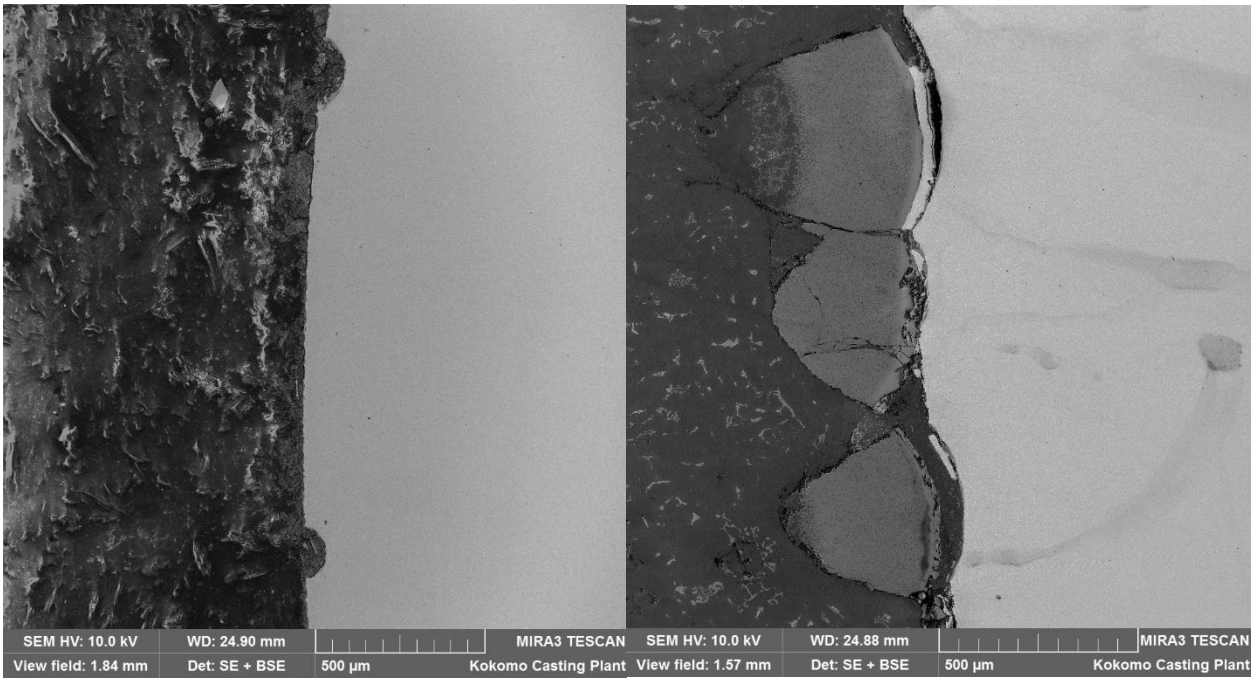

Figure 100. 150x and 175x SEM images of the H13 Al2O3 specimen dunked for 1440 minutes at 1150°F.

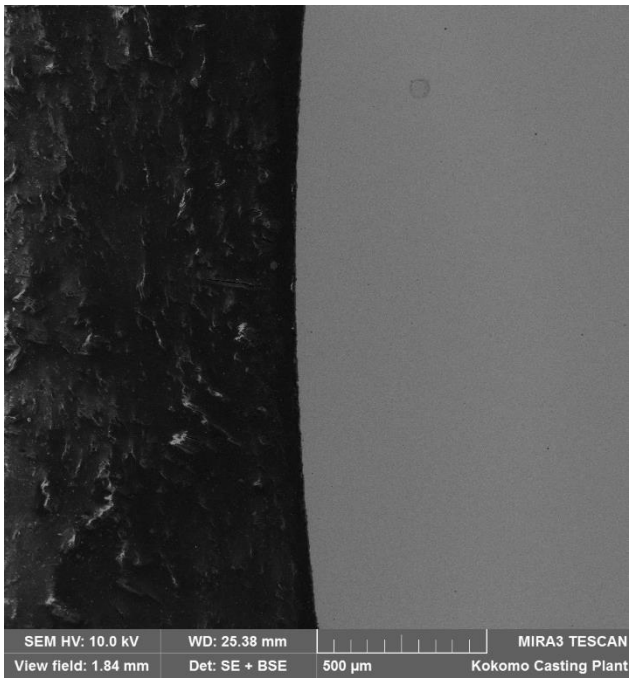

Figure 101. 150x SEM image of the H13 Al2O3 specimen dunked for 30 minutes at 1250°F.

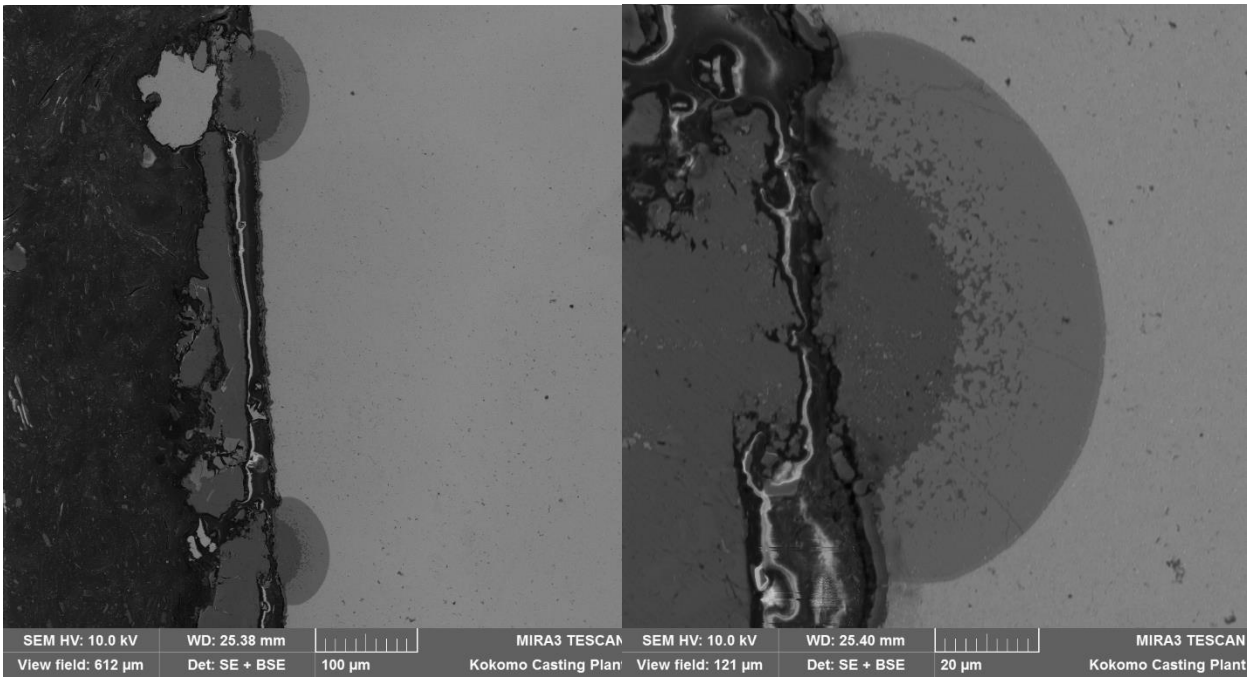

Figure 102. 450x and 2300x SEM images of the H13 Al2O3 specimen dunked for 30 minutes at 1250°F.

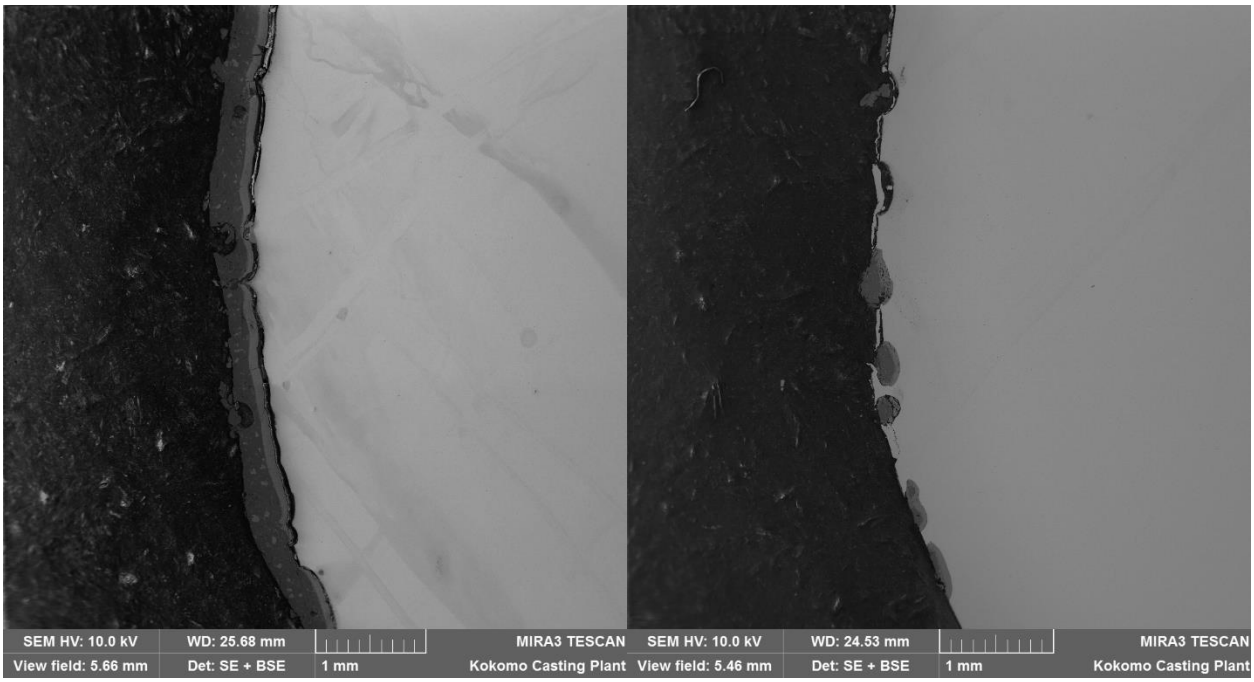

Figure 103. 50x and 50x SEM images of the H13 Al2O3 specimen dunked for 120 minutes at 1250°F.

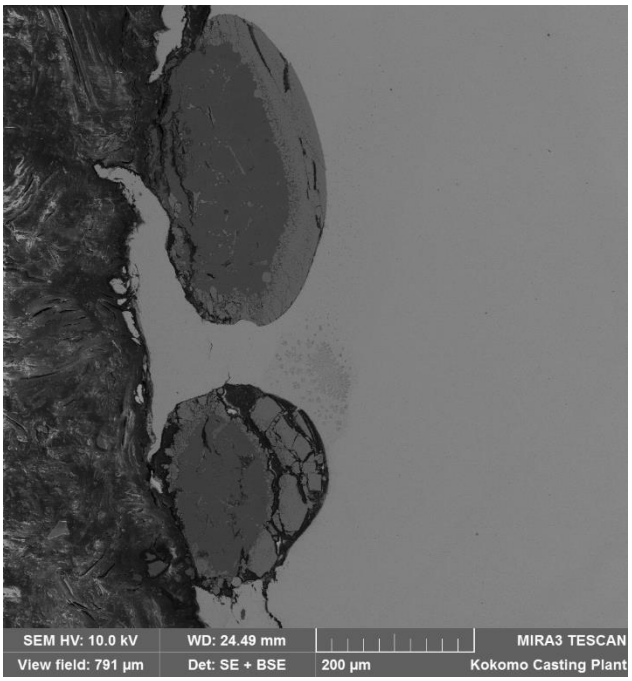

Figure 104. 350x SEM image of the H13 Al2O3 specimen dunked for 120 minutes at 1250°F, detailing two reactions growing together with a piece of unreacted steel ready to be broken free and released into the melt.

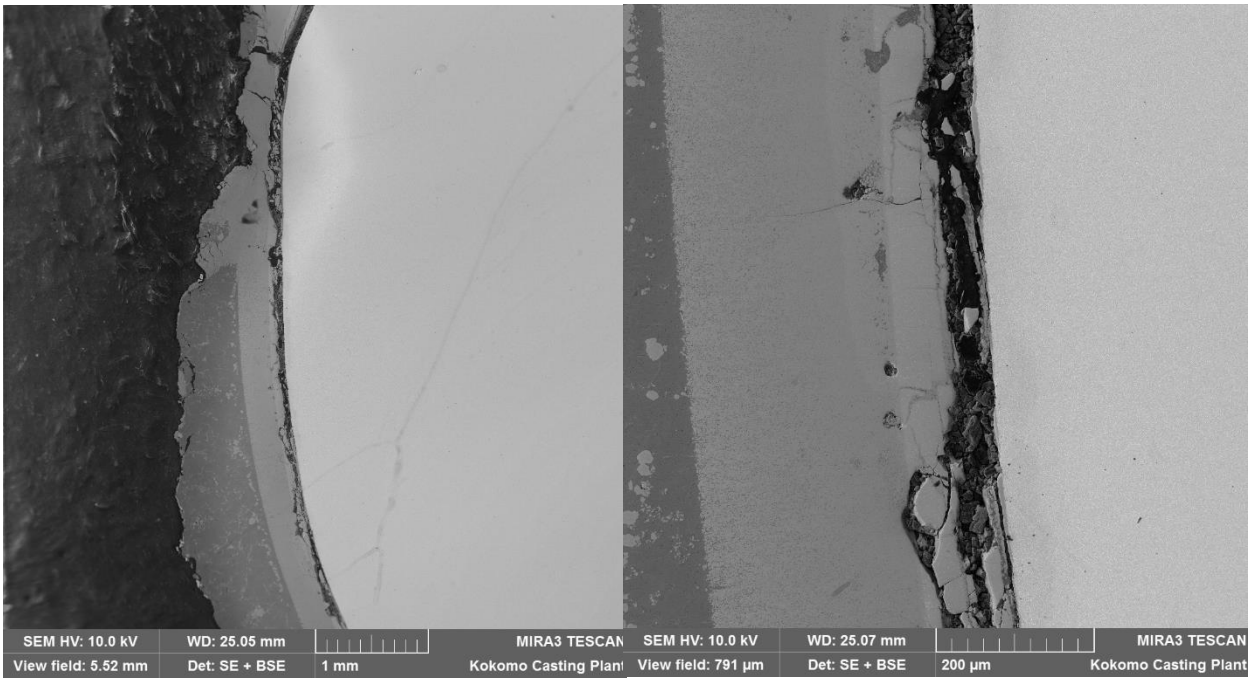

Figure 105. 50x and 350x SEM images of the H13 Al2O3 specimen dunked for 1440 minutes at 1250°F.

4.2.7 H13 with PVD Aluminum Chromium Nitride (H13 AlCrN)

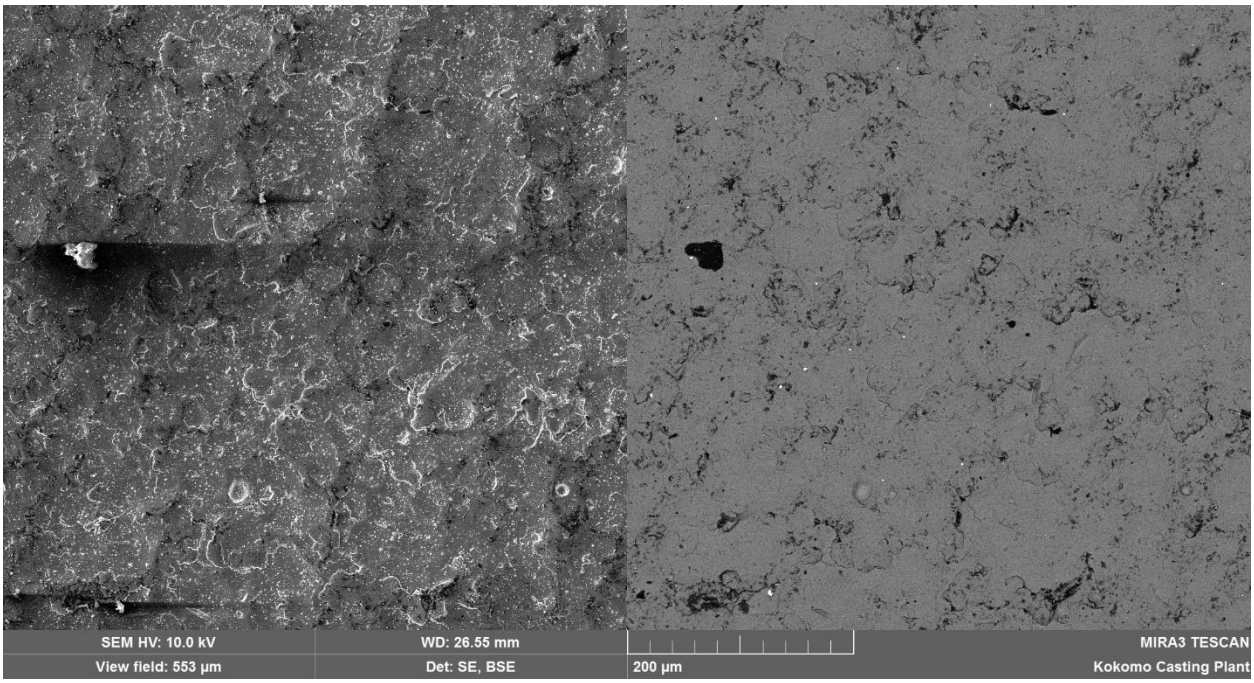

Figure 106. 500x SEM images of the AlCrN coating.

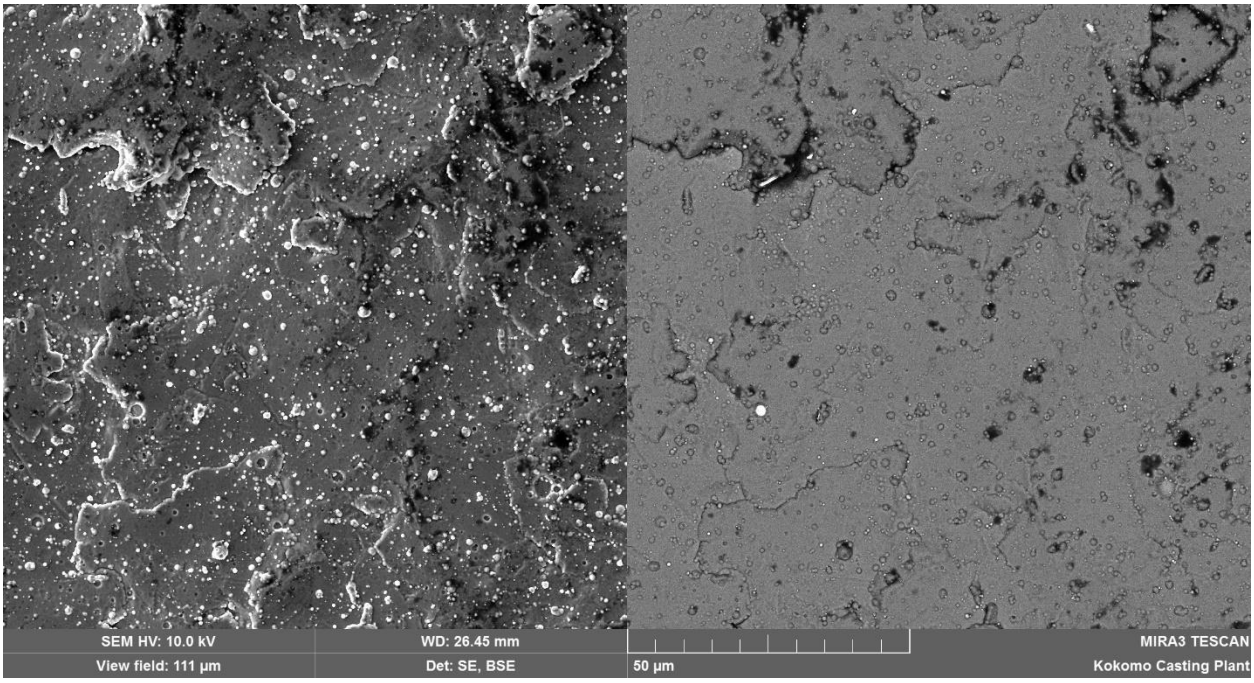

Figure 107. 2500x SEM images of the AlCrN coating.

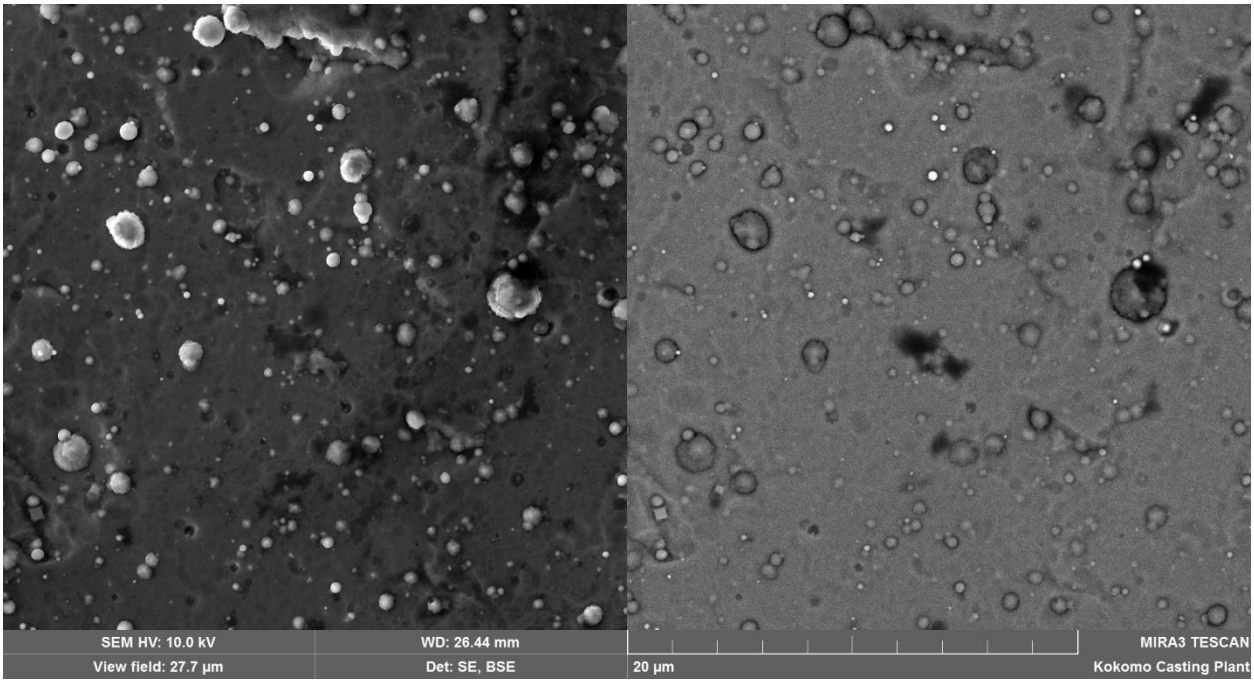

Figure 108. 10000x SEM images of the AlCrN coating.

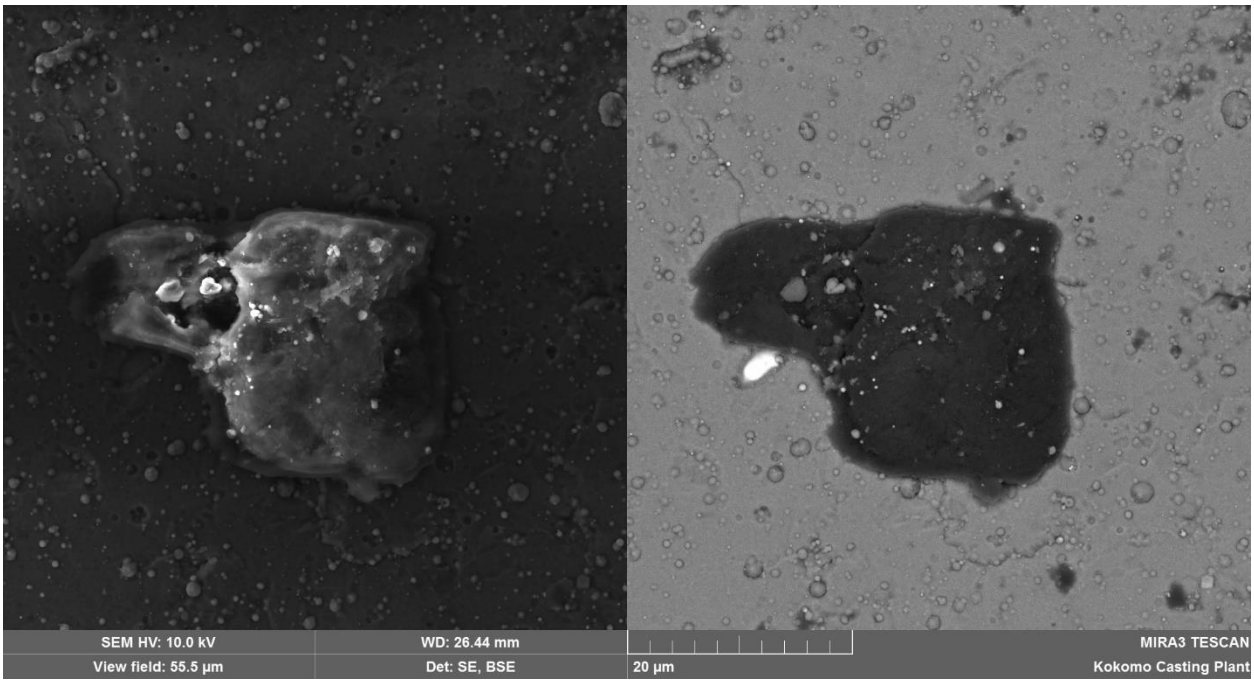

Figure 109. 5000x SEM images of the AlCrN coating detailing the large particle seen in Figure 106.

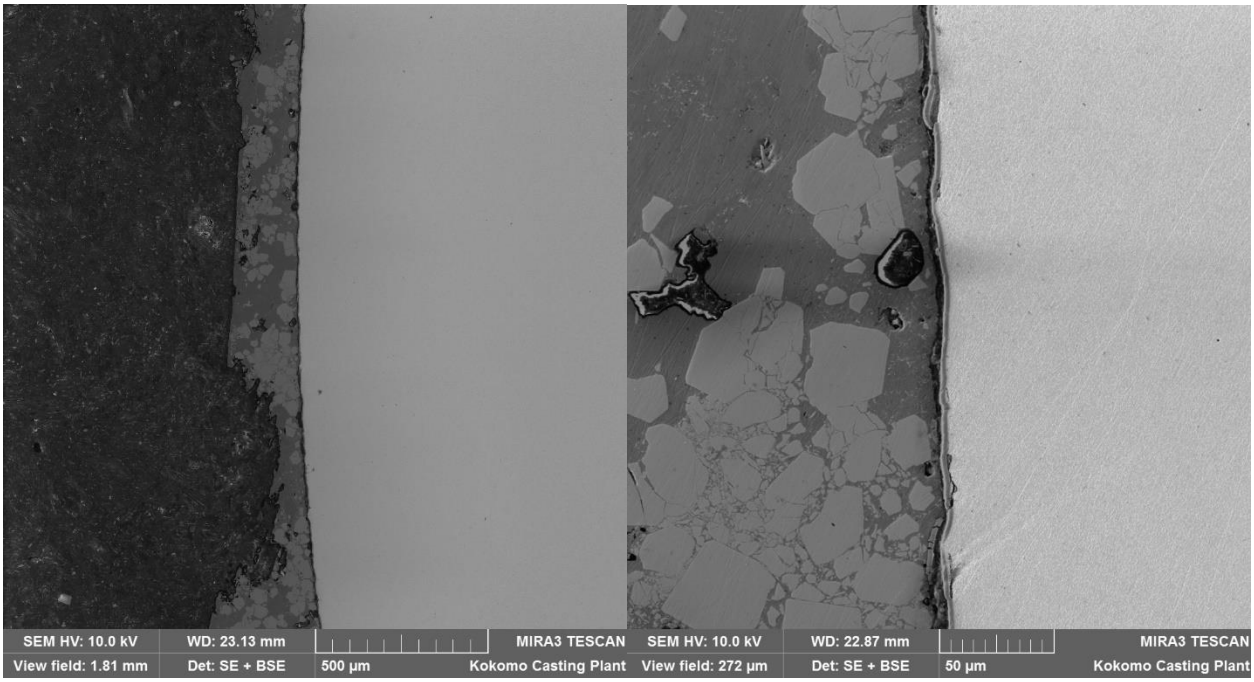

Figure 110. 150x and 1000x SEM images for the H13 AlCrN specimen dunked for 30 minutes at 1150°F.

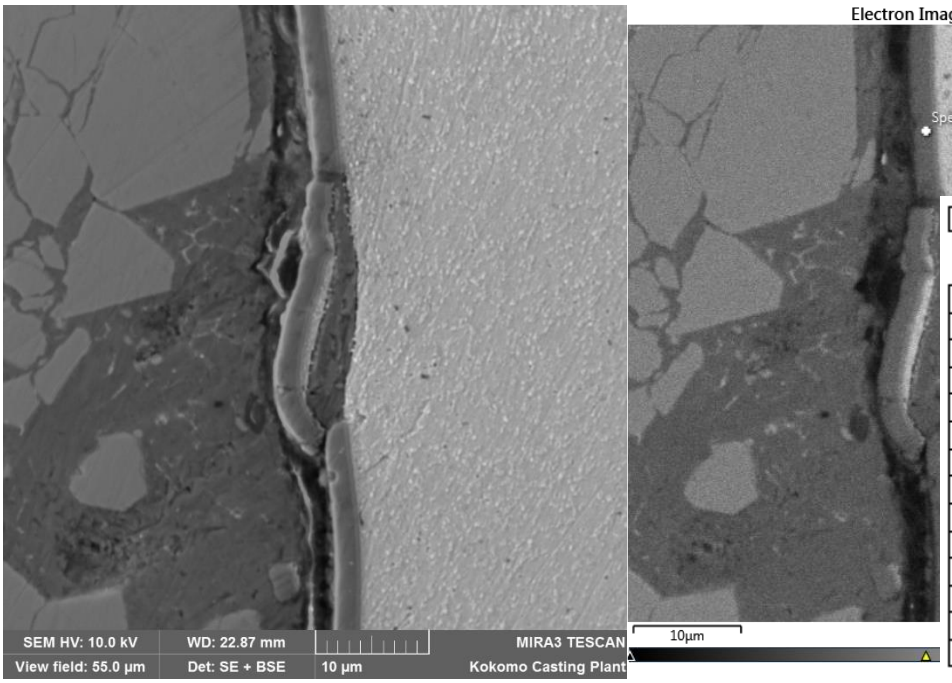

Result Type	Atomic %

Spectrum Label	Spectrum 203
N	45.57
O	2.31
Mg	0.00
Al	36.82
Si	0.31
V	0.00
Cr	14.56
Mn	0.00
Fe	0.43
Ni	0.00
Cu	0.00
Zn	0.00
Total	100.00

Figure 111. 5000x SEM image of the H13 AlCrN specimen dunked for 30 minutes at 1150°F, and the atomic chemistry of the coating.

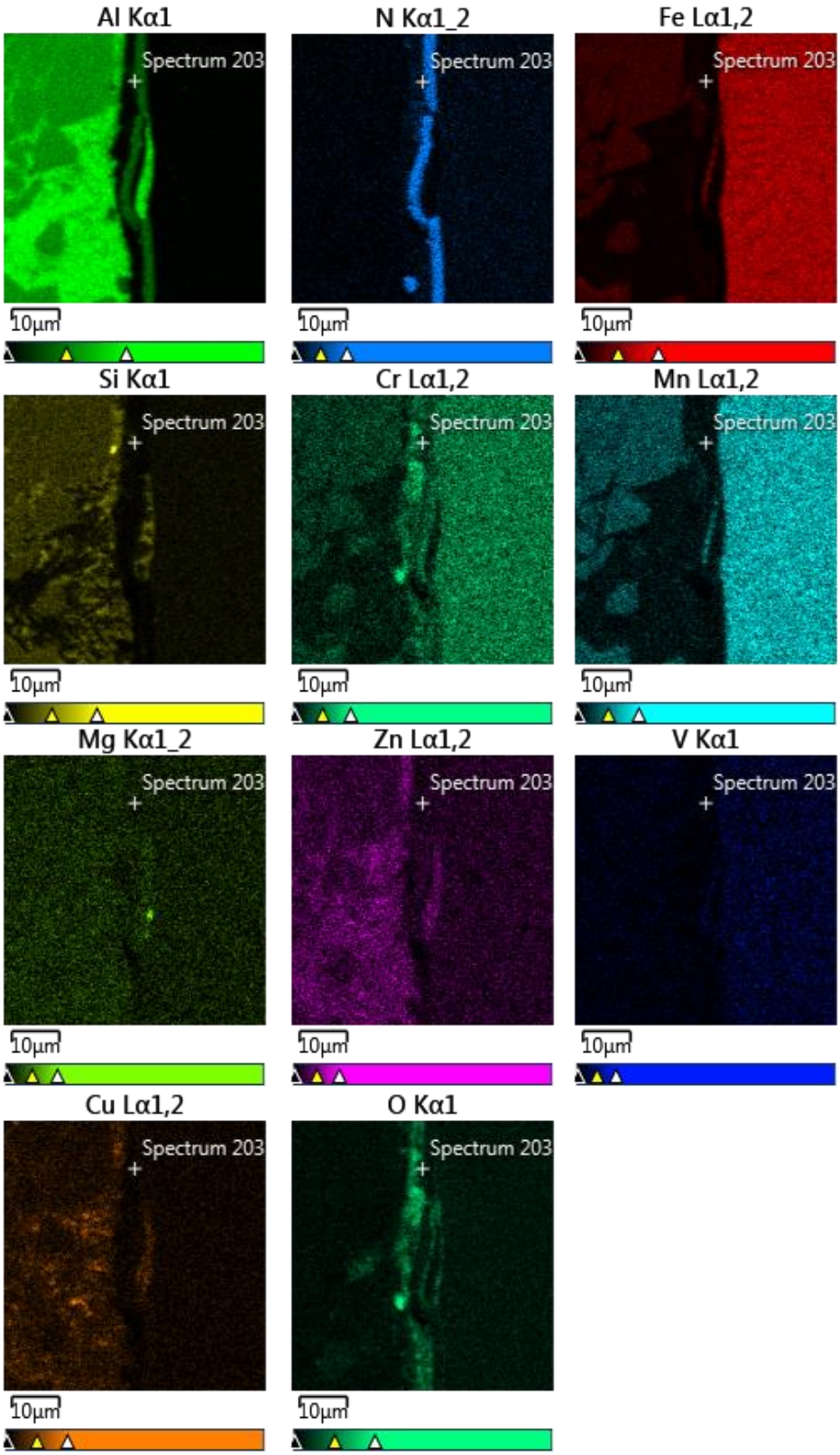

Figure 112. EDS maps corresponding to Figure 111.

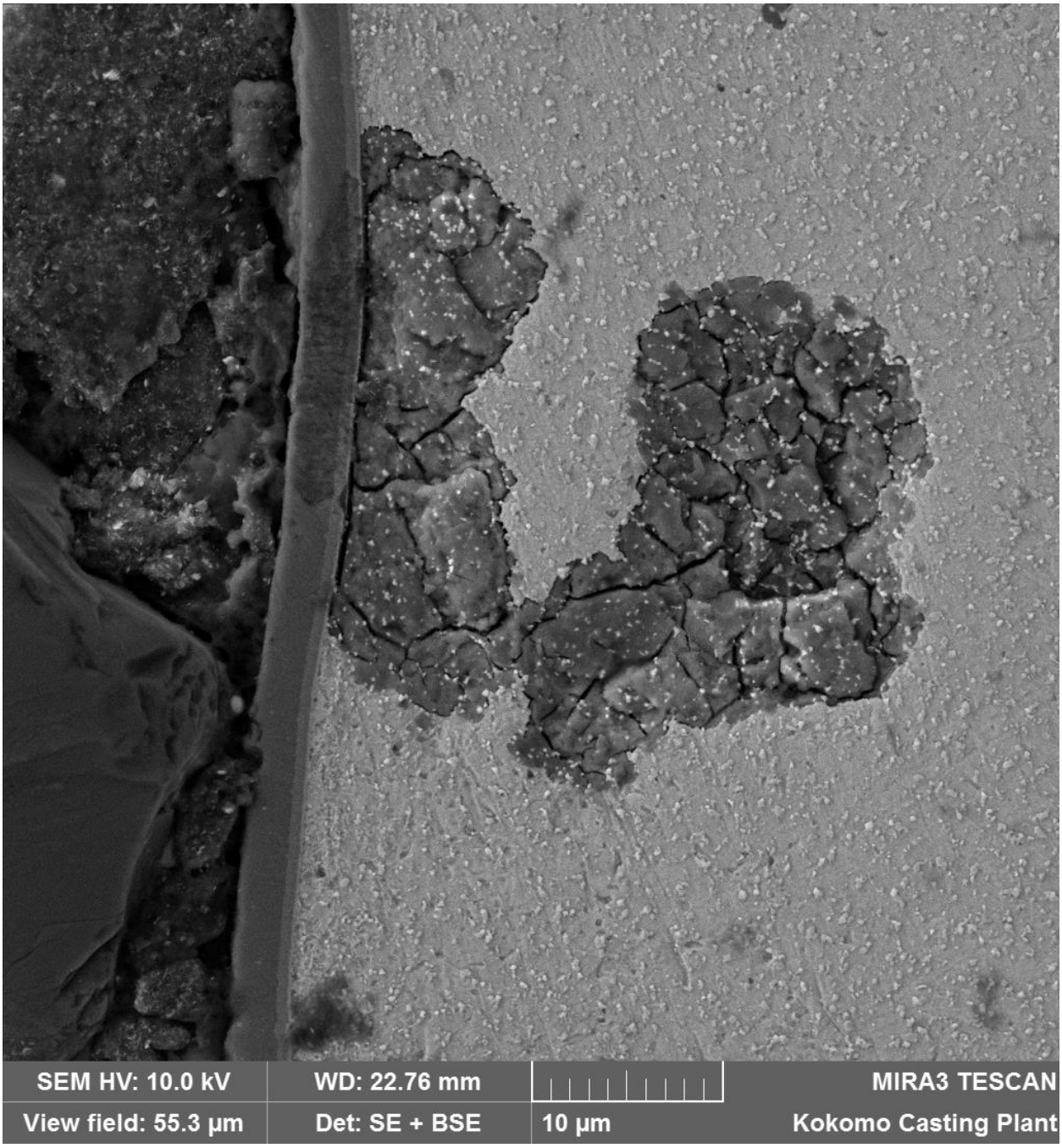

Figure 113. 5000x SEM image of the H13 AlCrN specimen dunked for 30 minutes at 1150°F.

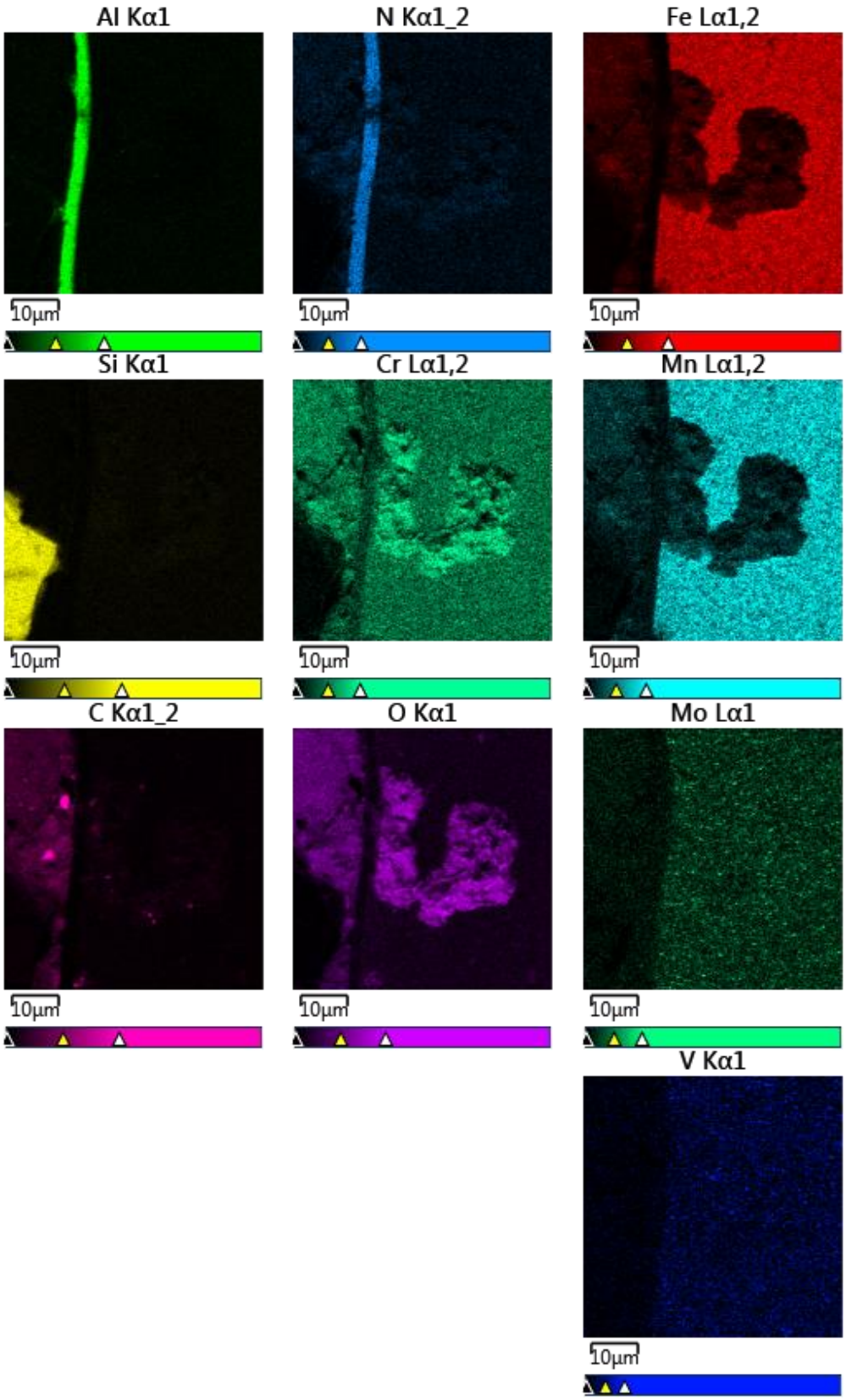

Figure 114. EDS maps corresponding to Figure 113.

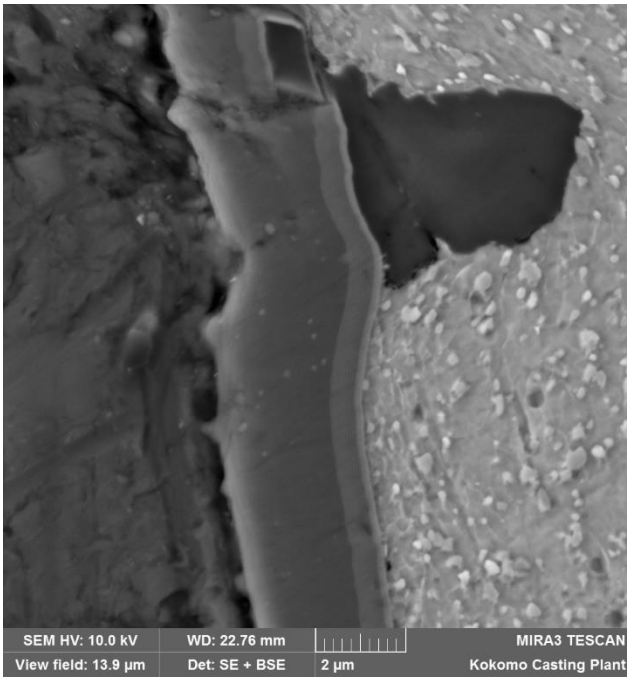

Figure 115. 20000x SEM image of the H13 AlCrN specimen dunked for 30 minutes at 1150°F.

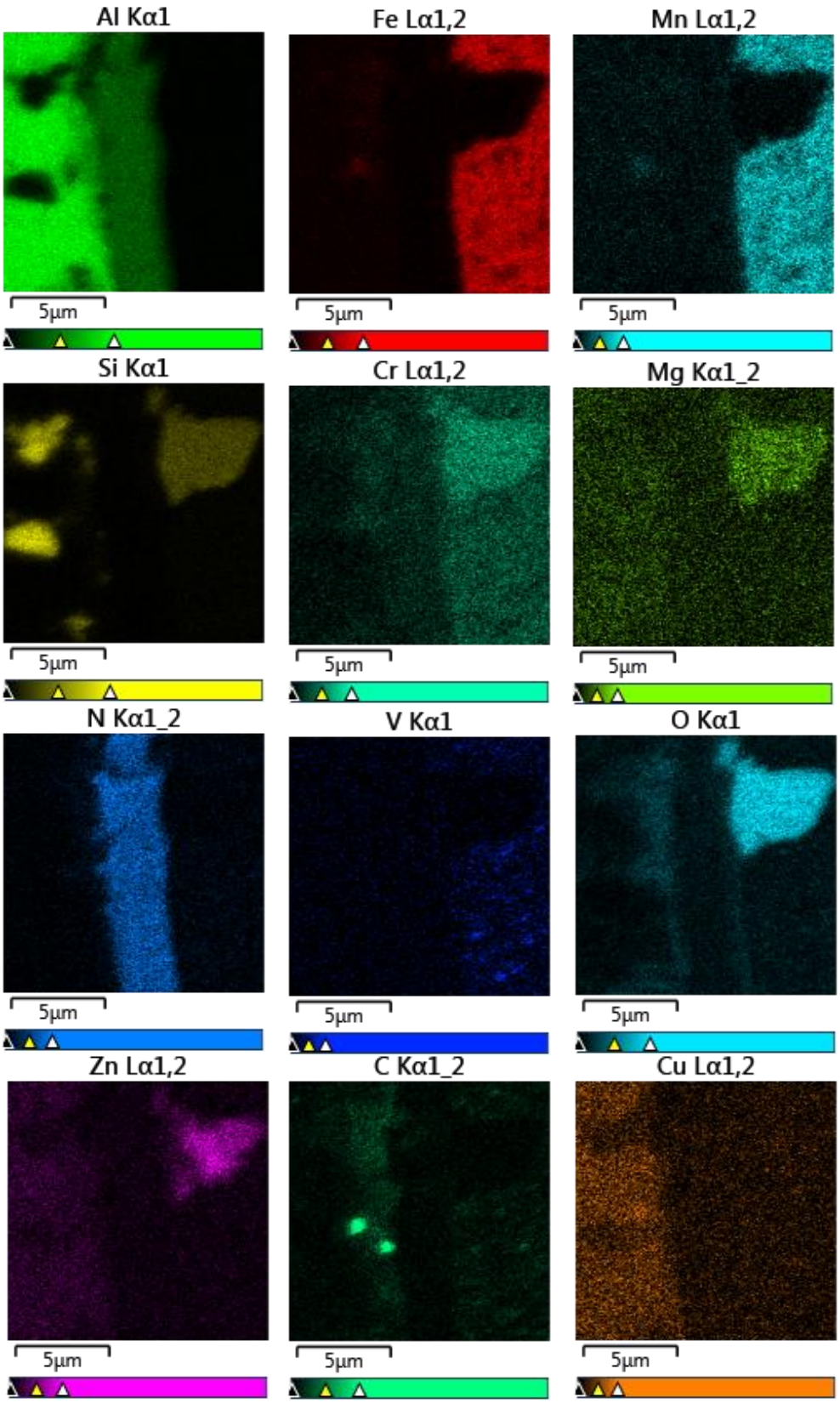

Figure 116. EDS maps corresponding to Figure 115.

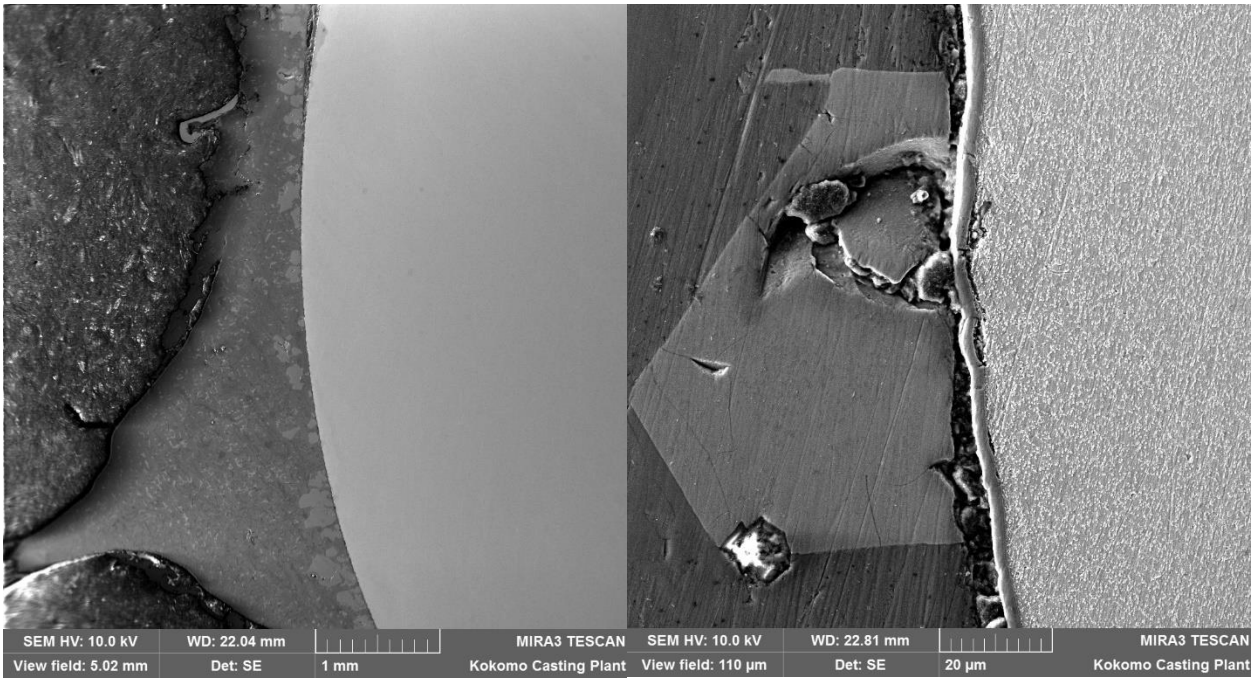

Figure 117. 50x and 2500x SEM images of the H13 AlCrN specimen dunked for 120 minutes at 1150°F.

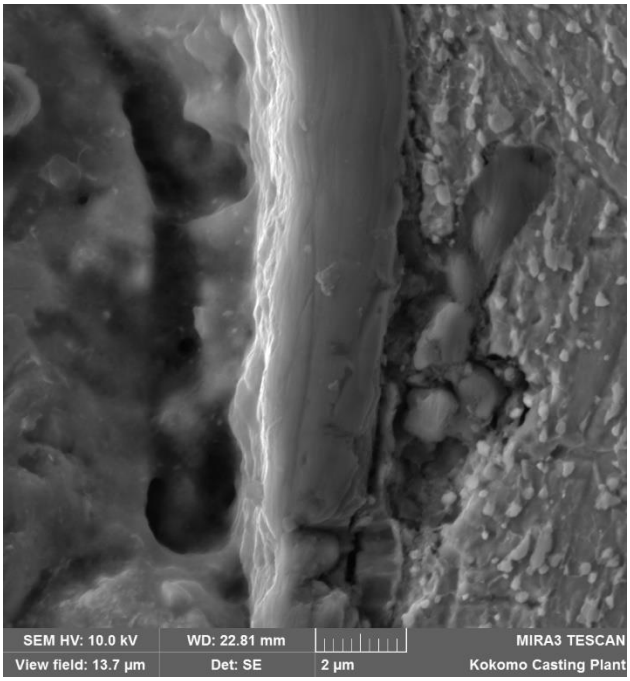

Figure 118. 20000x SEM image of the H13 AlCrN specimen dunked for 120 minutes at 1150°F.

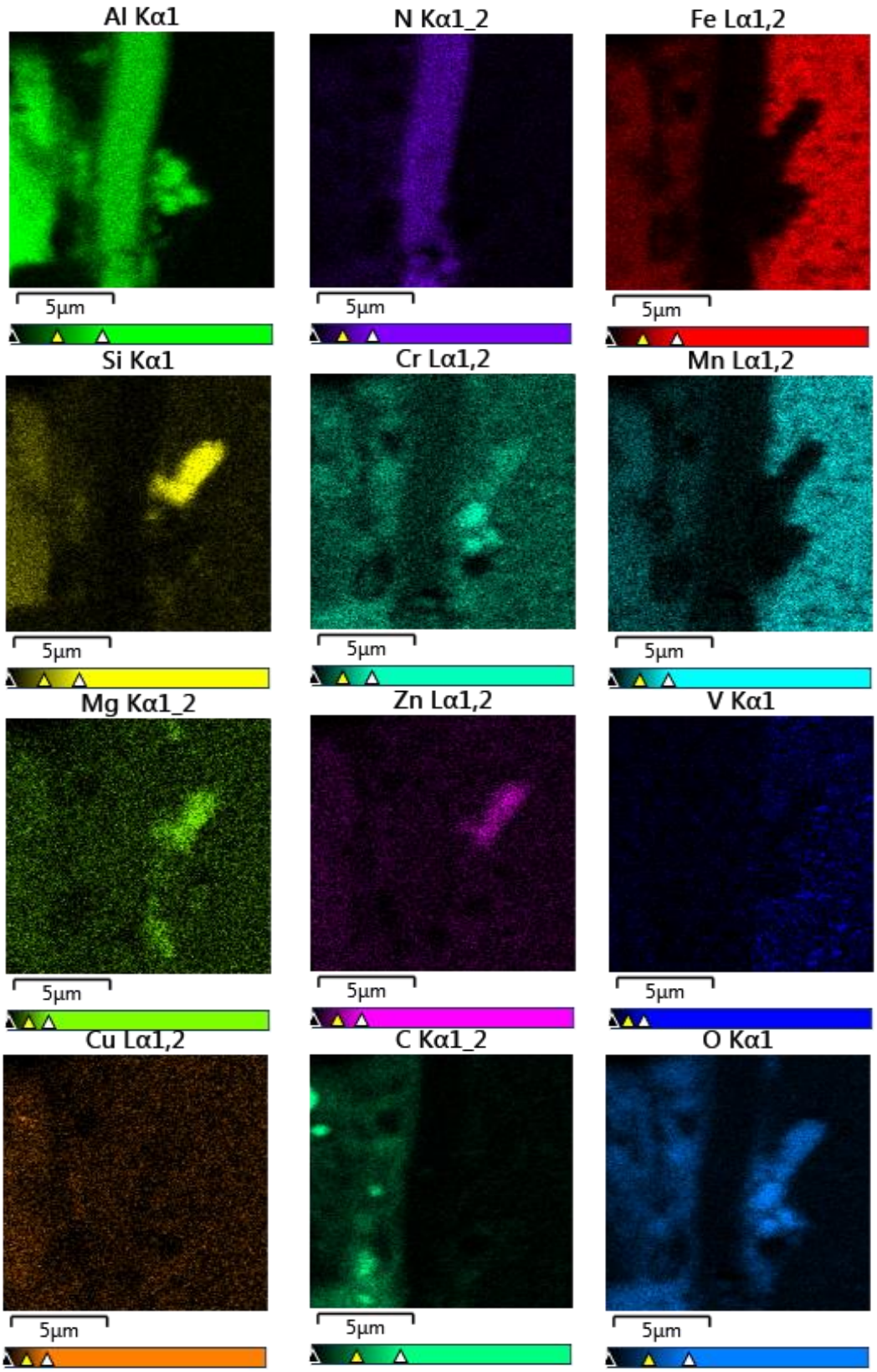

Figure 119. EDS maps corresponding to Figure 118.

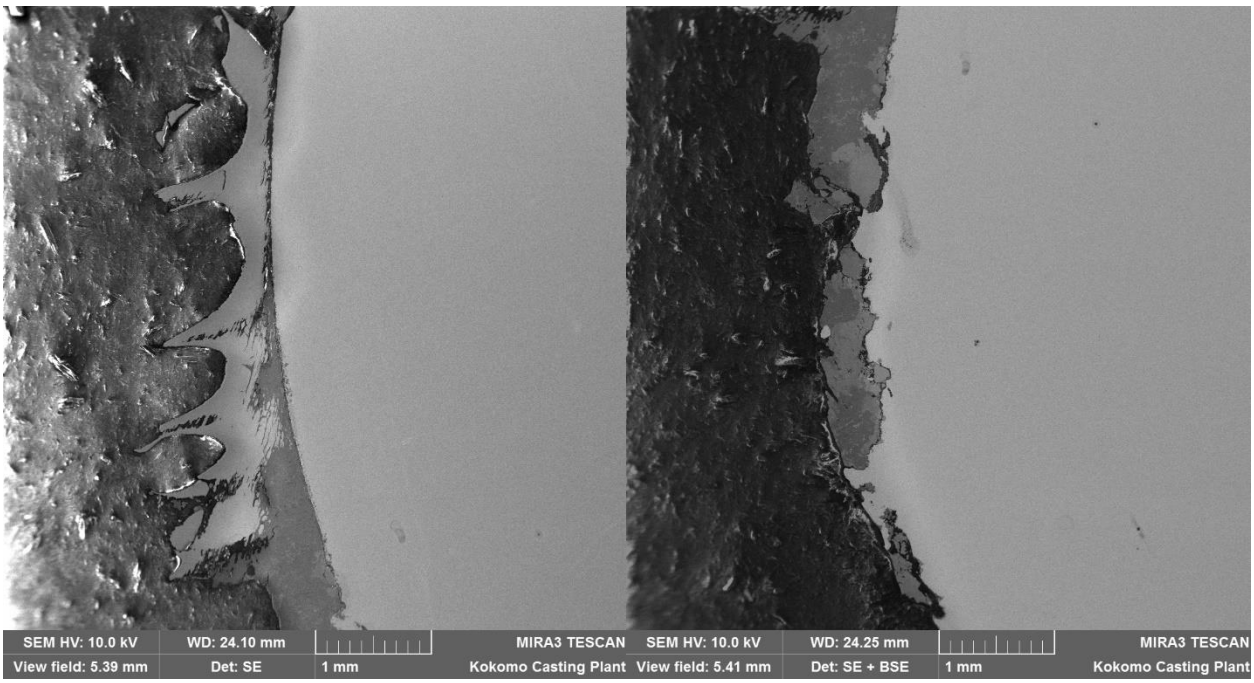

Figure 120. 50x and 50x SEM images of the H13 AlCrN specimen dunked for 1440 minutes at 1150°F.

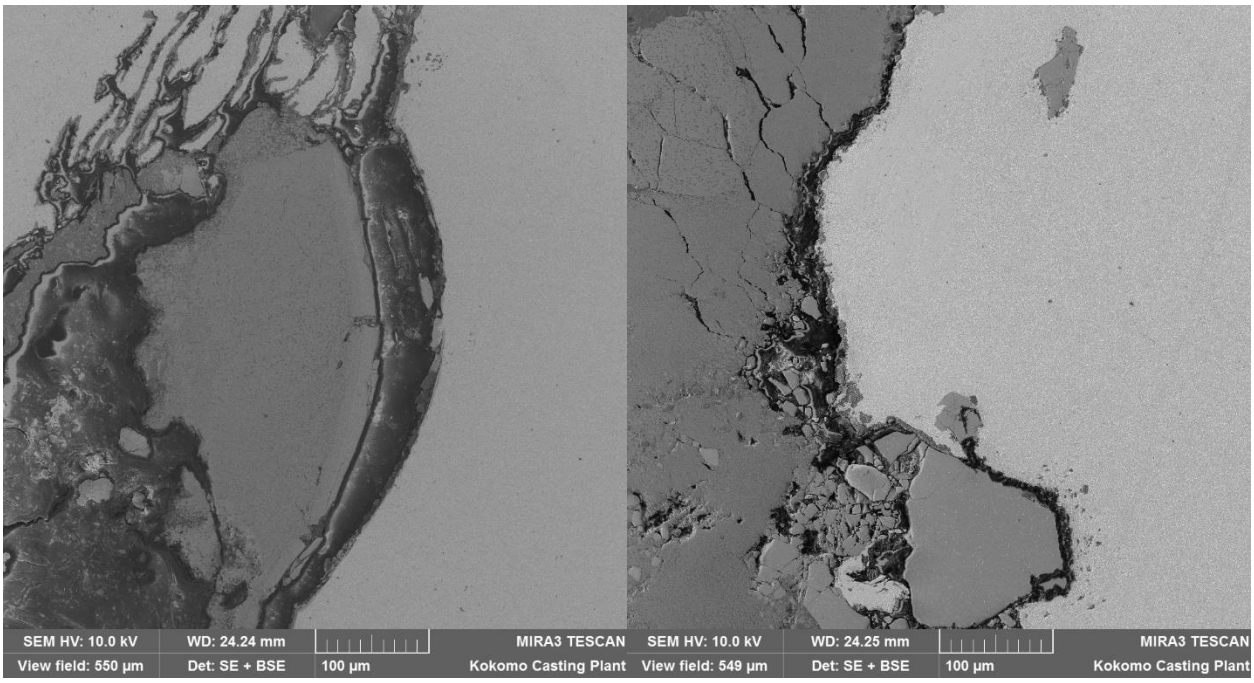

Figure 121. 500x and 5000x SEM images of the H13 AlCrN specimen dunked for 1440 minutes at 1150°F.

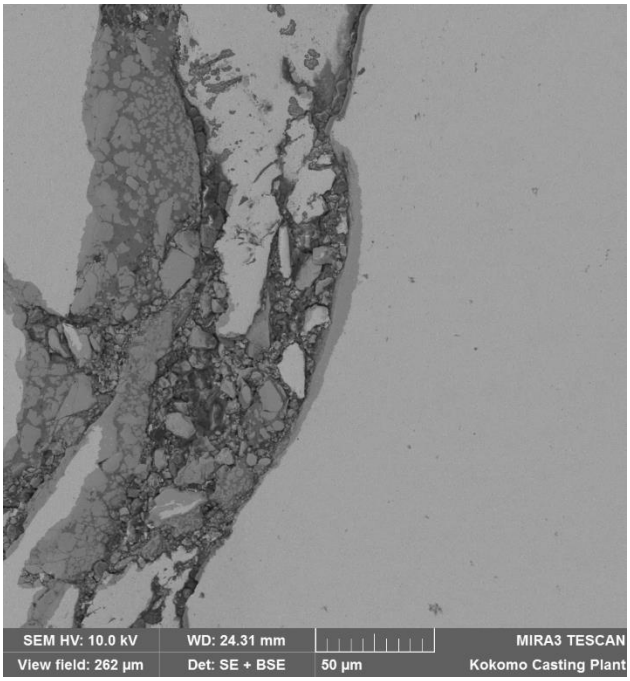

Figure 122. 1000x SEM image of the H13 AlCrN specimen dunked for 1440 minutes at 1150°F.

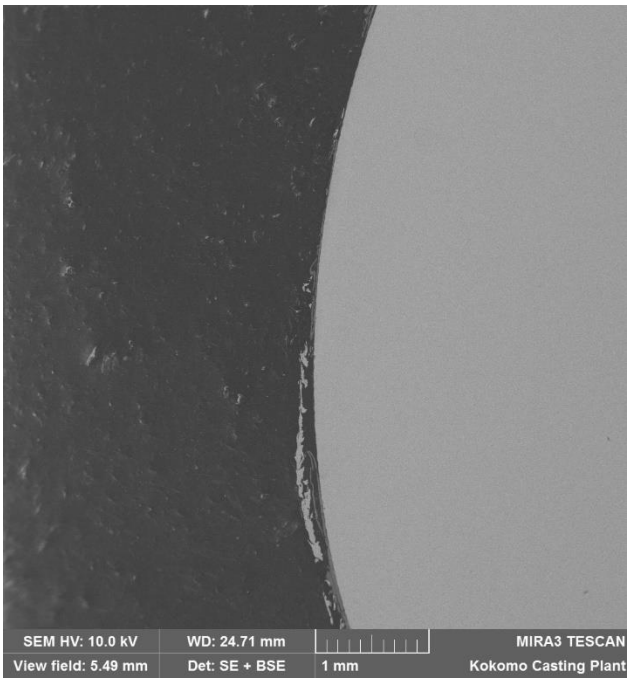

Figure 123. 50x SEM image of the H13 AlCrN specimen dunked for 30 minutes at 1250°F.

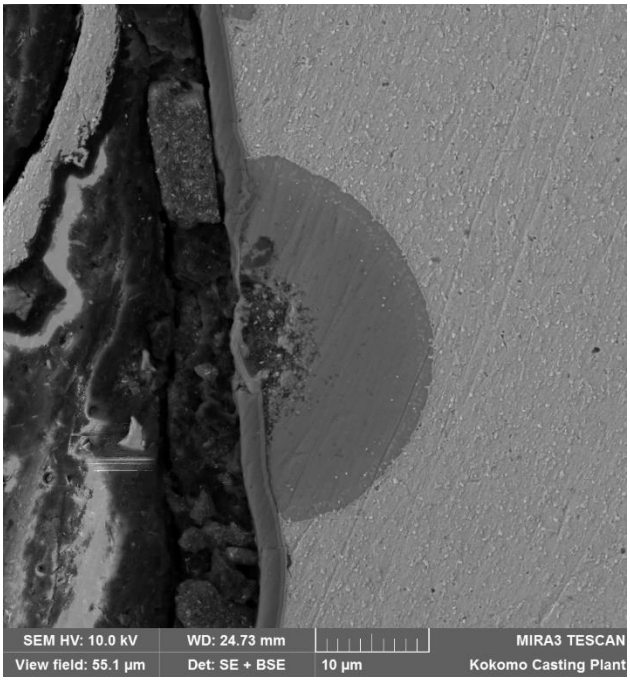

Figure 124. 5000x SEM image of the H13 AlCrN specimen dunked for 30 minutes at 1250°F.

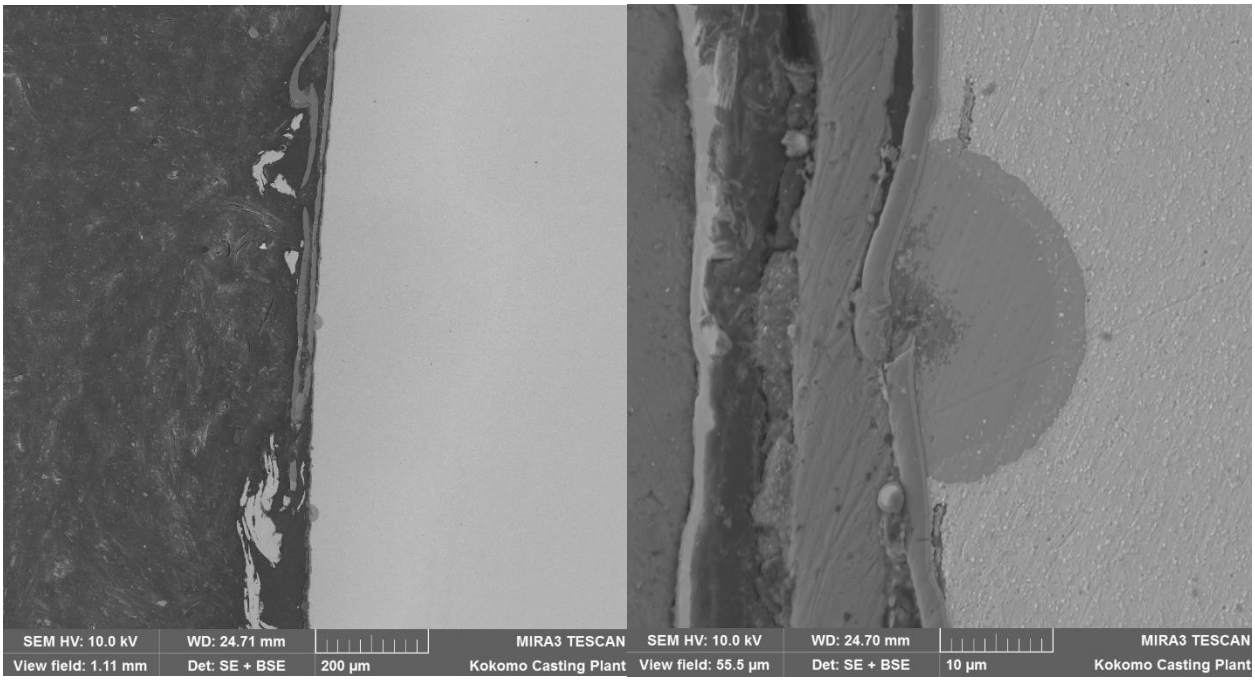

Figure 125. 250x and 5000x SEM images of the H13 AlCrN specimen dunked for 30 minutes at 1250°F.

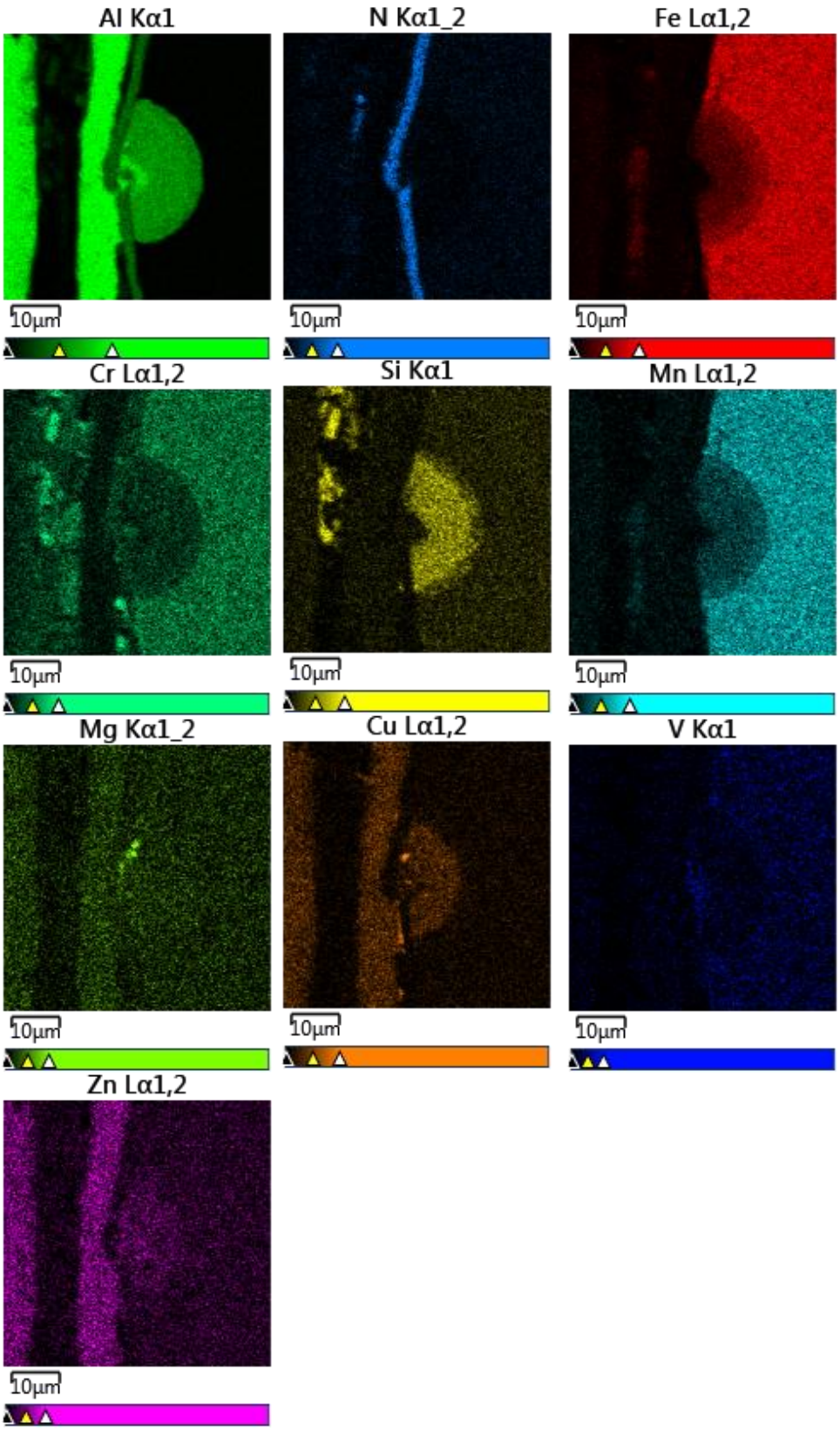

Figure 126. EDS maps corresponding to the 5000x image in Figure 125.

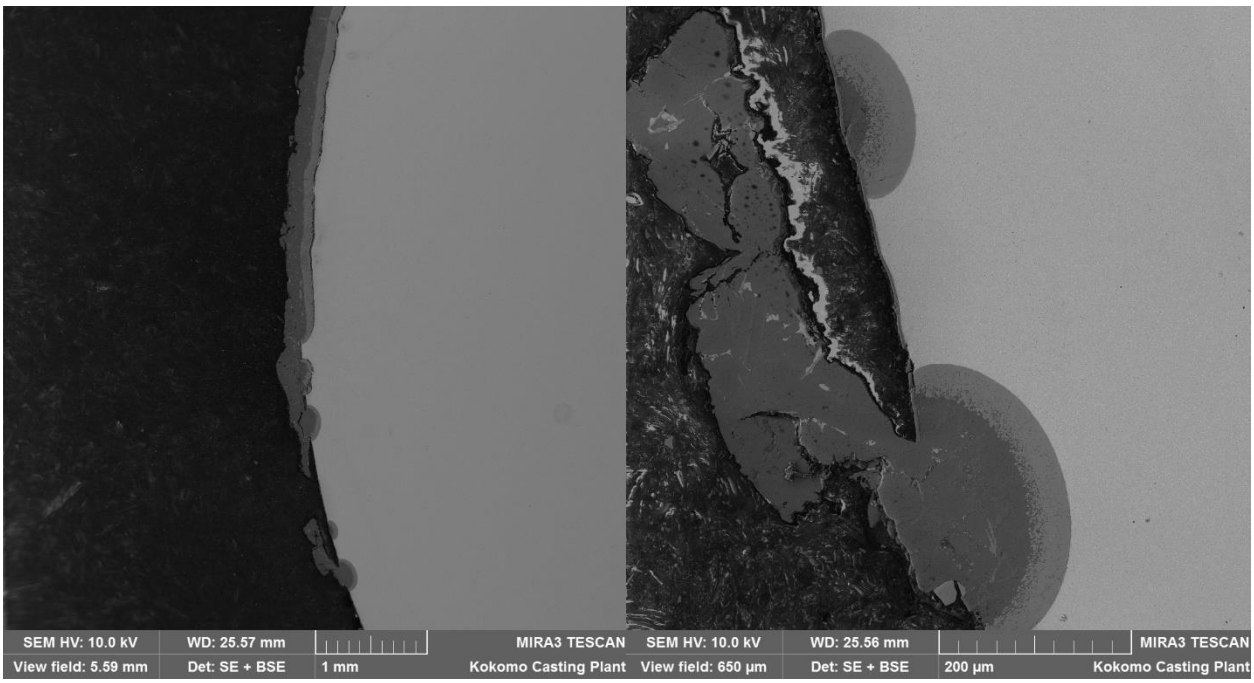

Figure 127. 50x and 425x SEM images of the H13 AlCrN specimen dunked for 120 minutes at 1250°F.

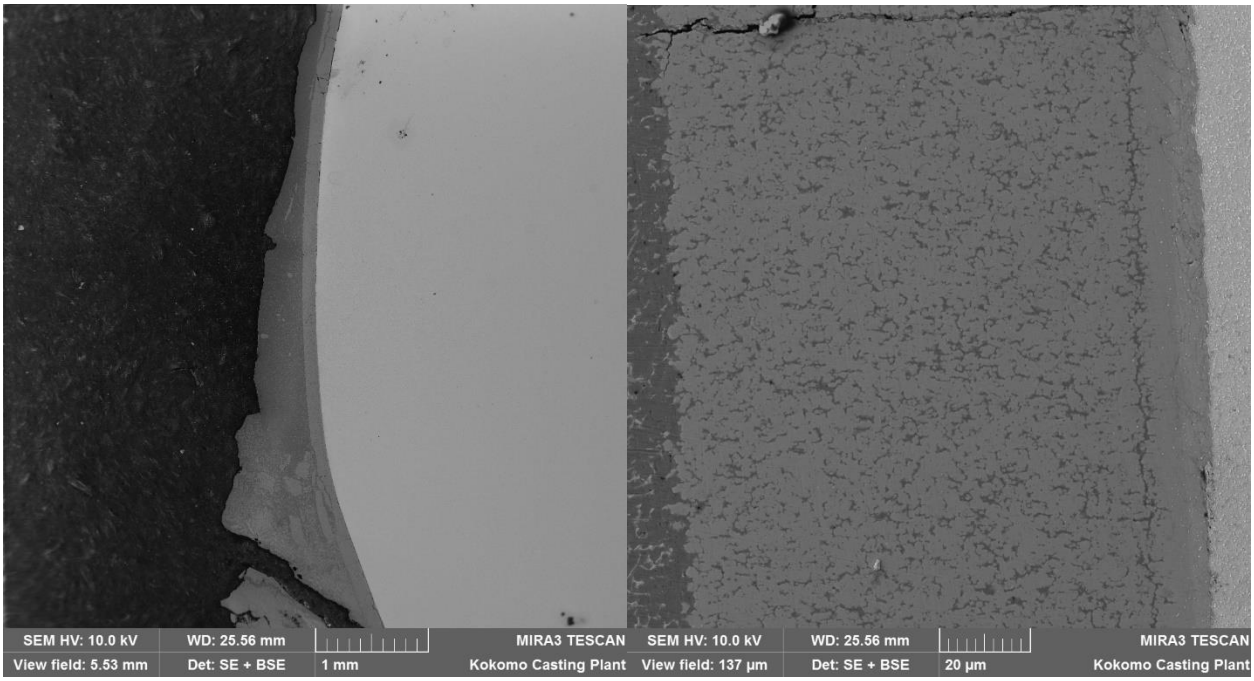

Figure 128. 50x and 2000x SEM images of the H13 AlCrN specimen dunked for 1440 minutes at 1250°F.

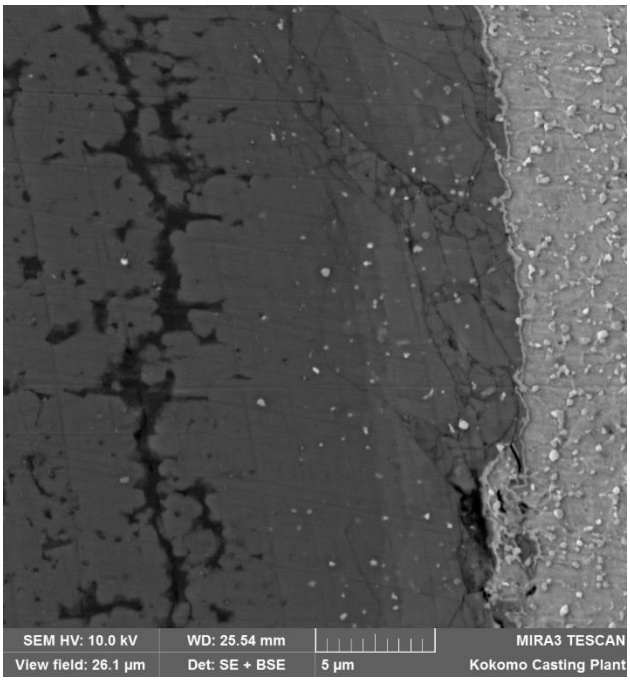

Figure 129. 10600x SEM image of the H13 AlCrN specimen dunked for 1440 minutes at 1250°F, showing stability of the H13 carbides throughout the intermetallic reaction zones.

4.2.8 Ranking of Coatings and Correlation to Back Scatter Electron Images

Qualitative review of the SEM images from the dunked specimen, such as those in Figure 130, showed the following ranking of performance from best to worse: Si-DLC, VCN, VC, AlCrN, AlO, NC, and Bare H13. As seen in Figure 131, the Si-DLC coating is of a very uniform structure with the boundaries between coating grains even showing relatively similar backscattering with the bulk grains. However, the other coatings show several relatively large defects that made it easier for aluminum to infiltrate the coating. It is possible that vanadium carbonitride could outperform Si-DLC if it could be made as defect free.

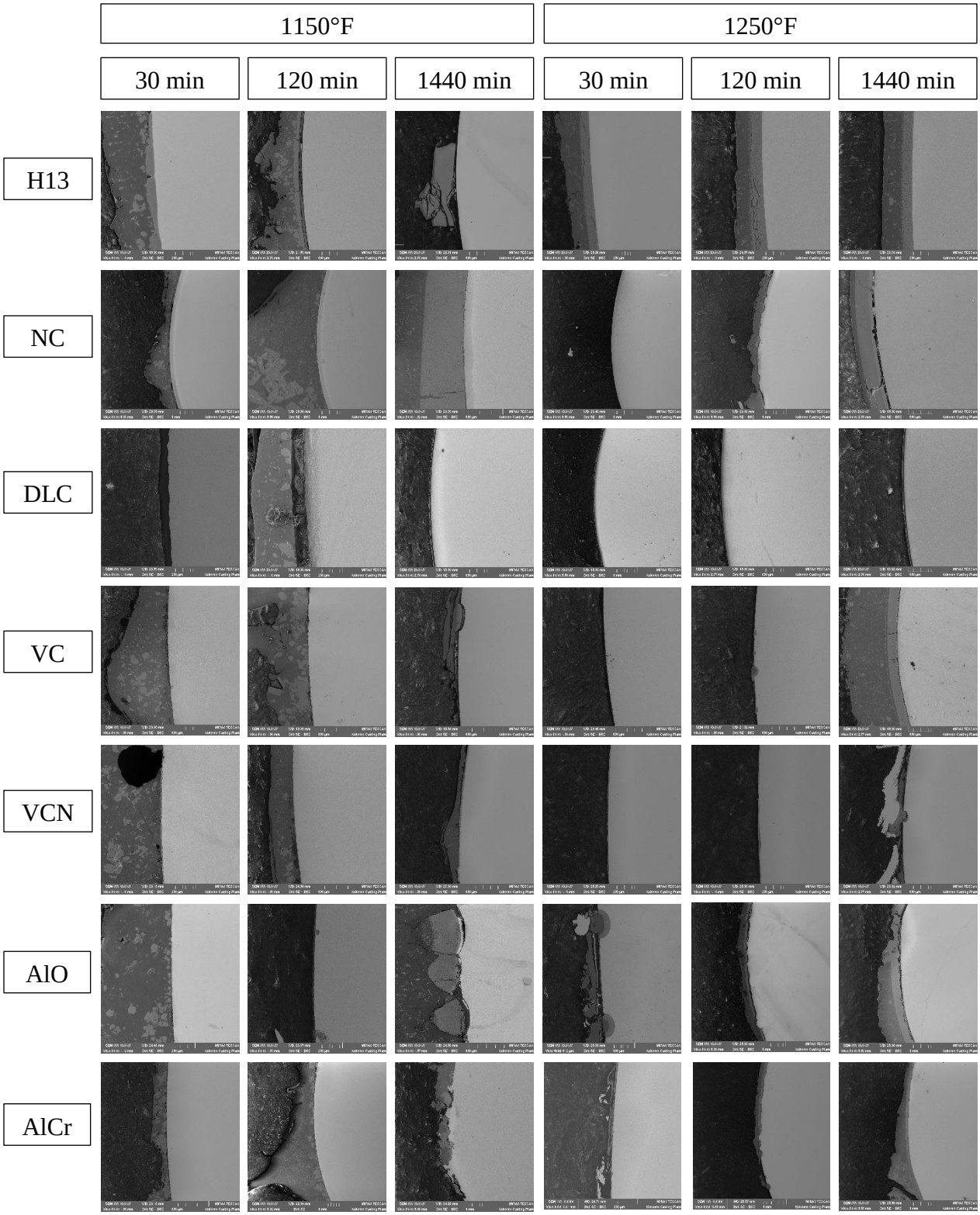

Figure 130. Composite image of dunk test results. Care should be employed during interpretation due to variation in image magnifications. Refer to the full-size images in the previous sections for better resolution.

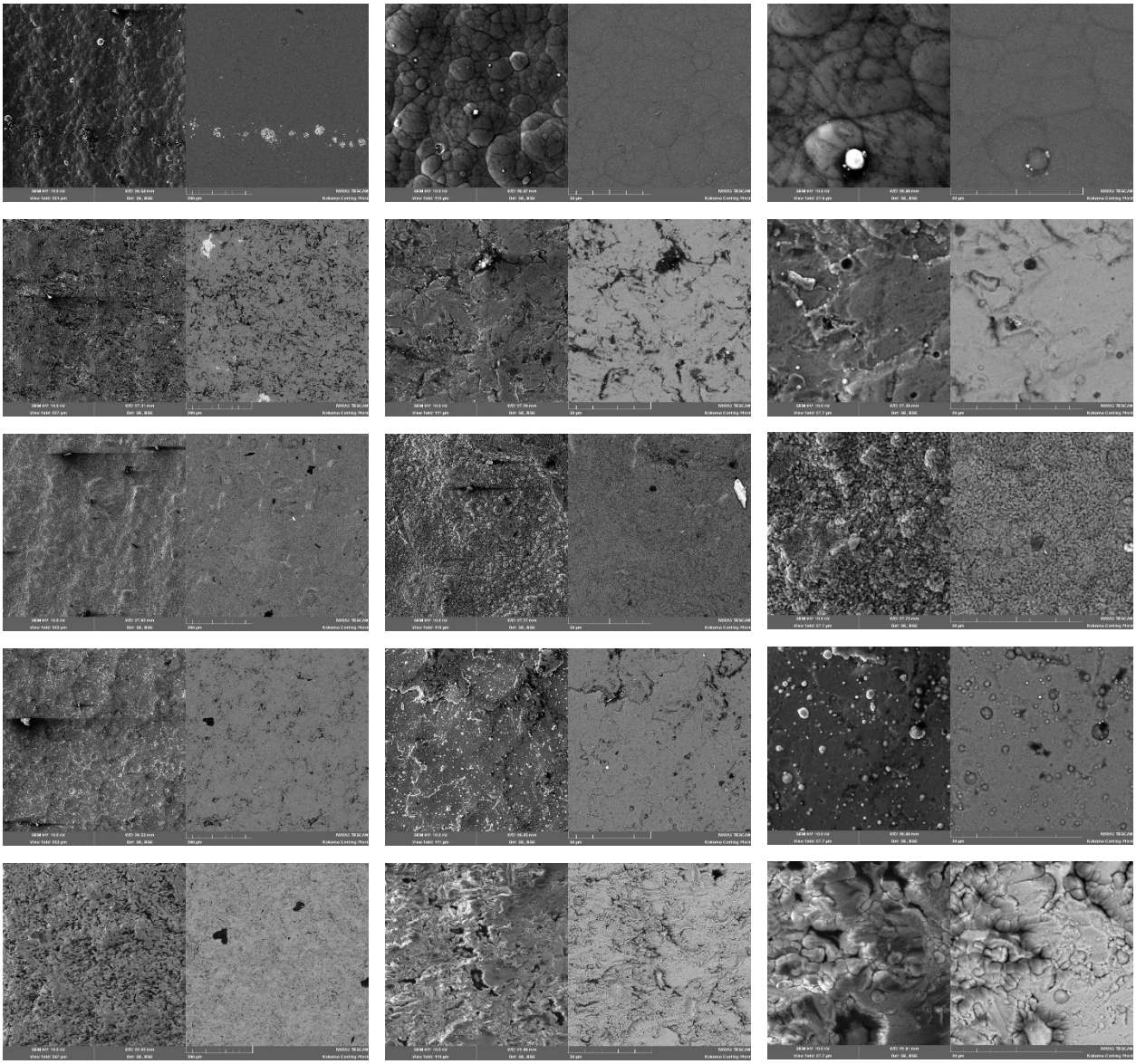

Figure 131. Composite showing coating structures in qualitative results rank order. Starting from the top: PACVD Si-DLC, PVD VCN, TRD VCN, PVD AlCrN, and PVD AlO. with 500x, 2500x, and 10000x magnifications and rows are.

4.2.9 Iron Depletion Behind Coatings

A phenomenon was observed in multiple specimens in which areas directly behind the coating were depleted of iron with no evidence of infiltration by the aluminum alloy. Multiple theories could explain this, such as the coating process causing a removal of iron from the steel matrix

before dunking, or the coating acting as a one-way filter in which the iron atoms are able to escape through the coating into the aluminum melt. The evidence of the study would suggest that the depletion was not caused by the coating process, since the depletion areas seem to follow the intermetallic reaction front in the NC specimen, as shown in Figure 132.

It is also possible that all reactions between H13 substrates and molten aluminum begin with a depletion of iron in the solid matrix, and the coatings in this study allowed the reaction rate to slow to a time scale that allowed the phenomenon to be observed in this study. A smaller time scale study on non-coated H13 could be used to test this theory. In addition, the theory of coating failures in die casting needs to be adjusted, as it has become evident that the coating can be intact while the reaction between the aluminum and steel substrate begins.

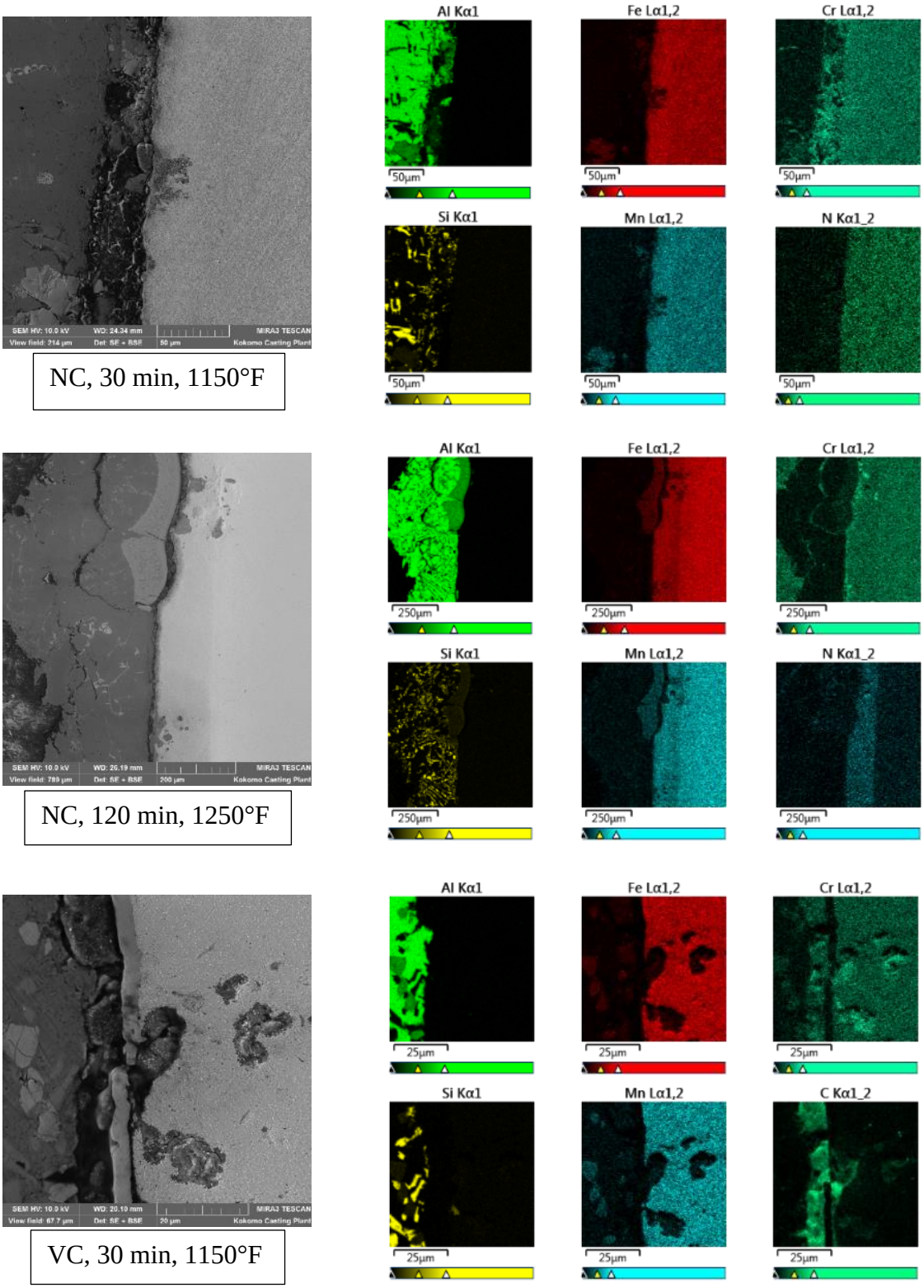

Figure 132. Composite showing iron depletion behind coatings with EDS maps.

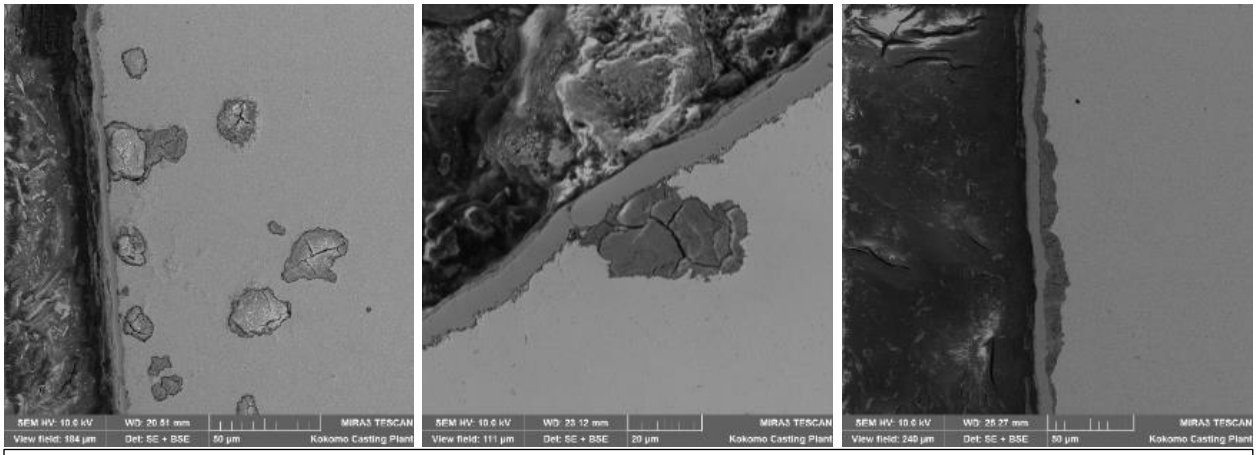

VC, 30 min, 1250°F VCN, 30 min 1150°F VCN, 120min, 1250°F

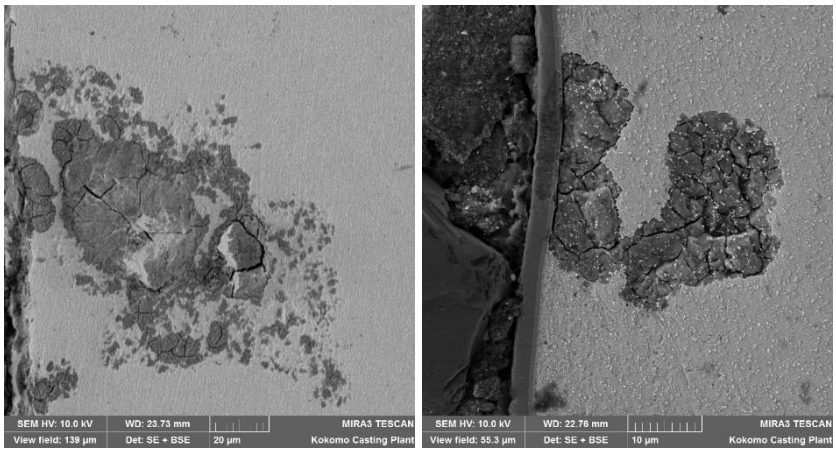

Al2O3, 30 min, 1150°F AlCrN, 30 min, 1150°F

Figure 133. Composite of additional evidence of iron depletion behind coatings.

4.2.10 Reactions and Wormholes in Silicon Doped DLC Coating

When examining the coating interface of the specimens that were dunked for 1440 minutes, multiple reaction phenomena were found. Magnesium from the melt infiltrated the first few microns of the Si-DLC coating, while carbon was pulled from the coating to form a layer consisting primarily of aluminum, chromium, and carbon. The chromium looked to be provided from the movement of chromium from the H13 matrix through a wormhole that formed in the coating.

The wormhole that formed allowed an exchange of material between the aluminum melt and H13 matrix. This exchange included the movement of aluminum, silicon, and magnesium into the H13 steel matrix, while also allowing chromium to move from the H13 matrix out to the interface of the coating and melt.

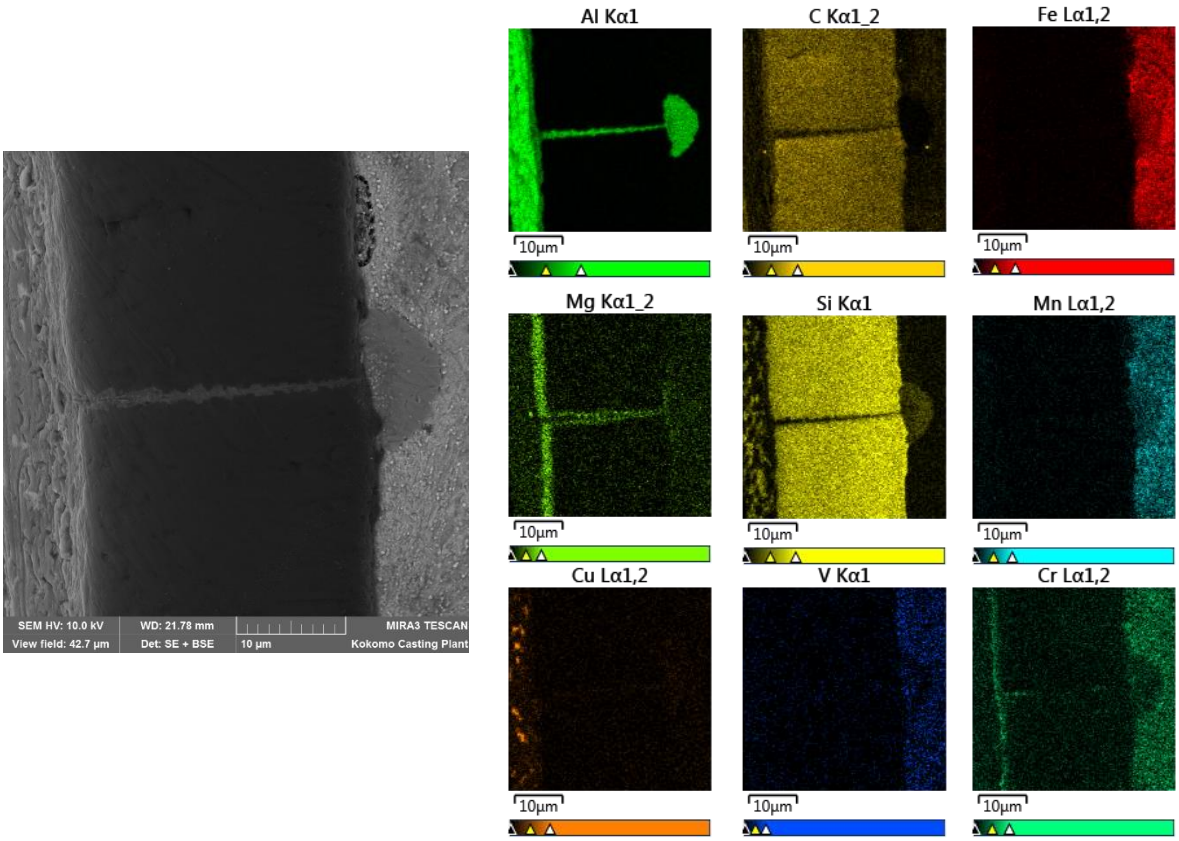

Figure 134. Composite showing the wormhole and reaction phenomena on a Si-DLC specimen dunked for 1440 minutes at 1250°F.

4.3 Friction Factors, Pressure Loss, and Heat Transfer Coefficients of LBP 3DP Conformal Cooling Lines

The plot of the measured results of the friction factor testing are shown in Figure 135. The data follows the trends of fluid flow in a pipe that were originally found by Moody, with an increasing friction factor through the transition zone from laminar (Reynold's number less or equal to 2000) to turbulent flow followed by a drop and stabilization once full turbulence is

achieved. Based on the empirical measurements, idealized curves are created and shown in Figure 136. It should be noted that the dashed portion of the idealized curve for the two-millimeter diameter line has been estimated based on the trends observed in the other diameters. This estimation was required due to the 50 psi water supply pressure used in the experiment being insufficient to create the flow rate required to reach the stabilized turbulent regime. These curves can be used by a die caster to estimate the expected pressure drop and heat transfer coefficients when using conformal cooling lines produced with laser powder bed additive manufacturing. In order to ease this estimation, contour plots of pressure loss per length of line and heat transfer coefficient are given as a function of conformal cooling line diameter and water flow rate.

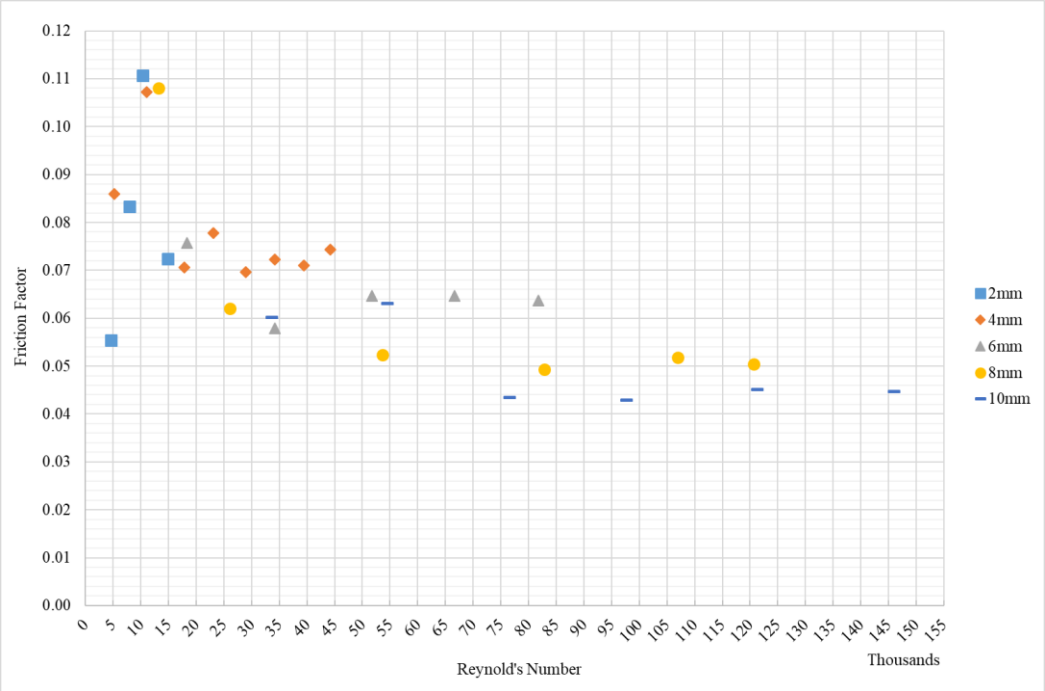

Figure 135. Measurement data of friction factor as a function of Reynold's number for metal pipes with different internal diameters produced by laser powder bed additive manufacturing.

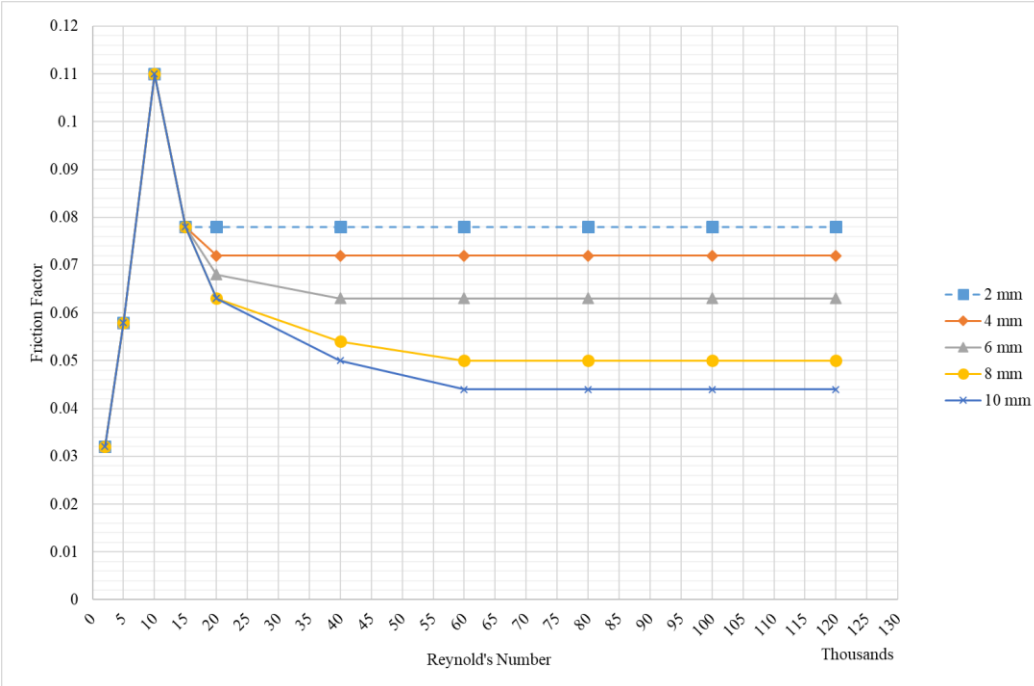

Figure 136. Idealized curves for friction factor as a function of Reynold's number for metal pipes with different internal diameters produced by laser powder bed additive manufacturing.

4.3.1 Allowable Length of Cooling Line for Pressure Drop

The pressure loss contour plots, shown in Figure 137 and Figure 138, can be used by a die caster to determine acceptable design combinations based on their available water supply pressures.

$$Allowable\ Length\ for\ Supply\ Pressure = \frac{Supply\ Pressure}{Pressure\ Loss\ per\ Length\ of\ Cooling\ Line}$$

For example, a die casting plant might be capable of providing 30 psi for the cooling water supply at the die casting die and the tool engineer is attempting to use a 5 mm diameter cooling line with a flow rate of 4 gal/min. In this case, the tool engineer would find they can use no more than approximately 6 inches of cooling line in their design. If the cooling line needed to be longer, a larger diameter or less flow would need to be used. If neither of these design

concessions are found acceptable, then more pressure must be provided, which can be done by raising the entire system pressure or locally boosting. A common practice is to use a booster pump for low flow die channels, with pressures as high as 300 psi provided. The same 5 mm channel could then flow approximately 60 inches at 4 gal/min.

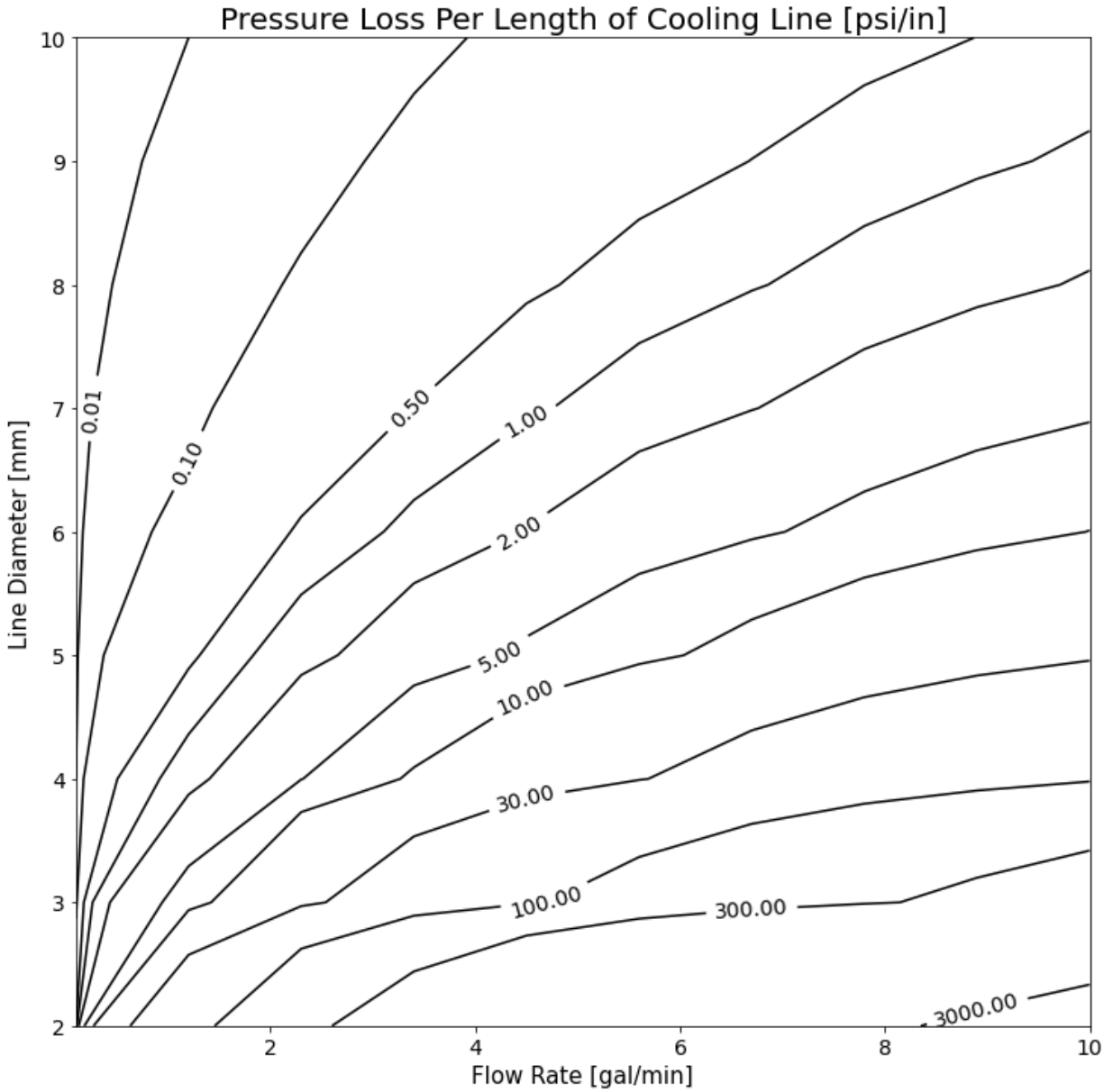

Figure 137. Contour plot showing pressure loss per length of conformal cooling line as a function of cooling line diameter and flow rate.

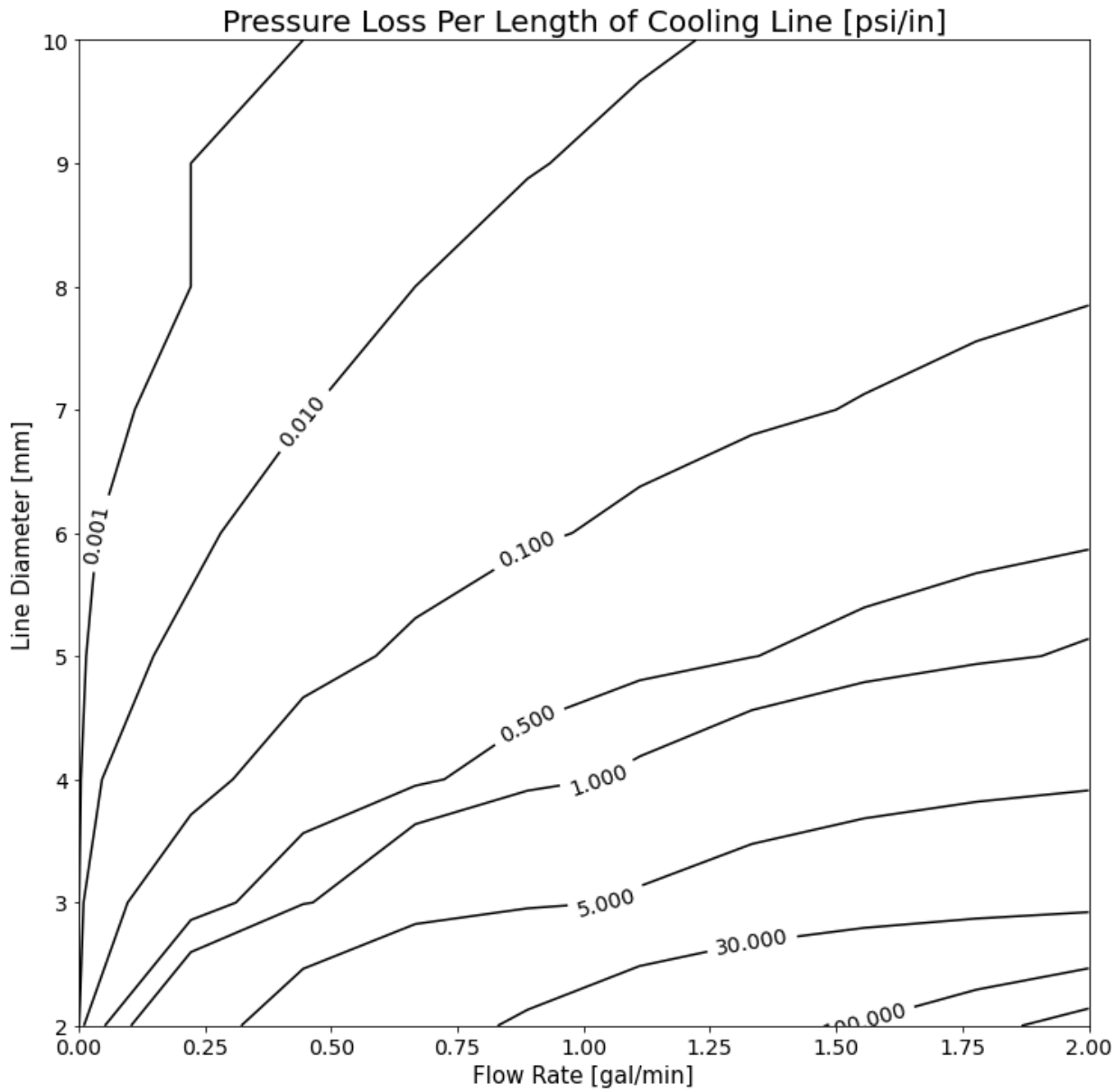

Figure 138. Contour plot showing pressure loss per length of conformal cooling line as a function of cooling line diameter and flow rate. The values of the lines in the lower right are 100 and 150 psi/in.

4.3.2 Heat Transfer Coefficient of Conformal Cooling Lines

The calculations performed in the application of the cooling line heat transfer model included an estimation of the heat transfer coefficient using the equations described in section 2.4.3.3. These

estimations are shown as contour plots in Figure 139 and Figure 140. A die casting tool engineer can use this plot to quickly select the heat transfer coefficient to use for conformal cooling lines in simulation software, based on the design constraints and decisions. It is suggested to first use the cooling water supply pressure to estimate the flow rate for a selected diameter, and then find the heat transfer with said diameter and flow rate.

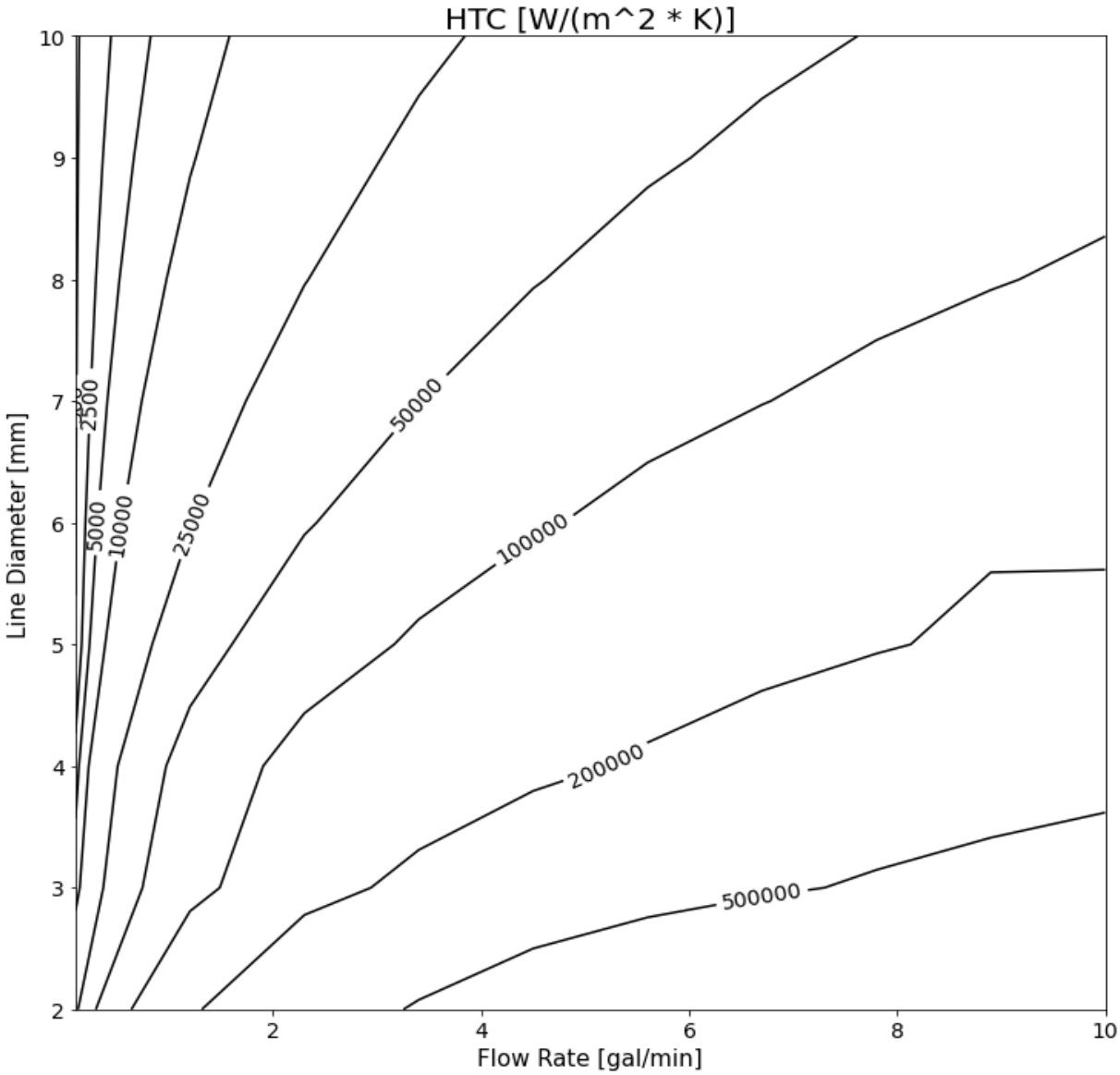

Figure 139. Contour plot showing the heat transfer coefficient of a conformal cooling line as a function of cooling line diameter and flow rate. The line in the upper left is 500 W/m^{2}K.

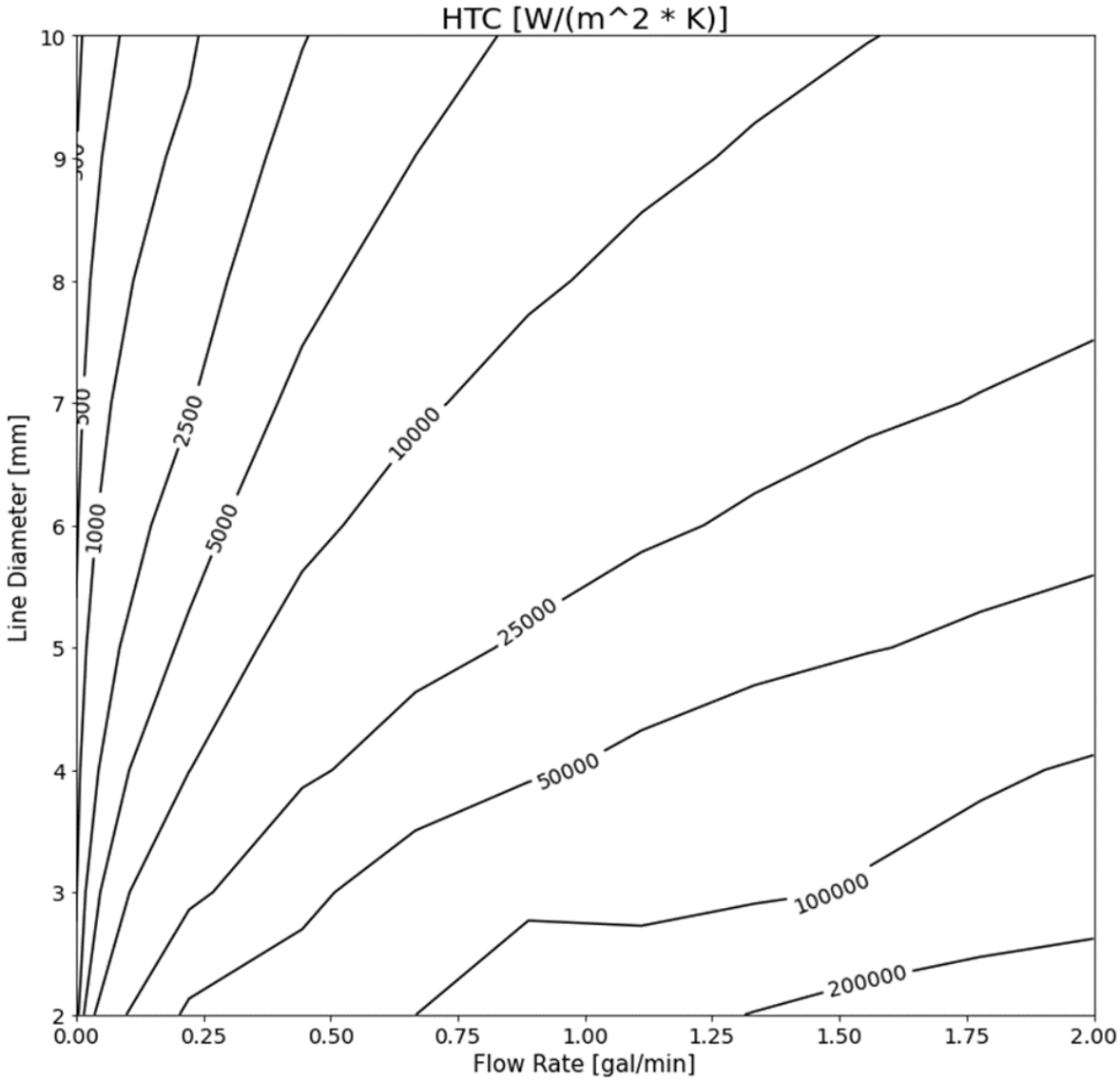

Figure 140. Contour plot showing the heat transfer coefficient of a conformal cooling line as a function of cooling line diameter and flow rate. The lines in the upper left are 300 and 500 W/m^2K.

4.3.3 Observations of the Printed Steel Tubes

The printed steel tubes showed some interesting phenomena that would impact the friction factors, and subsequently the heat transfer characteristics of conformal cooling lines in dies. Shown in Figure 141, the printed tubes have an area of increased roughness on the top side of the hole. This was caused by the printing process causing extra powder to be sintered to the

unsupported overhang. This affect was found to occur on all surfaces that were downward facing in the print orientation. This means that conformal cooling lines created by laser powder bed printing will have non-uniform flow and heat transfer around the circumference of the holes produced. The exact effects of this non-uniformity in surface roughness warrants further study in future work.

Figure 141. Laser powder bed printed steel tubes showing the holes with increased roughness on the top, downward facing surfaces.

4.4 Conformal Cooling Line Design Models

The cooling line experiment culminated with the creation of a set of design equations that guide design decisions for die cooling lines. The derivations from statistical modelling for these equations are shown in subsequent sections.

The maximum die surface temperature at the time of next cycle start can be calculated as:

$$T_{max} = 280 + 9.23 * D + 18.9 * SL + 9.99 * DS - 8.96 * tC - 15.1 * D * GPM$$

The average die surface temperature at the time of next cycle start can be calculated as:

$$T_{avg} = 263 + 11.5 * D + 14.7 * SL + 14.0 * DS - 8.46 * tC - 15.8 * D * GPM$$

The time required to solidify the casting being cooled by the waterline can be calculated as:

$$tSol = -7.12 + CT$$

$$* \left(2.23 + SL * \left(0.0814 + 0.0865 * DS - D * (0.00812 - 0.0124 * GPM)\right)\right)$$

The heat removal rate of the designed cooling line can be calculated as:

$$Designed\ Heat\ Removal\ Rate = C_g * WLHRR$$

$$DHRR = C_g * (2.92 - 0.0637 * D + 0.228 * SL - 0.0669 * DS - 0.162 * tC + 0.00677 * CT$$

$$* tC + 0.0148 * SL * D * GPM - 0.0000480 * SL * CT * DS * D)$$

The allowable cooling line length before boiling can be calculated as:

$$La = \frac{34.6 + GPM * [2290 - 0.103 * SL + 55.6 * DS + tC * (179 - 7.33 * SL - 4.29 * CT)]}{C_g}$$

4.4.1 Maximum Surface Temperature

The adjusted R-squared for the simple linear model is 0.941, which indicates that 94.1% of the variation in the simulated maximum surface temperature results can be explained without incorporating interactions. This model is easy to use, however there seems to be a physical anomaly in the prediction model, with a thicker casting causing a lower die temperature. Including interactions to the third order and performing a backward selection model thinning procedure, produces a model with one fewer term than the simple linear model, while maintaining similar prediction accuracy.

```
                            OLS Regression Results
==============================================================================
Dep. Variable:                   Tmax   R-squared:                       0.942
Model:                            OLS   Adj. R-squared:                  0.941
Method:                 Least Squares   F-statistic:                     1940.
Date:                Sun, 25 Apr 2021   Prob (F-statistic):               0.00
Time:                        00:30:34   Log-Likelihood:                -3300.7
No. Observations:                 729   AIC:                             6615.
Df Residuals:                     722   BIC:                             6648.
Df Model:                           6
Covariance Type:            nonrobust
==============================================================================
                 coef    std err          t      P>|t|      [0.025      0.975]
------------------------------------------------------------------------------
Intercept    344.3785      5.690     60.519      0.000     333.207     355.550
SL          1.885e+04    204.143     92.359      0.000    1.85e+04    1.93e+04
CT         -2526.4942    204.143    -12.376      0.000   -2927.279   -2125.709
DS          9985.4379    510.358     19.566      0.000    8983.475     1.1e+04
D           2689.8570    510.358      5.271      0.000    1687.894    3691.820
GPM          -90.8996      2.906    -31.275      0.000     -96.606     -85.193
tC            -8.9639      0.226    -39.600      0.000      -9.408      -8.520
==============================================================================
Omnibus:                       19.042   Durbin-Watson:                   0.880
Prob(Omnibus):                  0.000   Jarque-Bera (JB):               10.078
Skew:                           0.052   Prob(JB):                      0.00648
Kurtosis:                       2.434   Cond. No.                     5.24e+03
==============================================================================
```

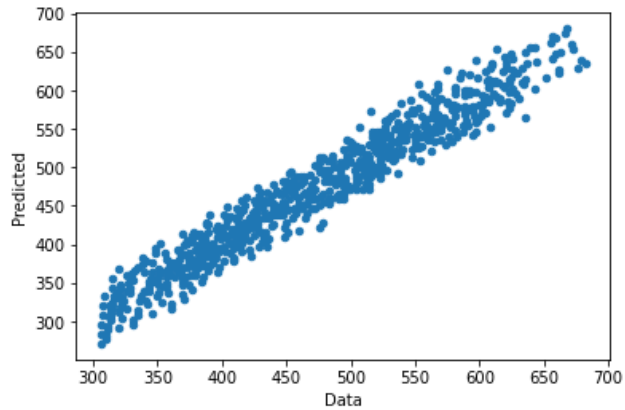

Figure 142. OLS regression results and predictions versus data for maximum surface temperature using the simple linear model.

```
                            OLS Regression Results
==============================================================================
Dep. Variable:                   Tmax   R-squared:                       0.934
Model:                            OLS   Adj. R-squared:                  0.934
Method:                 Least Squares   F-statistic:                     2062.
Date:                Sun, 25 Apr 2021   Prob (F-statistic):               0.00
Time:                        00:53:30   Log-Likelihood:                -3342.6
No. Observations:                 729   AIC:                             6697.
Df Residuals:                     723   BIC:                             6725.
Df Model:                           5
Covariance Type:            nonrobust
==============================================================================
                 coef    std err          t      P>|t|      [0.025      0.975]
------------------------------------------------------------------------------
Intercept    279.7237      5.462     51.214      0.000     269.001     290.447
D           9232.0011    581.180     15.885      0.000    8090.998    1.04e+04
SL          1.885e+04    216.078     87.257      0.000    1.84e+04    1.93e+04
DS          9985.4379    540.194     18.485      0.000    8924.901     1.1e+04
tC            -8.9639      0.240    -37.413      0.000      -9.434      -8.494
D:GPM       -1.51e+04    494.734    -30.516      0.000   -1.61e+04   -1.41e+04
==============================================================================
Omnibus:                        3.313   Durbin-Watson:                   0.749
Prob(Omnibus):                  0.191   Jarque-Bera (JB):                3.326
Skew:                           0.138   Prob(JB):                        0.190
Kurtosis:                       2.818   Cond. No.                     6.19e+03
==============================================================================
```

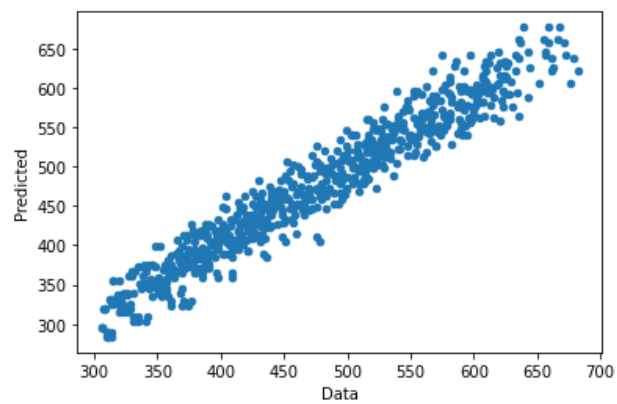

Figure 143. OLS regression results and predictions versus data for maximum surface temperature after model selection process.

$$T_{max} = 280 + 9.23 * D + 18.9 * SL + 9.99 * DS - 8.96 * tC - 15.1 * D * GPM$$

4.4.2 Average Surface Temperature

The simple linear model for the average surface temperature has an adjusted R-squared value of 0.938. Allowing for third order interactions, and performing a backward selection model

thinning procedure, can produce a model with one fewer term than the simple linear model, while maintaining similar prediction accuracy.

```
                            OLS Regression Results
==============================================================================
Dep. Variable:                   Tavg   R-squared:                       0.939
Model:                            OLS   Adj. R-squared:                  0.938
Method:                 Least Squares   F-statistic:                     1848.
Date:                Sun, 25 Apr 2021   Prob (F-statistic):               0.00
Time:                        01:23:59   Log-Likelihood:                -3207.6
No. Observations:                 729   AIC:                             6429.
Df Residuals:                     722   BIC:                             6461.
Df Model:                           6
Covariance Type:            nonrobust
==============================================================================
                 coef    std err          t      P>|t|      [0.025      0.975]
------------------------------------------------------------------------------
Intercept    327.4864      5.008     65.393      0.000     317.654     337.318
SL          1.465e+04    179.661     81.540      0.000    1.43e+04     1.5e+04
CT         -2323.3664    179.661    -12.932      0.000   -2676.086   -1970.646
DS          1.404e+04    449.152     31.256      0.000    1.32e+04    1.49e+04
D           4639.2592    449.152     10.329      0.000    3757.459    5521.059
GPM          -95.0822      2.558    -37.172      0.000    -100.104     -90.060
tC            -8.4611      0.199    -42.472      0.000      -8.852      -8.070
==============================================================================
Omnibus:                       31.417   Durbin-Watson:                   1.062
Prob(Omnibus):                  0.000   Jarque-Bera (JB):               13.772
Skew:                           0.041   Prob(JB):                      0.00102
Kurtosis:                       2.332   Cond. No.                     5.24e+03
==============================================================================
```

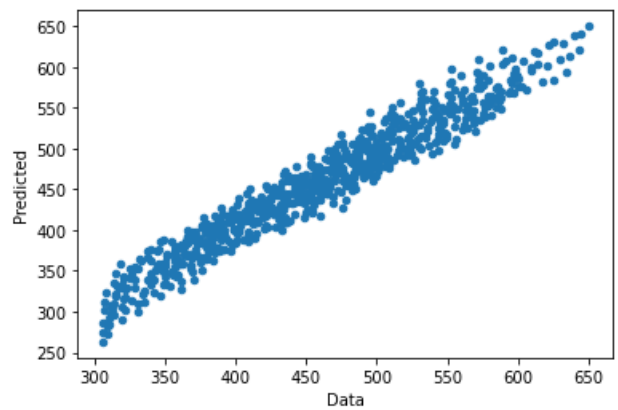

Figure 144. OLS regression results and predictions versus data for average die surface temperature using the simple linear model.

```
                            OLS Regression Results
==============================================================================
Dep. Variable:                   Tavg   R-squared:                       0.932
Model:                            OLS   Adj. R-squared:                  0.932
Method:                 Least Squares   F-statistic:                     1992.
Date:                Sun, 25 Apr 2021   Prob (F-statistic):               0.00
Time:                        01:24:19   Log-Likelihood:                -3244.6
No. Observations:                 729   AIC:                             6501.
Df Residuals:                     723   BIC:                             6529.
Df Model:                           5
Covariance Type:            nonrobust
==============================================================================
                 coef    std err          t      P>|t|      [0.025      0.975]
------------------------------------------------------------------------------
Intercept    263.0505      4.775     55.093      0.000     253.677     272.424
D           1.148e+04    508.056     22.592      0.000    1.05e+04    1.25e+04
SL          1.465e+04    188.891     77.556      0.000    1.43e+04     1.5e+04
DS          1.404e+04    472.227     29.728      0.000    1.31e+04     1.5e+04
tC            -8.4611      0.209    -40.397      0.000      -8.872      -8.050
D:GPM      -1.578e+04    432.486    -36.489      0.000   -1.66e+04   -1.49e+04
==============================================================================
Omnibus:                        3.816   Durbin-Watson:                   0.899
Prob(Omnibus):                  0.148   Jarque-Bera (JB):                3.144
Skew:                           0.055   Prob(JB):                        0.208
Kurtosis:                       2.698   Cond. No.                     6.19e+03
==============================================================================
```

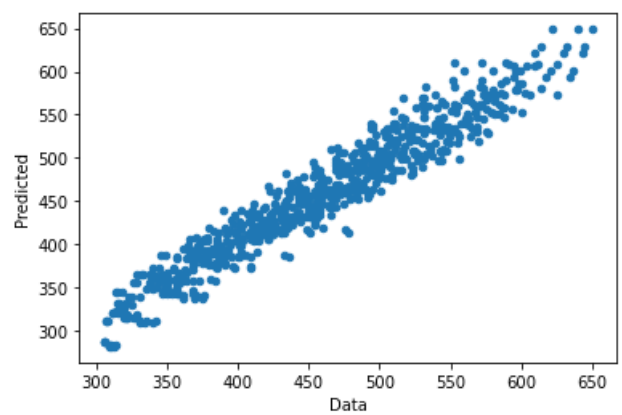

Figure 145. OLS regression results and predictions versus data for average die surface temperature, after the model selection process.

$$T_{avg} = 263 + 11.5 * D + 14.7 * SL + 14.0 * DS - 8.46 * tC - 15.8 * D * GPM$$

4.4.3 Solidification Time

```
                            OLS Regression Results
==============================================================================
Dep. Variable:                   tSol   R-squared:                       0.967
Model:                            OLS   Adj. R-squared:                  0.967
Method:                 Least Squares   F-statistic:                     3577.
Date:                Sun, 25 Apr 2021   Prob (F-statistic):               0.00
Time:                        08:09:20   Log-Likelihood:                -1816.1
No. Observations:                 729   AIC:                             3646.
Df Residuals:                     722   BIC:                             3678.
Df Model:                           6
Covariance Type:            nonrobust
==============================================================================
                 coef    std err          t      P>|t|      [0.025      0.975]
------------------------------------------------------------------------------
Intercept    -19.1006      0.743    -25.724      0.000     -20.558     -17.643
SL           969.9342     26.638     36.412      0.000     917.638    1022.231
CT          3724.2901     26.638    139.813      0.000    3671.994    3776.586
DS           838.8683     66.594     12.597      0.000     708.127     969.609
D            323.3076     66.594      4.855      0.000     192.567     454.049
GPM           -7.2037      0.379    -18.995      0.000      -7.948      -6.459
tC            -0.2053      0.030     -6.951      0.000      -0.263      -0.147
==============================================================================
Omnibus:                      210.595   Durbin-Watson:                   0.570
Prob(Omnibus):                  0.000   Jarque-Bera (JB):              558.675
Skew:                           1.465   Prob(JB):                    4.85e-122
Kurtosis:                       6.131   Cond. No.                     5.24e+03
==============================================================================
```

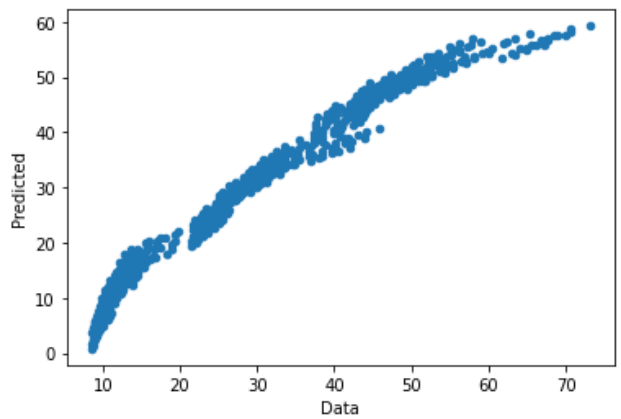

Figure 146. OLS regression results and predictions versus data for solidification time, using the simple linear model.

```
                            OLS Regression Results
==============================================================================
Dep. Variable:                   tSol   R-squared:                       0.987
Model:                            OLS   Adj. R-squared:                  0.987
Method:                 Least Squares   F-statistic:                 1.124e+04
Date:                Sun, 25 Apr 2021   Prob (F-statistic):               0.00
Time:                        08:19:08   Log-Likelihood:                -1473.1
No. Observations:                 729   AIC:                             2958.
Df Residuals:                     723   BIC:                             2986.
Df Model:                           5
Covariance Type:            nonrobust
==============================================================================
                 coef    std err          t      P>|t|      [0.025      0.975]
------------------------------------------------------------------------------
Intercept      -7.1238      0.180    -39.663      0.000      -7.476      -6.77
CT           2226.5044     32.354     68.817      0.000    2162.985    2290.02
SL:CT        8.136e+04   2634.567     30.881      0.000    7.62e+04    8.65e+0
CT:DS        8.651e+04   3848.764     22.477      0.000     7.9e+04    9.41e+0
SL:CT:D      8.124e+06   3.83e+05     21.192      0.000    7.37e+06    8.88e+0
SL:CT:D:GPM  -1.24e+07   3.26e+05    -37.986      0.000    -1.3e+07   -1.18e+0
==============================================================================
Omnibus:                       11.772   Durbin-Watson:                   1.099
Prob(Omnibus):                  0.003   Jarque-Bera (JB):               16.108
Skew:                          -0.160   Prob(JB):                     0.000318
Kurtosis:                       3.654   Cond. No.                     6.20e+06
==============================================================================
```

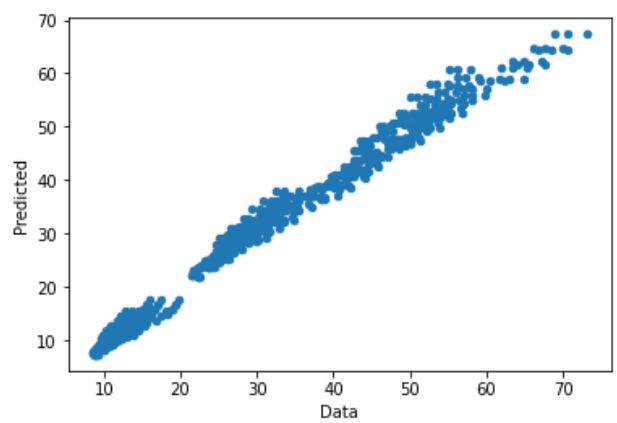

Figure 147. OLS regression results and predictions versus data for solidification time, after the model selection process.

$$tSol = -7.12 + 2.23 * CT + 0.0814 * SL * CT + 0.0865 * DS * CT - 0.00812 * SL * CT * D$$
$$- 0.0124 * D * GPM * SL * CT$$

$$tSol = -7.12 + CT$$
$$* \left(2.23 + SL * \left(0.0814 + 0.0865 * DS - D * (0.00812 - 0.0124 * GPM)\right)\right)$$

4.4.4 Heat Removal Rate

The results of the finite difference simulations give insight into how the temperature of the cooling line's water will change across the length of the cooling channel. Understanding that the heat removed by the cooling line is spread across the cycle time, a time average heat removal rate was calculated from the simulation results.

$$Heat\ Removal\ Rate = \frac{Heat\ Removed}{Cycle\ Time} = \frac{Heat\ Removed}{Solidifiction\ Time + Time\ for\ Cooling}$$

```
                            OLS Regression Results
==============================================================================
Dep. Variable:                  WLHRR   R-squared:                       0.927
Model:                            OLS   Adj. R-squared:                  0.926
Method:                 Least Squares   F-statistic:                     1520.
Date:                Sun, 25 Apr 2021   Prob (F-statistic):               0.00
Time:                        10:14:05   Log-Likelihood:                -193.89
No. Observations:                 729   AIC:                             401.8
Df Residuals:                     722   BIC:                             433.9
Df Model:                           6
Covariance Type:            nonrobust
==============================================================================
                 coef    std err          t      P>|t|      [0.025      0.975]
------------------------------------------------------------------------------
Intercept      2.2050      0.080     27.487      0.000       2.048       2.363
SL           249.0698      2.878     86.545      0.000     243.420     254.720
CT            30.4549      2.878     10.582      0.000      24.805      36.105
DS           -95.6423      7.195    -13.293      0.000    -109.768     -81.517
D            -28.3424      7.195     -3.939      0.000     -42.468     -14.217
GPM            0.8647      0.041     21.104      0.000       0.784       0.945
tC            -0.0946      0.003    -29.654      0.000      -0.101      -0.088
==============================================================================
Omnibus:                        7.715   Durbin-Watson:                   1.142
Prob(Omnibus):                  0.021   Jarque-Bera (JB):                7.844
Skew:                          -0.253   Prob(JB):                       0.0198
Kurtosis:                       2.951   Cond. No.                     5.24e+03
==============================================================================
```

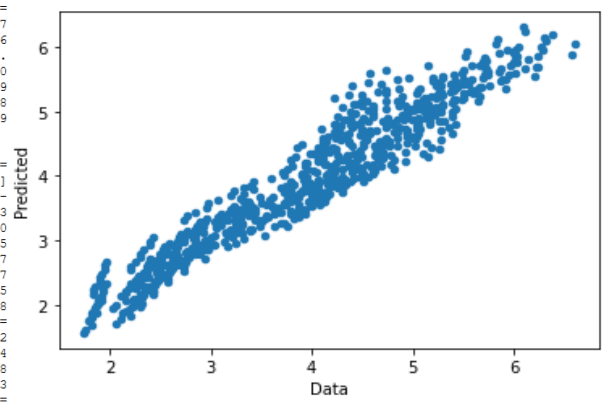

Figure 148. OLS regression results, and predictions versus data plot, for the water line heat removal rate, using the simple linear model.

```
                            OLS Regression Results
==============================================================================
Dep. Variable:                  WLHRR   R-squared:                       0.954
Model:                            OLS   Adj. R-squared:                  0.954
Method:                 Least Squares   F-statistic:                     2146.
Date:                Sun, 25 Apr 2021   Prob (F-statistic):               0.00
Time:                        10:29:28   Log-Likelihood:                -22.074
No. Observations:                 729   AIC:                             60.15
Df Residuals:                     721   BIC:                             96.88
Df Model:                           7
Covariance Type:            nonrobust
==============================================================================
                 coef    std err          t      P>|t|      [0.025      0.975]
------------------------------------------------------------------------------
Intercept      2.9235      0.079     36.888      0.000       2.768       3.079
D            -63.6648      7.468     -8.525      0.000     -78.327     -49.003
SL           227.8764      3.689     61.774      0.000     220.634     235.119
DS           -66.8624      7.237     -9.239      0.000     -81.071     -52.654
tC            -0.1624      0.005    -34.923      0.000      -0.172      -0.153
CT:tC          6.7743      0.391     17.345      0.000       6.008       7.541
SL:D:GPM    1.479e+04    477.496     30.980      0.000    1.39e+04    1.57e+04
SL:CT:DS:D -4.797e+07   7.46e+06     -6.432      0.000   -6.26e+07   -3.33e+07
==============================================================================
Omnibus:                        4.141   Durbin-Watson:                   0.637
Prob(Omnibus):                  0.126   Jarque-Bera (JB):                4.177
Skew:                           0.184   Prob(JB):                        0.124
Kurtosis:                       2.950   Cond. No.                     6.87e+09
==============================================================================
```

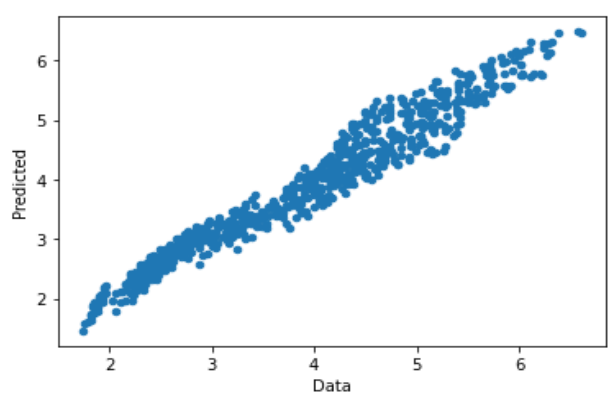

Figure 149. OLS regression results, and predictions versus data plot, for the heat removal rate, after the model selection process.

$$DHRR = C_g * (2.92 - 0.0637 * D + 0.228 * SL - 0.0669 * DS - 0.162 * tC + 0.00677 * CT * tC + 0.0148 * SL * D * GPM - 0.0000480 * SL * CT * DS * D)$$

It is important to realize that this heat removal rate is calculated from the symmetrical reduced model. The experienced heat removal rate in practice will be equal to the heat removal predicted from the symmetrically reduced model multiplied by a proper geometric factor, C_g, depending on the design situation. For a cooling line experiencing heating from one side, C_g is 2, for a cooling line experiencing heating from two sides, C_g is 4, and for a cooling line being heated from three sides, C_g is 6.

$$Designed\ Heat\ Removal\ Rate = C_g * WLHRR$$

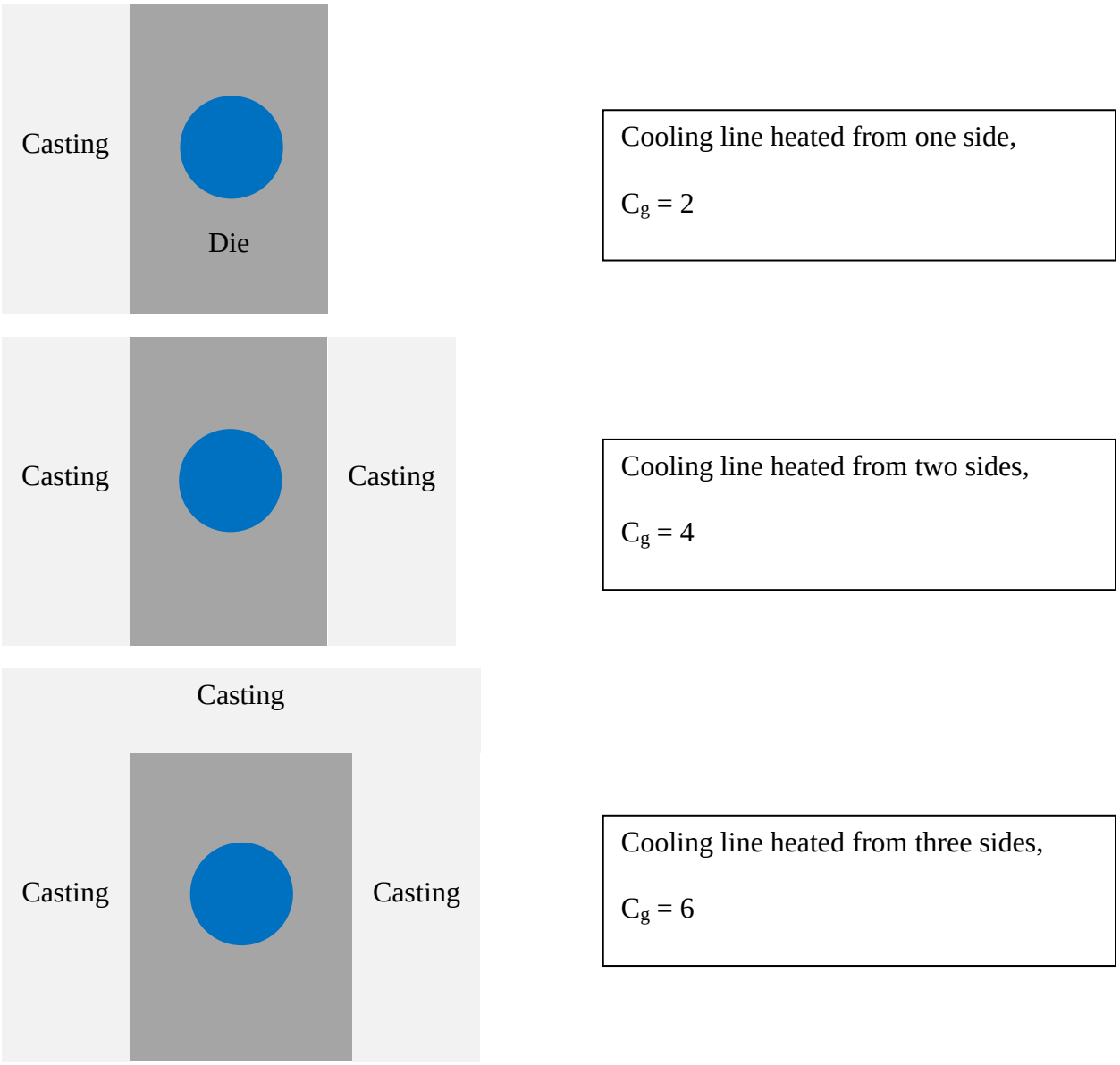

Figure 150. Geometric design situations, and corresponding geometric constants, to determine designed heat removal rate of a cooling line.

4.4.5 Allowable Cooling Line Length Before Boiling

The results of the simulated experiment also allow for the formulation and calculation of a characteristic length of cooling line for a given change in temperature. This is useful in order to avoid designing cooling lines whose water flow can boil. The formulation begins with the specific heat equation, with the mass flow rate of the cooling media expanded to allow the use of

the volumetric flow. This is convenient since volumetric flow is relatively easy to measure and control in industrial applications.

$$\dot{Q} = \dot{m}C\Delta T = \rho\dot{V}C\Delta T$$

We now introduce two new variables, both of a characteristic length. The heat removal rate of the water line is divided by a length that is equal to the length of the flow in the mathematical model. Since the flow length in the model was equal to the thickness of a single layer of control volumes, this value is a known input, and the heat removal rate per length of cooling line can be calculated. On the other side of the equation, the change in temperature of the cooling water is divided by a length of cooling line, creating a term that can be used to determine the length that a water line can be before it boils.

$$\frac{\dot{Q}}{l_{c1}} = \rho\dot{V}C\frac{\Delta T}{l_{c2}}$$

This equation is then rearranged to solve for the length of the cooling line.

$$l_{c2} = \frac{l_{c1}\rho\dot{V}C\Delta T}{\dot{Q}}$$

Since the inlet water temperature is a controlled process value, chosen to be 303 K in the mathematical model, and boiling of water is known to occur at 373 K, the maximum allowable length occurs when the change in temperature is equal to 70 K. Since the desire is to avoid boiling, a safety factor is employed by reducing the allowable change in temperature to 60 K.

$$Allowable\ Length, mm = 997\frac{kg}{m^3} * \frac{GPM\ \frac{gal}{min}}{15848\ \frac{gal * s}{m^3 * min}} * 4180\frac{J * K}{kg} * 60\ K * \frac{1\ mm}{C_g * WLHRR\ \frac{J}{s}}$$

$$Allowable\ Length, mm = 15778 \frac{mm * min * J}{gal * s} * \frac{GPM \frac{gal}{min}}{C_g * WLHRR \frac{J}{s}}$$

Table 16. Description of variables and constants used in the calculation of allowable length.

Physical Variable or Constant	Physical Phenomena	Python Model Variable Name (units)	Value Used (units)
$\dot{Q}$	Water line heat removal rate	WLHRR (J/s)	C_g * WLHRR (J/s)
ρ	Density of cooling water		997 (kg/m^3)
$\dot{V}$	Volumetric flow rate of cooling water	GPM (gal/min)	GPM (gal/min)
C	Specific heat of cooling water		4180 (J/(kg*K))
ΔT	Change in temperature of the cooling water		60 (K)
l_{c1}	Length of simulated flow		1 (mm)
l_{c2}	Length of cooling line		l_a (mm)
l_a	Allowable length before reaching ΔT		
C_g	Geometric constant based on cooling line design situation		2 if single sided, 4 if double sided, 6 if triple sided

The following is an example of the use of this equation, with the calculation made for the simulation data point shown in Table 17.

Table 17. A simulation data point

SL	CT	DS	D	GPM	tC	tSol	Tavg	Tmax	WLH
15	5	4	4	0.1	3	16.82	599.7577	676.6322	104.54

For the maximum waterline length for a 60 Kelvin temperature change in the design situation of the water line being heated on one side:

$$l_a = 15778 * \frac{0.1}{(\frac{2 * 104.5}{3 + 16.82})}$$

$$l_a = 150\ mm$$

From this concept, an allowable length is calculated as an output for each model run and regression analysis performed. The results of the initial model are shown in Figure 151. The model shows an adjusted R-squared value indicating a reduced prediction accuracy, but more alarming is that negative predictions are being made. Since negative lengths are not physically possible, the initial model is not acceptable for use. To find an acceptable model the model selection procedure is performed. After the model selection process, an acceptable, and easy to use equation is produced.

```
                            OLS Regression Results
==============================================================================
Dep. Variable:                     La   R-squared:                       0.877
Model:                            OLS   Adj. R-squared:                  0.876
Method:                 Least Squares   F-statistic:                     855.3
Date:                Sun, 25 Apr 2021   Prob (F-statistic):          4.94e-324
Time:                        16:15:45   Log-Likelihood:                -5062.7
No. Observations:                 729   AIC:                         1.014e+04
Df Residuals:                     722   BIC:                         1.017e+04
Df Model:                           6
Covariance Type:            nonrobust
==============================================================================
                 coef    std err          t      P>|t|      [0.025      0.975]
------------------------------------------------------------------------------
Intercept    465.2400     63.803      7.292      0.000     339.978     590.502
SL         -6.889e+04   2288.934    -30.098      0.000   -7.34e+04   -6.44e+04
CT         -1.177e+04   2288.934     -5.143      0.000   -1.63e+04   -7277.746
DS          2.415e+04   5722.335      4.220      0.000    1.29e+04    3.54e+04
D           3892.5365   5722.335      0.680      0.497   -7341.867    1.51e+04
GPM         2078.3829     32.588     63.777      0.000    2014.404    2142.362
tC            27.0927      2.538     10.675      0.000      22.110      32.076
==============================================================================
Omnibus:                      199.049   Durbin-Watson:                   1.041
Prob(Omnibus):                  0.000   Jarque-Bera (JB):              542.070
Skew:                           1.369   Prob(JB):                    1.95e-118
Kurtosis:                       6.217   Cond. No.                     5.24e+03
==============================================================================
```

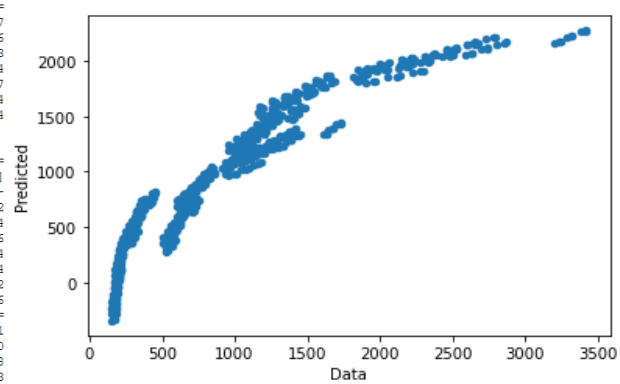

Figure 151. Regression results for simple model, and predictions versus data, for the allowable length of a waterline before 60K temperature change. This is the allowable length directly from the symmetrically reduced model, without the geometric constant applied.

```
                            OLS Regression Results
==============================================================================
Dep. Variable:                     La   R-squared:                       0.970
Model:                            OLS   Adj. R-squared:                  0.970
Method:                 Least Squares   F-statistic:                     3873.
Date:                Fri, 30 Apr 2021   Prob (F-statistic):               0.00
Time:                        21:31:47   Log-Likelihood:                -4549.0
No. Observations:                 729   AIC:                             9112.
Df Residuals:                     722   BIC:                             9144.
Df Model:                           6
Covariance Type:            nonrobust
==============================================================================
                 coef    std err          t      P>|t|      [0.025      0.975]
------------------------------------------------------------------------------
Intercept     34.5728      8.370      4.131      0.000      18.141      51.005
GPM         2294.0227     64.795     35.404      0.000    2166.814    2421.231
GPM:SL     -1.033e+05   5029.566    -20.541      0.000   -1.13e+05   -9.34e+04
GPM:DS       5.56e+04   5443.270     10.215      0.000    4.49e+04    6.63e+04
GPM:tC       179.3774      6.881     26.067      0.000     165.867     192.887
GPM:SL:tC  -7332.2068    591.373    -12.399      0.000   -8493.222   -6171.191
GPM:CT:tC  -4294.5449    256.006    -16.775      0.000   -4797.151   -3791.939
==============================================================================
Omnibus:                       31.914   Durbin-Watson:                   0.593
Prob(Omnibus):                  0.000   Jarque-Bera (JB):               89.127
Skew:                           0.086   Prob(JB):                     4.43e-20
Kurtosis:                       4.704   Cond. No.                     5.31e+03
==============================================================================
```

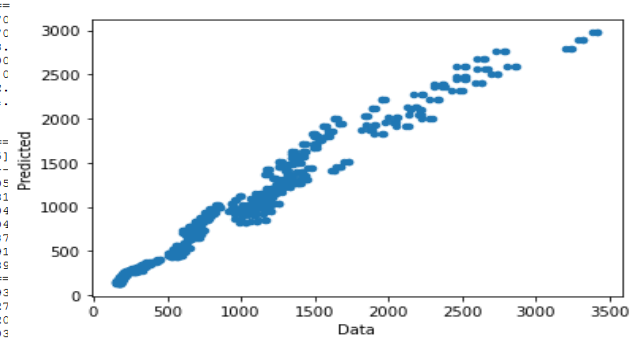

Figure 152. Regression results after model selection, and predictions versus data, for the allowable length of a waterline before 60K temperature change. This is the allowable length directly from the symmetrically reduced model, without the geometric constant applied.

$$La = 34.6 + GPM * [2290 - 0.103 * SL + 55.6 * DS + tC * (179 - 7.33 * SL - 4.29 * CT)]$$

REFERENCES

Akbarzadeh, M., Zandrahimi, M., & Moradpour, E. (2017). Molybdenum Disulfide (MoS2) Coating on AISI 316 Stainless Steel by Thermo-Diffusion Method. *Archives of Metallurgy and Materials*, 62(3), 1741–1748.

Allaby, M. (2013). Fick's laws of diffusion. In (Ed.), A Dictionary of Geology and Earth Sciences. Oxford University Press. Retrieved 3 Feb. 2019, from http://www.oxfordreference.com.ezproxy.lib.purdue.edu/view/10.1093/acref/9780199653065.001.0001/acref-9780199653065-e-9852.

Andresen, W. (2004). *Die cast engineering: A hydraulic, thermal, and mechanical process*. Hoboken: Taylor and Francis.

Armillotta, A., Baraggi, R., & Fasoli, S. (2014). SLM tooling for die casting with conformal cooling channels. *The International Journal of Advanced Manufacturing Technology*, *71*(1–4), 573–583. https://doi.org/10.1007/s00170-013-5523-7

Arrhenius, S. (1889). Über die Dissociationswärme und den Einfluss der Temperatur auf den Dissociationsgrad der Elektrolyte. *Zeitschrift Für Physikalische Chemie,* Vol.4(1).

Baba, K., Hatada, R., Flege, S., & Ensinger, W. (2014). DLC coating of interior surfaces of steel tubes by low energy plasma source ion implantation and deposition. *Applied Surface Science*, 310, 262–265.

Balloy, D., Tissier, J.-C., Giorgi, M.-L., & Briant, M. (2010). Corrosion Mechanisms of Steel and Cast Iron by Molten Aluminum. *Metallurgical and Materials Transactions A*, *41*(9), 2366–2376.

Carrera, E. A., Ramírez-Ramírez, J. H., Pérez-González, F. A., González, J. A., Crespo, I., Braceras, I., … Colás, R. (2017). Molten aluminium attack on iron based alloys. *International Journal of Cast Metals Research*, *30*(3), 171–179.

Çengel, Y. (2007). *Heat and mass transfer : A practical approach* (3rd ed., McGraw-Hill series in mechanical and aerospace engineering). Boston: McGraw-Hill.

Deqing, W., Ziyuan, S., & Longjiang, Z. (2003). A liquid aluminum corrosion resistance surface on steel substrate. *Applied Surface Science*, *214*(1–4), 304–311.

Dimla, D. E., Camilotto, M., & Miani, F. (2005). Design and optimisation of conformal cooling channels in injection moulding tools. *Journal of Materials Processing Technology*, *164–165*, 1294–1300. https://doi.org/10.1016/j.jmatprotec.2005.02.162

Doehler, H. (1951). *Die casting.* New York: McGraw-Hill.

Dybkov, V. I. (1993). Interaction of iron-nickel alloys with liquid aluminium. *Journal of Materials Science*, *28*(23), 6371–6380.

Dybkov, V.I. (2013) *Solid State Reaction Kinetics*. Kyiv: IPMS Publications.

Fick, A. (1855). On liquid diffusion. *The London, Edinburgh, and Dublin Philosophical Magazine and Journal of Science*, *10*(63), 30–39.

Frenkel, J. Z. Physik (1926) 37: 572. https://doi.org/10.1007/BF01397292

Gulizia, S., Jahedi, M. Z., & Doyle, E. D. (2001). Performance evaluation of PVD coatings for high pressure die casting. *Surface and Coatings Technology*, 140(3), 200–205.

Hairy, P., & Richard, M. (1997). Reduction of Sticking in Pressure Die Casting by Surface Treatment. Presented at the Many Faces of Die Casting, Minneapolis, MN: North American Die Casting Association.

Harvill, H., & Jordan, P. (1945). *High-pressure die casting; a design guide for engineers*. Vernon, Calif.: Harvill Mfg.

Herman, E.A., & Kirkman, J.S. (n.d). *Designing die casting dies series*. North American Die Casting Assocation.

Hintermann, H. E., & Hertz, D. (1985). United States Patent 4,556,098.

Hirt, G., & Kopp, R.. (2009). *Thixoforming semi-solid metal processing*. Weinheim Chichester: Wiley-VCH ; John Wiley distributor.

Hu, H., Chen, F., Chen, X., Chu, Y., & Cheng, P. (2004). Effect of cooling water flow rates on local temperatures and heat transfer of casting dies. *Journal of Materials Processing Technology*, *148*(1), 57–67. https://doi.org/10.1016/j.jmatprotec.2004.01.040

Huang, C. (2017). *Thermal Stress Analysis of Spot Cooling Line in Die Casting Die*. Die Casting Congress & Tabletop. North American Die Casting Association.

Hwang, S., Song, J., & Kim, Y. (2005). Effects of carbon content of carbon steel on its dissolution into a molten aluminum alloy. *Materials Science & Engineering A, 390*(1), 437-443.

Jahan, S.A. (2016). *Optimization of conformal cooling channels in 3d printed plastic injection molds.* [PhD Dissertation]. Purdue University.

Jiang, K., Münstermann, S., Günther, H.-J., & Schneider, J. M. (2010). Up-scaling of a Low Temperature PACVD Process for the Deposition of α/γ-Nanocrystalline Alumina Coated Tools for Thixocasting of 1.2208 steel. *Steel Research International*, *81*(7), 597–602.

Kaye, A., & Street, A. (1982). *Die casting metallurgy*. Cambridge. Butterworth Scientific.

Kind, R. (2011). *Proper cooling line diameter in a high pressure die casting die, is it really a good idea to increase the diameter of a cooling line?*. Die Casting Congress & Tabletop. North American Die Casting Association.

Lin, J. C. (2003). The Optimal Design of a Cooling System for a Die-Casting Die With a Free Form Surface. *The International Journal of Advanced Manufacturing Technology*, *21*(8), 612–619. https://doi.org/10.1007/s00170-002-1331-1

López, A.J., & Rams, J. (2015). Protection of carbon steel against molten aluminum attack and high temperature corrosion using high velocity oxygen-fuel WC–Co coatings. *Surface & Coatings Technology, 262*, 123-133.

Marques, S., Souza, A. F. de, Miranda, J., & Yadroitsau, I. (2015). Design of conformal cooling for plastic injection moulding by heat transfer simulation. *Polímeros*, *25*(6), 564–574. https://doi.org/10.1590/0104-1428.2047

Mehrer, H. (2007). *Diffusion in solids: fundamentals, methods, materials, diffusion-controlled processes* (Vol. 155). Springer Science & Business Media.

Mihelich, J., & Decker, R. F. (1996). *WO 97/45218*. World Intellectual Property Organization.

Mohsenifar, A., Aboutalebi, M., & Seyedein, S. (2014). High temperature oxidation effect on the dissolution rate of hot-dip aluminized steel in aluminum melt. *Advanced Materials Research, 970-970*, 248-251.

North American Die Casting Association. (2007). *Intro to die casting.* Arlington Heights, IL: Author.

Noyes, A. A., & Whitney, W. R. (1897). The rate of solution of solid substances in their own solutions. *Journal of the American Chemical Society*, *19*(12), 930–934.

Okayasu, M., Hitomi, M., & Yamazaki H. (2008). Hot chamber diecasting with Si 3 N 4 ceramic injection system: Application to aluminium alloy components. *International Journal of Cast Metals Research, 21*(5), 339-348.

Okayasu, M., Hitomi, M., & Yamazaki, H. (2010). New ceramic injection systems for hot chamber die casting of aluminium alloys. *International Journal of Cast Metals Research, 23*(4), 246-249.

Okayasu, M., Yoshifuji, S., Mizuno, M., Hitomi, M., & Yamazaki, H. (2009). Comparison of mechanical properties of die cast aluminium alloys: Cold v . hot chamber die casting and high v . low speed filling die casting. *International Journal of Cast Metals Research, 22*(5), 374-381.

OrjuelaG., A., Rincón, R., & Olaya, J. J. (2014). Corrosion resistance of niobium carbide coatings produced on AISI 1045 steel via thermo-reactive diffusion deposition. *Surface and Coatings Technology*, *259*, 667–675.

Panjan, P., Čekada, M., Panjan, M., & Kek-Merl, D. (2009). Growth defects in PVD hard coatings. *Vacuum*, 84(1), 209–214. https://doi.org/10.1016/j.vacuum.2009.05.018

Pfohl, C., Gebauer-Teichmann, A., & Rie, K.-T. (1999). Application of wear-resistant PACVD coatings in aluminium diecasting: economical and ecological aspects. *Surface and Coatings Technology*, *112*(1–3), 347–350.

Poirier, D.J., & Poirier, E.J. (1994). *Heat transfer fundamentals for metal casting*. Warrendale, Pennsylvania. The Minerals, Metals, and Materials Society.

Rie, K., Pfohl, C., Lee, S., & Kang, C. (1997). Development of zirconium and boron containing coatings for the application on aluminium diecasting tools by means of MO–PACVD. *Surface and Coatings Technology*, *97*(1–3), 232–237.

Schwam, D., Wallace, J. F., Zhu, Y., Courtright, E., & Adkins, H. (2005). Evaluation of Heat Checking and Washout of Heat Resistant Superalloys and Coatings for Die inserts. United States.

Schwam, D. (2015). *Additive Manufacturing for Die Casting Applications*. Die Casting Congress & Exposition. NADCA.

Schwam, D. (2016). *Additive Manufacturing for Cores with Conformal Cooling Lines*. Die Casting Congress & Tabletop. NADCA.

Sen, U., Pazarlıoglu, S. S., & Sen, S. (2008). Niobium boride coating on AISI M2 steel by boro-niobizing treatment. *Materials Letters*, 62(16), 2444–2446.

Shah, S.V., & Dahotre, N. B. (2002). Laser surface-engineered vanadium carbide coating for extended die life. *Journal of Materials Processing Technology, 124*(1), 105-112.

Shayfull, Z., Sharif, S., MohdZain, A., MohdSaad, R., & Fairuz, M. A. (2013). Milled Groove Square Shape Conformal Cooling Channels in Injection Moulding Process. *Materials and Manufacturing Processes*, 130122112458009. https://doi.org/10.1080/10426914.2013.763968

Song, J. (2014). *On the performance of commercial coatings for die casting* (PhD Disseration). Purdue University.

Stimpson, C. K. (2017). *COOLING PERFORMANCE OF ADDITIVELY MANUFACTURED MICROCHANNELS AND FILM COOLING HOLES* [PhD Dissertation]. The Pennsylvania State University.

Subramanian, R.S. (n.d.). *Heat transfer in flow through conduits.* Department of Chemical and Biomolecular Engineering Clarkson University.

Tang, N., Li, Y. P., Kurosu, S., Koizumi, Y., Matsumoto, H., & Chiba, A. (2012). Interfacial reactions of solid Co and solid Fe with liquid Al. *Corrosion Science*, *60*, 32–37.

Tentardini, E. K., Kunrath, A. O., Aguzzoli, C., Castro, M., Moore, J., & Baumvol, I. J.R. (2008). Soldering mechanisms in materials and coatings for aluminum die casting. *Surface & Coatings Technology, 202*(16), 3764-3771.

Upton, B., Allsop, D., & Kennedy, D. (1982). *Pressure diecasting*. Oxford; New York: Pergamon Press.

Wang, Q., Wang, W. J., Liu, H. J., & Zeng, C. L. (2017). Corrosion behavior of zirconium diboride coated stainless steel in molten 6061 aluminum alloy. *Surface and Coatings Technology*, *313*, 129–135.

Wang, Y. (1997). A study of PVD coatings and die materials for extended die-casting die life. *Surface & Coatings Technology, 94*, 60-63

Wang, Y., Yu, K.-M., & Wang, C. C. L. (2015). Spiral and conformal cooling in plastic injection molding. *Computer-Aided Design*, *63*, 1–11. https://doi.org/10.1016/j.cad.2014.11.012

Xiao, H., Chen, W., & Liu, Z. (2012). Corrosion resistance of 91W–6Ni–3Fe refractory metal, TiAl compound and iron based alloys in molten aluminum. *Transactions of Nonferrous Metals Society of China*, *22*(9), 2320–2326.

Yan, M., & Fan, Z. (2001). Review durability of materials in molten aluminum alloys. *Journal of Materials Science*, *36*(2), 285–295.

Yan, S., Wang, H., Sun, Q., He, P., Pang, C., Wang, H., & Wang, A. (2014). Growth characteristics and kinetics of niobium carbide coating obtained on AISI 52100 by thermal-reactive diffusion technique. *Journal of Wuhan University of Technology-Mater. Sci. Ed*., 29(4), 808–812.

Yu, M., Chu, Y.-L., & Shivpuri, R. (1993). *A Study of Corrosive Wear of Die Casting Materials* (No. ERC/NSM-C-93-06). National Science Foundation.

Zhu, H. (2014). *Dissolution rate and mechanism of metals in molten aluminum alloy A380* (Master Thesis). Retrieved from http://search.proquest.com.ezproxy.lib.purdue.edu/docview/1666812913

Zhu, Y., Schwam, D., Wallace, J. F., & Birceanu, S. (2004). Evaluation of soldering, washout and thermal fatigue resistance of advanced metal materials for aluminum die-casting dies. *Materials Science & Engineering A, 379*(1), 420-431.